Spring 2019

Nanoscale solidification of metals by atomistic simulations: From nucleation to nanostructural evolution

Avik Mahata

Department: Materials Science and Engineering

NANOSCALE SOLIDIFICATION OF METALS BY ATOMISTIC SIMULATIONS: FROM NUCLEATION TO NANOSTRUCTURAL EVOLUTION

by

AVIK KUMAR MAHATA

A DISSERTATION

Presented to the Faculty of the Graduate School of the

MISSOURI UNIVERSITY OF SCIENCE AND TECHNOLOGY

In Partial Fulfillment of the Requirements for the Degree

DOCTOR OF PHILOSOPHY

in

MATERIALS SCIENCE AND ENGINEERING

2019

Approved by:

Mohsen Asle Zaeem, Advisor
Ronald J. O'Malley
Aditya Kumar
Caizhi Zhou
Aleksandr V. Chernatynskiy

PUBLICATION DISSERTATION OPTION

This dissertation consists of the following six articles, which have been published or will be submitted for publications as follows:

Paper I: Pages 10-66 "Understanding Homogeneous Nucleation in Solidification of Aluminum by Molecular Dynamics Simulations" is published in *Modelling and Simulation in Materials Science and Engineering* 26.2 (2018): 025007.

Paper II: Pages 67-98 "Evolution of Solidification Defects in Deformation of Nano-Polycrystalline Aluminum" is accepted in *Computational Materials Science 163 (2019): 176-185.*

Paper III: Pages 99-125 "Size Effect on Nucleation Process during Solidification of Pure Metals by Atomistic Simulations" is ready for submission to the *Journal of Crystal Growth* (2019).

Paper IV: Pages 126-156 "Evidence of Liquid Ordering and Heterogeneities in Homogeneous Nucleation during Solidification of Pure Metals" is prepared for *Nature communication* (2019).

Paper V: Pages 157-196 "Solid–Liquid Coexistence of binary Al alloys by Molecular Dynamics Simulations Using the Modified Embedded-Atom Method" is prepared for submission to *Acta Materialia* (2019).

Paper VI: Pages 197-222 "Effects of Solidification Defects on Nanoscale Mechanical Properties of Rapid Directionally Solidified Al-Cu Alloy: A Large Scale Molecular Dynamics Study" is submitted to the *Journal of Metals* (2019).

ABSTRACT

Homogeneous nucleation during solidification in Al (fcc), Fe (bcc) and Mg (hcp) is studied by million-atom molecular dynamics (MD) utilizing the second nearest neighbor modified embedded atom method (2NN-MEAM) potentials. Spontaneous homogenous nucleation from the melt was produced without any influence of pressure, free surface effects and impurities. We also study the effect on the simulation size on homogenous nucleation and the heterogeneity in homogenous nucleation. The heterogeneity in homogenous nucleation originates from the twins, grain boundaries and short range order in the liquid during the initial stages of solidification.

To study the solid-liquid coexistence in binary Al alloys, interatomic potentials for binary Al-Cu, Al-Fe, Al-Ni, Al-Mg, Al-Si and Al-Ge alloys were developed based on 2NN-MEAM formalism. Using these interatomic potentials, we compare formation energies, elastic constants, lattice parameters, enthalpy of solid and liquid mixing with experimental or first principle data of the binary Al alloys. In addition, we also compare the liquidus temperature of the Al-alloys from the phase diagram to the MD simulation.

Finally, directional solidification of Al-11 at. % Cu is shown utilizing the 2NN-MEAM interatomic potential. The condition for directional solidification is produced by imposing dissimilar temperatures at the model boundaries along the [100] solidification direction to create a temperature gradient. Both the microstructural properties of solidified alloys and the mechanical properties under uniaxial tension is investigated.

ACKNOWLEDGMENTS

First, I would like to express my gratitude to my advisor, Dr. Mohsen Asle Zaeem for the continuous support of my Ph.D. study and related research, for his patience, motivation, and immense knowledge. Besides my advisor, I would like to thank the rest of my Ph.D. dissertation committee, Dr. Ronald J. O'Malley, Dr. Caizhi Zhou, Dr. Aditya Kumar and Dr. Aleksandr V. Chernatynskiy for their sincere help and suggestions during my Ph.D. work. They were very encouraging, understanding, supportive and always available to help me whenever I had any question. I also appreciate everything I have learned from my committee members in the classroom.

I would like to thank my friends, my colleagues and the faculty and staff in the department of Materials Science and Engineering who have helped me to achieve my research goals during my Ph.D. studies. It was a great pleasure working with them and I appreciate their ideas, help and good humor. Special thanks to The Extreme Science and Engineering Discovery Environment (XSEDE) (award number TG-DMR140008) , Department of Energy (DOE), University of Missouri High-Performance Computing for the necessary computational resources.

Last but by no means least, I would like to thank my family, the most important people in my world: my mom, dad, brother, and my gracious wife, Sarah who have totally supported me throughout my entire studies.

I also like to acknowledge the funding support from the National Science Foundation under Grant No. NSF-CMMI 1537170.

TABLE OF CONTENTS

LIST OF ILLUSTRATIONS

PAPER I

PAPER VI

LIST OF TABLES

PAPER VI

1. INTRODUCTION

Liquid-to-solid (solidification) and solid-to-solid (solid state) phase transformations are essential structural evolution behaviors in the processing of single and polycrystalline materials. In many manufacturing processes including casting, welding and additive manufacturing, these phase transformations are commonly observed. Moreover, the resulting nano and microstructures are responsible for the mechanical and physical properties, as well as the yield and failure of the materials. Therefore, fundamental understandings of these phenomena are in urgent demand in order to identify the nano/microstructure-property relations of materials, and also accelerate the design of new generation of materials with unprecedented properties. During solidification and solid state phase transformation of alloys several inherent processes are involved: crystal nucleation, segregation of alloying elements, defects formation (such as vacancies, voids, dislocations, stacking faults, etc.), metastable and/or intermetallic phase formations, grain growth, and recrystallization. Current understandings of the mechanisms of crystal nucleation and defect formation are extremely limited due to the challenges in conducting experimental studies. For example, experimental techniques are incapable of capturing the dynamic formation and evolution process of relatively small nuclei (~2 nm) at the melting point in an opaque bulk material.

In metal manufacturing processes involving solidification (e.g., casting [13] , welding [14], and laser additive manufacturing [15]), the crystal nucleation from the melt controls the formation and growth of nano- and micro-structures of metals. The solidification structures of materials significantly influence their mechanical and physical

properties. If large undercooling can be achieved before crystal nucleation occurs (as in rapid solidification), different and potentially useful forms of crystalline metals may be produced [16]. To predict and control the solidification nano- and micro-structures in different manufacturing processes, a fundamental understanding of mechanisms of crystal nucleation and solidification is necessary.

The crystallization process during liquid to solid transformation can be monitored by using X-ray scattering [19, 20], dilatometry [28], differential scanning calorimetry [29], or microscopic methods [30-32]. But there are several factors that limit the experimental studies of the nucleation process during solidification or crystallization, especially in pure materials (homogenous nucleation) [16]. There are difficulties in quantifying the surface free energy of liquid-solid interfaces and their anisotropy [33]. Also experiments are typically performed at temperatures that differ by hundreds of degrees from the actual nucleation conditions [16]. As a result, experimental measurements of nucleation rates in crystallization from the melt cannot provide reliable tests of the classical nucleation theory (CNT) [34, 35]. Another fundamental problem with homogenous nucleation experiments, especially for metallic materials, is that it is difficult to purify a liquid to exclude all the impurities that can catalyze nucleation [36, 37]. Recent experiments were done by Lee et al. [38] for an aqueous KH_2PO_4 solution by combination of electrostatic levitation, in situ micro-Raman and synchrotron X-ray scattering. They captured the nucleation pathways from supersaturated KH_2PO_4 transforming to crystalline KH_2PO_4 or metastable crystals with a monoclinic structure. Another recent study by Schreiber et al. [39] overcame the experimental challenges to observe formation of small crystal nuclei (five to thirty molecules) in aqueous solutions of an oval polyfluoroxometallate in the presence of NaCl;

they utilized cryogenic transmission electron microscopy for their study. Even for these materials with low solidification temperatures, formation and evolution of nanoscale defects during crystal nucleation could not be detected in the real time. Also, it should be noted that the experimental conditions for these studies are very different from solidification of metals. Solidification of metals happens at much higher temperatures and nucleation rates, and there are no studies on observation of nuclei formation during solidification of metals.

Nucleation often is facilitated by the action of foreign substances or surfaces, which results in what is commonly called heterogeneous nucleation. Although the conditions required to realize homogeneous nucleation in real systems can often be quite difficult to achieve, the concepts and principles of homogeneous nucleation are the simplest and form the starting point for analyzing other types of nucleation. Although nucleation has a strong impact on the properties of bulk materials, nucleation originates at the atomic or molecular level. Early studies of nucleation began with the liquid-vapor phase transition (i.e., vapor condensation or liquid boiling) but were soon extended to the crystal-liquid phase transition. The latter is somewhat more complex owing to the change of symmetry that takes place upon passing from a liquid phase to a crystal phase. Transitions between liquid and vapor phases can be continuous owing to the existence of the critical point, but transitions between liquid and solid phases are generally first order. In addition, the experimental observation of crystallization from solution or melt is complicated by the fact that it occurs within the interior of a dense liquid. Therefore, the molecular origins and microscopic mechanism of homogeneous crystal nucleation remain poorly understood and controversial. With the development of computer technology, numerical simulation has

become a useful tool in the study of homogeneous nucleation in the past 20 years, during which time new concepts and methods have been developed. This chapter reviews the development of simulation methods for the study of homogeneous nucleation, in particular that of crystal nucleation from a dense liquid.

Homogenous nucleation from metallic melts is a very complex phenomenon. It starts from the interior parts of an undercooled liquid, and due to the opaque nature of metallic melts, it is very difficult to experimentally detect the nuclei [33, 40]. Therefore, alternative theoretical or computational methods can be used to study homogenous nucleation in pure metals. The problem of nucleation from melt has been studied utilizing different approaches, including theoretical studies based on CNT [34, 35], density function theory (DFT) calculations [41], solid-liquid coexistence by molecular dynamics (MD) simulations [40], and other simulation studies based on phase-field [14], front tracking [42], cellular automata [43], and Monte-Carlo (MC) [44, 45] methods. CNT has been utilized as a theoretical tool for understanding the homogenous nucleation, and it has been applied for purely theoretical understanding [46-48], simulation based [49-52] studies or experimental studies [53-55] of nucleation. CNT offers an initial platform to understand the nucleation pathways; with more sophisticated sampling such as Brownian dynamics, Umbrella sampling, and forward flux sampling [56, 57], it may capture the complexity of atomic level events accompanied by the nucleation phenomenon. Daan Frenkel et al. provided further insights on how CNT can numerically predict the crystal nucleation rate closer to other simulation and experimental studies [46, 49, 56-58]. However, the probability of a system to follow a direct or indirect pathways is difficult to predict with the present theoretical understanding. The complicated kinetics of nucleation and the

various thermodynamic factors governing the formation of metastable clusters poses a major challenge in the theoretical treatments.

Studies utilizing electronic structure calculations based on DFT are limited to few hundreds of atoms and this limits investigation of formation of physical nuclei, which could become large clusters of atoms. In some other computational methodologies such as phase-field, cellular automata and front tracking methods, the length scale is microscale which limits a fundamental understanding of the nucleation process at atomic level. MD simulations can bridge the gap between the electronic and micro scale computational studies of nucleation and solidification from the melt. MD simulations act between the length scales of DFT and microscale studies, and with the recent advancements in supercomputing, it is now possible to run multi-million atom MD simulations to study phenomena occurring in several hundred nanometer systems. The reliability of MD simulation results significantly depends on the interatomic potentials. DFT calculations alongside experimental data are often used in developing semi-empirical interatomic potentials [59], and MD simulations results are frequently used to provided necessary input information for higher scale models like phase-field models [60-62].

There are few works on homogeneous nucleation during liquid-solid transformation [63, 64] and liquid-vapor transformation [65] by MD simulations. Yasuoka et al. [65] investigated the dynamics of vapor phase homogeneous nucleation in a water system; their predicted nucleation rate was three orders of magnitude smaller than that of the CNT. In metals, it is not straightforward to observe the homogeneous nucleation and solidification processes at the atomistic scale. Shibuta et al. [63] utilized MD simulations and linked the empirical interpretation in metallurgy with the atomistic behavior of

nucleation and solidification in pure iron (Fe). These major drawbacks of these works are the use of Finnis-Sinclair (FS) potential [66] and use of isothermal process for all the simulations. Utilizing an isothermal process in MD simulations does not resemble the experimental solidification process. In experiments with slow or fast cooling (quenching), the temperature change will affect the crystal nucleation and solidification processes. The utilized FS potential predicts the melting point of Fe to be 2,400 K, which is much higher than the experimental melting point of Fe (~1,811 K), and consequently results in inaccurate prediction of solid-liquid co-existence properties. Only one previous attempt was made to study heterogeneity in homogenous nucleation from a metallic melt of Fe by a billion atom MD simulation [63]. Finnis-Sinclair (FS) interatomic potential [66] was utilized for the simulations, predicts the melting point of Fe to be 2,400 K whereas the experimental melting point of Fe is ~1,811 K, and consequently results in inaccurate prediction of solid-liquid co-existence properties. After the solidification of single crystal Al solidification, we also study the heterogenity in homogenoud nucleation utilizing different crystal structures such as bcc-Fe and hcp-Mg. It is also worth to note that to study homogenous or heterogeneous nucleation it is not necessary to utilize such a large MD simulation, and several studies produced reliable and comparable results to experimental observations with only thousands to million atom MD simulations [67, 68]. In fact our recent study suggests the influence of the simulation size diminishes when a model size is larger than approximately 1 million[69]. It is also worth to note that a MD simulation using the less accurate FS potential utilizes orders of magnitudes less computational power compared to a case utilizing a more accurate interatomic potential, such as the Modified

Embedded Atom Method (MEAM) potential. However, the primary goal of scientific research should be accuracy rather than efficiency.

As the single elements 2NN-MEAM interatomic potentials were fitted high temperature and meting properties, it was expected that the potential for binary alloys can also be fitted for the same properties. Accoding to the author's knowledge there are no existing set of interatomic potentials for binary Al alloys that predict both low and high temperature properties accoding to their experiemental properties. In the present study, we developed and modified the interatomic potential for melting-solidification studies of Al-Cu, Al-Fe, Al-Ni, Al-Si and Al-Ge. In previous studies the thermal properties and melting temperature has been verified for Al, Cu, Ni, Fe and Mg by Asadi et. al. [59, 70, 71] and Kim et. al. [72]. The MEAM potential developed by Jelinek et. al. [73], is also studied for high temperature properties and melting point in this work. The melting point of Ge predicted by the MEAM is 2200 K, in the first step, the interatomic potential has been parameterized for formation energy for the B1 crystal structure or the available stable compounds. Then, the next stage of parameterization is done while verifying the solid and liquid mixing enthalpy of the alloys, thermal expansion, higher temperature lattice parameters. After the interatomic potential perform reasonably, with the low and high temperature properties we calculate the solid-liquid coexistence properties at different composition of Al and its alloying elements. Then we also, determine the formation energies of intermetallic and imaginary structures, which can be crucial doing the precipitating studies of the Al alloys. The MEAM potential for Al-Mg [72] was also studied for liquidus temperature by changing the Mg atomic composition in Al-Mg.

2. OBJECTIVE AND SIGNIFICANCE

The objective of this research is to develop and validate the fundamental understanding of phenomena occurring from the early stages to the late stages of solidification by performing large scale molecular dynamics (MD) simulations. We also develop and employ the most accurate interatomic potentials, and impose realistic size and time scales for gathering reliable data.

- Objective 1: Solidification in pure Al was performed and the results for critical nucleus size, temperature, defects during solidification, nano structural evolution were analyzed. Comparison of critical nucleus size with classical nucleation theory was also performed in this task.
- Objective 2: Once the polycrystalline Al solid is available from Objective 1, further study was performed on solidification defects and their evolution in uniaxial tensile deformation of solidified polycrystalline aluminum (Al) were investigated by molecular dynamics (MD) simulations solidification studies of pure Al. Evolution of nanostructures and defects in uniaxial tensile deformation of solidified Al under different temperatures and strain rates were also studied.
- Objective 3: Evaluation of optimum simulation size for studying nucleation during solidification were performed. A series of 2,000-8,000,000 atom simulation were perform to get the data for several quantities such as, diffusion coefficient, free energy, critical nucleus size, nucleation temperature. Then these data were analyzed of each of the simulation size to get the influence have on the solidification simulations.

- Objective 4: Heterogeneity in homogenous nucleation was studied for fcc (Al), bcc (Fe) and hcp (Mg). The metastable phases, grain boundary and twinning were visualized and quantitative analysis were performed to observer how it ease the homogenous nucleation in pure metals.
- Objective 5: Interatomic potentials for binary Al alloys were developed based on modified embedded-atom method (MEAM) potentials for predicting low temperature and melting properties. The binary alloys chosen for this study are, Al-Cu, Al-Fe, Al-Ni, Al-Si and Al-Ge. Using these interatomic potentials, we compare calculated low-temperature properties of the binary Al alloys such as formation energy of stable and unstable intermetallic, elastic constants, lattice parameters, enthalpy of solid and liquid mixing with experimental data. In addition, we also compare the liquidus temperature of the Al-alloys from the phase diagram to the molecular dynamics (MD) simulation. Available MEAM potential for Al-Mg is also considered for solid-liquid coexistence.
- Objective 6: The interatomic potential developed in Objective 5, were utilized to study directional solidification in Al-11 at % Cu. The unique Nanostructural pattern and its evolution, defect formation was analyzed in the solidification direction. After the simulation box is solidified, it was subjected to uniaxial load to study its mechanical properties.

PAPER

I. UNDERSTANDING HOMOGENEOUS NUCLEATION IN SOLIDIFICATION OF ALUMINUM BY MOLECULAR DYNAMICS SIMULATIONS

Avik Mahata[a], Mohsen Asle Zaeem[a*] and Michael I. Baskes[b,c,d]

[a] Department of Materials Science and Engineering, Missouri University of Science and Technology, Rolla, MO 65409, USA

[b] Department of Mechanical and Aerospace Engineering, University of California-San Diego, La Jolla, CA 92093, USA

[c] Department of Aerospace Engineering, Mississippi State University, Mississippi State, MS 39762, USA

[d] Los Alamos National Laboratory, NM 87544, USA

(*Published: Modelling Simul. Mater. Sci. Eng.26(2018)025007*)

ABSTRACT

Homogeneous nucleation from aluminum (Al) melt was investigated by million-atom molecular dynamics (MD) simulations utilizing the second nearest neighbor modified embedded atom method (MEAM) potentials. The natural spontaneous homogenous nucleation from the Al melt was produced without any influence of pressure, free surface effects and impurities. Initially isothermal crystal nucleation from undercooled melt was studied at different constant temperatures, and later superheated Al melt was quenched with different cooling rates. The crystal structure of nuclei, critical nucleus size, critical temperature for homogenous nucleation, induction time, and nucleation rate were determined. The quenching simulations clearly revealed three temperature regimes: sub-

critical nucleation, super-critical nucleation, and solid-state grain growth regimes. The main crystalline phase was identified as face-centered cubic (fcc), but a hexagonal close-packed (hcp) and an amorphous solid phase were also detected. The hcp phase was created due to the formation of stacking faults during solidification of Al melt. By slowing down the cooling rate, the volume fraction of hcp and amorphous phases decreased. After the box was completely solid, grain growth was simulated and the grain growth exponent was determined for different annealing temperatures.

1. INTRODUCTION

In metal manufacturing processes involving solidification (e.g., casting [1] , welding [2], and laser additive manufacturing [3]), the crystal nucleation from the melt controls the formation and growth of nano- and micro-structures of metals. The solidification structures of materials significantly influence their mechanical and physical properties. If large undercooling can be achieved before crystal nucleation occurs (as in rapid solidification), different and potentially useful forms of crystalline metals may be produced [4]. To predict and control the solidification nano- and micro-structures in different manufacturing processes, a fundamental understanding of mechanisms of crystal nucleation and solidification is necessary.

The crystallization process during liquid to solid transformation can be monitored by using X-ray scattering [5, 6], dilatometry [7], differential scanning calorimetry [8], or microscopic methods [9-11]. But there are several factors that limit the experimental studies of the nucleation process during solidification or crystallization, especially in pure

materials (homogenous nucleation) [4]. There are difficulties in quantifying the surface free energy of liquid-solid interfaces and their anisotropy [12]. Also experiments are typically performed at temperatures that differ by hundreds of degrees from the actual nucleation conditions [4]. As a result, experimental measurements of nucleation rates in crystallization from the melt cannot provide reliable tests of the classical nucleation theory (CNT) [13, 14]. Another fundamental problem with homogenous nucleation experiments, especially for metallic materials, is that it is difficult to purify a liquid to exclude all the impurities that can catalyze nucleation [15, 16]. Recent experiments were done by Lee et al. [17] for an aqueous KH_2PO_4 solution by combination of electrostatic levitation, in situ micro-Raman and synchrotron X-ray scattering. They captured the nucleation pathways from supersaturated KH_2PO_4 transforming to crystalline KH_2PO_4 or metastable crystals with a monoclinic structure. Another recent study by Schreiber et al. [18] overcame the experimental challenges to observe formation of small crystal nuclei (five to thirty molecules) in aqueous solutions of an oval polyfluoroxometallate in the presence of NaCl; they utilized cryogenic transmission electron microscopy for their study. Even for these materials with low solidification temperatures, formation and evolution of nanoscale defects during crystal nucleation could not be detected in the real time. Also, it should be noted that the the experimental conditions for these studies are very different from solidification of metals. Solidification of metals happens at much higher temperatures and nucleation rates, and there are no studies on observation of nuclei formation during solidification of metals.

Homogenous nucleation from metallic melts is a very complex phenomenon. It starts from the interior parts of an undercooled liquid, and due to the opaque nature of

metallic melts, it is very difficult to experimentally detect the nuclei [12, 19]. Therefore, alternative theoretical or computational methods can be used to study homogenous nucleation in pure metals. The problem of nucleation from melt has been studied utilizing different approaches, including theoretical studies based on CNT [13, 14], density function theory (DFT) calculations [20], solid-liquid coexistence by molecular dynamics (MD) simulations [19], and other simulation studies based on phase-field [14], front tracking [21], cellular automata [22], and Monte-Carlo (MC) [23, 24] methods.

CNT has been utilized as a theoretical tool for understanding the homogenous nucleation, and it has been applied for purely theoretical understanding [25-27], simulation based [28-31] studies or experimental studies [32-34] of nucleation. CNT offers an initial platform to understand the nucleation pathways; with more sophisticated sampling such as Brownian dynamics, Umbrella sampling, and forward flux sampling [35, 36], it may capture the complexity of atomic level events accompanied by the nucleation phenomenon. Daan Frenkel et al. provided further insights on how CNT can numerically predict the crystal nucleation rate closer to other simulation and experimental studies [25, 28, 35-37]. However, the probability of a system to follow a direct or indirect pathways is difficult to predict with the present theoretical understanding. The complicated kinetics of nucleation and the various thermodynamic factors governing the formation of metastable clusters poses a major challenge in the theoretical treatments.

Studies utilizing electronic structure calculations based on DFT are limited to few hundreds of atoms and this limits investigation of formation of physical nuclei, which could become large clusters of atoms. In some other computational methodologies such as phase-

field, cellular automata and front tracking methods, the length scale is microscale which limits a fundamental understanding of the nucleation process at atomic level.

MD simulations can bridge the gap between the electronic and micro scale computational studies of nucleation and solidification from the melt. MD simulations act between the length scales of DFT and microscale studies, and with the recent advancements in supercomputing, it is now possible to run multi-million atom MD simulations to study phenomena occurring in several hundred nanometer systems. The reliability of MD simulation results significantly depends on the interatomic potentials. DFT calculations alongside experimental data are often used in developing semi-empirical interatomic potentials [38], and MD simulations results are frequently used to provided necessary input information for higher scale models like phase-field models [39-41].

There are few works on homogeneous nucleation during liquid-solid transformation [42, 43] and liquid-vapor transformation [44] by MD simulations. Yasuoka et al. [44] investigated the dynamics of vapor phase homogeneous nucleation in a water system; their predicted nucleation rate was three orders of magnitude smaller than that of the CNT. In metals, it is not straightforward to observe the homogeneous nucleation and solidification processes at the atomistic scale. Shibuta et al. [42] utilized MD simulations and linked the empirical interpretation in metallurgy with the atomistic behavior of nucleation and solidification in pure iron (Fe). These major drawbacks of these works are the use of Finnis-Sinclair (FS) potential [45] and use of isothermal process for all the simulations. Utilizing an isothermal process in MD simulations does not resemble the experimental solidification process. In experiments with slow or fast cooling (quenching), the temperature change will affect the crystal nucleation and solidification processes. The

utilized FS potential predicts the melting point of Fe to be 2,400 K, which is much higher than the experimental melting point of Fe (~1,811 K), and consequently results in inaccurate prediction of solid-liquid co-existence properties.

To reliably study the crystal nucleation process from melt by MD simulations, the interatomic potentials used for MD simulations of solidification need to accurately predict the behavior of solid-liquid interfaces. In the early interatomic potentials, which were developed and used for MD simulations of Al such as Lennard-Jones (LJ) [46] and hard-sphere [47] models, only pair interactions of atoms were considered without including the effects of neighboring atoms. Pair potentials do not have environmental dependence (e.g., an atom in the bulk is not similar to an atom on the surface or near a defect site). In reality, the strength of the "individual bonds" should decrease or increase with the change in the local environment during the simulation. Pair potentials do not account for the directional nature of the bond. These are the reasons why pair potentials are not good for predicting the nonlinear phenomena such as failure, plasticity, solidification, melting etc. More complex interatomic potentials were developed for metals to address the shortcomings of pair potentials. Finnis–Sinclair [48] and embedded-atom method (EAM) [49] potentials were developed and used to predict mechanical and physical properties of Al. EAM is a semi-empirical many body potential for the atomistic simulations of metallic systems [50]. FS and EAM predict various properties of several metallic materials and alloys accurately. MEAM interatomic potentials were introduced later to include the directionality of bonding in covalent materials in the EAM and FS formalisms which make the property predications more accurate [51, 52].

Currently the MEAM potentials are widely used in the computational materials science and engineering community to simulate unary, binary, ternary and multi-component metallic systems with different nanostructural features, such as grain boundaries, defects, free surfaces, etc. [53, 54]. In our previous works, we demonstrated the capability of 2NN MEAM potentials in predicting solid-liquid coexistence properties of Fe [55, 56], Ni, Cu, Al [38], and Mg [57], such as melting point, latent heat, expansion in melting, liquid structure factor, and solid–liquid interface free energy and anisotropy. 2NN MEAM potential can also reliably predict room-temperature properties, such as elastic constants, surface energies, vacancy formation energy, and stacking fault energy. The detailed formalism of MEAM and 2NN MEAM can be found in works of Baskes et al. [51] and Lee et al. [58].

To the best of our knowledge, there has been only one experimental study on homogenous crystal nucleation from pure Al melt based on the free boundary (also called the CNT method) and interacting boundary models [59]; the incubation period (or the induction time) and small nuclei were undetectable in this study. There is only one work which used MD simulations [43] to study solidification of Al. However this study doesn't provide quantitative analysis on nucleation, critical nucleus formation, induction time, comparison of MD results to CNT, or details on solid state grain growth.

In this work, we studied the homogenous crystal nucleation from Al melt by MD simulations utilizing the second nearest-neighbor modified embedded atomic method (2NN MEAM) interatomic potential of Al [58]. Homogenous nucleation from Al melt was studied in both isothermal and quench processes. We also provide quantitative details of critical nucleus formation, and comparison of MD with CNT. The regimes of the

crystallization process during quenching have been identified. In the last section we also provide detailed analysis of the solid-state grain growth mechanism of pure Al after solidification.

2. SIMULATION DETAILS

2.1 INTERATOMIC POTENTIAL

The second nearest neighbor modified embedded atom method (2NN MEAM) interatomic potential of Al developed by Lee and Baskes [58] was used is this work to study solidification of Al by MD simulation. We recently tested this interatomic potential [38] which showed accurate prediction of solid-liquid coexistence properties (i.e. melting point, solid-liquid energy, melting point, specific heat etc.) of Al as provided in Table 1.

Table 1. Properties of Al predicted by MD simulations utilizing the 2NN MEAM interatomic potential and experimental results.

Properties	Experiments	MEAM MD [38]
Bulk Modulus (GPa)	76.4 [60]	79.4
C_{11} (GPa)	111.5 [60]	114.3
C_{12} (GPa)	58.8 [60]	61.9
C_{44} (GPa)	29.5 [60]	31.6
Specific Heat (J mol^{-1} K^{-1})	26.15 [61]	24.70
Thermal Expansion Coeff. (10^6 K^{-1})	17.31[61]	23.50
Melting Point (T_m) (K)	934 [62]	925
solid–liquid interface free energy (mJ/m^2)	168.9±21 to 158±30 [63]	172.6

2.2 SIMULATION METHODOLOGY

MD simulations of homogenous nucleation from pure Al melt were performed in a simulation box with size of 25×25×25 nm^3 (64×64×64 unit cells, with 1,000,188 atoms) and with the isothermal-isobaric (NPT) ensemble. Time step of 3 fs was used for all simulations. Temperature and pressure were controlled by Nose-Hoover thermostat and Parrinello-Rahman barostat [64] respectively. Periodic boundary conditions were employed in all three directions. All the MD simulations were performed in LAMMPS [65]. The 2NN MEAM interatomic potential of Al developed by Lee and Baskes [58] was used is this work; we recently tested this interatomic potential which showed accurate predication of solid-liquid coexistence properties of Al [38].

The OVITO visualization package was used to monitor the nucleation and solidification processes [66]. Within OVITO, common neighbor analysis (CNA) was used [67] to identify the local environment of atoms. Using CNA, one can distinguish atoms in different crystal structure regions by calculating the statistics of diagrams formed from the nearest neighbors (NN) of each atom and comparing it with those previously known for standard crystals. For example, if a central atom and its 12 NN form a structure such as fcc, CNA identifies the central atom as fcc. Any such atom is considered an fcc atom. Atoms not identified as fcc, hcp, or any other crystal type implemented in OVITO are identified as amorphous liquid or amorphous solid atoms.

The predicted melting point of Al using a 2NN MEAM MD simulation is 925 K [38], which is in a very good agreement with the experimental value of 934 K. We found that at a temperature close to the melt temperature, the liquid has a fluctuating number of fcc atoms. We wanted to start the nucleation simulations with a pure liquid having no solid

regions. In order to find the temperature at which a completely melted simulation box with no fcc crystal can be achieved in a relatively short simulation time (~150 ps), several simulations were performed by increasing the temperature of the simulation box higher than 925 K using 25 K intervals. After 16 intervals, when the temperature reached 1,325 K, we could obtain a completely melted simulation box in ~100 ps. The simulation is continued to 300 ps to make sure the initial melt is properly equilibrated. The CNA of the simulation box for very large time scale is provided in Figure 1(a). The percentage of amorphous liquid atoms keeps increasing with increasing the annealing temperature. Finally, the box had no crystalline atoms at 1,325 K. The radial distribution function (RDF, g(r)) of the simulation box was calculated for all the temperatures, which is plotted in Figure 1(b). There are no long-range peaks at 1,325 K. The CNA analysis and RDF plots confirmed that Al was completely melted at 1,325 K.

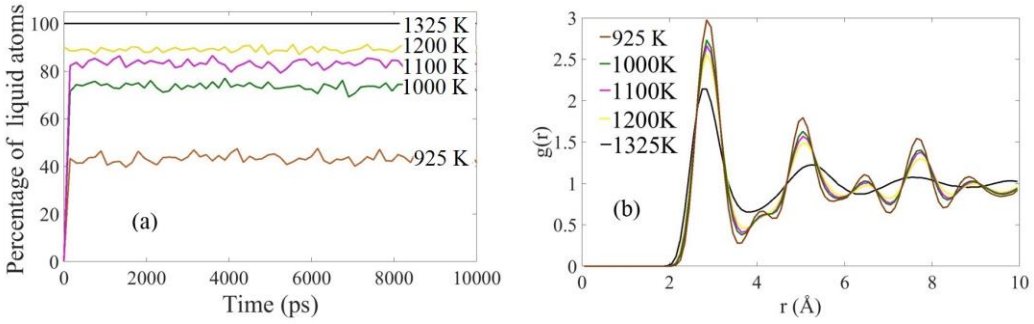

Figure 1. (a) Percentage of amorphous liquid atoms at different temperatures; (b) The radial distribution function of Al melt. Figure 1(a) is showing liquid characteristic with no long range peak at 1,325 K.

For isothermal simulations, the Al melt was isothermally solidified at temperatures between the range of 300 K and 800 K with 50 K intervals. Maximum nucleation rate was observed to be between 400 K and 500 K, so we ran more simulations with 25 K intervals to more accurately determine the exact critical temperature of nucleation (when the nucleation rate is maximum). Each isothermal simulation was repeated five times to evaluate the possible errors. Each isothermal simulation was run for a total of 500 ps (167,000 time steps) to simulate the crystal nucleation and solidification.

We also performed solidification by quenching with different cooling rates of 5.83×10^{10} Ks^{-1}, 5.83×10^{11} Ks^{-1} and 5.83×10^{12} Ks^{-1}. Different cooling rates were applied by changing the number of total time steps. The initial temperature of the melt was 1,325 K, then the melt was cooled down to 450 K in 150 ps, 1,500 ps and 15,000 ps (5,000,000 time steps), which resulted in cooling rates of 5.83×10^{12} Ks^{-1}, 5.83×10^{11} Ks^{-1} and 5.83×10^{10} Ks^{-1}, respectively. 450 K was chosen because it is lower than the critical temperature found in the isothermal process (see Section 3.6). The quenching method was used to mimic the actual experimental procedure to produce undercooling where the temperature decreases from above the melting temperature with a certain cooling rate. This method of simulation is closer to what is performed experimentally and differs from the previous MD simulations of homogenous nucleation which usually utilized isothermal simulations [42]. In experiments, cooling rates in rapid solidification of bulk Al lie between 10^4 and 10^7 K/s [68-70], notably much slower than the rates used in MD.

3. RESULTS AND DISCUSSIONS

3.1 CRYSTAL STRUCTURE OF NUCLEI

The primary observation of nucleation in MD simulations shows the formation of nuclei from the melt. CNA and visual inspection are used to study the structure of the nucleus throughout the quenching and annealing. The formation of crystal structures and stacking faults occurred in the same way for both the isothermal and quenching processes. Figure 2(a) shows that the crystalline nuclei form in different parts of the melt. The atomic coordinates of the cluster atoms in the specified nucleus in Figure 2(b) are extracted, and the measured distances from the surface atoms of the nucleus to the central atom show almost the same value in all directions. The magnified nucleus in Figure 2(b) shows atoms with fcc (green) and hcp (red) crystal structures using CNA. The nearest neighbor distance for fcc Al should be 2.86 Å as the lattice constant is 4.05 Å. The distance between two nearest atoms within the fcc (green) atoms in Figure 2(b) is ~ 2.86 Å. It should be mentioned that few solid amorphous atoms get trapped inside the fcc/hcp crystalline phase nucleus, which don't have enough neighbors to be detected as a solid crystalline phase.

We calculated the difference between formation energies of fcc and hcp Al to be only 0.03 eV, whereas the difference between formation energies of fcc and bcc Al was determined to be 0.12 eV [38]. Since there is a random thermal fluctuation of energy during solidification, this thermal fluctuation of energy can cause formation of hcp stacking faults in the Al system, but it is not enough to promote formation of bcc atoms.

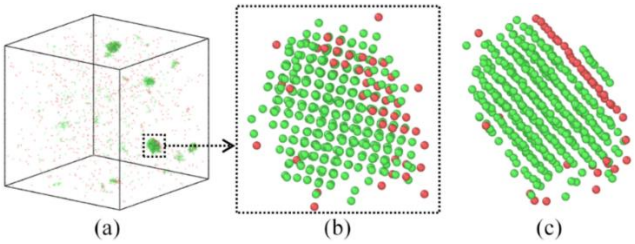

Figure 2. (a) Formation of nuclei after 1,050 ps of simulation at annealing temperature of 400 K, (b) Magnification of one of the nuclei in Figure 2(a), (c) Stacking fault around <111> direction. FCC atoms are in green and hcp atoms are in red.

3.2 CRITICAL NUCLEUS SIZE

The minimum size required for continuous growth of a crystalline nucleus is known as the critical nucleus size. In this study, the size of a nucleus is taken as the average, as discussed below, of the maximum length of the nucleus in x (100), y (010) and z (001) directions (Fig 3a). In Figure 3(a), one example is given to show how the nucleus size is determined in one of the three directions; the length in (001) direction is determined to be 15 Å for one of the nuclei. Measurements are taken in (100) and (010) directions as well. A similar process is applied to measure the size of all the nuclei at the different timesteps. Simulations are repeated 5 times to determine the uncertainty in the measurement in nucleus size. 5 different nuclei in each simulation are chosen and the nuclei sizes are measured in three directions. Total of 75 measurements are done for each nucleus to determine the average and the error bar for each case (3-directions × 5-nuclei × 5-replicate simulations).

This is assumed to be equivalent to the diameter of a spherical shaped nucleus. The nucleus size and number of atoms in the nucleus are determined by direct observations. Before a nucleus reaches its critical size, for a short period of time (nucleus origin time,

discussed in Section 3.9), the nucleus gains and loses atoms. We assume that a crystalline nucleus reaches its critical size when it doesn't lose any atom back into the liquid. Figure 3 shows examples of nuclei size and number of atoms in the nuclei versus simulation time for isothermal and quenching cases. The arrows in Figure 3(b) and (c) show when the nuclei reach the critical size. The number of atoms in the critical nucleus is ~1400 atoms at 700K (Figure 3(b)) and for the case with a cooling rate of 5.83×10^{11} Ks^{-1} in Figure 3(c), the critical sized nucleus has ~1000 atoms. After reaching the critical size, the crystalline nuclei grow in size and gather more fcc and hcp atoms. The evolution of critical nucleus can also be monitored by potential energy change with time and the visualization snapshots (Inset Figure 3b-c). The crystalline nuclei reach the critical size slightly before the sudden change of slope. At that point the nucleus has become large enough to overcome the free energy barrier for phase separation. A critical nucleus does not become smaller after it reaches the critical size. The critical nuclei are found to be quiet stable against the mobility of liquid phase, structural change, i.e. fcc-hcp, or continuously changing shape.

As it was mentioned before, each simulation was performed 5 times; after the nuclei reach the critical size, a set of 5 random critical nuclei are chosen at each annealing temperature from each isothermal simulation; total of 25 critical nuclei were selected for each annealing temperature. The average critical size and its standard deviation versus annealing temperature are plotted in Figure 4(a). The average size of critical nuclei is between ~0.82 nm and ~4 nm (Figure 4(a)) for all annealing temperatures in the isothermal process. The critical size of crystalline nuclei increases as the annealing temperature increases.

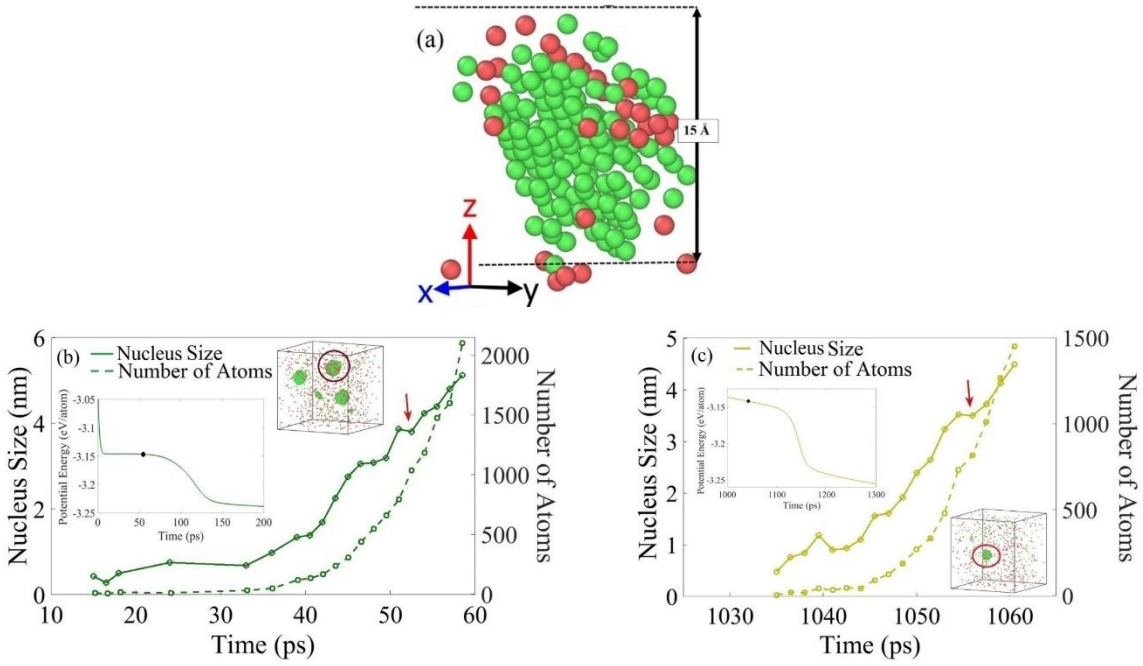

Figure 3. (a) A measurement of the nucleus size along the (001) direction. Nucleus size versus simulation time for: (b) isothermal process at 700 K annealing temperatures, and (c) quenching process at the cooling rate of 5.83×10^{11} Ks^{-1}. Arrows show the number of atoms in the critical sized nuclei. The inset graph of potential energy vs time shows the change in slope. The exact point of formation of critical nucleus formation is marked by a black dot. The other inset of the simulation box shows the critical nucleus

In the quench processes, the average critical size of nuclei is found to be ~1.8 nm for 5.83×10^{12} Ks^{-1}, ~3.49 nm for 5.83×10^{11} Ks^{-1}, and ~4.5 nm for 5.83×10^{10} Ks^{-1} cooling rate. With a slower cooling rate the nucleation occurs at higher temperatures, which results in a larger critical size for nuclei. It should be noted that nucleation rates decrease with slower cooling rates (discussed in Section 3.7), and the nuclei can grow larger before the whole simulation box becomes solid.

During the isothermal process, the maximum number of crystalline nuclei in the system varies (Figure 5) with annealing temperature. When a relatively low annealing temperature is applied (below 600 K), the nucleation starts instantly, and since the driving

force for solidification is very high, fcc crystalline atoms form all over the simulation box in the early stages of simulation. This will result in formation of multiple critical nuclei simultaneously, and a higher number of nuclei will form but they grow to a smaller size compared to the nuclei in higher annealing temperatures. The maximum number of separable nuclei in the simulation box for annealing temperatures between 350 K and 650 K is more than 40 nuclei in 25 nm^3.

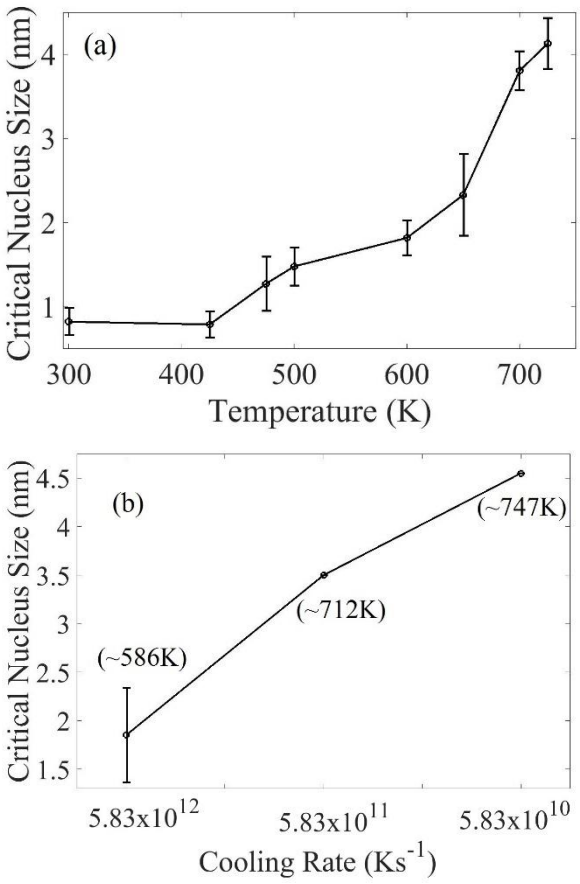

Figure 4. The critical nuclei size versus (a) annealing temperatures in the isothermal process and (b) different cooling rates. Error bars are shown as the standard deviation for 5 randomly chosen critical nuclei for isothermal simulations. The temperature at which the critical nucleus forms is shown for quenching in Section 3.3 below.

Above 650 K the maximum number of separable nuclei is reduced; for example, at 700 K and 725 K, 12 and 9 nuclei are detected, respectively. While the number of nuclei is reduced by increasing the annealing temperature above 500 K, each nucleus can grow to a much larger size before the simulation box is completely solid. In the quenching process, the maximum number of separable nuclei varies between 9 to 15 for different cooling rates, which is similar to that of 700 K and 725 K isothermal cases. The maximum number of separable nuclei is seen at 715 K, 665 K and 655 K for 5.83×10^{10} Ks^{-1}, 5.83×10^{11} Ks^{-1} and 5.83×10^{12} Ks^{-1} quench rates, respectively.

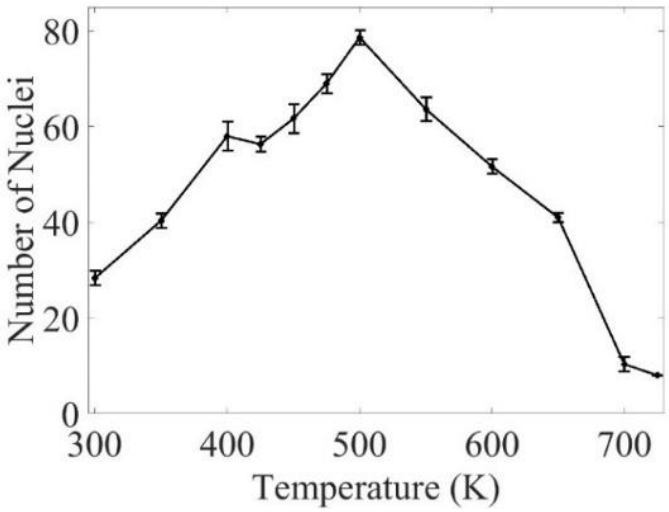

Figure 5. Maximum number of separable nuclei at different annealing temperatures during the isothermal process. The error bars show standard deviation for 5 replicate simulations at each annealing temperature.

3.3 TEMPERATURE DEPENDENCE OF NUCLEATION

The crystal nucleation from an undercooled Al melt predicted by MD simulations is shown in Figure 6 for two isothermal cases (annealing at 475 K and 700 K), and two quenching cases (cooling rates of 5.83×10^{10} Ks^{-1} and 5.83×10^{11} Ks^{-1}); only fcc Al atoms are shown for a better visualization of nuclei. The instantaneous time and temperatures during each quenching process are also shown in Figure 6(c) and Figure 6(d).

As mentioned before, the number of nuclei in the system is reduced with increasing the annealing temperature above 500 K (Figure 5); the same conclusion can be made by comparing Figure 6(a) and Figure 6(b). These figures also show that each nucleus can grow much bigger in size at a higher annealing temperature. Nucleation by quenching in Figure 6(c) and Figure 6(d) shows a very similar behavior to the nucleation of isothermal process at 700 K (Figure 6(b)). This indicates that in the quenching process nucleation starts at high temperatures with a small number of nuclei which can grow in size.

As shown in Figure 6 the number of nuclei differs at various temperature, so it is certain that the growth of nuclei must be affected by the growth of other nuclei in the system at a particular time steps. At lower temperature, the solid-liquid interfaces are very close to each other and that indicates that the solid-liquid interfacial energy shows large orientation dependence. As shown in Figure 7(a), different nuclei in a form simultaneously and in Figure 7(b) we can see in a very quick succession (~6 ps) another 2 critical nuclei form. Finally, within another 6 ps all these 4 nuclei come too close to each other to grow anymore. The free growth of nuclei during the crystallization fails for faceted nuclei.

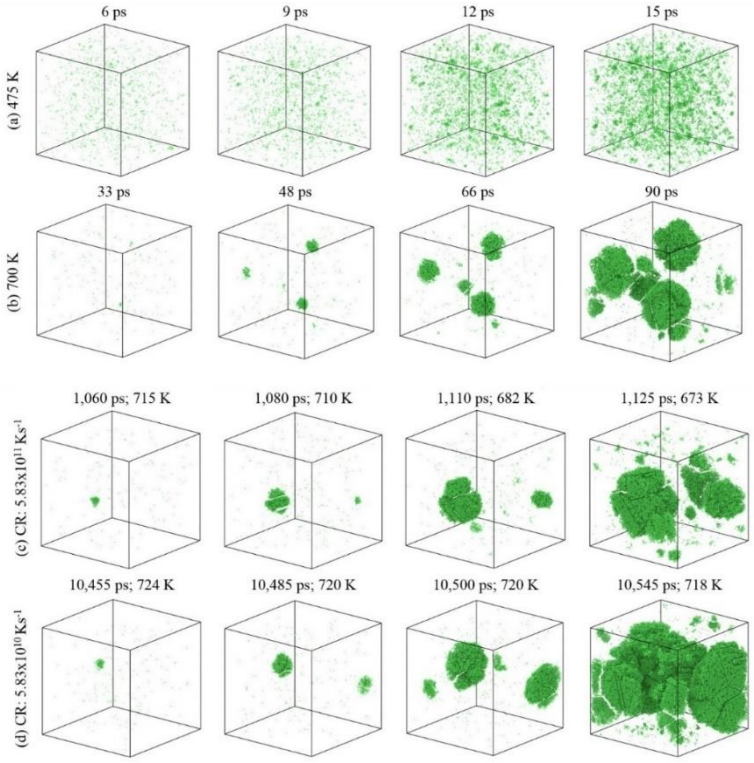

Figure 6. Snapshots of nuclei formation and growth during solidification for two isothermal processes at annealing temperatures of (a) 475 K and (b) 700 K, and for two quenching processes with cooling rate of (c) 5.83×10^{11} Ks^{-1} and (d) 5.83×10^{10} Ks^{-1}. Fcc are shown with green color; hcp and amorphous atoms are ignored for a better visibility of nuclei.

Due to this reason the equilibrium shapes of nuclei vary from sphere to the specific faceted shape. The shapes are illustrated in Figure 7(c). Unlike higher temperature, at 700 K the free growth is possible in most part of the solidification process. As shown in Figure 7 (d-f) the critical nuclei has no influence from the neighboring nuclei, which appears ~20 ps later than first critical nuclei. In Figure 7(f) the nuclei is reaching almost a spherical shape.

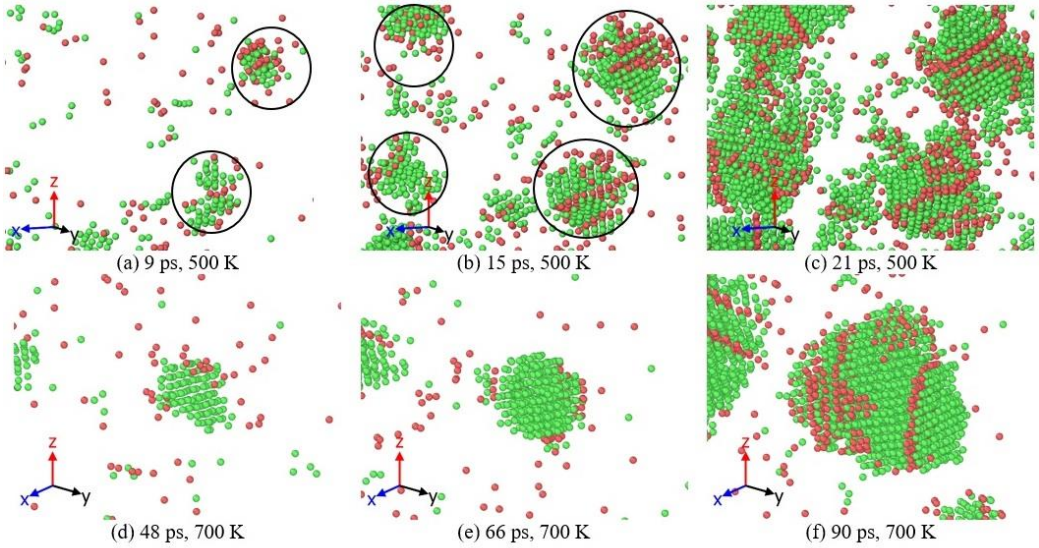

Figure 7. Snapshots of shape of the nuclei is shown at various time steps for 500 K and 700 K. At 500 K, the multiple nuclei form at the same time step of (a) 9 ps. Then other critical nuclei form within (b) 6 ps. The faceted nuclei shown at (c) 21 ps. At higher temperature (700 K), initial nucleus shown at (d) 48 ps, it free growth is shown at (e) 66 ps and it reaches spherical shape at (f) 90 ps.

The instantaneous temperature for crystal nucleation during quenching can be determined by plotting percentage of crystalline atoms versus temperature change (Figure 8). Figure 8 shows that during quenching the nucleation process starts between ~747 K and ~712 K for the slower cooling rates of 5.83×10^{10} Ks^{-1} (Figure 8 (b)) and 5.83×10^{11} Ks^{-1} (Figure 8 (c)). For a high cooling rate of 5.83×10^{12} Ks^{-1}(Figure 8 (a)) the nucleation starts below 700 K, and the exact temperature of formation of first nucleus is found to be ~586 K from dumps (per atom data) available from LAMMPS (such as Figure 6). The number of fcc/hcp atoms is very low for 5.83×10^{12} Ks^{-1} cooling rate that it doesn't reflect the nucleation starting temperature in Figure 8(a). The most solid atoms for this cooling rate remain at amorphous configuration, and the change in overall crystal structure is not

significant until about 575 K. Overall the quenching simulations suggest that the nucleation starting temperature is between 586 K -747 K.

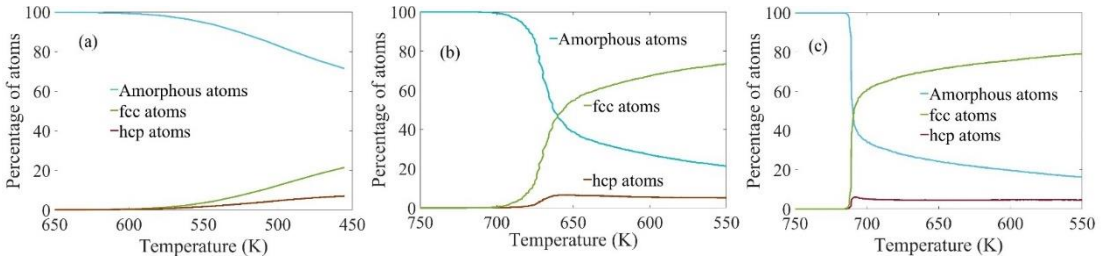

Figure 8. The change in types of atoms with temperature for three different cooling rates. The cooling rates are (a) 5.83×10^{12} Ks^{-1}, (b) 5.83×10^{11} Ks^{-1}, and (c) 5.83×10^{10} Ks^{-1}.

3.4 CRYSTALLIZATION DURING NUCLEATION

The percentage of atoms having different structures (amorphous, fcc or hcp) is plotted in Figure 9(a)-(c) at three different annealing temperatures for the isothermal process. The percentage of fcc atoms for 700 and 725 K (~60-65 %) is slightly higher than the percentage of fcc atoms generated at lower temperatures (~50-55 %). At very low temperatures such as 350 K, the percentage of fcc atoms is very low. The lower amount of fcc atoms also causes a very low nucleation rate at 350 K. At lower temperatures (below 600 K), the accumulation of fcc atoms starts immediately. At the same time number of hcp stacking faults grows and number of amorphous atoms decreases. At 725 K the initial nucleation starts later than any other temperature. At temperatures, higher than 725 K, there is no nucleation in 600 ps.

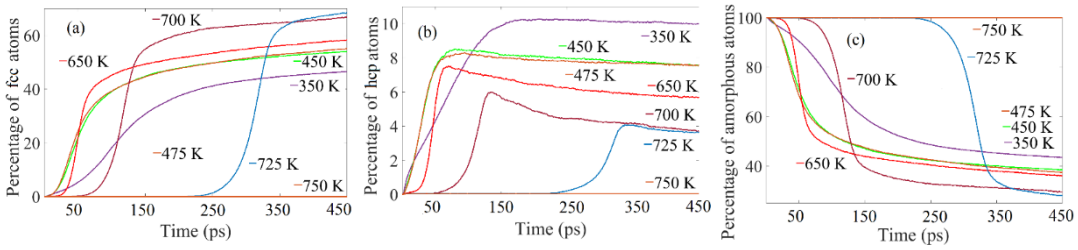

Figure 9. Percentage of atoms with fcc, hcp and non-structured amorphous configurations. The plots of different annealing temperatures is shown in (a) fcc atoms (b) bcc atoms and (c) amorphous atoms. Data from each the 1.5 ps were used to generate the figures.

Percentage of atoms having different structures (amorphous, fcc or hcp) for different quench rates are also plotted in Figure 10(a)-(c). In quenching the process of nucleation starts after first regime when mostly sub-critical nucleus/nuclei forms and dissolves. Slowly the temperature reduces to nucleation regime and then the nucleation happens very fast. However the rate of formation of fcc atoms differs for different cooling rates. The slower the cooling rate is the more time the melt has to solidify the fcc/hcp atoms and this lowers the number of amorphous atoms. With a slower cooling rate number of hcp stacking faults also decreases.

3.5 TEMPERATURE-DEPENDENT NUCLEATION REGIMES

As it was shown in the previous Section 3.3, nucleation is a temperature driven phenomenon, and a change in temperature affects the rate and behavior of nucleation. Potential energy is one of the fundamental quantities that correlates temperature with nucleation and solidification processes. Figure 11(a) shows the potential energy versus simulation time for different isothermal annealing temperatures. When the Al melt is

brought directly to a low annealing temperature, there is a very sharp drop in the initial potential energy due to the specific heat of the liquid.

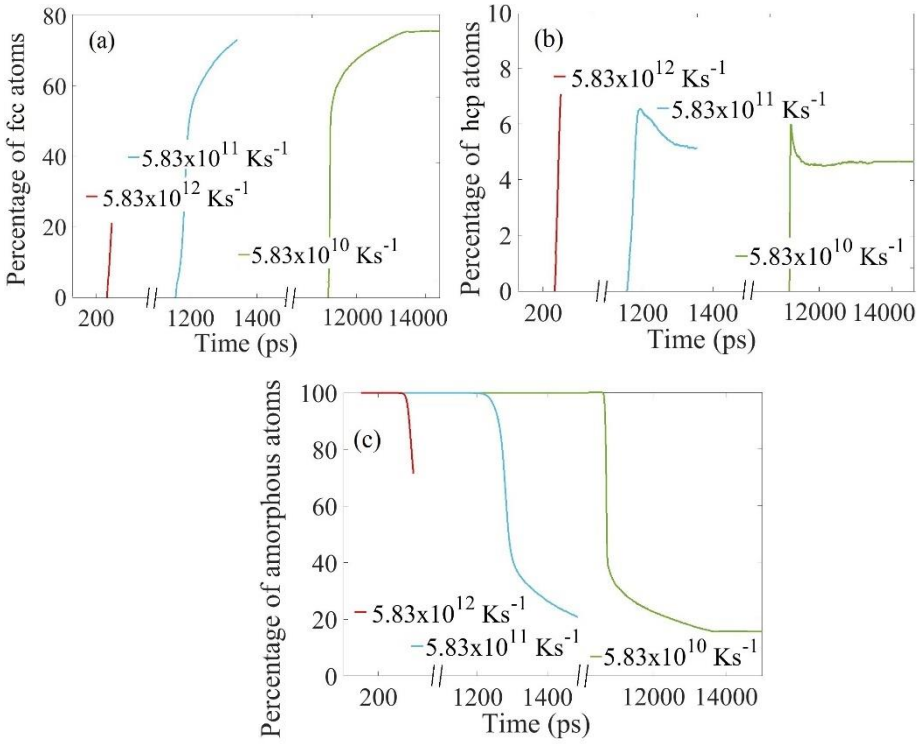

Figure 10. Percentage of atoms with (a) fcc, (b) hcp and (c) non-structured amorphous configurations. Quenching vs. time data from all the time-steps were used to generate the figures.

Below 600 K, the Al melt starts solidifying immediately within the first few time steps. For higher annealing temperatures (such as 650 K, 700 K and 725 K) the solidification doesn't happen immediately. The time required to form the first critical nucleus (or nuclei) after starting the annealing is ~40 ps, ~75 ps and ~ 250 ps for annealing temperatures of 650 K, 700 K and 725 K, respectively.

In isothermal cases, we can roughly see from Figure 11(a) that the behavior of melt changes with temperature. At 750 K and above, the potential energy is flat for the entire simulation time indicating that no nucleus forms. Between 600 K and 725 K three distinct regimes can be observed. We initially see a flat region similar to 750 K where no nucleation occurs. Then the curvy decay of the potential line indicates that nucleation happens at this stage. This indication is verified against per atom data (i.e. LAMMPS dumps), and it is found that the decay of potential energy and nuclei formation happen simultaneously. The final flat region shows the start of the solid-state grain growth. From 350 K to 575 K the sharp decrease in potential energy starts immediately and continues until the end of the simulation, which shows that the nucleation starts immediately, and towards the end of the simulation the potential energy curves becomes parallel to each other. At lower annealing temperatures (below 350 K), even though the Gibbs free energy difference between fcc/hcp and amorphous liquid atoms is large, the low mobility of atoms at low temperatures affects the kinetics of nucleation and not all the liquid atoms can form crystalline structures. An amorphous solid structure is retained. At the final stage of all cases, curves become slowly parallel to the time axis with an offset from each other. This offset is due to the specific heat of the solid phases, which results in lower potential energy at lower temperature. Overall, the isothermal simulations do not give the temperature range for the different stages of nucleation; these simulations only indicate that liquid Al melt has to be below 725 K for nucleation to occur.

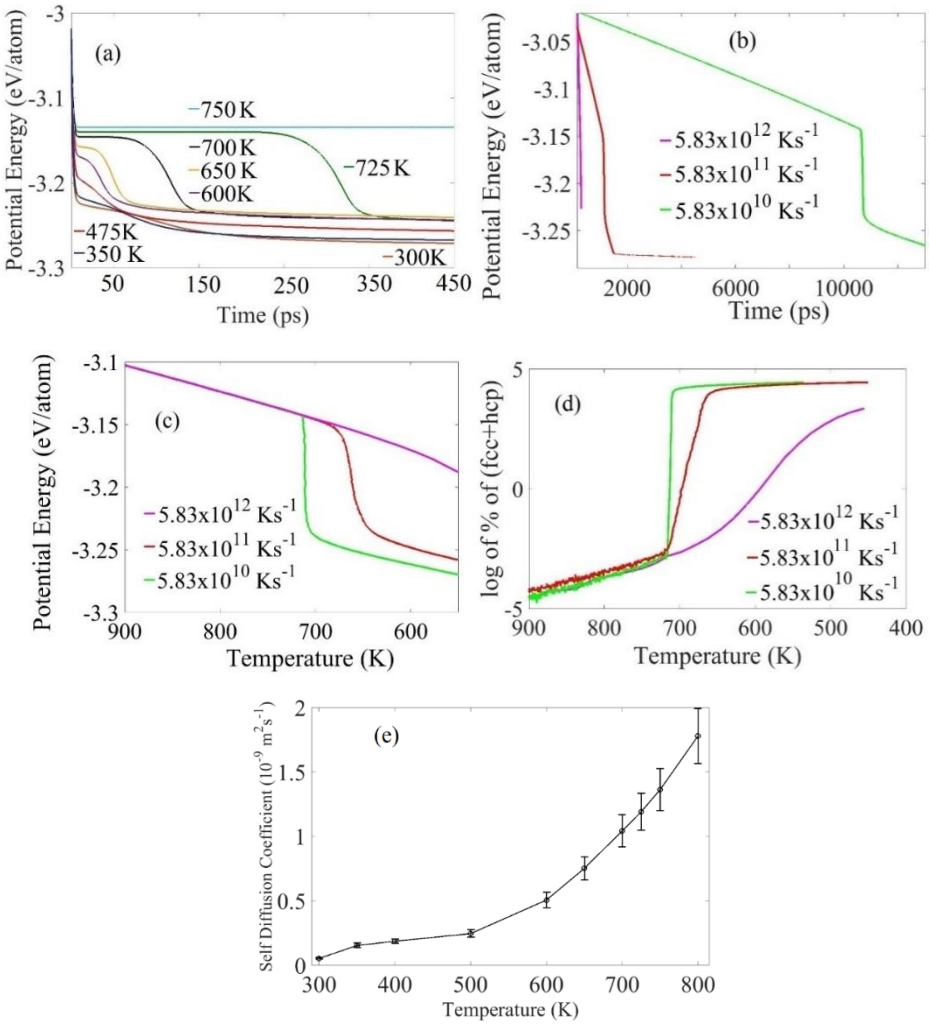

Figure 11. Potential energy versus time for (a) isothermal process at different annealing temperatures, and (b) quenching process with different cooling rates. We also calculate (c) Potential energy versus temperature for quenching process. (d) Log of percentage of fcc/hcp crystalline atoms versus temperature, (e) the self-diffusion coefficient of Al at various temperature.

Figure 11(b) shows the potential energy versus time for the quenching process with different cooling rates from 1,325 K to 450 K. It is not possible to identify the nucleation regimes by this figure, but the plot of the potential energy versus temperature, Figure 11(c), reveals three temperature-dependent regimes very clearly. As shown in Figure 11(c), the

potential energy decreases when temperature decreases during quenching simulations. During this period (> 725 K), sub-critical nucleus/nuclei form and dissolve back into the melt. For the low cooling rates (5.83×10^{10} Ks^{-1} and 5.83×10^{11} Ks^{-1}), the sharp change in the slope (Figure 11(b)) indicating a sudden decrease in potential energy occurs at temperatures range of 715-725 K. The beginning of the sharp change in slope shows the start of formation of critical nuclei (at ~725K), and once the first sub-critical nucleus reaches the critical size the crystallization happens very fast at low cooling rates. The super-critical nuclei grow bigger in size until the simulation box is completely solid, and solid-state grain growth starts; this region can be easily identified for low cooling rates (e.g., < 710 K for 5.83×10^{10} Ks^{-1}). For the low cooling rates, the almost vertical slope line (Figure 10(c)) signifies the release of latent heat due to crystallization (or solidification). This event represents the fast and spontaneous formation of solid nuclei during solidification. Figure 11(c) shows nuclei formation can only happen in a temperature range depending on the cooling rate. This finding shows the drawbacks of isothermal simulations and clearly shows the existence of different temperature regions in the solidification process.

Initially atoms attempt to crystallize from the melt by formation of small clusters of fcc and hcp atoms, but as the simulation progresses most of these clusters of atoms dissolve back into the liquid phase. This region can be identified as the sub-critical (unstable) nucleation regime in Figure 10(d) where there are small fluctuations in the total number of crystalline atoms. The sudden change in the slope shows the regime change from sub-critical to super-critical (stable) nucleation, and the temperature at which this transition occurs is named T_{sc}. The exact value of T_{sc} depends on the cooling rate, and remains between ~715-725 K for 5.83×10^{10} Ks^{-1} and 5.83×10^{11} Ks^{-1}. Multiple super-critical

nuclei are formed in the system following the formation of the first critical nucleus and they grow until the whole simulation box is solid and solid-state grain growth starts.

The second sudden change in the slope shows another regime change from super-critical nucleation to solid-state grain growth, and the temperature at which this transition occurs is named T_{gg}. The difference between T_{sc} and T_{gg}, is very small (only 9 K for 5.83×10^{10} Ks^{-1} cooling rate, T_{sc} = 724 K start and T_{gg} = 715 K end) for the slowest cooling rate. Super-critical nuclei will grow until the whole box is solid, and then solid-state grain growth occurs. This solid-state grain growth and end of nucleation are the same temperature (T_{gg}). The grain growth is not a part of nucleation process, but an essential part of solidification. So overall the solidification process can be divided into three temperature based thermodynamics regimes, i) the sub-critical (unstable) regime, ii) the super-critical (stable) nucleation regime when, multiple critical nuclei form along with the growth of the previously formed critical nuclei, and iii) solid-state grain growth regime.

In any experimental method, the Al melt needs to release heat to go down to a specific annealing temperature. Even if the Al melt can be brought to a constant temperature environment instantly, it is practically impossible that the Al melt will go down to the lower annealing temperature immediately. In other words, the quench rate in isothermal processes are infinite. In quenching we showed, the T_{sc} for 5.83×10^{10} Ks^{-1}, 5.83×10^{11} Ks^{-1}, 5.83×10^{12} Ks^{-1} are 724 K, 715 K and 586 K respectively. So, we can see as the cooling rate decreases the T_{sc} increases. In MD, the quench rates are very high. If we assume in bulk experiments the cooling rate to be 1-100 Ks^{-1} the nucleation temperature should be higher (above ~725 K). So, in the real world there is no nucleation at all at lower

annealing temperature (i.e. 650 K for Al). We also observed the slope in the super-critical region (Figure 11(d)) is getting more vertical as the cooling rate is reduced. So, in experiments when the cooling rate is much slower, the T_{sc} and T_{gg} can be almost the same temperature.

We can also relate the self-diffusion coefficient to the nucleation regime (Figure 11(e)). The increasing self-diffusion coefficient with increasing temperature results in higher mobility of the Al atoms or vice versa. As previously shown in Figure 11(a), the potential energy indicates that no nucleation occurs after 725 K. The reason for this phenomena is the higher mobility of atoms, with self-diffusion coefficient of 1.35 $x10^{-9}$ m^2s^{-1} at 750 K. The self-diffusion coefficient in MD is comparable to experimental finding [71].

3.6 NUCLEATION RATE: ISOTHERMAL SOLIDIFICATION

It is evident from the previous Section that annealing temperature certainly affects the nucleation process, so it is expected that it would also affect the nucleation rate. The nucleation rate for each annealing temperature is calculated by fitting a line to the data on number of nuclei versus time, where the slope of the line is the nucleation rate (Figure 12). The nucleation rate increases as the annealing temperature increases from 300 K to 475 K (Table 2). At room temperature (300 K) very few separable crystalline nuclei can be found; for higher annealing temperatures, the kinetic energy of atoms increases, which helps liquid atoms overcome the activation or free energy barrier to produce critical sized crystalline nuclei.

Our initial simulations were done for undercooling temperatures between 300 K and 800 K with an interval of 100 K. We found that the nucleation rate is a maximum between 400 K and 500 K; therefore to find the exact critical nucleation temperature, more simulations were performed between annealing temperatures of 400 K to 500 K with an interval of 25 K. From the slopes of the fitted lines in Figure 12, the maximum nucleation rate of 5.74×10^{35} $m^{-3}s^{-1}$ occurs at the annealing temperature of 475 K (Table 1). The typical nucleation rate for the homogeneous nucleation of a pure metal near the critical temperature has been estimated previously from experiment to be in the order of 10^{30} and 10^{40} m^{-3} s^{-1} [72], which is comparable to our MD results. Since the nucleation rate is maximum at 475 K, we can come to a conclusion that ~475 K is the critical temperature of nucleation for Al. The calculated critical temperature from MD is $\sim \frac{T_m}{2}$, where T_m is the melting temperature. Once the solidification progresses the distance between different nuclei is reduced, and the simulation box eventually transforms into the bulk solid crystalline Al with hcp solidification defects and grain boundaries.

Table 2. Nucleation rates at different annealing temperatures. The statistical error is estimated by obtaining the slopes for 5 different simulations of each annealing temperature.

Temperature (T) (K)	400	450	475	500	600	700
Nucleation rate (I) (10^{35} $m^{-3}s^{-1}$)	4.00±0.13	4.48±0.08	5.74±0.07	5.32±0.05	3.51±0.01	0.07±0.00

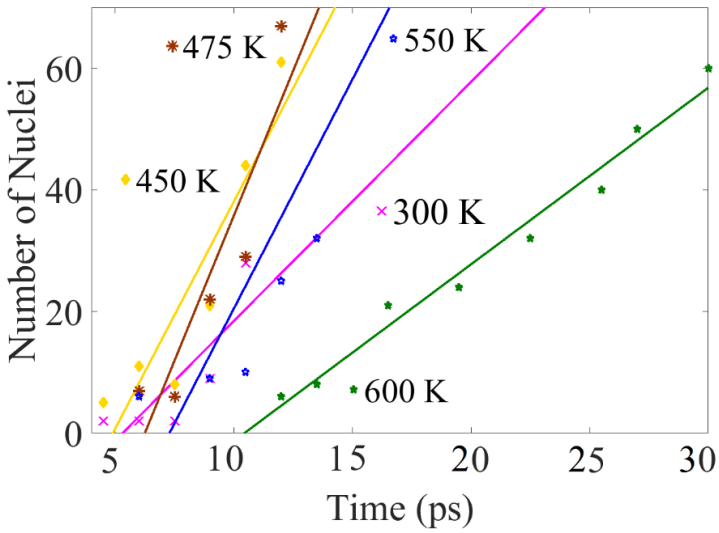

Figure 12. The number of nuclei as a function of time at various annealing temperatures. The slopes of lines are the nucleation rates at different annealing temperatures which are reported in Table 1. The slopes of lines are the nucleation rates at different annealing temperatures which are reported in Table 1. Note that the maximum nucleation rate occurs at 475 K, which defines the critical temperature of nucleation for Al.

3.7 NUCLEATION RATE: QUENCHING SOLIDIFICATION

In quenching crystallization begins by formation of small clusters of atoms at high temperatures. Many of them form and dissolve back into the liquid; a few will survive. The nuclei starts forming after sometime. The beginning time for the nuclei depends on the cooling rate, slower the cooling rate the later the nucleus (nuclei) forms. From Figure 12 and Table. 2, the nucleation rates are obtained in the same way it was obtained for the isothermal process. The time in Figure 13 is a small part of time among the whole time steps. Most of the nucleation happens between this part, so it is chosen to study the nucleation rate in quenching. It is shown in Table. 2 that the nucleation rate goes down

from 1.12×10^{35} $m^{-1}s^{-1}$ at cooling rate of 5.83×10^{12} Ks^{-1} to 8×10^{33} $m^{-1}s^{-1}$ at cooling rate of 5.83×10^{10} Ks^{-1}.

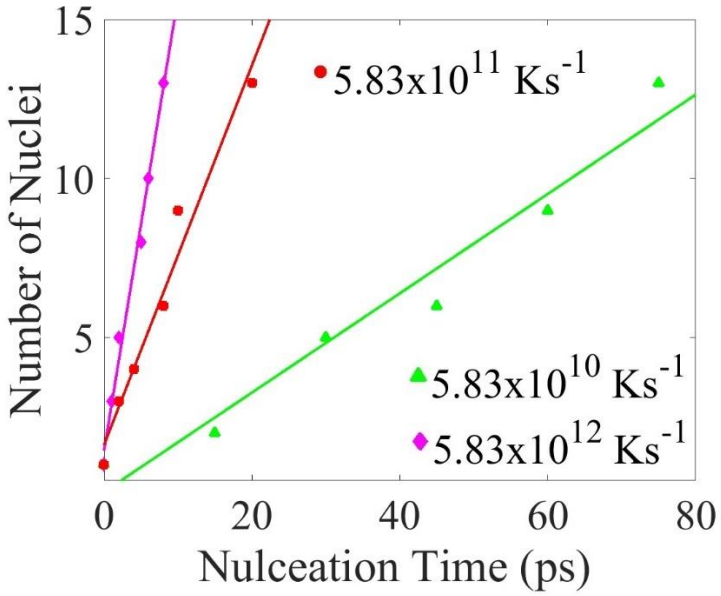

Figure 13. The number of nuclei as a function of time for various quench rates. The slope of these curves is the nucleation rate (see Table 2). The x axis shows the time between the start and finish of nucleation.

Table 3. Nucleation rates for different cooling rates in the quench process calculated from the fitted lines in Figure 12.

Cooling rate (10^{11} Ks^{-1})	58.30	5.83	0.58
Nucleation rate (I) (10^{35} $m^{-3}s^{-1}$)	1.12	0.41	0.08

The isothermal simulations in the previous section showed that the nucleation rate is temperature dependent. In quenching crystallization begins by formation of small

clusters of atoms at high temperatures. In Section 3.5 (Figure 11) the nucleation regimes for quenching show that the crystallization generally occurs between 586 K and 725 K. In a slower cooling rate, the crystallization occurs at a higher temperature.

In Figure 14 we show that the nucleation rates in the quenching process and the isothermal cases with high annealing temperatures are almost similar. At the highest cooling rate of 5.83x 10^{12} Ks^{-1} the nucleation rate is 1.12x10^{35} $m^{-3}s^{-1}$ (Table 2) lies between the nucleation rates isothermal cases at annealing temperatures of 650 K (1.12x10^{35} $m^{-3}s^{-1}$) and 700 K (0.07x10^{35} $m^{-3}s^{-1}$). The rate of nucleation is calculated using the same procedure used for isothermal process. Nucleation rate at cooling rate of 5.83x 10^{10} Ks^{-1} is very close to the nucleation of 725 K.

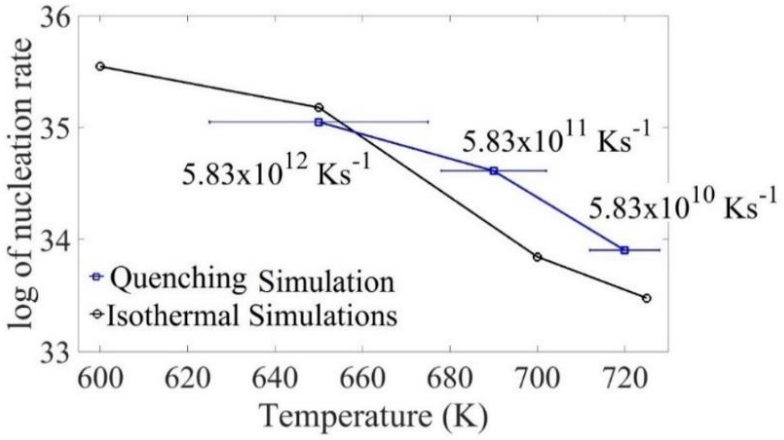

Figure 14. The log of nucleation rates for isothermal (600-725 K) and quenching cases are plotted. The corresponding nucleation temperature range is shown for the quenching simulations by horizontal bars.

3.8 TIME-TEMPERATURE-TRANSFORMATION (TTT) CURVE

Utilizing the isothermal MD simulation data, the time required to crystallize at least 40% of fcc and hcp atoms from undercooled liquid Al is determined as a function of temperature and plotted as a TTT curve in Figure 15. The TTT curve has the typical nose shape for crystallization, which has been observed in various experiments for different metallic materials and metallic glasses [73-75]. The TTT diagram was also replicated by some MD simulations previously [76-78].

In Figure 14, the top horizontal line (dotted red line) presents the TTT diagram for normal liquid Al. This is also the highest possible T_{sc} for Al. The bottom horizontal line (dotted green line) is the normal solid or it can be also referred to the minimum possible T_{gg} for Al. The circular points (with error bars) on the TTT diagram are the times taken to crystallize at least 40% of fcc and hcp atoms at different temperatures. The vertical line on the right side of the nose (dotted pink line) is the cooling with the highest quench rate of 5.83×10^{12} Ks^{-1} applied in our study. This line remains on the right side of the nose that suggests occurrence of crystal nucleation at 5.83×10^{12} Ks^{-1}. The tip of the nose is where the nucleation rate is the highest as the fastest crystallization occurs. As mentioned before in Section 3.6, the critical temperature for nucleation is determined to be around 475 K, and the nose area in Figure 15 also belongs to a similar temperature range.

A higher quench rate of 10^{13} Ks^{-1} is also applied, which is shown by the vertical line on the left side of the nose (dotted purple line) in Figure 15. The final structure obtained at this quench rate is a glassy structure. This result is consistent with the prediction of other TTT diagrams from MD simulations. In the work by Lu et al. [78], it was theoretically shown that the quench rate for forming glass structures is generally above 10^{12} Ks^{-1}. Other

MD simulation studies on bulk metallic glasses [79] also showed the critical cooling rate for glass formation is 10^{11}-10^{12} Ks^{-1}. Bulk metallic glasses are generally multi metallic compounds, so it is more difficult to promote homogeneous nucleation in bulk metallic glasses than in single element metals. This happens due to different sizes of atoms and also different thermal vibration at higher temperatures. Therefore, we suggest that the cooling rate for formation of glassy structure from pure Al melt is $5x10^{12}$ -$10^{13}Ks^{-1}$.

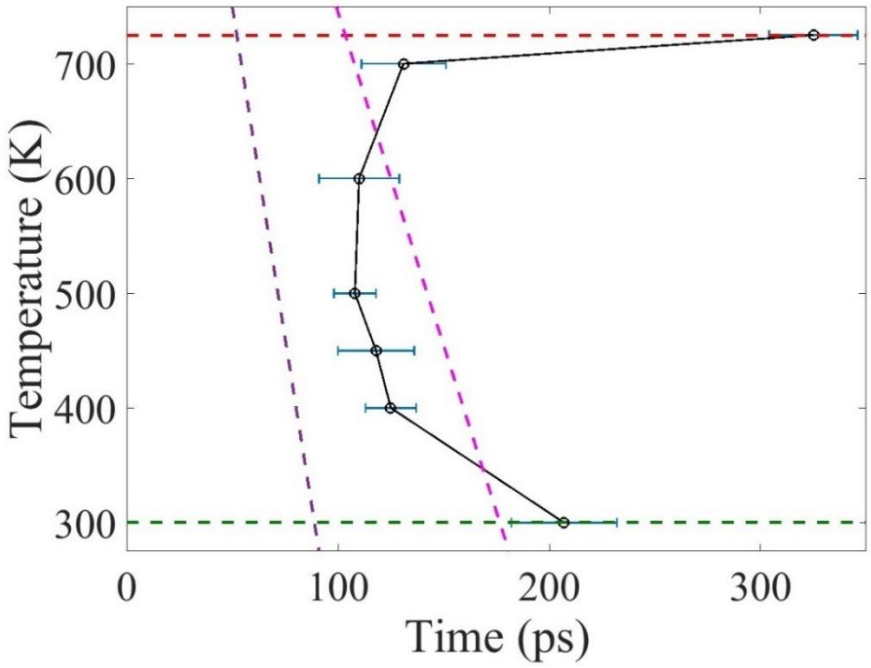

Figure 15. TTT diagram of Al determined by MD simulations. The top dotted red line is the liquid line, and the bottom green dotted line is the solid line. The circular points (with error bars) from isothermal MD simulations form the nose and are at the times needed to crystallize 40% of fcc and hcp atoms at different temperatures. The pink dotted line on the right of the nose is for cooling rate of 5.83x 10^{12} Ks^{-1} and the purple dotted line in the left is for the cooling rate of $10^{13}Ks^{-1}$.

3.9 COMPARISON WITH CLASSICAL NUCLEATION THEORY

CNT can provide some insights on the homogeneous nucleation process. CNT suggests that there is a free (activation) energy barrier, W^*, for formation of a solid nucleus with a critical size of r^*. The nucleation typically happens when the probability of energy fluctuation is sufficient to overcome the activation barrier. The probability of energy fluctuation is given by the Arrhenius type equation and the rate of homogeneous nucleation is [37, 80-82] ,

$$I = I_0 \exp\left(-\frac{W^*}{k_B T}\right) \tag{1}$$

where T is the temperature, k_B is the Boltzmann constant, and I_0 is a coefficient that depends on temperature and the interface free energy, σ_{SL} [82]. W^* is defined by [83],

$$W^* = \left(\frac{16\pi}{3}\frac{\sigma_{SL}^3}{(\Delta G_V)^2}\right) \tag{2}$$

ΔG_V is the difference between the free energies of liquid and solid crystal per unit volume. If the change in molar heat capacities is constant, ΔG_V according to Hoffman is equal to $\Delta H_m\left(T\Delta T / T_m^{\,2}\right)$ [84, 85], where ΔT is the undercooling ($\Delta T = T_m - T$), and ΔH_m is enthalpy of melting. By combining Eq. (1) and Eq. (2), the homogeneous nucleation rate becomes:

$$I = I_0 \exp\left[\left(-\frac{16\pi\sigma_{SL}^3 T_m^{\,4}}{3k_B(\Delta H_m)^2}\right)\frac{1}{T^3(\Delta T)^2}\right] = I_0 \exp\left(-\frac{A}{T^3(\Delta T)^2}\right) \tag{3}$$

where, A is a constant that depends on the solid-liquid interface energy and enthalpy. Eq. 3 also suggests that homogeneous nucleation rate strongly depends on the undercooling or

the annealing temperature. The nucleation rate is maximum at the critical temperature. The critical temperature can be derived from Eq. 3 by setting its first derivative to zero. This suggests that the critical temperature is $T_{cr} = \frac{3T_m}{5}$ (~550 K). As it was mentioned before, the calculated critical temperature from MD is ~ $\frac{T_m}{2}$ (475 K), which is a reasonable estimation from MD simulations and close to the CNT and experimental values of critical temperature of nucleation, which lies between 0.5-0.6 times of the melting temperature [86, 87].

We can also find the critical radius from CNT, which is suggested to be:

$$r^* = 2\frac{\sigma_{SL}}{\Delta G_V}, \tag{4}$$

We previously calculated σ_{SL} ,the specific free energy of the critical nucleus formation is estimated to be the interface the solid-liquid interface free energy of 172.6 mJ-m^{-2} and ΔH_m to be 11.50 kJmol^{-1} for Al [38]. The atomic volume in solidification is available from isothermal simulation. By utilizing Eq. 2 and considering the normalized temperature for annealing, $T_{normalized} = T / T_m$, ΔG_V is calculated for different annealing temperatures. So according to CNT the calculated critical radius (size/diameter) lies between 1.25 (2.5) nm and 2.0 (4.0) nm for different annealing temperatures.

The prediction of critical size from CNT is dependent on the annealing temperature (Figure 15). In Section 3.2, we showed at that the critical size calculated by MD simulations is between ~0.82 nm and 4 nm in the isothermal cases, and it is between ~1.8 to ~4.5 nm for quenching cases. CNT predicts almost similar critical sizes to MD simulations from 650 K. As it can be noticed in Figure 16, MD simulation results are closer to CNT

predictions at higher temperatures (700 K and 725 K) than at lower temperatures. Unlike at large undercooling temperatures (e.g., solidification at 450 K) where multiple critical nuclei form simultaneously, at lower undercooling temperatures (e.g., solidification at 700 K and 725 K) the critical nuclei form one after another (Figure 6). This is why each critical nucleus can grow in size without any influence from neighboring nuclei. So the nuclei can grow as much as predicted by CNT. Similarly, in MD simulations with slower quench rates of at 5.83×10^{10} Ks^{-1} and 5.83×10^{11} Ks^{-1}, the size of the critical nucleus matches well with the CNT predictions because the nucleation starts at temperature higher than 725 K. In Figure 6(c) and (d) this phenomenon can be clearly observed.

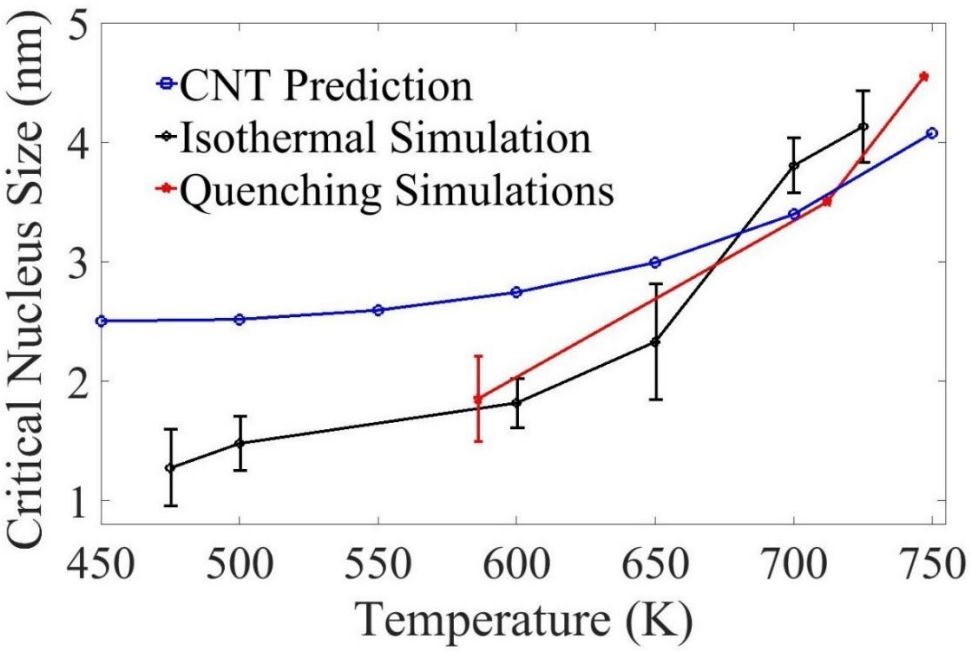

Figure 16. The critical nucleus size calculated by CNT at different temperatures is compared with the results of the isothermal and quenching simulations.

The difference between CNT and MD at lower annealing temperatures can be explained by analyzing Eq. (4). To calculate the critical nucleation size at different annealing (or undercooling) temperatures by Eq. (4), σ_{SL} at the melting point is used similar to the most of the other works in the literature [88-90]. This means the numerator of Eq. (4) is kept constant for calculating the critical size nucleus at different temperatures. However σ_{SL} decreases by lowering the annealing temperature (or increasing the undercooling) [91, 92]. Therefore the numerator of Eq. (4) should also decrease with lowering the annealing temperature, making the critical size predicted from CNT to become closer to the MD simulation data.

In Section 3.5 we divide the overall solidification process into three different parts. In the unstable nucleation regime, $T > T_{sc}$, and the grain growth regime, below T_{gg}, nucleation does not happen and CNT is not applicable. CNT is only applicable in the super-critical stable nucleation regime between T_{sc} and T_{gg}. As shown in Figure 16, CNT is in good agreement with MD simulations at higher temperatures, so CNT is mostly valid for the temperature range right below the super critical temperature (T_{sc}).

3.10 DETERMINATION OF INDUCTION TIME

In Sections 3.6 and 3.7, nucleation rates are calculated for both isothermal and quenching cases which show how frequently nucleation events occur in the superheated melt of Al. For higher nucleation rates, a system can escape the metastable superheated liquid state and form the crystalline phase. The ability of a system to sustain small thermal fluctuations while in a metastable equilibrium state is characterized by the induction time,

which is defined as the time elapsed between the establishment of supercooling and the appearance of persistent, stable nuclei [19]. The theory of homogenous nucleation suggests that the induction time is closely related to the nucleation rate, and the relationship depends on whether the system escapes the metastable state [19, 93, 94]. Nucleation can be divided into mono or polynuclear mechanisms [19]. When the system undergoes a phase transformation under conditions allowing the formation of many statistically independent nuclei it is called polynuclear mechanism, and for single nucleus it is called mononuclear mechanism. The formulations for the induction time for mononuclear, polynuclear, and combination of both mechanisms are given by Kashchiev et al. [94]. When the system volume is small, similar to our cases, polynuclear formulation reduces to that of the mononuclear case. The induction time for the mononuclear mechanism is given by, $\tau^* = \frac{1}{IV}$ where V is the volume of the system and I is the nucleation rate. Through this relationship, the induction time τ^* can be calculated from the previously obtained nucleation rate. It is worth mentioning that the role of *I* is weaker in the polynuclear case than in the mononuclear case [19]. As τ^* refers to the time required for the system to escape from the metastable to a stable crystalline state, we can also assume that it is the minimum time required for the first crystalline nucleus to form.

Mullin [93] alternatively defined the induction time as $\tau^* = t_r + t_n + t_g$; the induction time is divided into three periods. t_r is the relaxation time required for the system to achieve a quasi-steady-state distribution of molecules in the system; t_n is the time required for the formation of the first stable nucleus (critical sized); and t_g is the time

between formation of the first stable nucleus (or nuclei) and the second stable nucleus (or nuclei) inside the melt, and after this time the cluster of crystalline atoms do not dissolve back into the liquid phase.

The definition of induction time is valid for the quenching cases. But for isothermal processes superheated melt is kept at an annealing temperature directly and the nucleation occurs immediately. The time difference between first and second critical nucleus is very small until 600 K. Only at higher annealing temperatures such as 700 K or 725 K, there is a detectable time between formation and growth of the first critical nucleus and the formation of a secondary nucleus. This is evident by comparing the snapshots of nuclei formation and growth during solidification for isothermal and quenching processes in Figure 6(a) and (b). But as it was discussed before, in an isothermal process the whole process of crystallization happens without any change in temperature. It is not possible to generalize the induction time for isothermal processes, as we cannot get all the quantities for the Mullin's formulation for all the annealing temperatures. The isothermal process is equivalent to CNT which also assumes constant temperature for nucleation. Overall it is more meaningful to calculate the induction time for the quenching process.

During quenching solid atoms start gathering and attempt to form an initial nucleus before it reaches the critical size. The number of atoms and the size of the initial nucleus fluctuate for a few picoseconds before reaching the critical size. We refer to the time between the initial attempt to form a nucleus (20-25 clustered solid atoms) at a site and the formation of a critical size nucleus (1000-1500 clustered solid atoms, shown before in Figure 3(b)) as the nucleus origin time (t_o). In Figure 15, t_o and t_g are shown for the quench process at the cooling rate of 5.83×10^{11} Ks^{-1}.

We first determined t_o , t_n and t_g for different cooling rates by utilizing snapshots of MD simulations (Figure 17). The induction times calculated by using Eq. (5) and the Mullin's definition [93] are presented in Table 3. The initial relaxation time for the melt at 1,325 K (150 ps) is not included in the reported induction times. The problem with calculating induction time from Mullin's original formula is related to t_n. t_n is dependent on the superheat temperature and the nucleation rate. As it was shown previously in Section 3.3, the first nucleus (nuclei) occurs between 586 K and 725 K for Al for different cooling rates, but t_n will be significantly different for different cooling rates. In this work, the induction time is assumed to be the combination of t_o and t_g . These two quantities must be minimum for the nucleation rate to be maximum and vice versa. The results show a pattern of gradually increasing induction time with slower cooling rate.

Table 4**.** Induction time (ps) at different cooling rates.

Cooling Rate (10^{11} Ks^{-1})	58.3	5.83	0.58
t_n (MD)	273.0	1,053.0	10,471.0
t_o (MD)	5.0	12.0	15
t_g (MD)	13.0	20.5	27.5
$\tau^*(t_o + t_g)$ (Our Definition)	18.0	32.5	42.5
τ^* (Eq. (5))	0.57	1.46	7.52
$\tau^*(t_n + t_g)$ (Mullin's Definition)	286.0	1,073.5	10,498.5

t_o can be compared with the results of theory for τ^* in Eq. (5). However the theoretical values are much lower, because in theory, the induction time is based on the fact that nucleation is stationary [94]. Stationary means the temperature is constant throughout the solidification and a supersaturation is imposed on the system [94]. In a realistic nucleation system such as in quenching of a superheated melt, none of these conditions hold true.

3.11 GRAIN GROWTH

Grain growth is usually defined as an increase in the mean grain size in polycrystals with an increase in annealing time. As discussed in Section 3.5, solid-state grain growth occurs as soon as the simulation box is completely solid (the third regime), and this phenomenon is interesting both from the experimental and theoretical points of view, as it affects the mechanical properties of materials.

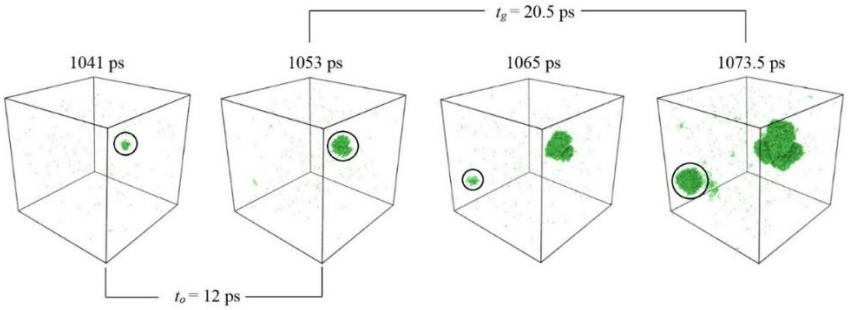

Figure 17. Formation of first and second critical sized nuclei is shown for quenching at the cooling rate of 5.83×10^{11} Ks^{-1}. The black circles show the process of first and second nuclei formation. Few solid atoms made the first attempt to form a solid cluster at 1,041 ps. At 1,053 ps, the first critical sized nucleus of 3.9 nm diameter is observed. Stable first nucleus and unstable second nucleus is shown at 1,065 ps.

To study solid-state grain growth, the simulation box is quenched from 1,325 K to 450 K, and then the resulting nanostructure is annealed at temperatures between 300 K and 725 K for 3,000 ps. The average grain size before starting the annealing process was ~5 nm.

Insignificant grain growth is observed for annealing temperatures lower than 450 K, (such as at 400 K and lower in Figure 18(a)). At higher annealing temperatures, the grain boundary motion results in formation of larger grains (Figure 18(b) and Figure 18(c)). The effect of temperature on grain growth is related to the mobility of atoms. This is also very relevant to experimental observations where more grain growth is generally detected at higher annealing temperatures [95-98].

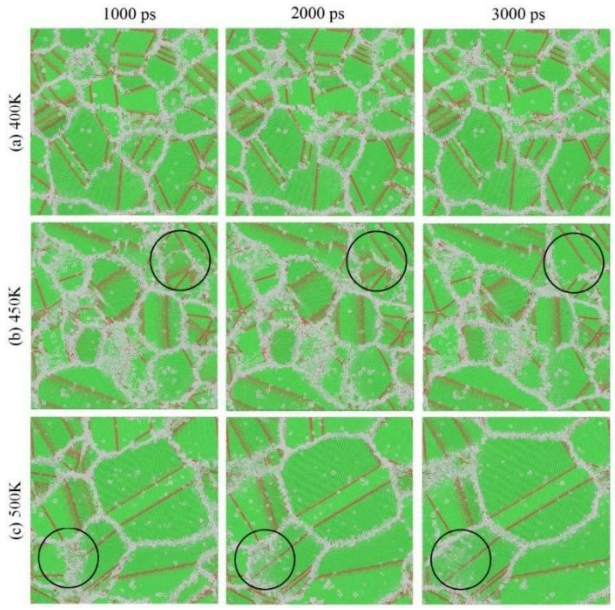

Figure 18. Snapshots of a 20 nm by 20 nm cross section from the simulation box. The simulation box was quenched from 1,325 K to 450 K, and then the resulting nanostructure was annealed at (a) 400 K, (b) 450 K and (c) 500 K. The black circles in (b) and (c) show the area where the grain growth happens and fcc atoms replaced amorphous solid atoms.

The average grain size versus simulation time is shown for different temperatures in Figure 19. The grain growth starts immediately for annealing temperatures higher than 600 K. For annealing temperatures below 450 K, the grain size remains below 10 nm at the end of 3,000 ps of annealing, whereas at 600 K the grains become as large as 15-20 nm. At 600 K and higher annealing temperatures no separate grains remain at the end of 3,000 ps of annealing, and the simulation box turned into a large single crystal, with a few stacking faults.

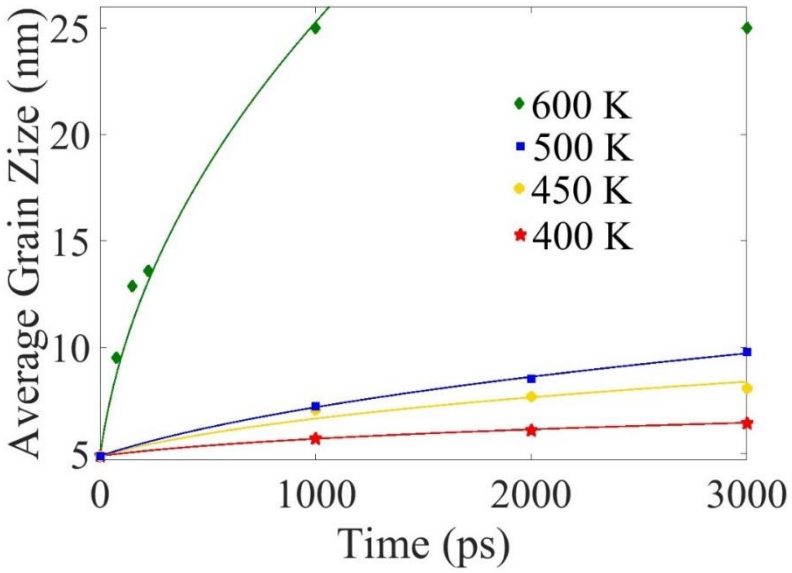

Figure 19. Average grain size versus simulation time at different annealing temperatures. Each data point is the average of five different simulations at the specific annealing temperature. The dashed lines show the result of the fit using Eq. (6) with parameters given in Table 4.

The temperature dependent grain growth can also be explained using a grain growth exponent (n). Grain growth can be described by a power law [99-101],

$$\left(D/D_0\right)^{1/n} - 1 = Kt \tag{5}$$

where D_0 is the initial average grain size before annealing (at t=0), D is the average grain size after a period of annealing, t is the time, and K is the overall rate constant. n is the grain growth exponent which depends on various factors such as grain boundary area, surface area, grain volume, and number of grains. The parameters are determined by fitting Eq. 6 to the simulation data (see Figure 19) and the results for n and K are presented in Table 4.

From Table 4, the grain growth exponent remains less than the ideal value (0.5 for parabolic growth). At 600 K the growth is almost parabolic until ~1,000 ps. After 1,000 ps the simulation box becomes a single crystal and the model does not apply. For lower annealing temperatures, the smaller values of n signify slower grain growth.

Table 5. The grain growth parameters n and K (ps^{-1}) in Eq. (6) for Al at various annealing temperatures.

	Temperature (K)			
Exponent	400 K	450 K	500 K	600 K
n	0.15	0.27	0.36	0.47
K	1.77×10^{-3}	2.11×10^{-3}	3.1×10^{-3}	3.18×10^{-2}

4. CONCLUSIONS

Homogenous nucleation from Al melt was investigated by million-atom MEAM-MD simulations. The main challenge of experimental studies of homogenous nucleation from pure Al is to observe the formation and growth of nuclei inside the melt during the solidification period, and the current work has enabled overcoming this challenge. We used both visual analysis such as direct observation of nuclei, and quantitative analysis of the data such as nucleation rate, induction time, fcc/hcp volume fraction, etc., to study the homogeneous nucleation process. Our MD simulations of homogenous nucleation utilizing a 3D simulation box with maximum of 5 million time steps allowed investigating the isothermal solidification process for 0.5 nanosecond and the quenching solidification process up to 15 nanoseconds.

Inspections by CNA showed that each nucleus had mainly fcc atoms with some hcp atoms. As the solidification process progressed, the hcp crystalline atoms aligned themselves to form stacking faults.

The average size of critical nuclei was determined to be between ~0.82 nm and ~4 nm in the isothermal processes, and between 1.8 nm and 4.5 nm in the quench processes. The size of critical nuclei follows the predictions of CNT. In the isothermal processes with annealing temperatures between 300 K to 475 K the critical nucleus size doesn't change significantly. But after that till 725 K the critical size increases with increasing annealing temperature. A relatively large number of nuclei formed (>50 nuclei in 25 nm^3). Below 350 K, the nucleation phenomenon was suppressed by fast solidification due to a very high driving force of solidification, and in cooperation with a low mobility of atoms resulted in

formation of more amorphous solid atoms and lowering the number of crystalline nuclei (<40 nuclei in 25 nm^3). Above 700 K, the number of critical nuclei was reduced (<10 nuclei in 25 nm^3); at these high temperatures since there is not nucleation and growth of considerable number of crystalline nuclei or amorphous solid atoms, the few crystalline nuclei can growth to a much larger size before the simulation box is completely solid.

Utilizing the potential energy and percent crystalline atoms versus temperature data for quenching simulations (Figure 10(c) and Figure 10(d)), the solidification process can be divided into three temperature based thermodynamics regimes, where the specific temperatures (T_{sc} and T_{gg}) depend upon the quench rate: Sub-critical unstable nucleation regime above T_{sc} ,Super-critical Stable nucleation regime between T_{sc} and T_{gg} , and Solid-state grain growth regime below T_{gg} . These regions were not clearly seen for isothermal cases with low annealing temperatures. Only at high temperature annealing of 650 K, 700 K and 725 K, could these three distinct regions be observed. The change in instantaneous temperature during nucleation (i.e. solidification) indicated that quenching is more realistic simulation procedure to study a nucleation process. As cooling rate decreases, the T_{sc} moves towards the melting point.

We also determined the percentage of different type atoms for both isothermal and quenching cases. In the isothermal cases with higher annealing temperatures such as 700 K and 725 K, the percentage of fcc atoms (~60-65 %) was higher compared with that of the cases with lower annealing temperatures (~50-55 %). At very low annealing temperatures such as 300K and 350 K, the percentage of fcc atoms was very low (< 45%).

In the quenching cases, by decreasing the cooling rate from 5.83×10^{12} Ks^{-1} to 5.83×10^{10} Ks, the percentage of fcc atoms increased from ~20% to ~80%.

To determine the critical temperature for homogenous nucleation in the isothermal cases, the nucleation rate was calculated by plotting the number of nuclei versus time. The critical temperature of Al was determined to be ~475 K, with a maximum nucleation rate of 5.74×10^{35} $m^{-3}s^{-1}$. The nucleation rate in quenching simulations was determined to be one to two orders of magnitude lower than that in isothermal cases with annealing temperatures lower than 600 K. This was attributed to the fact that in the quenching cases the nucleation occurred only between ~747 K to ~586 K, however in the isothermal cases with low annealing temperatures the nucleation and solidification occurred almost instantly. The nucleation rates for the isothermal cases with annealing temperatures of 700 K and 725 K are almost the same as those for quenching cases. Since nucleation during quenching occurs at much higher temperature than the critical temperature, it is not clear that the critical temperature and maximum nucleation rate has any significance for the actual nucleation process.

The critical nucleus size and the critical temperature for nucleation determined by MD simulations were compared to the CNT predictions. The critical temperature for nucleation obtained from CNT was close to the results obtained by MD simulations for the isothermal cases. The calculated critical size of nucleus using CNT increases with increasing annealing temperature, and is very close to the values obtained from MD simulations above 650 K. But, CNT estimates the critical size to be higher than MD simulations for lower annealing temperatures. One reason is that there are simultaneous critical nuclei forming in the system at lower annealing temperatures. But at higher

temperatures the critical nuclei form one after another, and the increase in size of a critical nucleus is not significantly influenced by other nuclei in the system. This is why each nucleus can grow much more independently at higher temperatures and can become closer to CNT predictions. The second reason is that, we have assumed σ_{SL} is independent of temperature. Since the solid-liquid interface energy is expected to decrease with decreasing temperature, using a temperature dependent σ_{SL} will result in an additional decrease in the critical size of the nucleus at lower temperatures, confirming the MD simulation results.

The induction time, which is closely related to the nucleation rate, was also calculated by MD simulation results. In theory (Eq. (5)), the induction time is inversely related to the nucleation rate and gives the time for formation of the first critical nucleus; however since it assumes a constant temperature and superheated melt throughout the solidification, it does not reasonably mimic the realistic experimental conditions. We compared the theoretical value of induction time to our defined nucleus origin time (t_o), both showing it increased by decreasing the cooling rate. We defined the actual induction time to be the time from the initial stages (3-5 clustered crystalline atoms) of formation of the first critical nucleus (nuclei) until the formation of the second critical nucleus (nuclei) ($t_o + t_g$).

Significant grain growth occurred in a temperature region above 500 K and below 650 K. At lower annealing temperatures, low mobility of atoms results in a very low grain growth rate. Grain growth exponent (*n*) increased by increasing the annealing temperature, and it reached the ideal value of 0.5 at 600 K.

REFERENCES

[1] J. Campbell, *Complete casting handbook: metal casting processes, metallurgy, techniques and design*: Butterworth-Heinemann, 2015.

[2] J. W. Christian, *The theory of transformations in metals and alloys*: Newnes, 2002.

[3] D. Hu and R. Kovacevic, "Sensing, modeling and control for laser-based additive manufacturing," *International Journal of Machine Tools and Manufacture,* vol. 43, pp. 51-60, 2003.

[4] D. W. Oxtoby, "Homogeneous nucleation: theory and experiment," *Journal of Physics: Condensed Matter,* vol. 4, p. 7627, 1992.

[5] P.-P. E. de Moor, T. P. Beelen, and R. A. van Santen, "In situ observation of nucleation and crystal growth in zeolite synthesis. A small-angle X-ray scattering investigation on Si-TPA-MFI," *The Journal of Physical Chemistry B,* vol. 103, pp. 1639-1650, 1999.

[6] D. Zhang and B. Cantor, "Heterogeneous nucleation of In particles embedded in an AI matrix," *Philosophical Magazine A,* vol. 62, pp. 557-572, 1990.

[7] D. Uhlenhaut, J. Kradolfer, W. Püttgen, J. Löffler, and P. Uggowitzer, "Structure and properties of a hypoeutectic chromium steel processed in the semi-solid state," *Acta Materialia,* vol. 54, pp. 2727-2734, 2006.

[8] C. Ho and B. Cantor, "Heterogeneous nucleation of solidification of Si in Al-Si and Al-Si-P alloys," *Acta metallurgica et materialia,* vol. 43, pp. 3231-3246, 1995.

[9] D. Turnbull and R. Cech, "Microscopic observation of the solidification of small metal droplets," *Journal of Applied Physics,* vol. 21, pp. 804-810, 1950.

[10] S. Ringer, K. Hono, I. Polmear, and T. Sakurai, "Nucleation of precipitates in aged Al Cu Mg (Ag) alloys with high Cu: Mg ratios," *Acta Materialia,* vol. 44, pp. 1883-1898, 1996.

[11] F. Humphreys, "The nucleation of recrystallization at second phase particles in deformed aluminium," *Acta Metallurgica,* vol. 25, pp. 1323-1344, 1977.

[12] B. Cantor and K. O'Reilly, *Solidification and casting*: CRC Press, 2016.

[13] G. Neilson and M. Weinberg, "A test of classical nucleation theory: crystal nucleation of lithium disilicate glass," *Journal of Non-Crystalline Solids,* vol. 34, pp. 137-147, 1979.

[14] D. Erdemir, A. Y. Lee, and A. S. Myerson, "Nucleation of crystals from solution: classical and two-step models," *Accounts of chemical research,* vol. 42, pp. 621-629, 2009.

[15] S. J. Lindsay, "Very High Purity Aluminum: An Historical Perspective," *JOM,* vol. 66, pp. 217-222, 2014.

[16] M. Kondo, H. Maeda, and M. Mizuguchi, "The production of high-purity aluminum in Japan," *Jom,* vol. 42, pp. 36-37, 1990.

[17] S. Lee, H. S. Wi, W. Jo, Y. C. Cho, H. H. Lee, S.-Y. Jeong, *et al.*, "Multiple pathways of crystal nucleation in an extremely supersaturated aqueous potassium dihydrogen phosphate (KDP) solution droplet," *Proceedings of the National Academy of Sciences,* vol. 113, pp. 13618-13623, 2016.

[18] R. E. Schreiber, L. Houben, S. G. Wolf, G. Leitus, Z.-L. Lang, J. J. Carbó, *et al.*, "Real-time molecular scale observation of crystal formation," *Nature Chemistry,* 2016.

[19] P. Yi and G. C. Rutledge, "Molecular origins of homogeneous crystal nucleation," *Annual review of chemical and biomolecular engineering,* vol. 3, pp. 157-182, 2012.

[20] G. Kahl and H. Löwen, "Classical density functional theory: an ideal tool to study heterogeneous crystal nucleation," *Journal of Physics: Condensed Matter,* vol. 21, p. 464101, 2009.

[21] D. Juric and G. Tryggvason, "A Front-Tracking Method for Dendritic Solidification," *Journal of Computational Physics,* vol. 123, pp. 127-148, 1996.

[22] R. Kobayashi, "Modeling and numerical simulations of dendritic crystal growth," *Physica D: Nonlinear Phenomena,* vol. 63, pp. 410-423, 1993.

[23] Z. H. Li, D. Bhatt, N. E. Schultz, J. I. Siepmann, and D. G. Truhlar, "Free Energies of Formation of Metal Clusters and Nanoparticles from Molecular Simulations: Al n with n= 2-60," *The Journal of Physical Chemistry C,* vol. 111, pp. 16227-16242, 2007.

[24] S. L. Girshick, P. Agarwal, and D. G. Truhlar, "Homogeneous nucleation with magic numbers: Aluminum," *The Journal of chemical physics,* vol. 131, p. 134305, 2009.

[25] P. R. ten Wolde and D. Frenkel, "Homogeneous nucleation and the Ostwald step rule," *Physical Chemistry Chemical Physics,* vol. 1, pp. 2191-2196, 1999.

[26] A. Laaksonen, V. Talanquer, and D. W. Oxtoby, "Nucleation: Measurements, theory, and atmospheric applications," *Annual Review of Physical Chemistry,* vol. 46, pp. 489-524, 1995.

[27] H. Reiss, W. Kegel, and J. Katz, "Role of the model dependent translational volume scale in the classical theory of nucleation," *The Journal of Physical Chemistry A,* vol. 102, pp. 8548-8555, 1998.

[28] A. Cacciuto, S. Auer, and D. Frenkel, "Onset of heterogeneous crystal nucleation in colloidal suspensions," *Nature,* vol. 428, pp. 404-406, 2004.

[29] M. Mandell, J. McTague, and A. Rahman, "Crystal nucleation in a three-dimensional Lennard-Jones system: A molecular dynamics study," *The journal of chemical physics,* vol. 64, pp. 3699-3702, 1976.

[30] M. Horsch, J. Vrabec, and H. Hasse, "Modification of the classical nucleation theory based on molecular simulation data for surface tension, critical nucleus size, and nucleation rate," *Physical Review E,* vol. 78, p. 011603, 2008.

[31] S. Wonczak, R. Strey, and D. Stauffer, "Confirmation of classical nucleation theory by Monte Carlo simulations in the 3-dimensional Ising model at low temperature," *The Journal of Chemical Physics,* vol. 113, pp. 1976-1980, 2000.

[32] K. Kelton and A. Greer, "Test of classical nucleation theory in a condensed system," *Physical Review B,* vol. 38, p. 10089, 1988.

[33] R. Heady and J. Cahn, "Experimental test of classical nucleation theory in a liquid-liquid miscibility gap system," *The Journal of Chemical Physics,* vol. 58, pp. 896-910, 1973.

[34] H. Vehkamäki, *Classical nucleation theory in multicomponent systems*: Springer Science & Business Media, 2006.

[35] L. Filion, R. Ni, D. Frenkel, and M. Dijkstra, "Simulation of nucleation in almost hard-sphere colloids: The discrepancy between experiment and simulation persists," *The Journal of chemical physics,* vol. 134, p. 134901, 2011.

[36] P. Rein ten Wolde, M. J. Ruiz-Montero, and D. Frenkel, "Numerical calculation of the rate of crystal nucleation in a Lennard-Jones system at moderate undercooling," *The Journal of chemical physics,* vol. 104, pp. 9932-9947, 1996.

[37] S. Auer and D. Frenkel, "Prediction of absolute crystal-nucleation rate in hard-sphere colloids," *Nature,* vol. 409, pp. 1020-1023, 2001.

[38] E. Asadi, M. A. Zaeem, S. Nouranian, and M. I. Baskes, "Two-phase solid–liquid coexistence of Ni, Cu, and Al by molecular dynamics simulations using the modified embedded-atom method," *Acta Materialia,* vol. 86, pp. 169-181, 2015.

[39] S. Wang, M. Asle Zaeem, M. F. Hortsmeyer, and P. T. Wang, "Thermal effects on the morphological evolution during crystallization of HCP metals: A three dimensional phase-field study," *Materials Technology,* vol. 27(5), pp. 355-363, 2012.

[40] M. Asle Zaeem and S. Felicelli, "Simulation of dendrite growth in solidification of Al-3% Cu using cellular automaton and phase-field methods," *Applied Mathematical Modeling,* 2013.

[41] M. Asle Zaeem, H. Yin, and S. D. Felicelli, "Comparison of Cellular Automaton and Phase Field Models to Simulate Dendrite Growth in Hexagonal Crystals," *Materials Science & Technology,* vol. 28, pp. 137-146, 2012.

[42] Y. Shibuta, S. Sakane, T. Takaki, and M. Ohno, "Submicrometer-scale molecular dynamics simulation of nucleation and solidification from undercooled melt: Linkage between empirical interpretation and atomistic nature," *Acta Materialia,* vol. 105, pp. 328-337, 2016.

[43] Z. Hou, K. Dong, Z. Tian, R. Liu, Z. Wang, and J. Wang, "Cooling rate dependence of solidification for liquid aluminium: a large-scale molecular dynamics simulation study," *Physical Chemistry Chemical Physics,* vol. 18, pp. 17461-17469, 2016.

[44] K. Yasuoka and M. Matsumoto, "Molecular dynamics simulation of homogeneous nucleation in supersaturated water vapor," *Fluid Phase Equilibria,* vol. 144, pp. 369-376, 1998.

[45] M. Finnis and J. Sinclair, "A simple empirical N-body potential for transition metals," *Philosophical Magazine A,* vol. 50, pp. 45-55, 1984.

[46] Ş. Erkoç and Ş. Katircioğlu, "Molecular-dynamics simulation of aluminum microclusters," *physica status solidi (b),* vol. 152, pp. K37-K41, 1989.

[47] M. Dharma-Wardana and G. Aers, "Determination of the pair potential and the ion-electron pseudopotential for aluminum from experimental structure-factor data for liquid aluminum," *Physical Review B,* vol. 28, p. 1701, 1983.

[48] M. Mendelev, M. Kramer, C. A. Becker, and M. Asta, "Analysis of semi-empirical interatomic potentials appropriate for simulation of crystalline and liquid Al and Cu," *Philosophical Magazine,* vol. 88, pp. 1723-1750, 2008.

[49] X.-Y. Liu, F. Ercolessi, and J. B. Adams, "Aluminium interatomic potential from density functional theory calculations with improved stacking fault energy," *Modelling and Simulation in Materials Science and Engineering,* vol. 12, p. 665, 2004.

[50] M. S. Daw and M. I. Baskes, "Embedded-atom method: Derivation and application to impurities, surfaces, and other defects in metals," *Physical Review B,* vol. 29, pp. 6443-6453, 1984.

[51] M. Baskes, "Modified embedded-atom potentials for cubic materials and impurities," *Physical Review B,* vol. 46, p. 2727, 1992.

[52] M. I. Baskes, "Application of the Embedded-Atom Method to Covalent Materials: A Semiempirical Potential for Silicon," *Physical Review Letters,* vol. 59, pp. 2666-2669, 1987.

[53] B.-J. Lee, J.-H. Shim, and M. I. Baskes, "Semiempirical atomic potentials for the fcc metals Cu, Ag, Au, Ni, Pd, Pt, Al, and Pb based on first and second nearest-neighbor modified embedded atom method," *Physical Review B,* vol. 68, p. 144112, 2003.

[54] B. Jelinek, S. Groh, M. F. Horstemeyer, J. Houze, S. G. Kim, G. J. Wagner, *et al.*, "Modified embedded atom method potential for Al, Si, Mg, Cu, and Fe alloys," *Physical Review B,* vol. 85, p. 245102, 2012.

[55] E. Asadi, M. A. Zaeem, and M. I. Baskes, "Phase-field crystal model for Fe connected to MEAM molecular dynamics simulations," *JOM,* vol. 66, pp. 429-436, 2014.

[56] E. Asadi and M. Asle Zaeem, "A modified two-mode phase-field crystal model applied to face-centered cubic and body-centered cubic orderings," *Computational Materials Science,* vol. 105, pp. 110-113, 2015.

[57] E. Asadi and M. Asle Zaeem, "The anisotropy of hexagonal close-packed and liquid interface free energy using molecular dynamics simulations based on modified embedded-atom method," *Acta Materialia,* vol. 107, pp. 337-344, 2016.

[58] B.-J. Lee and M. Baskes, "Second nearest-neighbor modified embedded-atom-method potential," *Physical Review B,* vol. 62, p. 8564, 2000.

[59] L. Moraru and M. Vlad, "Nucleation of Crystals in Undercooled Molten Aluminium," *REVISTA DE CHIMIE-BUCHAREST-ORIGINAL EDITION-,* vol. 58, p. 129, 2007.

[60] G. Simmons and H. Wang, "Single crystal elastic constants and calculated aggregate properties," 1971.

[61] W. F. Gale and T. C. Totemeier, *Smithells metals reference book*: Butterworth-Heinemann, 2003.

[62] A. M. James and M. P. Lord, *Macmillan's chemical and physical data*: Macmillan, 1992.

[63] Q. Jiang and H. Lu, "Size dependent interface energy and its applications," *Surface Science Reports,* vol. 63, pp. 427-464, 2008.

[64] M. Parrinello and A. Rahman, "Polymorphic transitions in single crystals: A new molecular dynamics method," *Journal of Applied physics,* vol. 52, pp. 7182-7190, 1981.

[65] S. Plimpton, "Fast parallel algorithms for short-range molecular dynamics," *Journal of computational physics,* vol. 117, pp. 1-19, 1995.

[66] A. Stukowski, "Visualization and analysis of atomistic simulation data with OVITO–the Open Visualization Tool," *Modelling and Simulation in Materials Science and Engineering,* vol. 18, p. 015012, 2009.

[67] H. Tsuzuki, P. S. Branicio, and J. P. Rino, "Structural characterization of deformed crystals by analysis of common atomic neighborhood," *Computer physics communications,* vol. 177, pp. 518-523, 2007.

[68] S. Das and L. Davis, "High performance aerospace alloys via rapid solidification processing," *Materials science and engineering,* vol. 98, pp. 1-12, 1988.

[69] F. Froes, Y.-W. Kim, and S. Krishnamurthy, "Rapid solidification of lightweight metal alloys," *Materials Science and Engineering: A,* vol. 117, pp. 19-32, 1989.

[70] A. Kulovits, R. Zhong, J. Wiezorek, and J. Leonard, "Electron microscopy of geometrically confined copper thin films after rapid lateral solidification," *Thin Solid Films,* vol. 517, pp. 3629-3634, 2009.

[71] F. Kargl, H. Weis, T. Unruh, and A. Meyer, "Self diffusion in liquid aluminium," in *Journal of Physics: Conference Series*, 2012, p. 012077.

[72] J. A. Dantzig and M. Rappaz, *Solidification*: EPFL press, 2009.

[73] M. Pohl, O. Storz, and T. Glogowski, "Effect of intermetallic precipitations on the properties of duplex stainless steel," *Materials characterization,* vol. 58, pp. 65-71, 2007.

[74] J. F. Löffler, J. Schroers, and W. L. Johnson, "Time–temperature–transformation diagram and microstructures of bulk glass forming Pd 40 Cu 30 Ni 10 P 20," *Applied Physics Letters,* vol. 77, pp. 681-683, 2000.

[75] F. Caballero, H. Bhadeshia, K. Mawella, D. Jones, and P. Brown, "Very strong low temperature bainite," *Materials science and technology,* vol. 18, pp. 279-284, 2002.

[76] E. V. Levchenko, A. V. Evteev, I. V. Belova, and G. E. Murch, "Molecular dynamics determination of the time–temperature–transformation diagram for crystallization of an undercooled liquid Ni 50 Al 50 alloy," *Acta Materialia,* vol. 59, pp. 6412-6419, 2011.

[77] E. B. Moore and V. Molinero, "Structural transformation in supercooled water controls the crystallization rate of ice," *Nature,* vol. 479, pp. 506-508, 2011.

[78] Z. Lu and C. Liu, "Glass formation criterion for various glass-forming systems," *Physical review letters,* vol. 91, p. 115505, 2003.

[79] E. V. Levchenko, A. V. Evteev, I. V. Belova, and G. E. Murch, "Molecular dynamics determination of the time–temperature–transformation diagram for crystallization of an undercooled liquid Ni50Al50 alloy," *Acta Materialia,* vol. 59, pp. 6412-6419, 2011/09/01/ 2011.

[80] V. Kalikmanov, "Classical nucleation theory," in *Nucleation theory*, ed: Springer, 2013, pp. 17-41.

[81] J. W. Schmelzer, *Nucleation theory and applications*: John Wiley & Sons, 2006.

[82] I. Gutzow and J. Schmelzer, *The vitreous state*: Springer, 1995.

[83] A. Myerson, *Handbook of industrial crystallization*: Butterworth-Heinemann, 2002.

[84] K. Kelton, "Crystal nucleation in liquids and glasses," *Solid state physics,* vol. 45, pp. 75-177, 1991.

[85] V. M. Fokin, E. D. Zanotto, N. S. Yuritsyn, and J. W. Schmelzer, "Homogeneous crystal nucleation in silicate glasses: a 40 years perspective," *Journal of Non-Crystalline Solids,* vol. 352, pp. 2681-2714, 2006.

[86] W. Pan, A. B. Kolomeisky, and P. G. Vekilov, "Nucleation of ordered solid phases of proteins via a disordered high-density state: Phenomenological approach," *The Journal of chemical physics,* vol. 122, p. 174905, 2005.

[87] S. Sen and T. Mukerji, "A generalized classical nucleation theory for rough interfaces: application in the analysis of homogeneous nucleation in silicate liquids," *Journal of Non-Crystalline Solids,* vol. 246, pp. 229-239, 1999.

[88] Z. Lin, E. Leveugle, E. M. Bringa, and L. V. Zhigilei, "Molecular Dynamics Simulation of Laser Melting of Nanocrystalline Au," *The Journal of Physical Chemistry C,* vol. 114, pp. 5686-5699, 2010/04/01 2010.

[89] X.-M. Bai and M. Li, "Calculation of solid-liquid interfacial free energy: A classical nucleation theory based approach," *The Journal of Chemical Physics,* vol. 124, p. 124707, 2006/03/28 2006.

[90] D. Turnbull, "Formation of crystal nuclei in liquid metals," *Journal of Applied Physics,* vol. 21, pp. 1022-1028, 1950.

[91] Z. Jian, K. Kuribayashi, and W. Jie, "Solid-liquid interface energy of metals at melting point and undercooled state," *Materials Transactions,* vol. 43, pp. 721-726, 2002.

[92] T. Frolov and Y. Mishin, "Solid-liquid interface free energy in binary systems: Theory and atomistic calculations for the (110) Cu–Ag interface," *The Journal of chemical physics,* vol. 131, p. 054702, 2009.

[93] J. Mullin, "Crystallisation, 4th Edition'," ed: Butterworth-Heinemann, Oxford, UK, 2001.

[94] D. Kashchiev, "Nucleation: basic theory with applications," ed: Butterworth Heinemann: Boston, 2000.

[95] J. Wyrzykowski and M. Grabski, "Effect of annealing temperature on structure and properties of fine-grained aluminium," *Metal science,* 2013.

[96] T. R. Malow and C. C. Koch, "Grain growth in nanocrystalline iron prepared by mechanical attrition," *Acta Materialia,* vol. 45, pp. 2177-2186, 1997/05/01 1997.

[97] L. Lu, N. R. Tao, L. B. Wang, B. Z. Ding, and K. Lu, "Grain growth and strain release in nanocrystalline copper," *Journal of Applied Physics,* vol. 89, pp. 6408-6414, 2001.

[98] F. Liu and R. Kirchheim, "Grain boundary saturation and grain growth," *Scripta Materialia,* vol. 51, pp. 521-525, 9// 2004.

[99] M. Asle Zaeem, H. El Kadiri, P. T. Wang, and M. F. Horstemeyer, "Investigating the effects of grain boundary energy anisotropy and second-phase particles on grain growth using a phase-field model," *Computational Materials Science,* vol. 50, pp. 2488-2492, 2011.

[100] R. Vandermeer and H. Hu, "On the grain growth exponent of pure iron," *Acta Metallurgica et Materialia,* vol. 42, pp. 3071-3075, 1994.

[101] P. A. Beck, J. C. Kremer, L. Demer, and M. Holzworth, "Grain growth in high-purity aluminum and in an aluminum-magnesium alloy," *Trans. Am. Inst. Min. Metall. Eng,* vol. 175, pp. 372-400, 1948.

II. EVOLUTION OF SOLIDIFICATION DEFECTS IN DEFORMATION OF NANO-POLYCRYSTALLINE ALUMINUM

Avik Mahata[1] and Mohsen Asle Zaeem[1,2*]

[1] Department of Materials Science and Engineering, Missouri University of Science and Technology, Rolla, MO 65409, USA

[2] Department of Mechanical Engineering, Colorado School of Mines, Golden, CO 40801, USA

(*Published in Computational Materials Science 163 (2019): 176-185*)

ABSTRACT

Formation of solidification defects and their evolution in uniaxial tensile deformation of solidified polycrystalline aluminum (Al) were investigated by molecular dynamics (MD) simulations. First, solidification process was simulated both isothermally and with different quench rates. At the initial stages of nucleation, coherent twin boundaries and/or fivefold twins formed depending on the quench rate or the undercooling temperature. The solidified polycrystalline Al consisted of randomly distributed grains, twin boundaries, and vacancies. Evolution of nanostructures and defects in uniaxial tensile deformation of solidified Al under different temperatures and strain rates were studied. Void formation at grain boundaries and detwinning of preexisting solidification twins and deformation twins were observed during the uniaxial deformation. It was also found that the temperature of deformation has a stronger effect than the applied strain rate on the strength of solidified samples. For solidified cases with grain sizes lower than 10 nm, the yield strength and Young's modulus increased with increasing grain size, indicating an inverse Hall-Petch relationship. Similar to experimental data, MD simulations showed a

higher yield strength for single crystal Al and a large plastic deformation for polycrystalline Al.

1. INTRODUCTION

Solidification plays a significant role in various manufacturing processes such as casting and additive manufacturing. The nano- and micro-structures that form during solidification determine the mechanical response and deformation behavior of solidified materials, which can be distinctly different from those of the single crystal counterparts. Study the process-mediated defects at the nanoscale and their effect on deformation and mechanical response of materials is very important for their reliable use in practical applications.

Crystal defects such as dislocations (one dimensional line defects) and twins (two dimensional planar defects) form in metallic materials during the solidification process. These defects play critical roles in facilitating plastic deformation and ultimately control various mechanical behaviors of most polycrystalline metals and alloys [1-3]. Formation of twin phases in metallic alloys by means of deformation has been reported quite frequently in the literature [4-8]. Formation of twins in solidified [9-11] and annealed [12-14] metals are also reported. The final grain structure after solidification is modified by multiple twins and they can affect the distribution of crystallographic orientations of grains in the ingot [15]. It is essential to know the evolution of twin structures as the solidification progresses. However, the initial stages of formation of twins during solidification have never been investigated in depth. Tracing the origin of the twin formation in a

manufacturing process is extremely difficult because the real-time monitoring of nucleation and solidification process in metals and alloys at atomic scale is almost impossible experimentally [16-19].

Controlling factors such as strain rate (SR) and temperature during plastic deformation have critical effects on the deformation mechanisms (stacking faults, twinning, voids, dislocations, and grain boundaries). These factors also affect the mechanical properties of metallic systems. Usually dislocations govern the plastic deformation [20-22], but as grain size decreases the dislocation activity is suppressed by the grain boundaries (GBs) and twinning. When a critical average grain size is achieved, which was reported previously to be ~10 nm for Al [4, 23]), GB related phenomena and twinning become the primary deformation mechanisms.

In the particular case of aluminum (Al), first efforts to study solidification twins were done more than half a century ago [24, 25]. The study by Fredriksson and Hillert on Al showed how all the twin tips grow in the same (112) growth direction, and this gives the tip a favorable shape. By producing sharp edges, feathery crystal growth is observed during continuous casting. This proposed twining process during solidification of Al has never been explained in depth. The study by Fredriksson and Hillert found a particularly interesting case to correlate twinning and feathery growth of Al, and they reported twin boundary motions in both (112) and (110) directions. Few other experimental studies reported both solidification and deformation twins in single crystal of Al [4, 12, 26]. Also, a previous study reported fivefold twining of Al during nanoindentation based on a quasicontinuum method [27]. Most studies related to twinning in Al are based on deformation induced twins, but studying twinning during solidification is also important in

order to understand the origin and evolution of twins. However, five-fold twins are studied using MD simulations for some other metals such as Cu [28, 29] and Fe [30].

Materials with a high SFE have difficulty undergoing twinning by deformation. Al for example with a high SFE of 104-142 mJ m^{-2} has difficulty twinning [4, 31-34]. This is due to the much higher shear stress needed for nucleation of the twinning partial dislocations than the trailing partial dislocations , and also because of the large amount of slip systems in the fcc structure, which make the slip a dominant deformation mechanism [26, 35]. However, it has been shown that twinning in nanocrystalline Al is quite possible [32, 35, 36]. Plastically deformed Al with a thickness between 200 nm and 400 nm and an average grain size between 10 nm and 35nm [4] shows deformation twins, dislocations and stacking faults. The interplay between twinning, stacking faults and dislocations was also revealed extensively in nanocrystalline Al by MD simulations of tensile testing with a load of 2.5 GPa and at 300 K [35]. Nanocrystalline twinning can be explained by a dislocation based model. Glides of Shockley partial dislocations, twinning dislocations with a Burges vector = a_o<112>/6 (a_o is the lattice constant), on consecutive planes create multilayered intrinsic stacking faults which produces a twin [37]. Even though twinning in bulk Al is less common, twinning in nanocrystalline Al is frequently reported in the literature. Twinning is generally a permanent deformation, but under high SRs detwinning has been observed in Al [32, 38]. Detwinning is usually a two-step process. First, the twin boundaries come closer together causing the twin to get thinner, and then the twin boundaries will get shorter and eventually disappear [38].

In the literature, there are several deformation studies done on polycrystalline metals by MD simulations. But in these studies, the polycrystalline metals were created

artificially by building the structure using Voronoi tessellation methods [39-42] or introducing multiple nanotwins [3, 8]. The artificially created grain boundaries can only observe twins/dislocations when the deformation process starts. In reality, the solidified metals are supposed to have randomly distributed defects and solidification twins. The other disadvantages of artificially created grains are that the initial twinning and dislocations do not have any interactions with other defects other than the GBs.

In this work, we study twins that formed during solidification of Al melt and the deformation twins caused by deformation of nanocrystalline Al. The twinning defects are captured during crystal nucleation at the early stages of solidification and twinning growth directions are identified as the solidification proceeds. Due to formation of defects and GBs during the solidification, spontaneous formation of polycrystalline Al is achieved. The solidified polycrystalline Al is deformed by a uniaxial tensile load. The effect of solidification quenching rate, tensile testing temperature, and SR are investigated. Also, the evolution of defects (twinning, detwinning, and voids) are studied under different tensile loading conditions.

2. COMPUTATIONAL METHODOLOGY

2.1 INTERATOMIC POTENTIAL

Second nearest neighbor modified embedded atom method (2NN-MEAM) potential is one of the most advanced and efficient semi-empirical interatomic potentials for predicting both low temperature properties (e.g., elastic properties, stable-unstable stacking fault energy, vacancy formation energy, and surface energy) and high temperature

properties (e.g., thermal expansion coefficient, solid-liquid interface free energy, and melting point) of metals very accurately [34, 43-45]. The 2NN-MEAM was initially developed by Lee and Baskes [43], and recently we evaluated its performance in calculating high temperature and solid-liquid coexistence properties of Al [34, 46], showing good agreement with the experimental data. We used the OVITO to investigate nucleation, solidification and deformation processes [47]. The local crystalline environment of the crystalline atoms were studied by using common neighbor analysis (CNA) in OVITO [48]. The CNA algorithm identifies the closet neighbor and calculate number of neighbor atoms, then group them as fcc, bcc, hcp or other crystal structures [48].

2.2 SIMULATION DETAILS

MD simulations of solidification and uniaxial deformation of solidified pure Al were completed using simulation boxes consisting of ~1 M atoms (25×25×25 nm^3 or 64×64×64 unit cells). We utilized periodic boundary conditions for solidification simulations and free boundary conditions for deformation simulations in all three directions. The time step of simulations was 0.003 ps. Nose-Hoover thermostat governed the temperature and the Parrinello-Rahman barostat to maintain the pressure [49]. We utilized the LAMMPS code [50] (Large-scale Atomic/Molecular Massively Parallel Simulator) for our MD simulations. The melt and a polycrystalline solidified structure are shown in Figure 1. The melt (Figure 1(a)) is equilibrated for 100 ps to create a homogenous liquid. As shown in Figure 1(b), the solidified Al is having GBs and twin boundaries (TBs), which can be easily determined by visual investigation.

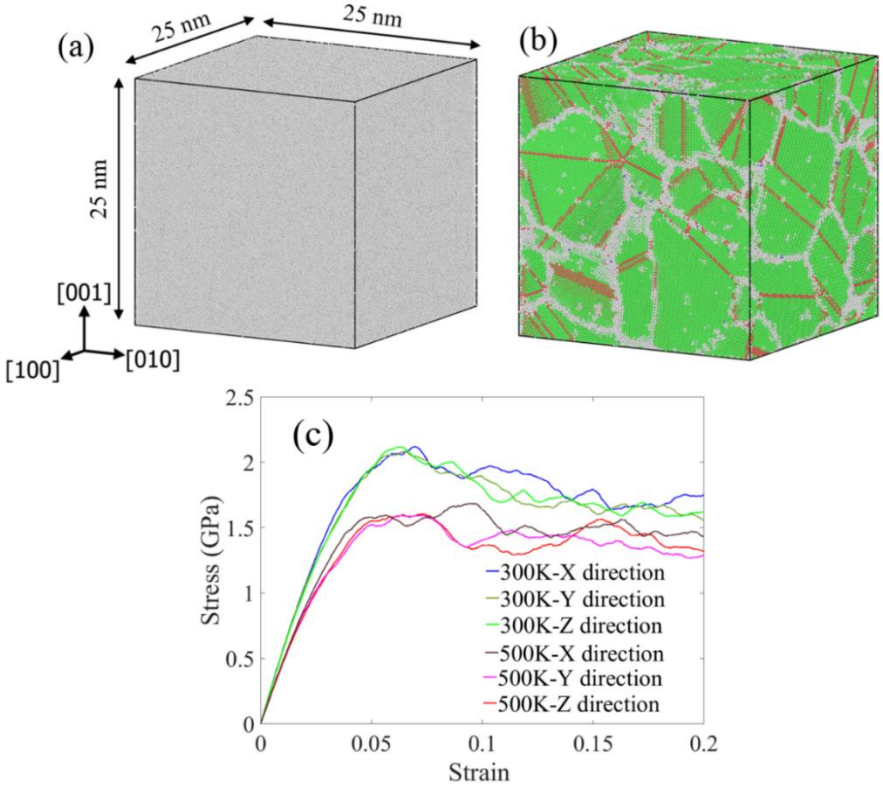

Figure 1. Simulation box at (a) initial melt with temperature of 1,325 K, and (b) after the solidification with the quench rate of $2.5x10^{11}$ Ks^{-1} to 300 K. Green atoms are fcc, and red atoms are hcp, (c) Stress-strain curves for tensile deformation in x, y and z direction at the strain-rate of 10^9 s^{-1}. Temperatures show the tensile testing temperature. Amorphous solid and liquid atoms are presented by grey color.

Solidified polycrystalline samples were prepared by both isothermal condition and quenching. The isothermal samples were prepared by keeping the Al melt at a constant undercooling temperature such as 300, 400 and 500 K for 3ns (3,000 ps). Average grain size increases with increasing the undercooling temperature. The results on the effect of undercooling temperature on the average grain size was provided in our previous work [46], showing that the average grain size increases with increasing the undercooling temperature. In a later part of our article, the grain-size dependent mechanical properties of Al are studied. In the same way, Al melt is quenched from a high temperature such as,

1,325 K to 300 K at constant cooling rates of 10^{11}, 2.5×10^{11} and 5×10^{11} Ks^{-1}. Six polycrystalline samples are created, three for isothermal and three for quenching cases. All the polycrystalline Al models are deformed at three different deformation temperatures (300, 400 and 500 K) and three SRs (10^8, 10^9 and 10^{10} s^{-1}), as shown in Table 2. For the purpose of comparison, we also deform a single crystal Al at the same SRs and temperatures (9 cases). To calculate the statistical error from all the simulations, each uniaxial tensile simulation is replicated in (100), (010) and (001) directions. So, overall 195 simulations (6 solidification cases, and 63 deformation cases each at 3 directions) were performed to analyze the deformation behavior and mechanical properties of solidified polycrystalline Al.

Table 1. The quench rate and isothermal temperature of solidification cases. The SR and temperature of deformation cases (54 deformation cases); a single crystal Al is also deformed at the same SRs and temperatures (9 cases). Each uniaxial tensile deformation simulation is replicated in (100), (010) and (001) directions.

Quench rate of solidification	10^{11} Ks^{-1}, 2.5×10^{11} Ks^{-1}, and 5×10^{11} Ks^{-1}
Isothermal solidification at	300 K, 400 K, and 500 K
SR (s^{-1})	10^8, 10^9, and 10^{10}
Deformation temperature	300 K, 400 K, and 500 K

The polycrystalline samples are prepared by spontaneous solidification. The location, size, and orientation of grains or twins are not controlled in this method. Due to the arbitrary locations of the GBs and TBs, each of the polycrystalline samples are deformed separately in three orthogonal directions to get the statistical scatter. Figure 1(c) shows a sample that is created by isothermal solidification at 400 K, and then deformed at

300 K and 500 K with a SR of 10^9 s^{-1}. For each tensile testing temperature, Figure 1(c) shows slight differences in the elastic region, but more visible differences in the plastic region based on different directions. The difference in stress-strain curves indicates that the evolution of the pre-existing GBs and TBs are different and dependent on the applied load direction. Therefore, the statistical error from direction-dependence is considered in analyzing the mechanical properties of polycrystalline Al.

3. RESULTS AND DISCUSSIONS

3.1 FORMATION OF COHERENT AND FIVE-FOLD TWINS

The magnified crystalline nucleus in Figure 2(a-b) displays atoms with different crystal structures, calculated by CNA [48]. In Figure 2 (a-b), the distance between two nearest-neighbor atoms in Al matrix is ~ 2.86 Å, and this is consistent with the lattice constant of 4.05 Å for Al. There is a small amount of thermal fluctuation of energy during the solidification of Al melt. The fcc to hcp energy difference is only 0.03 eV whereas the fcc to bcc energy difference is 0.12 eV [34]. During solidification while thermal fluctuations happen, hcp stacking faults form in the Al system, and no bcc phase forms. Depending on the cooling rate, different types of twins form within the critical nuclei. In the quenching process when the crystallization occurs by homogenous nucleation, two types of twinning are observed. Fivefold twins form for the relatively higher quench rate of $2.5x10^{11}$ Ks^{-1} (Figure 2a), and coherent twin boundaries (CTBs) form for the quench rare of 10^{11} Ks^{-1} (Figure 2b). The isothermally solidified Al also shows fivefold twins for all the examined solidification temperatures. It takes about 60 ps from the formation of

initial staking faults to formation of fivefold twins. Unlike the multifold twins by deformation, the solidification twins are not assisted by sequential emission of Shockley partial dislocations. CTBs and multifold twins both form spontaneously in the fcc crystal nuclei during solidification. The twins grow further in the same direction of growth of the fcc crystalline solid.

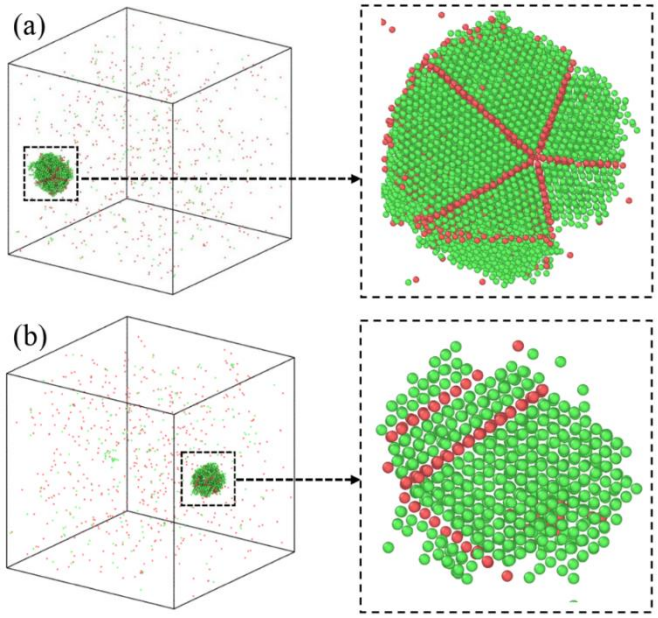

Figure 2. Formation of (a) five-fold twins and (b) CTBs during solidification at the nuclei; the cooling rate is 2.5×10^{11} Ks^{-1} and 10^{11} Ks^{-1}. Green atoms indicate fcc, and red atoms are hcp. Amorphous solid liquid atoms are removed to only show the nuclei.

The instability in the solidification process caused by thermal fluctuations at solid-liquid interfaces is the only reason that creates the twins. In general, Al has a relatively high SFE which makes it difficult for twins to form in pure Al. But, this high theoretical SFE happens at 0 K. It is a well-known that SFE gradually decreases as the temperature

increases [51, 52]. Recent studies by Bhogra et al. [53] showed that the SFE of Al reduces drastically by increasing the temperature. At higher temperatures, the SFE of Al is almost equivalent to that of Nickel (Ni) [54], and formation of fivefold twins was observed during electrodeposition of Ni thin films [55]. During solidification, crystal nucleation occurs at very high temperatures where SFE is significantly lower that its value at 0 K, thus formation of twins is probable.

In general the multifold twinning happens in different scenarios such as layer-by-layer growth during nucleation, successive growth twinning, or deformation twinning [55]. Twining during growth is observed in semiconductor growth process, but it is extremely difficult to experimentally observe the same for metals due to the much higher temperatures during solidification. The formation steps and direction of five-fold twins and the CTBs are presented in Fig 4(a-f). To study the formation of five-fold structure in the nucleus, we present only a sliced portion of the simulation box between 15-100 ps in Figure 3. In the initial stages of nucleation, a solid cluster consisting of nearly 50 fcc and hcp atoms was formed at ~15 ps inside the undercooled Al met, which can be regarded as the seed for both the nucleus and the twin. Then the initial TB1 seed (hcp atoms) elongates and forms a complete TB1 while the nucleus becomes critical simultaneously. Between 30 and 45 ps, as the nucleus grows in size and TB2 began to form. Subsequently at ~45 ps, a lamellar twined structure with two hcp planes apart by 73° formed at the bottom right of the particle. The initial stage of formation of TB3 is noticeable by the extension of upper hcp plane to connect at the junction of TB1 and TB2, forming a three-fold twin. The TB4 and TB5 subsequently appears after ~60 ps, whereas TB1, TB2 and TB3 were still growing. At the three-point twin junction, the hcp atoms start forming two other TBs, namely TB4 and

TB5. As the solidification proceeds, these twins are arranged into a closed five-membered circle at the twinning axis. Finally, the entire five-fold twins were formed at ~75 ps, when the TB4 and TB5 are fully stretched out.

The five-fold twins should be producing 360° while distributed in a circle, but the average twin angle remains in a range of 70 to 73°. The twins also has a thickness, which leave a gap while closing 360° (Figure 3(f)), and that later result in elastic strain during deformation. The result shows consistency with the literature values of other fcc metals [55-57]. Fivefold twin structure formations by successive twinning growth on alternate cozonal twin planes also has been previously observed in the solid phase crystallization of metal [52].

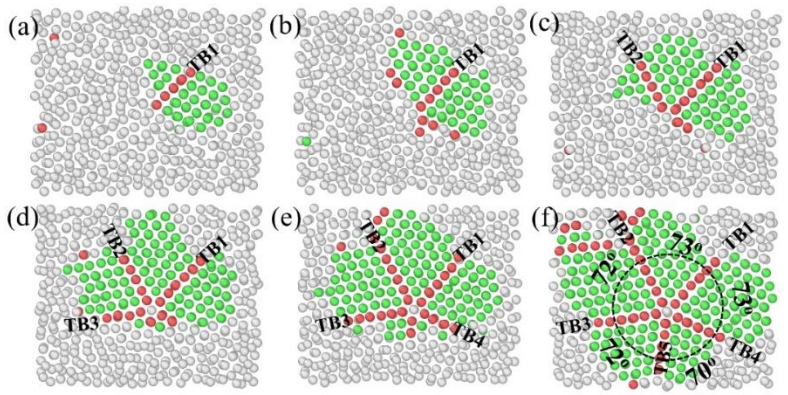

Figure 3. The sequence of formation of (a-f) five-fold twins at the nuclei at 500 K isothermal temperature. The steps of twin formation is shown for (a) 15 ps, (b) 30 ps, (c) 45 ps, (d) 60 ps, (e) 75 ps and (f) 100 ps. The angle between the twins are measured which remains between 70° and 73°.

During the nucleation and growth of the noncrystallographic packing of atoms to a crystalline fcc Al, small size ordered subunits of hcp atoms form as a twin to compensate the angular misfit between different fcc growth planes.

Along with the fivefold twins, several CTBs are also identified during both isothermal and quenching solidification (see Figure 4 for example). Some initial CTBs occur within the fcc nuclei during solidification, Figure 4(b). In the annealing stage, more twins form on the GBs, see Figure 4(a) and Figure 4(b) for example. Some TBs connect with each other at the GBs, see Figure 4(c) and Figure 4(d) for example. As the grain size increases with annealing, the smaller grains combine with the larger ones and some GBs vanish, and during this process some hcp TBs form within the fcc Al grains.

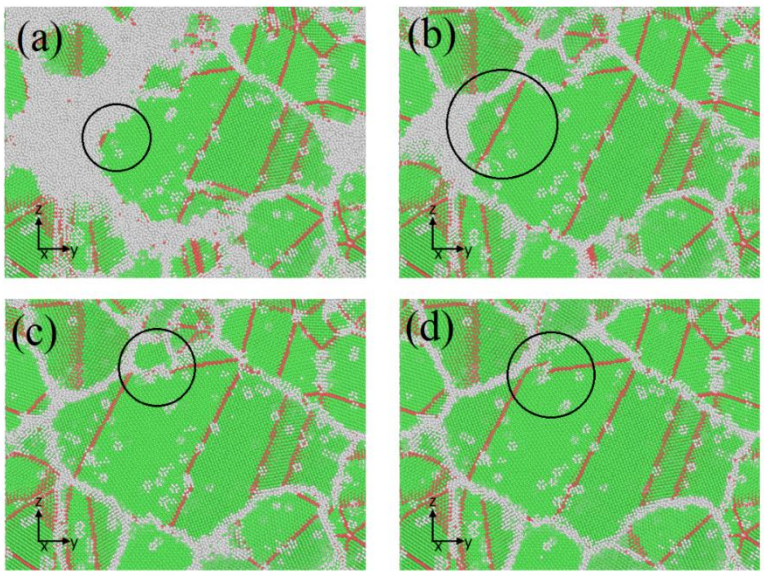

Figure 4. The formation steps of coherent TBs at (a) 15 ps, (b) 50 ps, (c) 100 ps, (d) 250 ps at 400 K. The circles show the hcp TB formation and merger at a GB.

3.2 TWINNING AND DETWINNING DURING TENSILE LOADING

Several phenomena simultaneously happen during the tensile loading of polycrystalline Al. New deformation twins form and some of the preexisting solidification twins detwin. Then some of the deformation twins also detwin while the simulation box is stretched in a uniaxial direction. Along with the formation of usual CTBs, we also observed formation of several fivefold twins during the deformation. Snapshots of formation of a fivefold twin during deformation at 300 K and SR of 10^8 s^{-1} are revealed in Figure 5; the initial nanostructures for this deformation simulation was for the solidification case with the quench rate of 2.5×10^{11} Ks^{-1}. The angles between the TBs of the fivefold twin remain between 70 and 73^0, which is similar to those of the fivefold twins in solidification cases. No fivefold twins were detected in planes perpendicular to the loading direction. Formation of Fivefold twins has been observed for several nanocrystalline materials during experimental deformation [58-60]. The arrow in Figure 5(a) shows one of the preexisting solidification TB (TB1). This pretexting twin can be referred to as a microtwin, as it grows in length when the uniaxial tension applied. Below the TB1 several other twins are present but during the deformation some of them detwin by the GB movement; however, in this case one of them forms the TB2 (shown in Figure 5(b)). The emission of partial dislocations from GBs in different grains results in formation of other twins of the fivefold twin. By simply applying uniaxial tension in a perfect single crystal Al, multifold twins cannot be created, however by introducing pretwins in grain regions, multifold/fivefold deformation twins can form in grains of a nanocrystalline system which undergoes a uniaxial tension [61].

In Figure 5 formation of several coherent and incoherent TBs can be seem as well. A pair of CTBs are shown in Figure 5 with a dotted circle. The thickness (distance between two twin planes) of the TB reduces from ~2.23 nm at 0.15 strain to 1.35 nm at 0.25 strain. As shown in the dotted circle some gray atoms at the front end of the TB. These atoms can be referred to as partial dislocations [62, 63]. As shown in Figure 5(c) and Figure 5(d), a partial dislocation glides in the opposite direction of TB growth. Consequently, detwinning happens with a combination of both reduction in twin thickness and the layer-by-layer TB removal by the opposite glide of partial dislocations having a Burgers vector identical to that of the twinning partial dislocations.

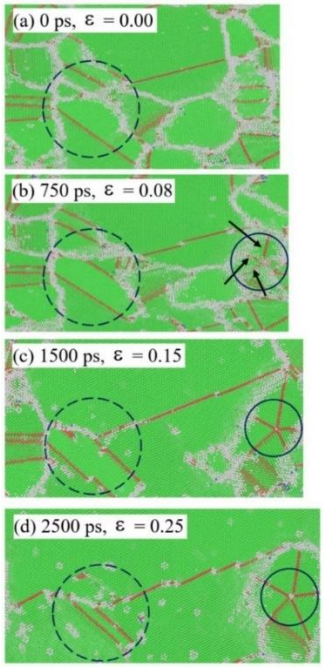

Figure 5. Fivefold twin formation during tensile deformation (in x direction) of polycrystalline Al created from a quench rate of 2.5×10^{11} Ks^{-1} at SR of 10^{8} s^{-1}. The normal black circle shows the fivefold twin formation and the dotted circle shows the formation of CTB.

The solidification TBs detwin by GB movements and dissolution into to the fcc matrix, Figure 6(a)-(d). Once TBs are present from the solidification process, the subsequent tensile deformation favors detwinning of the TBs over activating dislocation slip. Since the TBs are already present from the solidification defects, it is not required to generate new partial dislocations, and the trailing partial dislocations can dismantle the stacking fault on the TBs. In this particular case, which was solidified at 400 K and then deformed at 300K with SR of 10^9 Ks^{-1} (Figure 6), the initial GB transformed to one CTB, then as the simulation box stretched up to total strain of strain ~0.45 (Figure 6(d)), the TB dissolved back into the primary fcc Al matrix.

The deformation temperature influences the detwinning process. When the TBs dissolve into the fcc Al matrix, the detwinning process mostly happens due to the stretching of the TBs in the direction of applied uniaxial tension, and SR controls this process. But when the detwinning happens due to GB movement, the detwinning process is mostly influenced by the deformation temperature; as the temperature of deformation increases from 300 K to 500 K, the detwinning happens more frequently. Multiple twins at the GB are absorbed by both the GB and the fcc Al matrix. This detwinning phenomena is observed for all the different samples prepared by isothermal annealing or quenching. The detwinning process during deformation identified by MD simulations is similar to the results obtained from previous experimental works on various fcc metals such as Al , Cu , Ni [64], etc. So MD simulations of polycrystalline metals can replicate the detwinning observed in experiments such as thinning of the twins and shortening, and GB movement during deformation [38].

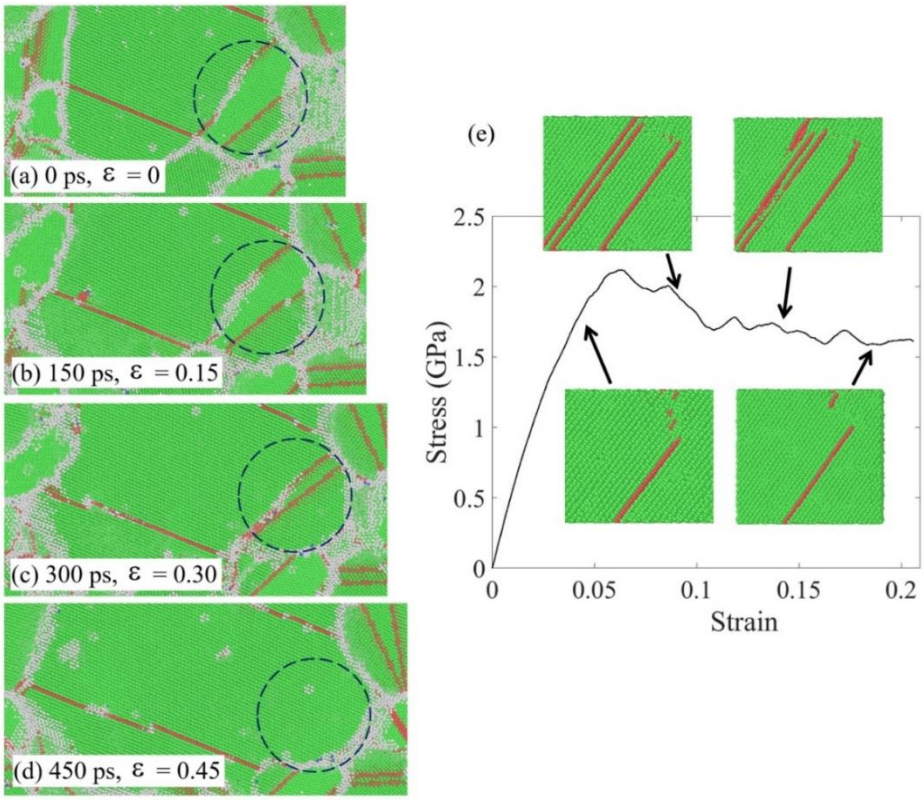

Figure 6. A solidification twin detwin as tensile deformation in x direction proceeds. (a) The initial condition (t=0) is the nanostructure of an isothermally solidified sample at 400 K, and (b-d) the SR of 10^9 Ks^{-1} is applied at 300 K. (e) A typical Stress-strain plot of polycrystalline Al produced by 400 K isothermal annealing, deformed at SR of 10^9 s^{-1} and 300 K. The inset images show twinning-detwinning during plastic deformation. The microstructures are removed for clarity.

Typical detwinning of deformation twins is observed while the sample is plastically deformed, which is similar to the observations in experimental work [38]. The stages of detwinning of deformation twins is similar to those of the solidification TBs. It should be noted that during the deformation only smaller sized TBs detwin. The small sized twins at high SRs do not entangle with other defects (such as dislocations and GBs) in the Al matrix. The length of TBs do not increase significantly during deformation due to the high SFE of Al [65] at low temperatures.

Some of the fivefold twins also detwin as the tensile deformation continues. The driving force behind the detwinning comes from the excess energy variation of the system during the tensile deformation. But for the detwinning of fivefold twins, grain sizes also play a significant role. In Figure 7(a), the double fivefold twins are developed inside a much larger grain during isothermal solidification of Al melt at 500 K. While tensile strain is applied in [100] direction, the grain is stretched. During the grain elongation, the GBs shrink the size of the fivefold twins. For nanocrystalline metals with average grain sizes between 10 and 100 nm, it is recognized that the competition between dislocation- and GB-mediated deformation mechanisms govern the deformation mechanism. Previous works by MD simulations suggested that GBs in nanocrystalline metals act as both source and sink for crystal defects such as dislocation, vacancy, and twins [66, 67]. The snapshots in Figure 7 show how GBs absorb the twins as the polycrystalline Al becomes plastic (See the stress-strain plot of a typical polycrystalline sample in Figure 6(e)).

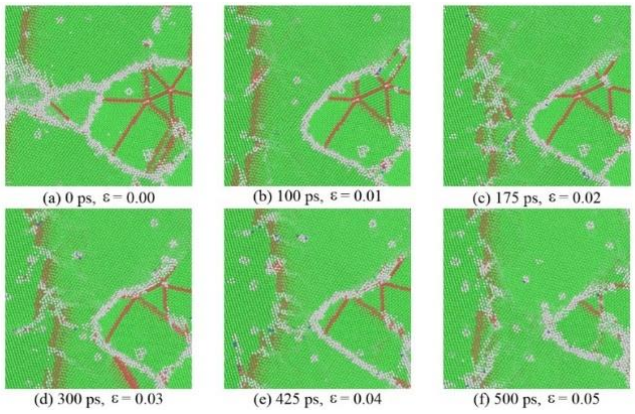

Figure 7. At 500 K with a SR of 10^9 s^{-1} in the single crystal Al a twin formed and then detwinned in the direction. The sample is quenched at 10^{11} Ks^{-1}.

3.3 VOID FORMATION

The void formation process and the associated strain levels during the tensile deformation are shown in Figure 8. The solid circle in Fig 8 shows the formation of a void at a GB with increasing strain. The increase of void volume in a stretched area starts during the plastic flow of polycrystalline Al. The void under tensile load generally happens due to local shear stress by the GB movement. Comparing Figure 8(a) and (b), we see several full and partial dislocation emission at a strain of 0.16. The emission of dislocation loops from the GBs leads to void nucleation. Upon increased loading and strain, voids grow while other dislocations are consumed by increasing void and GB volumes. In general, ductile metals normally fail in monotonic loading through nucleation, growth and coalescence of voids. The evidence of ductile fracture behavior via void formation/growth at GBs has also been observed on facture surfaces by scanning electron microcopy in monocrystalline Al under uniaxial tension [68, 69].

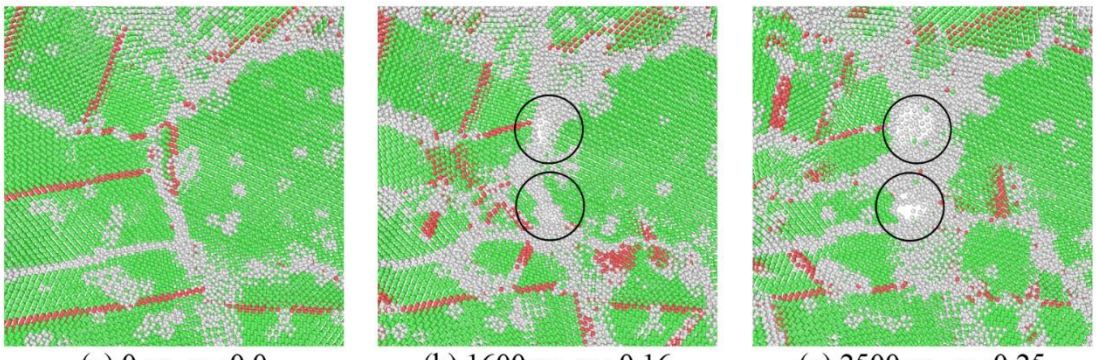

Figure 8. Atomistic illustration of the onset of void under the tensile stress. The solid black circle shows formation of void at the grain boundary. The sample is solidified at 500 K, and the deformation is done at 10^9 s^{-1} at 300 K.

3.4 MECHANICAL PROPERTIES OF SOLIDIFIED POLYCRYSTALS

In this sub-section, we investigate the mechanical behavior of the polycrystalline Al created by solidification at different isothermal temperatures and quench rates. Utilizing uniaxial tension of polycrystalline Al samples having different solidified structures, the stress-strain plots are obtained. From these curves, the mechanical properties such as yield strength, Young's modulus, and ultimate tensile strength (UTS) are derived. The yield strength is found from the linear regression of the stress data with 0.2% offset on strain. The intersecting point of the linear fit from the regression and the actual stress-strain curve is the yield strength. No permanent deformation happens in the elastic (linear) part of the curve. The highest point in the stress-strain curve is the UTS. The inverse Hall-Petch relationship is discussed in this context of increasing yield strength with increasing grain size for solidification at higher solidification temperatures or slower quench rates (Figure 10).

Young's modulus of the solidified polycrystalline samples is compared with that of the single crystall Al in Figure 9(a)-(d). The expected decline of Young's modulus is observed with increasing the deformation temperature when the SR is kept constant (between 10^8 to 10^{10} s^{-1}). A higher SR and/or a lower deformation temperature produced a stronger sample in all the cases; for example, compare cases in Figure 9(a) with SR of 10^{10} s^{-1} to those in Figure 9(a) with SR of 10^8 s^{-1}. In tension at 300 K and the SR of 10^{10} s^{-1}, the single crystal has a Young's modulus of ~60-65 GPa which is comparable to the previous experimental and computational results [70-72]. Under the same tensile loading conditions, the polycrystalline samples prepared by isothermal solidification at 500 K could reach a maximum Young's modulus of 58 GPa (Figure 9 (a)). Overall the Young's modulus

remains between 46-65 GPa; these values are similar to those achieved by experiments performed on nanocrystalline Al by Haque et al. [73]. Table 2 shows a comparison of the Young's modulus determined by our MDs simulations to those for single crystal and nanocrystalline experiments. The margin of error is less than 5% for Young's modulus of a single crystal Al determined by indentation test [70, 74].

Table 2. Young's modulus values at 300K for single crystal and nanocrystalline Al determined by MD calculations or experiments. The average grain size of polycrystalline cases is given in the parenthesis.

Al Bulk	Young's Modulus (GPa)	
	Current MD work	Previous Results (Methods)
Single Crystal	58-64	67.2-69.5 (Expt.) [70], 64 (MD) [72], 62.3 ± 3.1 (Expt.) [74]
Nanocrystalline	40-65 (Average grain size: 5-11nm)	67 (MD, Grain size 11.1nm) [72], 60.2 (Expt., Average grain size: 11.1nm) [73]

The UTS for single and polycrystals are shown in Figure 9(e) and (f). The UTS for single crystal is much higher than the polycrystalline Al. The UTS of single crystal remains between 5.5 GPa and 7.5 GPa (Figure 9(e-f)), and when the deformation temperature increases by 200 K a decrease of strength by almost 24% is observed. However, this change in UTS in polycrystalline samples solidified isothermally or by quenching is only less than 10%; for example in Figure 9(e) for the isothermal solidification at 500 K, the strength goes down from 3.5 GPa to 3.25 GPa from deformation temperature of 300K to 500 K. A

detailed discussion of mechanical properties of nanocrystalline metals by Meyers et al. [31] shows the extremely high strength of 3.5-4 GPa for nanocrystalline Al with an average grain size between 5 nm and 10 nm. The high strength results from our MD simulations are comparable to the reported experimental data for nanocrystalline Al.

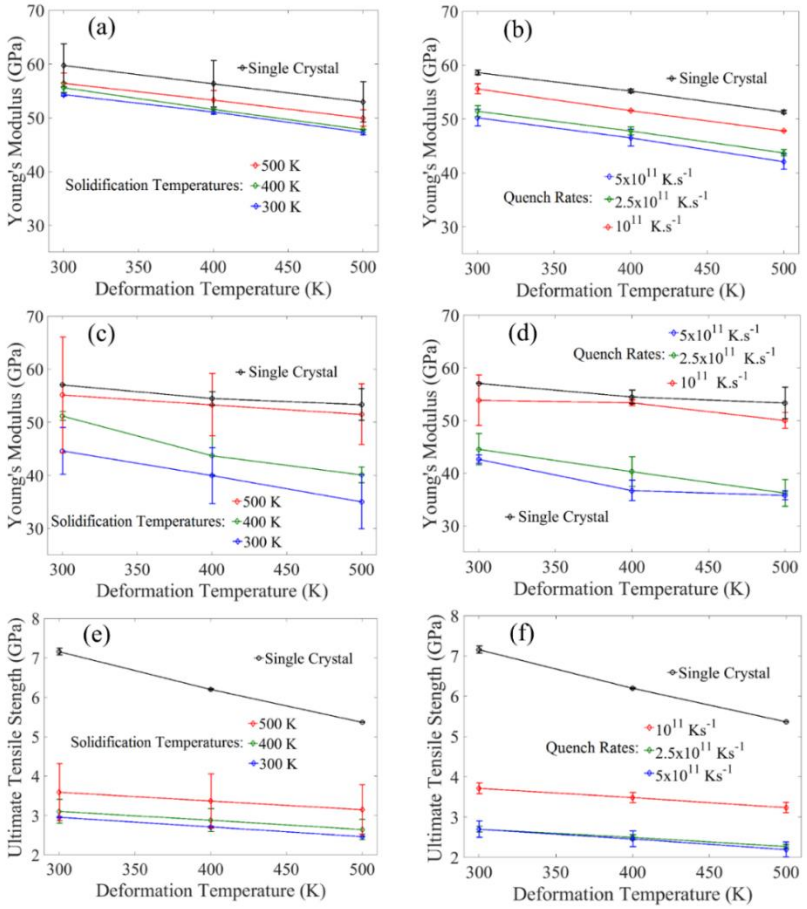

Figure 9. Mechanical properties of single and polycrystalline Al are plotted. (a) Young's modulus of isothermally solidified polycrystalline samples in tension at the SR of $10^{10}\,s^{-1}$, (b) Young's modulus of solidified polycrystalline samples prepared by quenching in tension at the SR of $10^{10}\,s^{-1}$. (c) Young's modulus of isothermally solidified polycrystalline samples in tension at the SR of $10^{8}\,s^{-1}$, (d) Young's modulus of solidified polycrystalline samples prepared by quenching in tension at the SR of $10^{8}\,s^{-1}$, (e) Ultimate tensile strength of isothermally solidified polycrystalline samples in tension at the SR of $10^{10}\,s^{-1}$, (f) Ultimate tensile strength of solidified polycrystalline samples prepared by quenching in tension at the SR of $10^{10}\,s^{-1}$.

The yield strength of single and polycrystals can be studied by direct relationship between the grain size of a metal and its yield strength, which is known as the Hall-Petch (HP) relation. When the grain size is above its critical value, the strength increases as the grain size decreases. At the critical grain size, the material has its maximum strength [20, 75]. Below the critical grain size, an inverse HP relationship is expected: the smaller the grain size the weaker the metal [20, 76]. This is because an alternative deformation mechanisms take over [31].

In general, the yield strength (σ_y) increases by creasing the average grain size based on the HP equation [77, 78]:

$$\sigma_y = \sigma_0 + kd^{-1/2}, \quad (1)$$

where σ_0 is a materials constant which can be calculated in the absence of GBs, k is strengthening coefficient and d refers to the grain size. The dislocation density becomes a more dominating factor than the total number of dislocations, so when the grain size is decreased the dislocation density increases. Due to that the dislocation pile up increases with finer grain size and the yield strength increases. However, for very small grain sizes, this mechanism will fail because grains are not able to support dislocation pile-ups. Usually for Al, this is anticipated to happen for average grain sizes below 25 nm *[71]*. Additionally, the shift in the HP slope usually happens for grain sizes larger than 10 nm. The inverse HP relationship is shown in Figure 10; as the grain size increases (with increasing isothermal solidification temperature from 300K to 500K) the tensile yield strength increases for all the polycrystalline samples. The similar behavior is observed for the samples prepared by quenching; in higher quench rates resulting in smaller grain sizes, the yield strength is lower. The average grain sizes are also shown in the inset table of Figure 10.

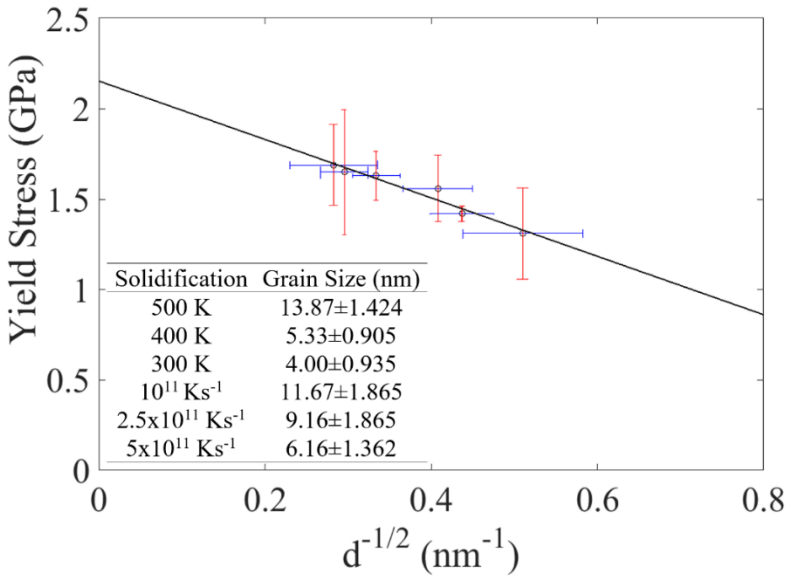

Figure 10. Inverse HP relationship is shown for different grain size (nm) and yield stress (GPa); data for the uniaxial tensile deformation at 300 K and the SR of 10^{10} s^{-1} are used to plot this figure. The average grain sizes for 3 isothermal and 3 quenching solidification cases are shown in the inset table.

4. CONCLUSION

We performed MD simulations utilizing 2NN MEAM interatomic potential to study defect evolution process and deformation mechanisms of solidified polycrystalline Al under uniaxial tension. The polycrystalline Al samples were created by solidification at different quench rates and at different isothermal solidification temperatures. Several SRs and deformation temperatures were investigated. Since the GBs, vacancies, and TBs form spontaneously in arbitrary directions, the solidified polycrystalline Al was deformed in three different (100), (010) and (001) directions to account for potential statistical errors.

For all different simulations at various isothermal temperatures and cooling rates several defects such as twinning, dislocations, voids have been observed. The instability in

the solidification process caused by thermal fluctuations at solid-liquid interfaces is the primary reason for twin formation. The primary Al is identified as fcc whereas the twins are hcp crystal structures. The evolution of solidification defects such as CTBs and fivefold twins were analyzed. In case of the fivefold twins, the average twin angle was ~70-73° to form almost 360°. Ideally it should be fully circular, but during the spontenous solidfication the nuclei are not pefectly spherical and also TBs have have a few Angstrom thickness themsleves, leaving a few degrees gap in the five-fold twins. Overall, our simulations confirm the formation of CTB and multifold twins during solidification, which is extremely difficult to observe in experiments as the entire process of layer by layer twin formation happens in the interior part of the liquid metal. During the tensile deformation, detwinning occurred for both solidification and deformation twins. The detwinning during plastic straining is more evident at higher deformation temperatures. Nucleation of voids at GBs were also observed due to the emission of dislocation loops from the GBs.

The effect of tensile testing temperature and SR was taken into account in analyzing the mechanical properties of solidified samples. The Young's modulus, yield strength, and ultimate tensile strength reduced by increasing the deformation temperature. However, the effect of SR is opposite, and the Young's modulus and ultimate tensile strength increased by increasing the SR of deformation. The uniaxial tensile strength of single crystal Al was determined to be almost twice as that of the polycrystalline Al, but single crystal Al is brittle in nature whereas the polycrystalline Al can be plastically deformed considerably. Lower quench rates and higher isothermal solidification temperatures created larger grains during solidification, and samples with larger grains showed higher yield strength and Young's modulus, and this is an indication of an Inverse Hall-Petch relationship. In the

literature, there are several studies predicted the inverse Hall Petch for metals with average grain sizes less than 10 nm which is consistence with our predications.

Overall the polycrystalline model prepared by spontaneous solidification can reproduce the similar mechanical behavior of Al (i.e., dependency on temperature, SR effects, etc.) expected from experimental or other simulation studies. This also indicates that with larger computational resources the studies of polycrystalline Al and its alloys can be extended to microstructural level comparable to experimentally available data.

REFERENCES

[1] G. E. Dieter and D. J. Bacon, *Mechanical metallurgy* vol. 3: McGraw-Hill New York, 1986.

[2] M. Meyers, O. Vöhringer, and V. Lubarda, "The onset of twinning in metals: a constitutive description," *Acta materialia,* vol. 49, pp. 4025-4039, 2001.

[3] T. Mukhopadhyay, A. Mahata, S. Dey, and S. Adhikari, "Probabilistic Analysis and Design of HCP Nanowires: An Efficient Surrogate Based Molecular Dynamics Simulation Approach," *Journal of Materials Science & Technology,* vol. 32, pp. 1345-1351, 2016/12/01/ 2016.

[4] M. Chen, E. Ma, K. J. Hemker, H. Sheng, Y. Wang, and X. Cheng, "Deformation twinning in nanocrystalline aluminum," *Science,* vol. 300, pp. 1275-1277, 2003.

[5] B. Li, B. Y. Cao, K. T. Ramesh, and E. Ma, "A nucleation mechanism of deformation twins in pure aluminum," *Acta Materialia,* vol. 57, pp. 4500-4507, 9// 2009.

[6] Y. T. Zhu, X. Z. Liao, S. G. Srinivasan, Y. H. Zhao, M. I. Baskes, F. Zhou, *et al.*, "Nucleation and growth of deformation twins in nanocrystalline aluminum," *Applied Physics Letters,* vol. 85, pp. 5049-5051, 2004.

[7] F. Zhao, L. Wang, D. Fan, B. X. Bie, X. M. Zhou, T. Suo, *et al.*, "Macrodeformation Twins in Single-Crystal Aluminum," *Physical Review Letters,* vol. 116, p. 075501, 02/17/ 2016.

[8] M. Avik, M. Tanmoy, and A. Sondipon, "A polynomial chaos expansion based molecular dynamics study for probabilistic strength analysis of nano-twinned copper," *Materials Research Express,* vol. 3, p. 036501, 2016.

[9] K. Dragnevski, R. Cochrane, and A. Mullis, "The solidification of undercooled melts via twinned dendritic growth," *Metallurgical and Materials Transactions A,* vol. 35, pp. 3211-3220, 2004.

[10] M. A. Salgado-Ordorica and M. Rappaz, "Twinned dendrite growth in binary aluminum alloys," *Acta Materialia,* vol. 56, pp. 5708-5718, 11// 2008.

[11] S. Henry, M. Rappaz, and P. Jarry, "〈110〉 dendrite growth in aluminum feathery grains," *Metallurgical and Materials Transactions A,* vol. 29, pp. 2807-2817, 1998.

[12] J. Li, F. Seki, S. Saimoto, K. Itoh, and T. Kamijo, "Annealing twins in nominally pure Al," *Scripta Materialia,* vol. 36, pp. 1261-1266, 1997/06/01 1997.

[13] D. Field, L. Bradford, M. Nowell, and T. Lillo, "The role of annealing twins during recrystallization of Cu," *Acta materialia,* vol. 55, pp. 4233-4241, 2007.

[14] Q. Li, J. Cahoon, and N. Richards, "On the calculation of annealing twin density," *Scripta materialia,* vol. 55, pp. 1155-1158, 2006.

[15] T. Duffar, "Recent Research Developments in Crystal Growth," vol. 5, pp. 61-113, 2010.

[16] N. Iqbal, N. H. van Dijk, S. E. Offerman, M. P. Moret, L. Katgerman, and G. J. Kearley, "Real-time observation of grain nucleation and growth during solidification of aluminium alloys," *Acta Materialia,* vol. 53, pp. 2875-2880, 6// 2005.

[17] B. Li, H. D. Brody, D. R. Black, H. E. Burdette, and C. Rau, "Real time observation of dendritic solidification in alloys by synchrotron microradiography," *Journal of Physics D: Applied Physics,* vol. 39, p. 4450, 2006.

[18] G. Zeng, K. Nogita, S. Belyakov, J. Xian, S. McDonald, K. Yang, *et al.*, "Real-Time Observation of AZ91 Solidification by Synchrotron Radiography," in *Magnesium Technology 2017*, ed: Springer, 2017, pp. 597-603.

[19] A. Tandjaoui, N. Mangelinck-Noel, G. Reinhart, B. Billia, and X. Guichard, "Twinning occurrence and grain competition in multi-crystalline silicon during solidification," *Comptes Rendus Physique,* vol. 14, pp. 141-148, 2013/02/01 2013.

[20] D. Wolf, V. Yamakov, S. Phillpot, A. Mukherjee, and H. Gleiter, "Deformation of nanocrystalline materials by molecular-dynamics simulation: relationship to experiments?," *Acta Materialia,* vol. 53, pp. 1-40, 2005.

[21] Y. Xu, B. Yan, H.-J. Zhang, J. Wang, G. Xu, P. Tang, *et al.*, "Large-gap quantum spin Hall insulators in tin films," *Physical review letters,* vol. 111, p. 136804, 2013.

[22] D. Gianola, S. Van Petegem, M. Legros, S. Brandstetter, H. Van Swygenhoven, and K. Hemker, "Stress-assisted discontinuous grain growth and its effect on the deformation behavior of nanocrystalline aluminum thin films," *Acta Materialia,* vol. 54, pp. 2253-2263, 2006.

[23] D. E. Spearot, K. I. Jacob, and D. L. McDowell, "Nucleation of dislocations from [001] bicrystal interfaces in aluminum," *Acta Materialia,* vol. 53, pp. 3579-3589, 2005.

[24] K. Aust, F. Krill, and F. R. Morral, "Observations on twinning in semicontinuous cast aluminum," *Journal of Metals,* vol. 4, pp. 865-866, 1952.

[25] H. Fredriksson and M. Hillert, "On the mechanism of feathery crystallisation of aluminium," *Journal of Materials Science,* vol. 6, pp. 1350-1354, 1971.

[26] W. Han, G. Cheng, S. Li, S. Wu, and Z. Zhang, "Deformation induced microtwins and stacking faults in aluminum single crystal," *Physical review letters,* vol. 101, p. 115505, 2008.

[27] Y. F. Shao and S. Q. Wang, "Quasicontinuum study on formation of fivefold deformation twin in nanocrystalline aluminum," *Scripta Materialia,* vol. 62, pp. 419-422, 3// 2010.

[28] E. Bringa, D. Farkas, A. Caro, Y. Wang, J. McNaney, and R. Smith, "Fivefold twin formation during annealing of nanocrystalline Cu," *Scripta Materialia,* vol. 59, pp. 1267-1270, 2008.

[29] P. Huang, G. Dai, F. Wang, K. Xu, and Y. Li, "Fivefold annealing twin in nanocrystalline Cu," *Applied Physics Letters,* vol. 95, p. 203101, 2009.

[30] T. Shen, Y. Wu, and X. Lu, "Structural evolution of five-fold twins during the solidification of Fe 5601 nanoparticle: a molecular dynamics simulation," *Journal of molecular modeling,* vol. 19, pp. 751-755, 2013.

[31] M. A. Meyers, A. Mishra, and D. J. Benson, "Mechanical properties of nanocrystalline materials," *Progress in materials science,* vol. 51, pp. 427-556, 2006.

[32] F. Zhao, L. Wang, D. Fan, B. Bie, X. Zhou, T. Suo, *et al.*, "Macrodeformation twins in single-crystal aluminum," *Physical review letters,* vol. 116, p. 075501, 2016.

[33] F.-f. Zhu, W.-j. Chen, Y. Xu, C.-l. Gao, D.-d. Guan, C.-h. Liu, *et al.*, "Epitaxial growth of two-dimensional stanene," *Nature materials,* vol. 14, pp. 1020-1025, 2015.

[34] E. Asadi, M. Asle Zaeem, S. Nouranian, and M. I. Baskes, "Two-phase solid–liquid coexistence of Ni, Cu, and Al by molecular dynamics simulations using the modified embedded-atom method," *Acta Materialia,* vol. 86, pp. 169-181, 2015.

[35] V. Yamakov, D. Wolf, S. Phillpot, and H. Gleiter, "Deformation twinning in nanocrystalline Al by molecular-dynamics simulation," *Acta Materialia,* vol. 50, pp. 5005-5020, 2002.

[36] J. Schiotz, F. D. Di Tolla, and K. W. Jacobsen, "Softening of nanocrystalline metals at very small grain sizes," *Nature,* vol. 391, p. 561, 1998.

[37] S. Kibey, J. Liu, D. Johnson, and H. Sehitoglu, "Predicting twinning stress in fcc metals: Linking twin-energy pathways to twin nucleation," *Acta materialia,* vol. 55, pp. 6843-6851, 2007.

[38] B. Li, M. Sui, B. Li, E. Ma, and S. Mao, "Reversible twinning in pure aluminum," *Physical review letters,* vol. 102, p. 205504, 2009.

[39] R.-Z. Qiu, C.-C. Li, and T.-H. Fang, "Mechanical properties and crack growth behavior of polycrystalline copper using molecular dynamics simulation," *Physica Scripta,* vol. 92, p. 085702, 2017.

[40] F. Zhang, Z. Liu, and J. Zhou, "Molecular dynamics simulation of micro-mechanical deformations in polycrystalline copper with bimodal structures," *Materials Letters,* vol. 183, pp. 261-264, 2016.

[41] A. AlMotasem, J. Bergström, A. Gåård, P. Krakhmalev, and L. Holleboom, "Atomistic Insights on the Wear/Friction Behavior of Nanocrystalline Ferrite During Nanoscratching as Revealed by Molecular Dynamics," *Tribology letters,* vol. 65, p. 101, 2017.

[42] H. Van Swygenhoven, A. Caro, and D. Farkas, "A molecular dynamics study of polycrystalline fcc metals at the nanoscale: grain boundary structure and its influence on plastic deformation," *Materials Science and Engineering: A,* vol. 309-310, pp. 440-444, 2001/07/15/ 2001.

[43] B.-J. Lee and M. Baskes, "Second nearest-neighbor modified embedded-atom-method potential," *Physical Review B,* vol. 62, p. 8564, 2000.

[44] E. Asadi, M. Asle Zaeem, S. Nouranian, and M. I. Baskes, "Quantitative modeling of the equilibration of two-phase solid-liquid Fe by atomistic simulations on diffusive time scales," *Physical Review B,* vol. 91, p. 024105, 2015.

[45] E. Asadi and M. Asle Zaeem, "The anisotropy of hexagonal close-packed and liquid interface free energy using molecular dynamics simulations based on modified embedded-atom method," *Acta Materialia,* vol. 107, pp. 337-344, 2016/04/01/ 2016.

[46] A. Mahata, M. Asle Zaeem, and M. I. Baskes, "Understanding homogeneous nucleation in solidification of aluminum by molecular dynamics simulations," *Modelling and Simulation in Materials Science and Engineering,* vol. 26, p. 025007, 2018.

[47] A. Stukowski, "Visualization and analysis of atomistic simulation data with OVITO–the Open Visualization Tool," *Modelling and Simulation in Materials Science and Engineering,* vol. 18, p. 015012, 2009.

[48] H. Tsuzuki, P. S. Branicio, and J. P. Rino, "Structural characterization of deformed crystals by analysis of common atomic neighborhood," *Computer physics communications,* vol. 177, pp. 518-523, 2007.

[49] M. Parrinello and A. Rahman, "Polymorphic transitions in single crystals: A new molecular dynamics method," *Journal of Applied physics,* vol. 52, pp. 7182-7190, 1981.

[50] S. Plimpton, "Fast parallel algorithms for short-range molecular dynamics," *Journal of computational physics,* vol. 117, pp. 1-19, 1995.

[51] M. Ball and D. Lloyd, "Particles apparently exhibiting five-fold symmetry in Al□ Li□ Cu□ Mg alloys," *Scripta metallurgica,* vol. 19, pp. 1065-1068, 1985.

[52] J. Narayan, "Dislocations, twins, and grain boundaries in CVD diamond thin films: Atomic structure and properties," *Journal of Materials Research,* vol. 5, pp. 2414-2423, 1990.

[53] M. Bhogra, U. Ramamurty, and U. V. Waghmare, "Temperature-dependent stability of stacking faults in Al, Cu and Ni: first-principles analysis," *Journal of Physics: Condensed Matter,* vol. 26, p. 385402, 2014.

[54] L. Liu, R. Wang, X. Wu, L. Gan, and Q. Wei, "Temperature effects on the generalized planar fault energies and twinnabilities of Al, Ni and Cu: First principles calculations," *Computational Materials Science,* vol. 88, pp. 124-130, 2014.

[55] H. Hofmeister, "Forty Years Study of Fivefold Twinned Structures in Small Particles and Thin Films," *Crystal Research and Technology,* vol. 33, pp. 3-25, 1998.

[56] A. J. Cao and Y. G. Wei, "Formation of fivefold deformation twins in nanocrystalline face-centered-cubic copper based on molecular dynamics simulations," *Applied Physics Letters,* vol. 89, p. 041919, 2006/07/24 2006.

[57] Y. T. Zhu, X. Z. Liao, and R. Z. Valiev, "Formation mechanism of fivefold deformation twins in nanocrystalline face-centered-cubic metals," *Applied Physics Letters,* vol. 86, p. 103112, 2005/03/07 2005.

[58] Q. Qin, S. Yin, G. Cheng, X. Li, T.-H. Chang, G. Richter, *et al.*, "Recoverable plasticity in penta-twinned metallic nanowires governed by dislocation nucleation and retraction," *Nature communications,* vol. 6, p. 5983, 2015.

[59] Z. L. Wang, "Characterization of nanophase materials," *Particle & Particle Systems Characterization: Measurement and Description of Particle Properties and Behavior in Powders and Other Disperse Systems,* vol. 18, pp. 142-165, 2001.

[60] X. An, Q. Lin, S. Wu, Z. Zhang, R. Figueiredo, N. Gao, *et al.*, "Formation of fivefold deformation twins in an ultrafine-grained copper alloy processed by high-pressure torsion," *Scripta Materialia,* vol. 64, pp. 249-252, 2011.

[61] A. Cao and Y. Wei, "Formation of fivefold deformation twins in nanocrystalline face-centered-cubic copper based on molecular dynamics simulations," *Applied physics letters,* vol. 89, p. 041919, 2006.

[62] S. Lee, J. Im, Y. Yoo, E. Bitzek, D. Kiener, G. Richter, *et al.*, "Reversible cyclic deformation mechanism of gold nanowires by twinning–detwinning transition evidenced from in situ TEM," *Nature Communications,* vol. 5, p. 3033, 01/08/online 2014.

[63] J. Wang, N. Li, O. Anderoglu, X. Zhang, A. Misra, J. Y. Huang, *et al.*, "Detwinning mechanisms for growth twins in face-centered cubic metals," *Acta Materialia,* vol. 58, pp. 2262-2270, 2010/04/01/ 2010.

[64] J. Li, J. Zhang, L. Jiang, P. Zhang, K. Wu, G. Liu, *et al.*, "Twinning/detwinning-mediated grain growth and mechanical properties of free-standing nanotwinned Ni foils: Grain size and strain rate effects," *Materials Science and Engineering: A,* vol. 628, pp. 62-74, 2015.

[65] S. Ogata, J. Li, and S. Yip, "Energy landscape of deformation twinning in bcc and fcc metals," *Physical Review B,* vol. 71, p. 224102, 2005.

[66] J. Schiøtz and K. W. Jacobsen, "A maximum in the strength of nanocrystalline copper," *Science,* vol. 301, pp. 1357-1359, 2003.

[67] V. Yamakov, D. Wolf, S. Phillpot, A. Mukherjee, and H. Gleiter, "Deformation-mechanism map for nanocrystalline metals by molecular-dynamics simulation," *Nature materials,* vol. 3, p. nmat1035, 2003.

[68] H. J. Choi, S. W. Lee, J. S. Park, and D. H. Bae, "Tensile behavior of bulk nanocrystalline aluminum synthesized by hot extrusion of ball-milled powders," *Scripta Materialia,* vol. 59, pp. 1123-1126, 2008/11/01/ 2008.

[69] A. A. Benzerga and J.-B. Leblond, "Ductile fracture by void growth to coalescence," in *Advances in applied mechanics*. vol. 44, ed: Elsevier, 2010, pp. 169-305.

[70] J.-C. Kuo and I.-H. Huang, "Extraction of plastic properties of aluminum single crystal using Berkovich indentation," *Materials transactions,* vol. 51, pp. 2104-2108, 2010.

[71] W. Xu and L. P. Dávila, "Tensile nanomechanics and the Hall-Petch effect in nanocrystalline aluminium," *Materials Science and Engineering: A,* vol. 710, pp. 413-418, 2018/01/05/ 2018.

[72] W. Xu and L. P. Dávila, "Size dependence of elastic mechanical properties of nanocrystalline aluminum," *Materials Science and Engineering: A,* vol. 692, pp. 90-94, 2017.

[73] M. Haque and M. A. Saif, "Mechanical behavior of 30–50 nm thick aluminum films under uniaxial tension," *Scripta Materialia,* vol. 47, pp. 863-867, 2002.

[74] S.-H. Kim, H.-K. Kim, J.-H. Seo, D.-M. Whang, J.-P. Ahn, and J.-C. Lee, "Deformation twinning of ultrahigh strength aluminum nanowire," *Acta Materialia,* vol. 160, pp. 14-21, 2018/11/01/ 2018.

[75] T. Nieh and J. Wadsworth, "Hall-Petch relation in nanocrystalline solids," *Scripta Metallurgica et Materialia,* vol. 25, pp. 955-958, 1991.

[76] C. Carlton and P. Ferreira, "What is behind the inverse Hall–Petch effect in nanocrystalline materials?," 1359-6454, 2007.

[77] J. Schiøtz, F. D. Di Tolla, and K. W. Jacobsen, "Softening of nanocrystalline metals at very small grain sizes," *Nature,* vol. 391, p. 561, 1998.

[78] S. Yip, "Nanocrystals: the strongest size," *Nature,* vol. 391, p. 532, 1998.

III. SIZE EFFECT ON NUCLEATION PROCESS DURING SOLIDIFICATION OF PURE METALS BY ATOMISTIC SIMULATIONS

Avik Mahata[1] and Mohsen Asle Zaeem[1,2*]

[1] Department of Materials Science and Engineering, Missouri University of Science and Technology, Rolla, MO 65409, USA

[2] Department of Mechanical Engineering, Colorado School of Mines, Golden, CO 40801, USA

(*This manuscript is ready for submission in Journal of Crystal Growth in March, 2019*)

ABSTRACT

Due to significant increase in computing power in recent years, the simulation size of atomistic methods for studying the nucleation process during solidification has been gradually increased, even to billion atom simulations (micrometer length scale). But the question is how big of a model is required for size-independent and accurate simulations of the nucleation process during solidification? In this work, molecular dynamics (MD) simulations with model sizes ranging from ~2 K to ~8 M atoms were used to study nucleation during solidification. The most advanced second nearest-neighbor modified embedded method (2NN-MEAM) interatomic potentials for Al (face-centered cubic), Fe (body-centered cubic), and Mg (hexagonal-close packed) were utilized for MD simulations. We have analyzed several quantitative characteristics such as nucleation time, density of nuclei, nucleation rate, self-diffusion coefficient, and change in free energy during solidification. The results showed that by increasing the model size up to 1 M atoms, the simulations and measurable quantities become entirely independent of simulation cell size. The prediction of cell size required for size-independent computed data can

considerably reduce the computational costs of atomistic simulations and at the same time increase the accuracy and reliability of the computational data.

1. INTRODUCTION

Solidification and crystallization by nucleation is very common in casting of different materials, including metals and alloys. The major challenge in experimental observation of nucleation is that the entire process of nuclei formation and growth happens in the interior part of the liquid metals. Therefore it is beneficial to use theoretical or computational tools such as classical nucleation theory (CNT) [1, 2], density function theory (DFT) calculations [3], molecular dynamics (MD) [4-6], Monte Carlo (MC) [7, 8], phase-field [9-13], and cellular automata [14, 15] to study solidification and nucleation phenomena. Theoretical tools such as CNT do not predict the dependability on system size as the probability of forming crystal nuclei is per unit time and unit volume and is related to the free energy barrier for formation of the critical nucleus [16]. On the other hand, even the most advanced and hybrid MC simulations are limited to very small number of atoms [17, 18], whereas phase-field or cellular automata are applied in a considerably larger length scales and unable to study nucleation [19, 20]. Among the mentioned methods, MD simulations have the flexibility to cover length scales between sub-nanometer to sub-micrometer scales depending on the computing resources and they seem to be the suitable computational method to study the nucleation process.

MD simulations have been used to study the nucleation process in different metals and alloys at different length scales [21-23]. However, it is a well-established fact that the

accuracy of MD simulations depends on the interatomic potentials. In the literature, the nucleation process during solidification has been studied for model sizes ranging from a few thousand atoms [24, 25] to million [6, 25] and billion atoms [26]. However by increasing the model size the accuracy of the predictions is not necessarily improved. For example, the interatomic potential used for the billion atom MD simulation of pure Fe solidification [26] predicts the meting temperature to be 2,400 K, which is ~600 K higher than the physical melting temperature of Fe. On the other hand, the simulation size can influence the results, and to circumvent simulation size effects, it is customary to use larger simulation boxes. There has been some disagreements on how large the simulation size should be for a reliable study of nucleation [22, 27], however the expectation has always been that a sufficiently large simulation cell would resolve the issues related to finite size effect.

Size effect in MD simulations was studied by Streitz et al. [22] who predicted at least 8 M atoms are required for size-independent MD models when utilizing many-body, angular-dependent interaction potentials; it should be mentioned that this interatomic potentials were not explicitly fitted to solid-liquid coexistence properties (e.g., melting point). The other studies were done by utilizing Lennard-Jones [28] and hard-sphere model [29] potentials, which are also very simple interatomic potential models and incapable of predicting high temperature properties; basically such potentials should not be used to study nucleation during solidification. As the interatomic potential becomes more accurate to predict solid-liquid coexistence properties, it becomes more expensive computationally [30]. Thus, it is important to determine the optimum model size for simulating the nucleation process by MD simulations, in order to be scientifically accurate without any

finite size effects. In recent literature, there are a few theoretical, computational and experimental studies which investigated the size effect in crystal nucleation [31-33]. They studied various aspects of nucleation such as free energy change, nucleation rate, and solid-liquid coexistence properties, but they did not provide enough details about an optimum finite size that can be used in general to get accurate insights about nucleation during solidification of different material systems.

To address the issues related to the finite size effect of atomistic simulations, we performed MD simulations ranging from a few thousand atoms to several million atoms utilizing 2NN-MEAM potentials to predict an optimum simulation size for nucleation studies. We performed computations for three different metals, Al with face-centered cubic (fcc), Fe with body-centered cubic (bcc) and Mg with hexagonal-close packed (HCP) crystal structures to ensure that the results can be extended to other metallic systems with different crystal structures. Isothermal solidification is used in all the simulation, and we quantified the nuclei size, density, diffusivity, free energy and also nucleation rate for different model sizes in order to identify the size-independent models.

2. SIMULATION METHODOLOGY

We built MD simulation models using 10 different box sizes, ranging from 2 K to 8 M atoms. Solidification temperatures was chosen between 300 K and 750 K for Al, between 800 K and 1,250 K for Fe, and between 300 K and 700 K for Mg, with 50 K intervals. Therefore total of 10 solidification temperatures were tested for MD simulations of each of the studied metals. Each simulation was repeated 5 times with slightly different

initial velocity of atoms to determine the statistical errors. Total of 1,500 MD simulations were estimated (3 materials x 10 temperatures x 10 model sizes x 5 times) to complete the study. However, below a specific box size and above a specific temperature (see Section 3.2, Table 3), the nucleation doesn't occur under any conditions. Therefore about 1,000 simulation runs were sufficient to compete study on the size effect. The details of the various simulations that we performed are given in Table 1. As the lattice constants (Al, Fe and Mg are 4.05 Å, 2.86 Å, and 3.20 Å) and crystal structures are different, the total number of atoms are not exactly same for the same supercells of these three metals. We used isothermal-isobaric (NPT) ensemble and a time step size of 3 fs for all simulations. Temperature and pressure were controlled by Nose-Hoover thermostat and Parrinello-Rahman barostat [34], respectively. All the MD simulations were performed in LAMMPS [35]. The OVITO visualization package was used to monitor the nucleation and solidification processes [36]. Within OVITO, common neighbor analysis (CNA) was used [37] to identify the local environment of atoms. MATLAB was used to solve equations numerically [38].

Table 1. The initial simulation set up for the MD simulation of solidification of Al, Fe and Mg.

Element	Unit Cells	Box Size (nm^3)	Atoms (approx.)	Temperature Range (K)
Al	10-160	2.86-45.80	2,000-8,000,000	300-750
Fe	10-125	4.05-50.70	4,000-8,000,000	700-1,250
Mg	10-178	5.0-55.39	5,000-8,000,000	300-700

Many body interatomic potentials such as Finnis–Sinclair (FS) [39, 40] and Embedded Atom Method (EAM) [41] have been extensively used for solidification studies [6, 42-44]. Both FS and EAM potentials fail to predict the melting point or the solid-liquid coexistence properties accurately for the most metallic systems. Extended FS potentials were studied for solidification of various metals such as Fe, Mo, Ta, and W by Dai et al. [45]. On the other hand semi-empirical many body EAM potentials has been used for solid-liquid coexistence more often [41, 46] and predict the melting point properties more accurately [47]. In this work, we are using the 2NN-MEAM potentials, which are the most accurate interatomic potentials for high and low temperature properties of metals. The detailed comparison of both low and high temperature experimental properties and those calculated by MD simulations utilizing 2NN-MEAM potentials [42-44, 48] are given in Table 2.

Table 2. Properties of Al, Fe and Mg predicted by MD simulations utilizing the 2NN MEAM interatomic potential and experimental results.

	Al		**Fe**		**Mg**	
Properties	Experiments	MEAM MD [42]	Experiments	MEAM MD [43]	Experiments	MEAM MD [49]
Bulk Modulus (GPa)	76.4[a]	79.4	167[e]	166	36.9 [a]	36.9
C_{11} (GPa)	111.5[a]	114.3	230[e]	231	63.5[a]	62.9
C_{44} (GPa)	29.5[a]	31.6	117[e]	116	1.84 [a]	1.71
Specific Heat ($J\ mol^{-1}\ K^{-1}$)	26.15[b]	24.70	25.50[e]	26.18	25.9[f]	25.6
Thermal Expansion Coeff. ($10^6\ K^{-1}$)	17.31[b]	23.50	12.10[e]	11.80	26[f]	27.8
Melting Point (T_m) (K)	934[c]	925	1811[e]	1807	937.9[f]	923.2

[a] [50] , [b] [51], [c] [51-53], [d] [54-56], [e] [57-60], [f] [61], [g] [62]

3. RESULTS AND DISCUSSIONS

3.1 VISUALIZATION OF NUCLEATION

Regardless of the nature of solidification, the number of solid nuclei increases as the simulation size increases. Figure 1(a-l) shows the nucleation for Al, Fe, and Mg in an intermediate stage before the solid nuclei grown enough to merge and form grain boundaries. The Al in the display (Figure 1(a-d)) was solidified at 500 K, Fe (Figure 1(e-h)) at 1,100 K, and Mg (Figure 1(i-l)) at 600 K. The process of solidification by nucleation is random and the solidification can start from any parts of the simulation box. In Al solidification, the nucleation happens primarily by formation of fcc (green) atoms (Figure 1(a-d)) and it also accompanied by some solidification defects, which can be identified as hcp stacking faults as shown in Mahata et al. [6]. The Fe and Mg nucleate by formation of bcc (blue) atoms (Figure 1(e-h)) and hcp (red) atoms (Figure 1(i-l)), respectively. This is clear from Figure 1 that the system size for MD simulations needs to be large enough to support the formation and growth of multiple critical nuclei. It is important to point out that this system-size dependence is due to the increased probability of forming a critical nucleus when the system size is larger, and it is not an artifact due to the periodic boundary conditions.

3.2 SIZE EFFECT CRITERIA IN MD SIMULATIONS

Both the solidification temperature and simulation size influence the solidification process in MD simulations. Temperature is always the primary factor that impacts the solidification, and beyond a threshold temperature range the simulation box cannot be solidified for any box sizes in MD simulations. For example, above 725 K, the Al atoms

cannot be solidified regardless of the simulation box size [63]. In the same way, there is no solidification observed above 700 K for Mg and 1,250 K for Fe in MD simulations. However, when the solidification temperature remains within the threshold range, the box size can change the nucleation temperature.

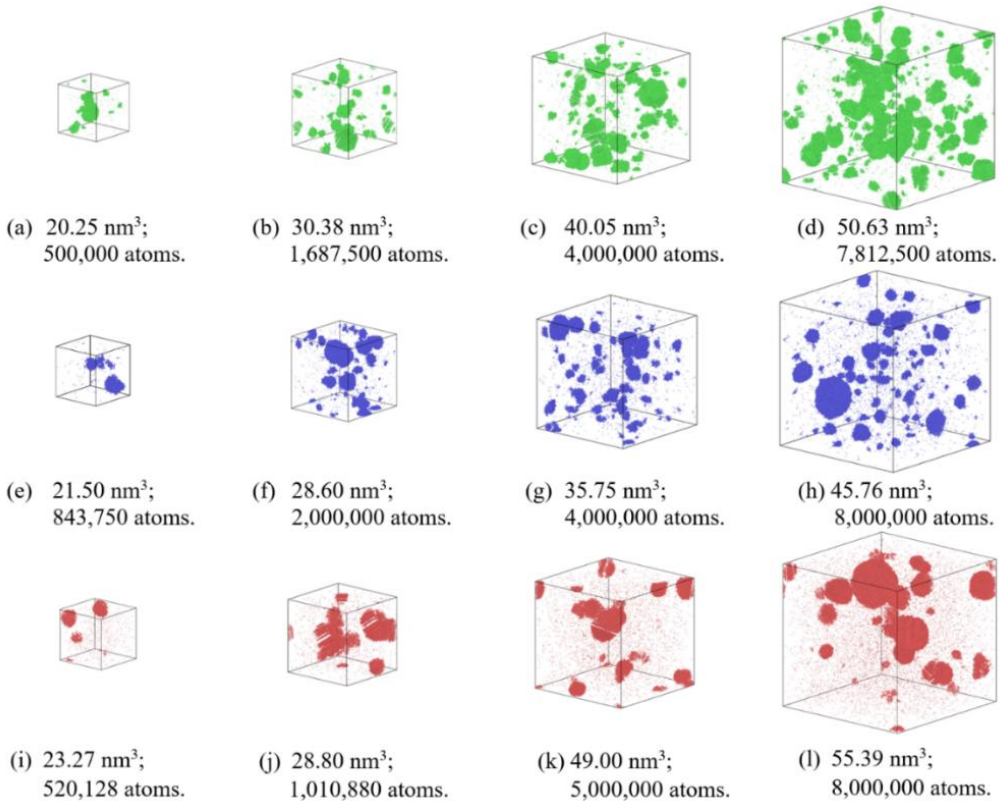

Figure 1. Nucleation in different simulation sizes of (a-d) Al at 500 K, (e-h) Fe at 1100 K, and (i-l) Mg at 600 K. The green atoms represent the fcc atoms, blue atoms represent the bcc atoms, and red atoms represent the HCP atoms. This figure only shows the primary crystalline phase, and hcp atoms in Al, ico atoms in Fe, fcc atoms in Mg, and the liquid atoms in all the cases are not shown for better visualization of the nuclei.

There is no maximum threshold size for simulation to observe nucleation, because increasing the simulation size (number of atoms) will statistically favor nucleation and

crystallization. But it was observed that there is a minimum model size required for nucleation and consequently for solidification to occur. Table 3 shows for isothermal solidification of Al at 450 K and 500 K, a simulation box with only 24 K atoms was required to observe nucleation and solidification, whereas a minimum of 62.5 K atoms was required to form a critical nucleus at 700 K. The same applies for Fe and Mg, and the number of atoms in the simulation box to observe nucleation during solidification varies by solidification temperature. The nucleation happens optimally between a temperature range of 400 K and 500 K for Al, between 1,000 K and 1,100 K for Fe, and between 500 K and 600K for Mg. At lower solidification temperatures (or higher undercoolings) such as 300-400 K the solidification will occur, but crystal nucleation is rare. As shown in our previous work on Al [63] and Fe by Shibuta et al. [64], a high undercooling results in formation of a glassy solid. Therefore, to study the nucleation process by MD simulations, the temperature-dependent simulation size effect should be considered.

In order to discuss the effects of mobility of atoms on nucleation from an under-cooled melt, the self-diffusion coefficients of the undercooled Al, Fe and Mg melts are estimated from the mean-square displacement (MSD) analysis, which is a common technique to discuss the diffusion process. The MSD can be defined as the squared difference of current and initial potions of atoms, $|r_i(t) - r_i(0)|^2$, where $r_i(t)$ and $r_i(0)$ are the position of atom i at time t and 0, respectively [65]. The self-diffusion coefficient can be estimated from Einstein's relation [66], which is the slope of the MSD versus time divided by six, $\lim_{t\to\infty} \frac{1}{6t}|r_i(t) - r_i(0)|^2$. As shown in Figure 2(a-c), the self-diffusion coefficient fluctuates when the simulation size is very small (typically a simulation box

with less than 20 K atoms). Diffusivity generally fluctuates in simulations with smaller box sizes and tend to be more stable in larger size simulations [67-69]. By increasing the simulation size to 1 M atoms, the self-diffusion stabilizes and converges to the value of the simulation with the largest size box (~8M). This suggests that a million-atom simulation can be the optimum simulation size for MD simulation of solidification. Figure 2 also suggests that temperature is the primary factor in solidification, as the diffusion coefficient increases with increasing the solidification temperature. At very high undercooling or very low isothermal solidification temperatures, the solidification happens very fast due to higher differences in mobility of high and low temperature atoms. The melt solidifies extremely fast and a glassy solid is formed with a very few solid nuclei [6, 63, 64]. When the solidification temperature is too high (or at very low undercooling temperatures), the atoms have a higher mobility; the atoms remain liquid for solidification temperatures higher than 725 K (0.77 T_m) for Al, 1,200 K (0.69 T_m) for Fe, and 700 K (0.75 T_m) for Mg in MD simulations. As the simulation temperature approaches these threshold limits for nucleation, the excessive thermal vibration and self-diffusivity makes it difficult to form solid nuclei. As suggested in Figure 2, the simulation size at a specific temperature has to be in an optimum range to observe the nucleation process. We present the minimum simulation size to observe nucleation at different isothermal temperatures. Increasing the simulation size will guarantee the nucleation to happen as the diffusivity becomes almost constant with increasing the box size. But there is always a minimum simulation size to stabilize the mobility or the thermal vibration in the atoms to form stable solid crystals.

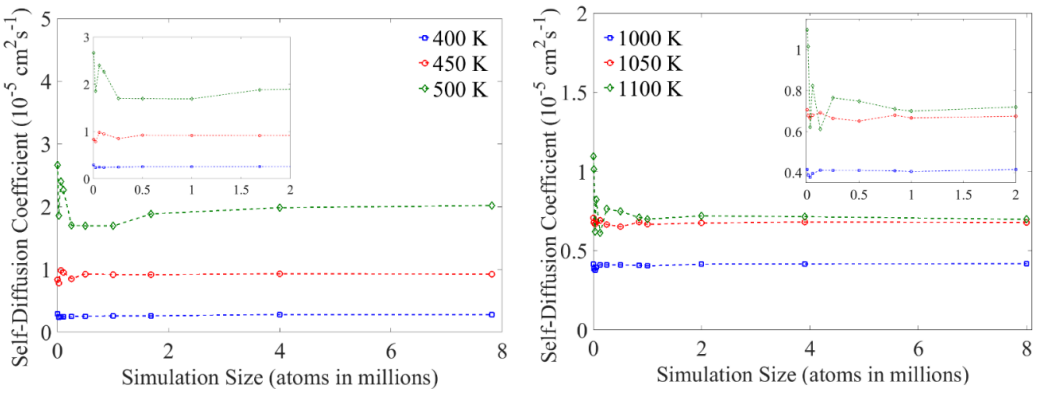

Figure 2. Self-Diffusion coefficient for different simulation sizes for (a) Al at 400 K, 450 K and 500 K, (b) Fe at 1,000 K.

The overall number of nuclei increases before the coarsening or grain boundary formation as we increase the simulation sizes. The number of maximum number of separable critical nuclei per unit volume (nuclei density) is plotted as a function of the simulation size in Figure 3(a-c). At lower simulation size (up to 1,000, 000) for all the metallic systems, a constant number of nuclei forms. This happens due to increasing number of nuclei increases linearly with increasing box size. The lowest simulation size considered for Al, Fe and Mg were 4000, 2000 and 5,000 respectively no nuclei formation happens. Then simulation sizes of between 25,000-2,000,000 the number of total nuclei only remains between 1.5-2.5x10^{-3} per nm^3 (Figure 3(a)). Then the nuclei density actually dropped and shows less fluctuation for 2 and 4M atom simulation sized. For Fe, the nuclei density actually drops with increasing simulation sizes (Figure 3(b)). However, once the system size reaches 2M the nuclei density for Al, Fe or Mg, the nuclei density remains within an error margin of 0.20x10^{-3} per nm^3.

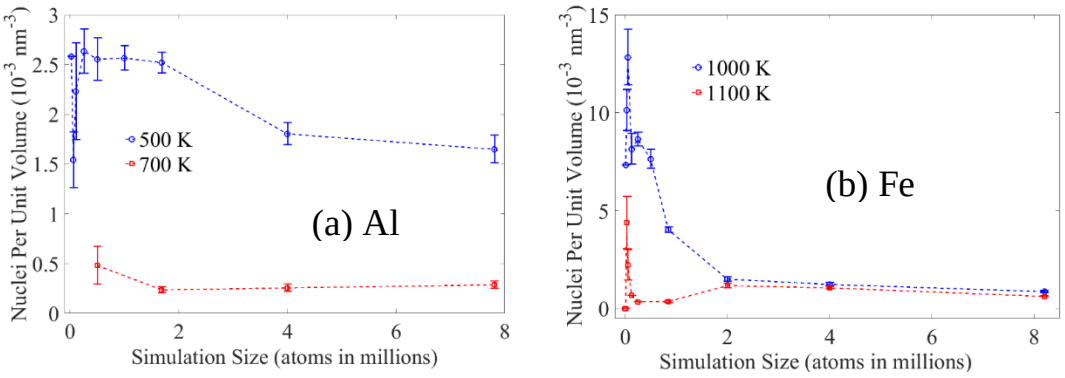

Figure 3. The increasing number of critical nuclei with increasing box size shown for (a) Al, (b) Fe at different temperatures.

We also illustrate the variation of incubation time depending on the system-size in Fig 4. The incubation time is referred to the time taken by the liquid metal to form first critical solid nucleus. This can be also referred to as induction time or nucleation time. The nucleation time for the smaller simulation size is relatively much higher than the simulation size of 2-8M for both Al and Fe. The nucleation time goes down with increasing box size. This happens due to increasing probability of forming critical nuclei as there are more number of metastable crystalline atoms for bigger simulation boxes.

The bigger the simulation size is, the larger the nuclei are expected to grow before coarsening (microstructure formation). The size of the largest nucleus linearly increases for the Al at 500 K (Figure 5(a)), and it also shows the size effect in Fe and Mg (Figure 5(b)) at 1100 K and 600 K respectively. The size effect is very significant at very small size simulations up to 1M atoms. The maximum nuclei size increases linearly till 1M atoms simulation size. However, when the simulation size is at least 1M for Al, 843,000 for Fe and 2M for Mg the biggest nuclei in the simulation coarsen almost at a constant size.

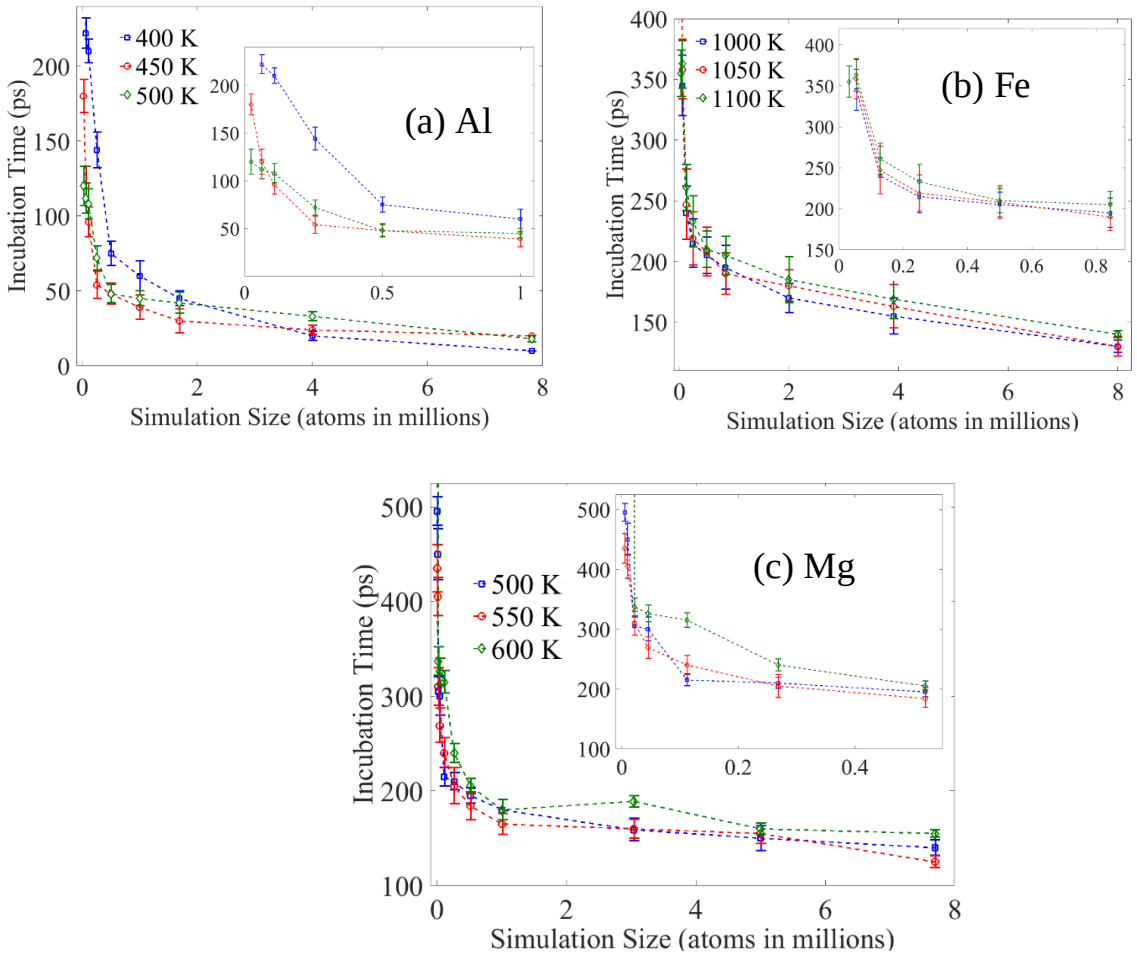

Figure 4. The formation time for the first critical nucleus is calculated for (a) Al and (b) Fe and (c) Mg for different temperatures and system sizes.

The difference between number of atoms in the largest cluster reduce remain within the error range. Even though the increasing simulation size increases the number of critical nuclei, it also produces a large number of nuclei. Due to that the coarsening starts at a constant size varies between 1M to 8M atoms simulation sizes. Howwver, the beginning of the coarsening varies fof different metals, but this is certain that atleast 1-2M atoms required for nucleation study.

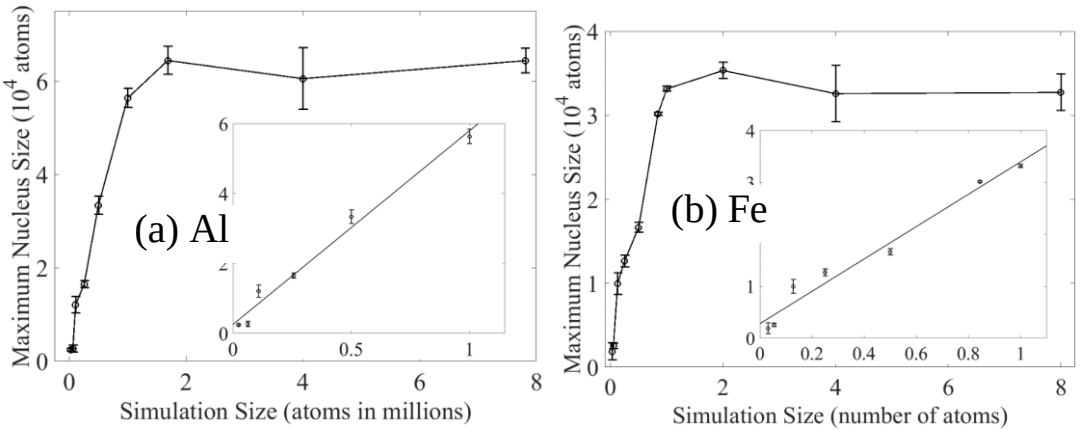

Figure 5. The maximum nuclei size is shown for (a) Al at 500 K, (b) Fe at 1100 K for different simulation sizes.

3.3 SIZE EFFECT ON FREE ENERGY AND NUCLEATION RATE

The free energy landscape during solidification by nucleation can be described by the mean first-passage time (MFPT) method [70, 71]. The MFPT is defined as the average elapsed time for a system that crosses the activated barrier to another steady state for the first time When the system reaches a transition state (in our case its liquid to solid), it is thought that the free energy barrier climbs its top and the system has a 50% probability of stepping into a new steady state. So, the MFTP (or time), solid atom fraction and the free energy are interrelated quantities and the dynamics of various nonequilibrium and activated process can be described by Fokker-Plank equation [72],

$$\frac{\partial P(x,t)}{\partial t} = \frac{\partial}{\partial x}\left[D(x)e^{-\beta\Delta G(x)} \frac{\partial}{\partial x}(P(x,t)e^{\beta\Delta G(x)} \right] = -\frac{\partial J(x,t)}{\partial x} \qquad (1)$$

Where x is the number of particles/atoms in the system, $P(x,t)$ is the probability density that the number of atoms in the system is x at time t. $J(x,t)$ can be referred to the

nucleation rate for our case and $D(x)$ is the diffusion coefficient. $\Delta G(x)$ is referred to the free energy landscape and $\beta = 1/k_B T$, where T is temperature and k_B is Boltzmann's constant. When the system is in steady state, the probability density $P_{st}(x)$ becomes time independent and also $\frac{\partial P_{st}}{\partial t} = -\frac{\partial J}{\partial t} = 0$, and thus Eqn. (1) yields to,

$$\frac{\partial(\beta \Delta G(x))}{\partial x} = -\frac{\partial \ln P_{st}(x)}{\partial x} - \frac{J(x,t)}{D(x)P_{st}(x)} \tag{2}$$

By integrating Eqn. 2 we get,

$$\beta \Delta G(x) = \ln[B(x)] - \int \frac{dx'}{B(x')} + C \tag{3}$$

$B(x)$ can be evaluated from below Eqn. (4),

$$B(x) = \frac{1}{P_{st}(x)}\left[\int_a^x P_{st}(x')dx' - \frac{\tau(x)}{\tau(b)}\right] \tag{4}$$

$\tau(x)$ and $\tau(b)$ are the time at any time before the formation of the maximum size cluster or coarsening and the time required for coarsening respectively. The original MFTP method was applied to very large number of systems but to a very small (200-1000 atoms) simulation sizes in MD. The quantities and the computations for the MFTP and free energy have been modified according to the large scale system like modern MD simulations [32, 73, 74]. In our cases of liquid to solid transformation the maximum nucleus size happens right when the coarsening starts. As shown in Figure 6(a) and (b), the dotted circles show one area of the coarsening for Al at 500 K. For a smaller system (Figure 6(a)), the coarsening is very clear and it happens only at one area. So the probability ($P_{st}(x)$) of finding the maximum size solid cluster (or nucleus) is just the 1 divided by the total number

of nuclei. However, for a larger size (Figure 6(b)), the coarsening can be identified but there can be multiple maximum size clusters. The size and shape of the nuclei are weakly defined and it's hardly gets a perfectly spherical shape. At the same time, it is fairly simple to compute the fraction of crystalline atoms in the system. As shown in Figure 6(c), the crystallization time varies as we varied the simulation size. To form the crystalline nuclei, each of the crystalline atoms had to overcome the free energy barrier. So, the formation of crystalline atoms and nucleation time can also help us compute the free energy landscape.

Instead of the probability we utilize the solid fraction for estimate the free energy landscape ($\beta\Delta G(x)$). The solid fractions in the liquid Al, Fe and Mg have been estimated by averaging over five different simulations with different initial condition. Then we applied standard discretization method to numerically evaluate Eqn. 4 and we get similar free energy landscape in Figure 6(d) described by Wedekind et. al. [28, 71]. As shown in Figure 6(d) in the marked points on the free energy landscape is that the fraction of solid crystalline required for coarsening happens at different times for different simulation sizes. The $\beta\Delta G(x)$ generally goes down monotonically as the isothermal temperature of 500 K guarantees the nucleation to happens. However, as the sample size is changing the time required coarsening or the formation of the maximum size cluster is changing and also the fraction of atoms in nucleate before the coarsening changes. In this way, we can estimate the change in free energy before formation of the maximum nucleus size or coarsening. In the same way, we also repeat the same procedure for Fe at 1100 K and Mg at 600 K, to obtain the change in free energy for Fe.

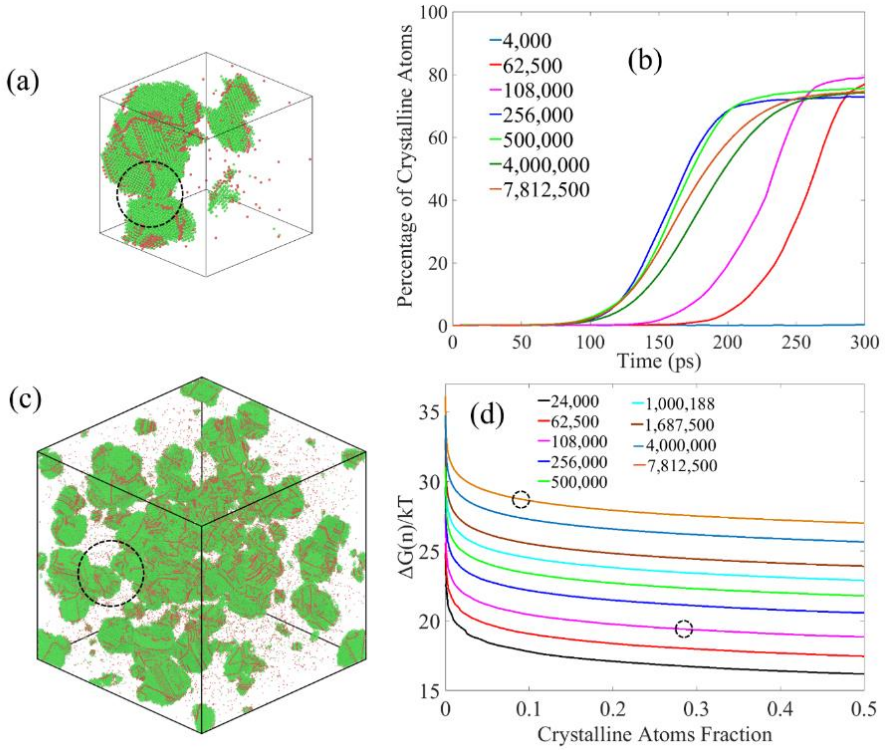

Figure 6. The maximum nuclei size (or beginning of coarsening) is shown for Al at 500 K for simulation size (a) 108,000 atoms and (b) 8,000,000 atoms. Then calculated. (c) The percentage of crystalline atoms shown for different simulation size for Al at 500 K for different simulation sizes. (d) The free energy landscape for Al at 500 K for different simulation size.

As shown in Figure 7 the change is free energy is linear for simulation size 1 M atoms for Al, Fe or Mg. The amount of free energy change gradually drops for Al till 1 million, then it becomes linear till 8 million. At the same time for Fe the free energy fluctuates for very small size such as 31,500 and 100,000 atoms but then it almost linearly reduces and becomes flat after 500,000 atoms. This observation suggests the simulation becomes size independent after the system size is taken 1 million for any metallic system.

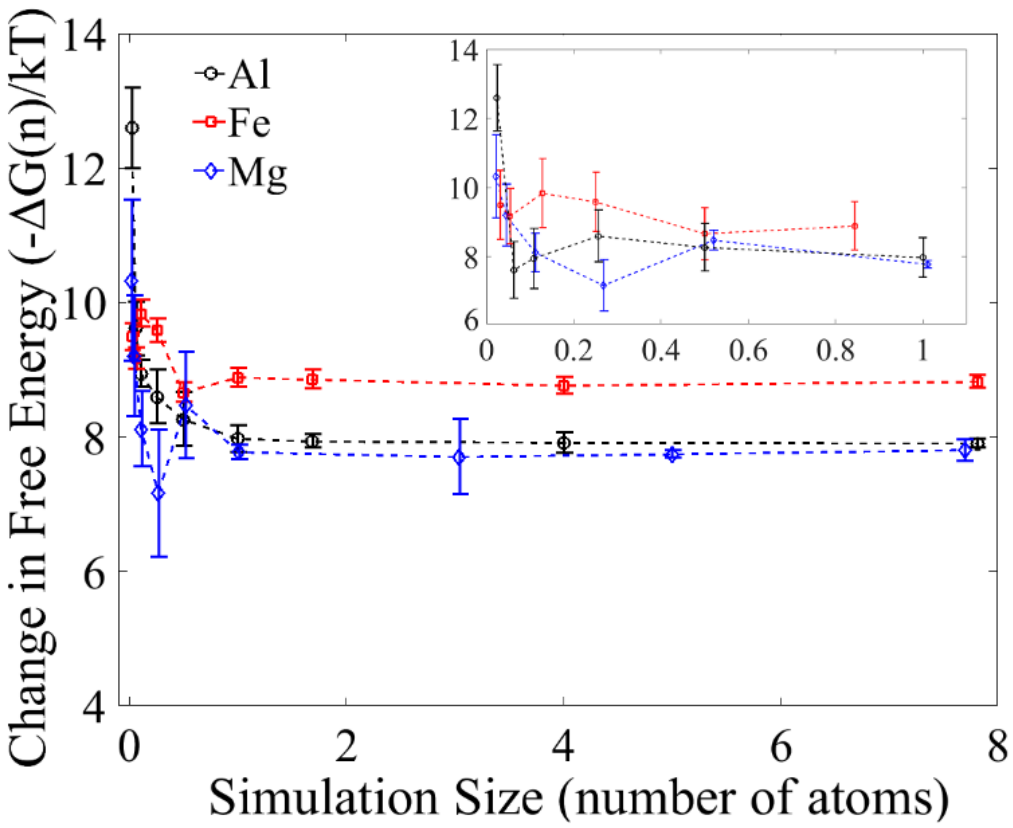

Figure 7. The change in free energy $\left(-\Delta G(x)/k_B T\right)$ Al (500 K), Fe (1100 K) and Mg (600K) for different simulation size.

The nucleation rate for each annealing temperature is calculated by fitting a straight line to the data on number of nuclei versus time, where the slope of the line is the nucleation rate [6]. Nucleation rate doesn't show any significant change for system size beyond 1 million for Al, 500,000 for Fe and 1M for Mg (Figure 8(a-c)). The size effect is shown for smaller simulation sizes in the inset of Figure 8, and it almost linearly increases with increasing simulation size. As discussed earlier the incubation time (time to form first critical nucleus) reduces gradually by increasing the size of the system (Figure4). The other analysis shows nuclei density reduces with increasing box size (Figure 3). So, even though

in the larger size simulations the nucleation starts earlier than smaller size boxes, the nucleation rate remain constant because the number of nuclei density gradually reduces for bigger simulation size.

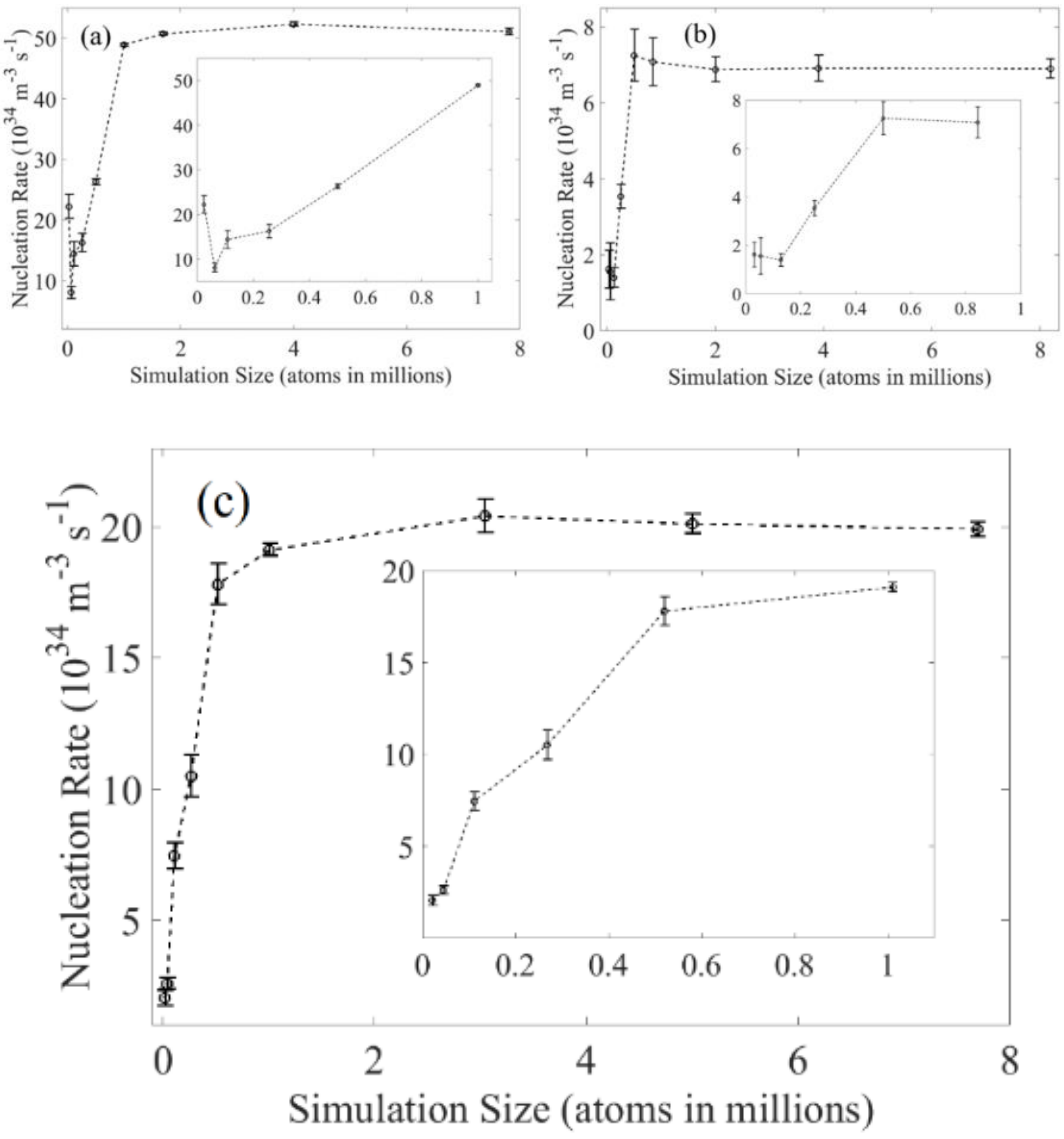

Figure 8. The nucleation rate for different simulation size is shown for (a) Al at 500 K, (b) Fe at 1,100 K, (c) Mg at 600 K.

4. CONCLUSION

To summarize, we present the results of large-scale atomistic simulations of solidification of molten metals such as Al, Fe, Mg and attempt to study the effect of simulation size at various temperatures. The temperature of nucleation is the most important criterion for determining the minimum simulation size. At higher temperature, the mobility of the atoms increases due to increasing kinetic energy in system, and the metastable solid crystalline atoms fail to form nuclei. At much lower temperatures (such as 300 K) the undercooling is so high, that the solidification happens by formation of glassy amorphous solid. The mobility of the atoms remains in an optimum level between 400-500 K for Al, 1000 -1100 K for Fe and 500-600 K for Mg. However, there is a minimum simulation size is required to nucleation to happen. At least 10,000-25,00 atoms required to form solid nuclei in the undercooled liquid. By increasing the number of liquid atoms above 100,000, the nuclei density (and also total number of nuclei) can be increased and the solidification can happen below the threshold temperature for a particular metallic system. However, the simulation remain size dependent as the maximum critical nuclei size increases linearly. The nucleation time, nucleation rate or the free energy for nucleation also influenced for increasing system size. The metallic systems show the stable nuclei size, nucleation rate or the free energy when a 1 M atoms system size is considered. 1M atoms should be sufficient for simulating a size-independent nucleation phenomena under the condition that the interatomic potential is verified in details for melting and solid-liquid coexistence.

REFERENCES

[1] G. Neilson and M. Weinberg, "A test of classical nucleation theory: crystal nucleation of lithium disilicate glass," *Journal of Non-Crystalline Solids,* vol. 34, pp. 137-147, 1979.

[2] D. Erdemir, A. Y. Lee, and A. S. Myerson, "Nucleation of crystals from solution: classical and two-step models," *Accounts of chemical research,* vol. 42, pp. 621-629, 2009.

[3] G. Kahl and H. Löwen, "Classical density functional theory: an ideal tool to study heterogeneous crystal nucleation," *Journal of Physics: Condensed Matter,* vol. 21, p. 464101, 2009.

[4] S. Toxvaerd, "Molecular-dynamics simulation of homogeneous nucleation in the vapor phase," *The Journal of Chemical Physics,* vol. 115, pp. 8913-8920, 2001.

[5] X. Sui, Y. Cheng, N. Zhou, B. Tang, and L. Zhou, "Molecular dynamics simulation of solidification process of multicrystalline silicon from homogeneous nucleation to grain coarsening," *CrystEngComm,* 2018.

[6] A. Mahata, M. Asle Zaeem, and M. I. Baskes, "Understanding homogeneous nucleation in solidification of aluminum by molecular dynamics simulations," *Modelling and Simulation in Materials Science and Engineering,* vol. 26, p. 025007, 2018.

[7] K. Oh and X. C. Zeng, "Formation free energy of clusters in vapor-liquid nucleation: A Monte Carlo simulation study," *The Journal of chemical physics,* vol. 110, pp. 4471-4476, 1999.

[8] D. Srolovitz, G. Grest, and M. Anderson, "Computer simulation of recrystallization—I. Homogeneous nucleation and growth," *Acta metallurgica,* vol. 34, pp. 1833-1845, 1986.

[9] B. Böttger, J. Eiken, and I. Steinbach, "Phase field simulation of equiaxed solidification in technical alloys," *Acta materialia,* vol. 54, pp. 2697-2704, 2006.

[10] L. Gránásy, T. Börzsönyi, and T. Pusztai, "Nucleation and bulk crystallization in binary phase field theory," *Physical review letters,* vol. 88, p. 206105, 2002.

[11] L. Gránásy, T. Pusztai, D. Saylor, and J. A. Warren, "Phase field theory of heterogeneous crystal nucleation," *Physical review letters,* vol. 98, p. 035703, 2007.

[12] S. Wang, M. Asle Zaeem, M. F. Horstemeyer, and P. T. Wang, "Investigating thermal effects on morphological evolution during crystallisation of hcp metals: three-dimensional phase field study AU - Wang, S," *Materials Technology,* vol. 27, pp. 355-363, 2012/11/01 2012.

[13] M. Asle Zaeem, H. Yin, and S. D. Felicelli, "Modeling dendritic solidification of Al–3%Cu using cellular automaton and phase-field methods," *Applied Mathematical Modelling,* vol. 37, pp. 3495-3503, 2013/03/01/ 2013.

[14] L. Liu, S. Pian, Z. Zhang, Y. Bao, R. Li, and H. Chen, "A cellular automaton-lattice Boltzmann method for modeling growth and settlement of the dendrites for Al-4.7% Cu solidification," *Computational Materials Science,* vol. 146, pp. 9-17, 2018.

[15] M. Asle Zaeem, H. Yin, and S. D. Felicelli, "Comparison of Cellular Automaton and Phase Field Models to Simulate Dendrite Growth in Hexagonal Crystals," *Journal of Materials Science & Technology,* vol. 28, pp. 137-146, 2012/02/01/ 2012.

[16] D. W. Oxtoby, "Homogeneous nucleation: theory and experiment," *Journal of Physics: Condensed Matter,* vol. 4, p. 7627, 1992.

[17] M. E. McKenzie and J. C. Mauro, "Hybrid Monte Carlo technique for modeling of crystal nucleation and application to lithium disilicate glass-ceramics," *Computational Materials Science,* vol. 149, pp. 202-207, 2018.

[18] J. R. Espinosa, C. Vega, C. Valeriani, and E. Sanz, "Seeding approach to crystal nucleation," *The Journal of Chemical Physics,* vol. 144, p. 034501, 2016.

[19] A. Jokisaari, C. Permann, and K. Thornton, "A nucleation algorithm for the coupled conserved–nonconserved phase field model," *Computational Materials Science,* vol. 112, pp. 128-138, 2016.

[20] Y. Lin, Y.-X. Liu, M.-S. Chen, M.-H. Huang, X. Ma, and Z.-L. Long, "Study of static recrystallization behavior in hot deformed Ni-based superalloy using cellular automaton model," *Materials & Design,* vol. 99, pp. 107-114, 2016.

[21] R. S. Aga, J. R. Morris, J. J. Hoyt, and M. Mendelev, "Quantitative parameter-free prediction of simulated crystal-nucleation times," *Physical review letters,* vol. 96, p. 245701, 2006.

[22] F. H. Streitz, J. N. Glosli, and M. V. Patel, "Beyond finite-size scaling in solidification simulations," *Physical review letters,* vol. 96, p. 225701, 2006.

[23] M. Descamps and J.-F. Willart, "Scaling laws and size effects for amorphous crystallization kinetics: Constraints imposed by nucleation and growth specificities," *International Journal of Pharmaceutics,* vol. 542, pp. 186-195, 2018/05/05/ 2018.

[24] T. Koishi, K. Yasuoka, and T. Ebisuzaki, "Large scale molecular dynamics simulation of nucleation in supercooled NaCl," *The Journal of chemical physics,* vol. 119, pp. 11298-11305, 2003.

[25] Y. Shibuta, S. Sakane, T. Takaki, and M. Ohno, "Submicrometer-scale molecular dynamics simulation of nucleation and solidification from undercooled melt: Linkage between empirical interpretation and atomistic nature," *Acta Materialia,* vol. 105, pp. 328-337, 2016.

[26] Y. Shibuta, S. Sakane, E. Miyoshi, S. Okita, T. Takaki, and M. Ohno, "Heterogeneity in homogeneous nucleation from billion-atom molecular dynamics simulation of solidification of pure metal," *Nature Communications,* vol. 8, p. 10, 2017/04/05 2017.

[27] B. O'malley and I. Snook, "Crystal nucleation in the hard sphere system," *Physical review letters,* vol. 90, p. 085702, 2003.

[28] J. Wedekind, D. Reguera, and R. Strey, "Finite-size effects in simulations of nucleation," *The Journal of chemical physics,* vol. 125, p. 214505, 2006.

[29] M. S. Watanabe, "Percolation with a periodic boundary condition: The effect of system size for crystallization in molecular dynamics," *Physical Review E,* vol. 51, p. 3945, 1995.

[30] L. Xiong, F. Guo, X. Wang, Q. Cao, D. Zhang, Y. Ren, *et al.*, "Structural evolution and dynamical properties of Al2Ag and Al2Cu liquids studied by experiments and ab initio molecular dynamics simulations," *Journal of Non-Crystalline Solids,* vol. 459, pp. 160-168, 2017.

[31] S. Sohn, Y. Jung, Y. Xie, C. Osuji, J. Schroers, and J. J. Cha, "Nanoscale size effects in crystallization of metallic glass nanorods," *Nature communications,* vol. 6, p. 8157, 2015.

[32] Y. Lü, X. Zhang, and M. Chen, "Size Effect on nucleation rate for homogeneous crystallization of nanoscale water film," *The Journal of Physical Chemistry B,* vol. 117, pp. 10241-10249, 2013.

[33] A. Statt, P. Virnau, and K. Binder, "Finite-size effects on liquid-solid phase coexistence and the estimation of crystal nucleation barriers," *Physical review letters,* vol. 114, p. 026101, 2015.

[34] M. Parrinello and A. Rahman, "Polymorphic transitions in single crystals: A new molecular dynamics method," *Journal of Applied physics,* vol. 52, pp. 7182-7190, 1981.

[35] S. Plimpton, "Fast parallel algorithms for short-range molecular dynamics," *Journal of computational physics,* vol. 117, pp. 1-19, 1995.

[36] A. Stukowski, "Visualization and analysis of atomistic simulation data with OVITO–the Open Visualization Tool," *Modelling and Simulation in Materials Science and Engineering,* vol. 18, p. 015012, 2009.

[37] H. Tsuzuki, P. S. Branicio, and J. P. Rino, "Structural characterization of deformed crystals by analysis of common atomic neighborhood," *Computer physics communications,* vol. 177, pp. 518-523, 2007.

[38] A. J. Cao and Y. G. Wei, "Formation of fivefold deformation twins in nanocrystalline face-centered-cubic copper based on molecular dynamics simulations," *Applied Physics Letters,* vol. 89, p. 041919, 2006/07/24 2006.

[39] A. Sutton and J. Chen, "Long-range finnis–sinclair potentials," *Philosophical Magazine Letters,* vol. 61, pp. 139-146, 1990.

[40] M. Finnis and J. Sinclair, "A simple empirical N-body potential for transition metals," *Philosophical Magazine A,* vol. 50, pp. 45-55, 1984.

[41] S. Foiles, M. Baskes, and M. S. Daw, "Embedded-atom-method functions for the fcc metals Cu, Ag, Au, Ni, Pd, Pt, and their alloys," *Physical review B,* vol. 33, p. 7983, 1986.

[42] E. Asadi, M. A. Zaeem, S. Nouranian, and M. I. Baskes, "Two-phase solid–liquid coexistence of Ni, Cu, and Al by molecular dynamics simulations using the modified embedded-atom method," *Acta Materialia,* vol. 86, pp. 169-181, 2015.

[43] E. Asadi, M. A. Zaeem, S. Nouranian, and M. I. Baskes, "Quantitative modeling of the equilibration of two-phase solid-liquid Fe by atomistic simulations on diffusive time scales," *Physical Review B,* vol. 91, p. 024105, 2015.

[44] E. Asadi and M. Asle Zaeem, "The anisotropy of hexagonal close-packed and liquid interface free energy using molecular dynamics simulations based on modified embedded-atom method," *Acta Materialia,* vol. 107, pp. 337-344, 2016/04/01/ 2016.

[45] X. Dai, Y. Kong, J. Li, and B. Liu, "Extended Finnis–Sinclair potential for bcc and fcc metals and alloys," *Journal of Physics: Condensed Matter,* vol. 18, p. 4527, 2006.

[46] M. S. Daw, S. M. Foiles, and M. I. Baskes, "The embedded-atom method: a review of theory and applications," *Materials Science Reports,* vol. 9, pp. 251-310, 1993.

[47] D. Y. Sun, M. I. Mendelev, C. A. Becker, K. Kudin, T. Haxhimali, M. Asta, *et al.*, "Crystal-melt interfacial free energies in hcp metals: A molecular dynamics study of Mg," *Physical Review B,* vol. 73, p. 024116, 01/31/ 2006.

[48] Y.-M. Kim, N. J. Kim, and B.-J. Lee, "Atomistic modeling of pure Mg and Mg–Al systems," *Calphad,* vol. 33, pp. 650-657, 2009.

[49] E. Asadi and M. A. Zaeem, "The anisotropy of hexagonal close-packed and liquid interface free energy using molecular dynamics simulations based on modified embedded-atom method," *Acta Materialia,* vol. 107, pp. 337-344, 2016.

[50] G. Simmons and H. Wang, "Single crystal elastic constants and calculated aggregate properties," 1971.

[51] W. F. Gale and T. C. Totemeier, *Smithells metals reference book*: Butterworth-Heinemann, 2003.

[52] A. M. James and M. P. Lord, *Macmillan's chemical and physical data*: Macmillan, 1992.

[53] J. G. Speight, *Lange's handbook of chemistry* vol. 1: McGraw-Hill New York, 2005.

[54] Q. Jiang and H. Lu, "Size dependent interface energy and its applications," *Surface Science Reports,* vol. 63, pp. 427-464, 2008.

[55] L. Gránásy, M. Tegze, and A. Ludwig, "Solid–liquid interfacial free energy," in *Rapidly Quenched Materials*, ed: Elsevier, 1991, pp. 577-580.

[56] M. Gündüz and J. Hunt, "The measurement of solid-liquid surface energies in the Al-Cu, Al-Si and Pb-Sn systems," *Acta Metallurgica,* vol. 33, pp. 1651-1672, 1985.

[57] M. S. Daw and M. I. Baskes, "Embedded-atom method: Derivation and application to impurities, surfaces, and other defects in metals," *Physical Review B,* vol. 29, p. 6443, 1984.

[58] R. Boehler, "Temperatures in the Earth's core from melting-point measurements of iron at high static pressures," *Nature,* vol. 363, p. 534, 1993.

[59] L. Swartzendruber, "Melting point of iron," *Journal of Phase Equilibria,* vol. 5, pp. 339-339, 1984.

[60] J. Liu, R. Davidchack, and H. Dong, "Molecular dynamics calculation of solid–liquid interfacial free energy and its anisotropy during iron solidification," *Computational Materials Science,* vol. 74, pp. 92-100, 2013.

[61] E. Brandes, "G. B (Editors), Smithells Metals Reference Book, Butter worth," ed: Heinemann, Oxford, 1992.

[62] D. Sun, M. Mendelev, C. Becker, K. Kudin, T. Haxhimali, M. Asta, *et al.*, "Crystal-melt interfacial free energies in hcp metals: A molecular dynamics study of Mg," *Physical Review B,* vol. 73, p. 024116, 2006.

[63] A. Mahata, M. A. Zaeem, and M. I. Baskes, "Understanding homogeneous nucleation in solidification of aluminum by molecular dynamics simulations," *Modelling and Simulation in Materials Science and Engineering,* vol. 26, p. 025007, 2018.

[64] Y. Shibuta, K. Oguchi, T. Takaki, and M. Ohno, "Homogeneous nucleation and microstructure evolution in million-atom molecular dynamics simulation," *Scientific Reports,* vol. 5, p. 13534, 08/27/online 2015.

[65] S. Nosé, "A molecular dynamics method for simulations in the canonical ensemble," *Molecular physics,* vol. 52, pp. 255-268, 1984.

[66] A. Di Cicco, A. Trapananti, S. Faggioni, and A. Filipponi, "Is there icosahedral ordering in liquid and undercooled metals?," *Physical review letters,* vol. 91, p. 135505, 2003.

[67] G. Kikugawa, S. Ando, J. Suzuki, Y. Naruke, T. Nakano, and T. Ohara, "Effect of the computational domain size and shape on the self-diffusion coefficient in a Lennard-Jones liquid," *The Journal of chemical physics,* vol. 142, p. 024503, 2015.

[68] I.-C. Yeh and G. Hummer, "System-size dependence of diffusion coefficients and viscosities from molecular dynamics simulations with periodic boundary conditions," *The Journal of Physical Chemistry B,* vol. 108, pp. 15873-15879, 2004.

[69] N. Volkov, M. Posysoev, and A. Shchekin, "The Effect of Simulation Cell Size on the Diffusion Coefficient of an Ionic Surfactant Aggregate," *Colloid Journal,* vol. 80, pp. 248-254, 2018.

[70] J. Wedekind and D. Reguera, "What is the best definition of a liquid cluster at the molecular scale?," *The Journal of chemical physics,* vol. 127, p. 154516, 2007.

[71] J. Wedekind and D. Reguera, "Kinetic reconstruction of the free-energy landscape," *The Journal of Physical Chemistry B,* vol. 112, pp. 11060-11063, 2008.

IV. EVIDENCE OF LIQUID ORDERING AND HETEROGENEITIES IN HOMOGENEOUS NUCLEATION DURING SOLIDIFICATION OF PURE METALS

Avik Mahata[a], Tanmoy Mukhopadhyay[b] and Mohsen Asle Zaeem[a,c]

[a] Department of Materials Science and Engineering, Missouri University of Science and Technology, Rolla, MO 65409, USA

[b] Department of Engineering Science, University of Oxford, Oxford, OX1 3PJ, UK

[c] Department of Mechanical Engineering, Colorado School of Mines, CO 80401, USA

ABSTRACT

Understanding the homogenous crystal nucleation process is of great fundamental importance in processing of many crystalline materials. It is prone to formation of defects and often experiences heterogeneities, and it has been debated in literature if the associated heterogeneities are an integrated part of the homogenous nucleation. By large-scale molecular dynamics (MD) simulations utilizing the most advanced interatomic potentials, we attempted to settle the debate over the sources of heterogeneities in homogenous nucleation during solidification of variety of metals, such as face-centered cubic Aluminum (Al), body-centered cubic Iron (Fe), and hexagonal close-packed Magnesium (Mg). An investigation based on an integrated probabilistic approach utilizing the MD simulation data shows the densification of the liquid metal, which results in various short range and medium range orderings of atoms prior to final crystallization process. Regardless of the element type or the solidified crystal structure, the presence of the short lived metastable phases during solidification attributes to the heterogeneities formed during homogenous nucleation.

1. INTRODUCTION

Crystal nucleation plays a major role in processing of materials and controlling their properties [1, 2]. The prediction and control of this nonequilibrium phenomena is necessary across various fields of materials science and technology. The nucleation pathways are classified as homogenous or heterogeneous nucleation, depending on how the process of solidification (liquid to solid transformation) gets affected by inherent homogeneities or foreign contaminants. In literature, the process of nucleation in materials has been argued over if the mechanism can be completely homogenous or has to be partly heterogeneous[3]. In principle the homogenous nucleation in metals can occur during the solidification of a single element without the influence of any other factors such as impurities (in other words, pure metal solidification). Homogeneous nucleation can be fairly described in the framework of classical nucleation theory (CNT). The experimental detection of a critical nucleus and study its possible heterogeneities are extremely difficult as the nucleation process starts at the interior part of the melt. Consequently, the study of formation of a crystal nucleus, specially is solidification of metals, is rarely observed under the microscope [4, 5]. This is why theoretical or computational tools such as CNT [6, 7], density function theory (DFT) calculations [8], MD [9, 10], Monte Carlo (MC) [11, 12], phase-field [13-15], and cellular automata [16] have been often used to study the nucleation process in solidification of metals.

The presence and influence of heterogeneity in homogenous nucleation is found to be suspected in literature. The work by Granasy et al. [17] showed a two-step method for homogenous nucleation for bcc crystals, first a dense amorphous precursor forms, and then

the crystalline phase appears via heterogeneous nucleation in/on the precursor cluster. MD simulations of nucleation of crystalline solids from metastable liquids have often produced results which are difficult to understand from the point of view of CNT. Utilizing a hard sphere model, MD simulations by Kawasaki et al. [18] showed a hidden ordering in a supercooled liquid suggesting an intimate link between crystallization and glass transition. They concluded that a supercooled liquid is intrinsically heterogeneous, and in other words the homogeneous nucleation may necessarily be heterogeneous. However, the study was limited to imaginary hard sphere solid-liquid instead of a realistic example of metallic elements.

Only one previous attempt was made to study heterogeneity in homogenous nucleation from a metallic melt of Fe by a billion atom MD simulation [19]. Finnis-Sinclair (FS) interatomic potential [20] was utilized for the simulations, predicts the melting point of Fe to be 2,400 K whereas the experimental melting point of Fe is ~1,811 K, and consequently results in inaccurate prediction of solid-liquid co-existence properties. It is worth to note that to study homogenous or heterogeneous nucleation it is not necessary to utilize such a large MD simulation, and several studies produced reliable and comparable results to experimental observations with only thousands to million atom MD simulations [18, 21]. In fact our recent study suggests the influence of the simulation size diminishes when a model size is larger than approximately 1 million[22]. It is also worth to note that a MD simulation using the less accurate FS potential utilizes orders of magnitudes less computational power compared to a case utilizing a more accurate interatomic potential, such as the Modified Embedded Atom Method (MEAM) potential. However, the primary goal of scientific research should be accuracy rather than efficiency.

In this work, we aim to provide comprehensive insights on the homogenous nucleation process of crystalline pure metals with fcc (Al), bcc (Fe) and hcp (Mg) structures utilizing the most advanced interatomic potentials for metals, second nearest neighbor MEAM (2NN-MEAM) [23, 24], to accurately predict the homogenous-heterogeneous nucleation phenomena during solidification of pure metals. The interatomic potentials utilized in this work has been fully investigated for their low, high temperature and solid-liquid coexistence properties and shows promising similarity with experimental results[23-25]. Common neighbor analysis (CNA) method[26] and bond order parameters[27] would be used to determine the structures of the solid and metastable phases in the super cooled liquid metals during solidification. The probability distribution of the density over the bond order parameter and density is also studied to capture the underlying heterogeneities in homogenous nucleation of pure metals. This work reveals the inherent heterogeneities during the homogenous nucleation of pure metals in a probabilistic framework generically considering different crystal structures.

2. RESULTS

The nucleation process differs for different crystalline metals as shown in Figure 1. The Al and Mg nuclei generally form twin boundaries (Figure 1b and 1h). A twin boundary creates a misorientation angle inside the nucleus, which is the preliminary observation of heterogeneity in the homogenous nucleation. The twinning has a different crystal structures than the actual crystal structure of the metallic system. So, two different solidification phases cause the heterogeneity in homogenous nucleation. The twin boundaries grow within with the fcc or hcp matrix until the solidification process is complete. Unlike a

metastable precursor which transform to one of crystalline structures or deposit in the grain boundaries, the twinning exists during the entire nucleation and solidification process. As suggested in previous literature[28] Fe has a different path to its nucleation where the stable bcc phase appears via metastable icosahedral (ico) coordination (Figure 1(d-f)). Bcc atoms forms along with the ico atoms, and some of the ico atoms transformed to bcc, however major bcc formation happens from short range ordered (SRO) atoms. It will be discussed later in the article. However, the major differences from Al and Mg is the absence of a second solid phase twin boundaries.

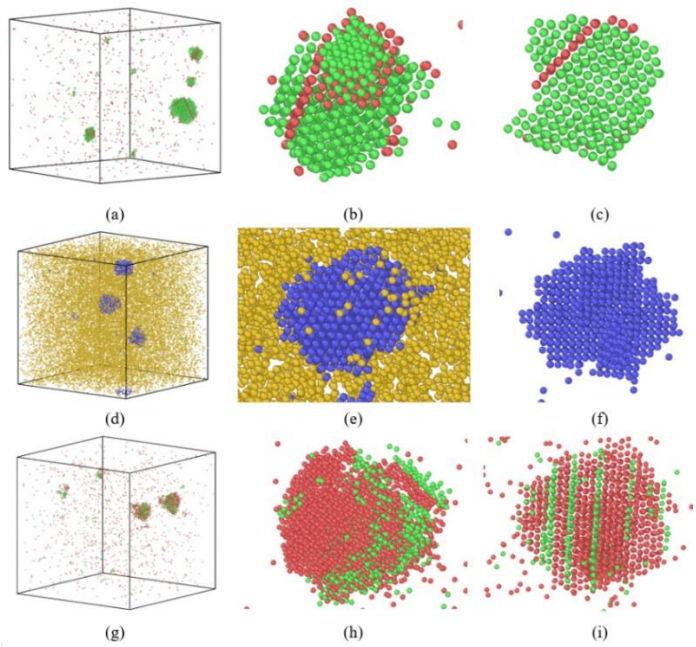

Figure 1**.** The homogenous nucleation of supercooled (a-c) Al at 500 K, (d-f) Fe at 1100 K and (g-i) Mg at 550 K. The green atoms are fcc, red atoms are hcp, blue atoms are bcc and yellow atoms are icosahedral structure. The amorphous atoms are removed from the box for better visualization of the crystalline atoms. Common neighbor analysis method is applied for coloring the atoms.

From the thermodynamics point of view the transformation of a molecular (atomic for our case) liquid into a molecular crystal in homogenous nucleation is a first-order phase transition. In the absence of a foreign surface or particle to promote heterogeneous nucleation, this phase transition begins with the spontaneous nucleation of the crystalline phase into small aggregates which, if they reach a critical size, form the seeds for the new phase. But as we see from Figure 1, the single crystal phases always get trap with a different crystalline phase inside a region of a metastable crystalline or glassy states. 2NN MEAM predicts the structural energy difference between bcc-Fe and fcc is 0.044 eV/atom[25] and bcc to hcp transformation energy is negative. In case of fcc-Al the structure energy difference between fcc and hcp are 0.03 eV/atom[24] and in hcp-Mg the difference in hcp to fcc is 0.008 eV/atom[23]. The higher structural energy difference between bcc-Fe and other crystal structures, suggests its very unlikely to observe a second solid phase twins in Fe during solidification. For Al and Mg, due to very little difference in energy between fcc and hcp atoms, they form both crystalline phases. One phase (fcc for Al and hcp for Mg) is the primary phase, the other phase remains present inside the crystalline phase as a stacking fault mediated twinning defect.

Heterogeneity is observed as a stacking fault in Al and Mg just by visual inspection by using CNA method in Figure 1, however the heterogenous nucleation also happen without twins or grain boundaries also. The twin boundaries act as a barrier between two different nuclei. As shown in Figure 2 (a) there are multiple nuclei formation happens simultaneously and this process of nucleation involves both homogenous and heterogenous nucleation. The primary fcc crystal structure has been identified by common neighbor analysis. These fcc atoms are always align along the coordination axes (i.e. x', y', z').

These coordination axes are not always aligned with the principle axes system (i.e. x, y, z) of simulation box. The orientation coloring shows, orientation of the grains from the principle axes. For the coloring purposes, we only considered the orientation from the principle Z axis. The coloring scheme is applied in Ovito, and the details can be found Larsen et. al. [29]. In Figure 2b heterogenous nucleation by both twin boundary formation and embryo formation are shown. The twin formation starts at 96 ps has a higher angle of misorientation than the fcc Al matrix. As both sides of the twin boundary are fcc they have the same orientation angle but they have a relative misorientation with each other as shown in Figure 2c.

We can also observe heterogenous nucleation by capturing the embryo formation on top of the previously formed crystalline Al. In CNA method both the preexisting nuclei and the newly formed embryo will be detected as fcc so the difference between the nuclei and the embryo can be detected by the orientation coloring. The previously formed solid nuclei in this cases can be considered as the foreign particle relative to the newly formed nuclei. The process continues beyond one heterogeneous nucleus. As shown in Figure 2b at 138 ps there are 8 different orientation for the atoms, so it forms 7 different embryos from the liquid Al. At the same time we also has the heterogeneity from the twin formation, which adds one more embryo to the cluster of nuclei.

The heterogeneity in Mg is similar to Al, and both twinning and embryo formation is observed during the nucleation process. Figure 3a shows the simultaneous homo and heterogeneous nucleation in the entire simulation box. The step by step heterogeneous nucleation by formation of embryo on the solid nucleus is shown in Figure 3b. The

heterogeneity from twin formation is also shown in Figure 3c. Along with the twins there are also different orientation of atoms align successively.

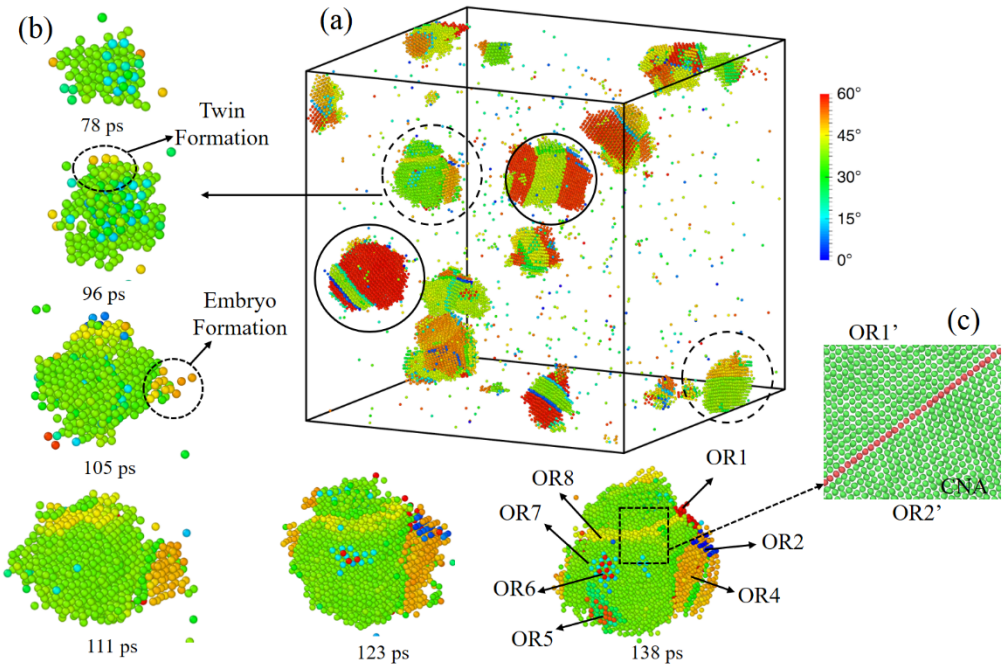

Figure 2. Snapshots showing the atomic configuration at an intermediate stages of nuclei formation. (a) The complete simulation box with multple nuclei formation. The solid circles show homogenous nculeation with twin boundaries, the dotted circles show heterogeneous nucleation during the process of homogenous nucleation. (b) The steps of heterogenous nculeation, both twin boundary changes the relative orientaion of the atoms and embryo formation on previously formed solid nuclei is shwon. OR represenation orienatation along the simulation box axes. OR' represents the orientation with respect to the coordination axes.

In the initial stages of the nucleation there might be more than two different orientation as shown in Figure 2c at 180 ps. Only two of the configuration finally become critical and remain in the solid form, rest either dissolve back to the liquid or reorient according to the existing solid nuclei. At 234 ps both the stacking fault and orientation

coloring is shown (Figure 3c). Orientation coloring is clearly a better method of detecting the heterogeneity as the CNA only detects one twinning where are there is a difference in their absolute orientation in each layer of atoms.

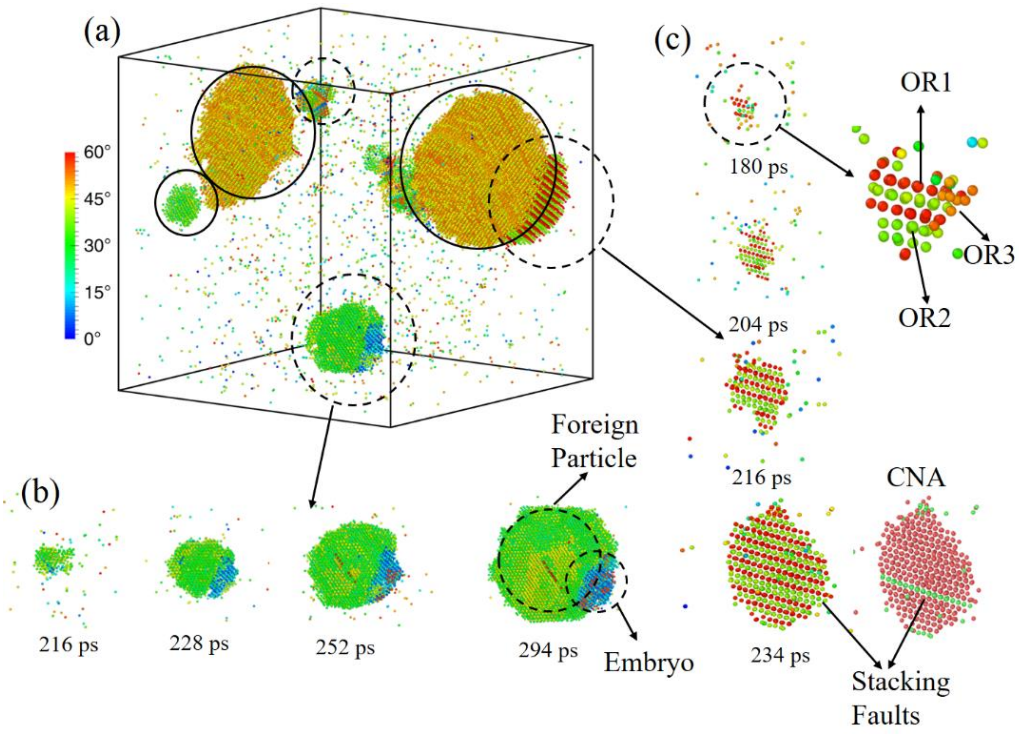

Figure 3. Snapshots showing the atomic configuration at an intermediate stages of nuclei formation in liquid-Mg. (a) The complete simulation box with multple nuclei formation by orientation coloring. The solid circles show homogenous nculeation with twin boundaries, the dotted circles show heterogeneous nucleation during the process of homogenous nucleation. (b) The steps of heterogenous nculeation is shown for embryo formation on prexisting solid Mg nucleus. (c) Heterogenity from twinning formation is shown for both orientational coloring and CNA.

As mentioned before unlike the Al and Mg, Fe doesn't produce twins with any other crystalline form. The twin investigation in Fe needs careful investigation with orientation of the atoms to find the twins. As shown in Figure 4a, formation of several nuclei, and among them there are both twin boundaries (Figure 4b) and heterogeneous nucleation by embryo formation on the foreign particle (Figure 4c). The heterogeneity in Fe originates as early as the critical nuclei formation. The foreign particle is a bcc Fe nucleus that forms earlier than the embryo and has a different orientation. In case of heterogeneous nucleation by formation of embryo after the initial foreign nuclei gets critical. As suggested before [28], the pathway for the heterogeneity in homogenous nucleation is the satellite nuclei (grain) get attached to the larger nuclei. As shown in Figure 4c, this not a necessary criteria or this criteria comes much later stages of the nucleation. The local heterogeneity can originate form crystallization of liquid or short range ordered atoms on top of a previously formed nucleus.

The spontaneous formation of heterogeneous nuclei formation can be attributed to the use of highly accurate 2NN meam interatomic potential developed and verified in our group[23-25]. The heterogeneity in homogenous nucleation is expected to be an atomic scale phenomena which should originate in the earlier stages of solidification. As it is shown for both Al and Mg that the heterogeneity starts along with formation of the critical nuclei, Fe is no exception. In case of Al and Mg the heterogeneity during the twin formation becomes a part of the initial nuclei formation. The nature of heterogeneity emphasize the fact that heterogeneity in homogenous nucleation is also a part of Fe and it starts as early formation of the critical nuclei formation.

It should be noted that in nucleation from pure elements there is no difference between a crystal nucleus and a grain. In case of Fe, if the crystal nuclei grow large, it encounters other crystalline nuclei and form grain boundaries (GBs). So, if we consider the orientation of the different grains in the semi-solid simulation box, it can be found that they have heterogeneity based on the orientation of the grains.

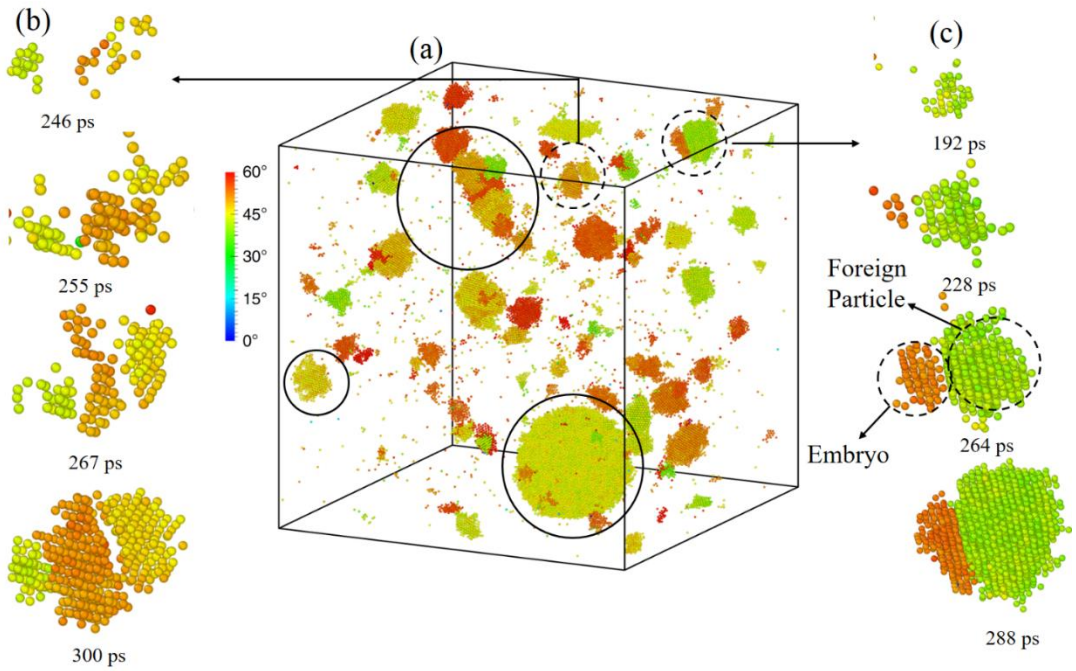

Figure 4. Snapshots showing the atomic configuration at the initial stages of nculei formation. (a) the entire simulation box with multiple critical nculei. The solid circles show homogenous nculeation with twin boundaries, the dotted circles show heterogeneous nucleation during the process of homogenous nucleation. (b) steps of twin boundary formation in liquid Fe, (c) The heterogeneous nucleation by formation of embryo on preexisting solid nucleus.

Because the grains have different orientations, it is obvious that different critical nuclei also have different orientations during the solidification. This difference in the

orientation also gives rise to the heterogeneity in homogenous nucleation. The similar phenomenon also happens to Al and Mg, but for Al and Mg the twin boundary (TB) also initiate the heterogeneity during the formation and growth of the critical nuclei.

As TBs and GBs both form during the solidification process we can apply the Young's relation [30] for heterogeneous nucleation and study how TBs and GBs influence the free energy. The change in free energy will indicate that the homogenous nucleation is influenced by any heterogeneity or not. The wetting angle θ for heterogeneous nucleation involving GBs and TBs can be approximated by Eqn. 1. The wetting angle in solid-liquid phase change can be expressed in terms of the misorientation angle between the fcc crystalline grain in both side of the TBs. Then the Young's relation[31] for the case of solidification is below,

$$\cos\theta = 1 - \frac{\sigma_{GB}}{\sigma_{SL}} \tag{1}$$

Where σ_{GB} is the grain boundary energy and σ_{SL} is the solid liquid interface energy. We can also consider σ_{TB}, which is the twin boundary energy for the heterogeneity. Now if the change in free energy in homogenous and heterogenous nucleation are ΔG_{Homo} and ΔG_{Hetero} respectively, then the change in free energy of crystal nucleation in general can be approximated by Eqn. 2,

$$\Delta G_{Hetero} = f(\theta)\Delta G_{Homo} = \frac{(1-\cos\theta)^2(2+\cos\theta)}{4}\Delta G_{Homo} \tag{2}$$

If $f(\theta)$ is less than 1 then there is heterogeneity in homogenous nucleation. The solid-liquid interface free energy is provided in Table 1 for Al, Fe and Mg. The solid-liquid

interfacial free energy for Al is 0.17 J.m^{-2} (Table 1), and the TB/GB interface free energy for Al is ~0.23-030 J.m^{-2} [32] (for $\sum 3(111)$ coherent GB/TB structure). The TB/GB interface free energy values have been taken for misorienatation angle of ~120^0. Then we get $f(\theta) = 0.61 - 0.90$ from Eqn. 2. As a result the free energy for heterogeneous nucleation is lower than that of the homogenous nucleation in Al. For Fe, the TB/GB free energy is ~0.3 J.m^{-2} (for $\sum 3(111)$ coherent GB/TB structure) [33], and the solid-liquid interfacial free energy is 0.188 J.m^{-2} (Table 1). These values give the wetting angle of 127^0 and $f(\theta)$ = 0.89 for Fe. For Mg, the solid-liquid interfacial free energy is ~0.122 J.m^{-2} (Table 1) and the GB energy is 0.114 J.m^{-2} [34, 35] , therefore the wetting angle is calculated to be ~105^0, and $f(\theta)$ = 0.65-0.80, which also results in drop in required free energy for nucleation. In case of Mg the GB energies are not relevant as the heterogeneity mostly occurs from the stacking faults or embryo formation. The calculated $f(\theta)$ values for all these pure elements indicate that the free energy of nucleation goes down during the formation of crystalline nuclei, and it indicates possible heterogeneities in homogenous nucleation.

It was hypothesize that the ico atoms are precursor of the bcc crystalline Fe atoms and the bcc nuclei are more probable to form where the ico has a higher density[28]. If we consider the complete solidification simulation, as shown in Figure 5, the ico atoms goes down when the bcc atoms increase at time beyond 300 ps. The hypothesis is right for a small amount of Fe cryustallization in the beginning of the solidification, howebver in the total simulation this can said that ico and bcc Fe are not completely interrelated.

Table 1. The solid-liquid interface free energy, grain and twin boundary energy of Al, Fe and Mg.

Elements	$\sigma_{SL}(J.m^{-2})$	$\sigma_{GB}(J.m^{-2})$	$\sigma_{TB}(J.m^{-2})$	$f(\theta)$
Al	0.17 [24]	0.25-0.3 [36, 37], 0.23 (427K) [38]	0.08-0.20 [39, 40]	0.61-0.90
Fe	0.19 [25]	0.30 [41]	0.16 [42], 0.135 [43]	0.89, 0.29-0.38
Mg	0.12 [23]	-	0.14±0.05[44]	0.65-0.81

So, apparently, it might be mistaken that the ico atoms are bcc precursor. But just by comparing the maximum number of ico atoms which is only ~5% at any moment of the simulation, whereas the number of bcc atoms can reach as much as 70-80% or more depending on the undercooling temperature. Number of ico atoms in the simulation box can be also influenced by the amount of cut off use to identify them or the algorithm used for identification (See Supplementary information). Number of ico atoms will also be impacted by the accuracy of the interatomic potentials as well.

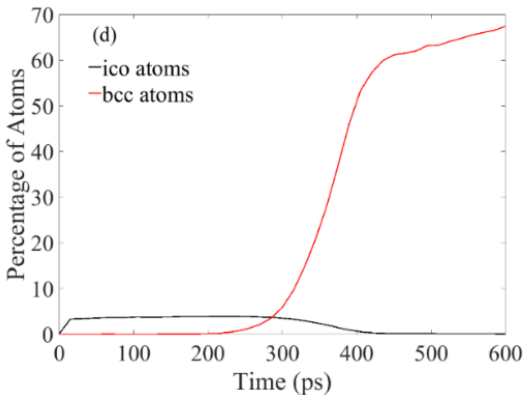

Figure 5. Time evolution of bcc and ico atoms in nucleation of Fe at 1100 K isothermal solidfication simulation.

In Figure 6 we study the how actually Fe atoms are forming in the undercooled Fe-liquid. As shown in Figure 6a in the initial statges of the nculeation (~200-250 ps) both ico and bcc atoms increases in the system. So as we looked into the detailed structure of the undercooled Fe (Figure 6b-d), it is not necessary to have a dense ico atoms for the origination of bcc Fe. In bond order parameters we assume the atoms having $0.3< Q_6 <0.45$ having short range order (SRO). Instead of the ico atoms, there are a large number of short range order (solid or liquid) atoms remain in the system before bcc atoms forms. The density of the SRO atoms increases in the areas where the bcc-Fe nuclei forms and vice versa.

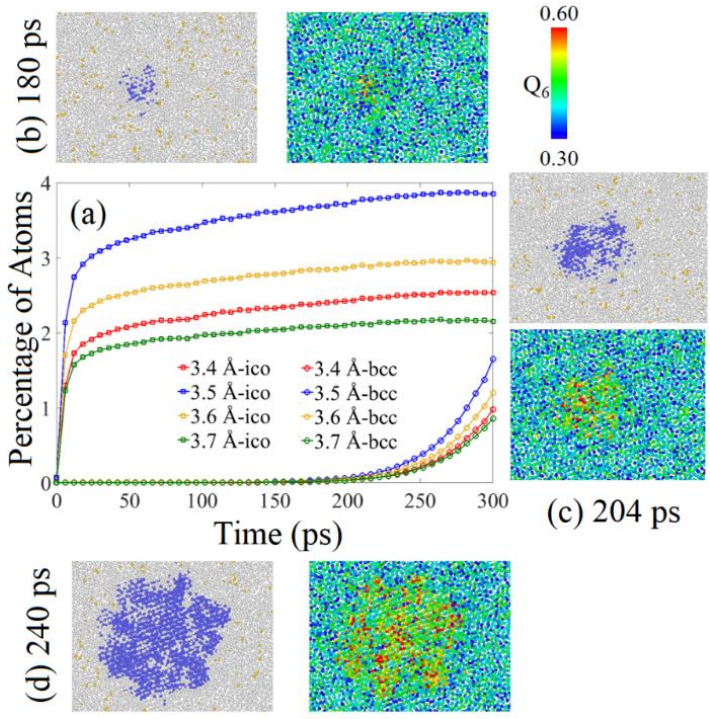

Figure 6. (a) Bcc and ico Fe atoms during the initial critical nuclei formation, The CNA and the bond orientational order parameters at (b) 180 ps, (c) 204 ps and (d)240 ps. In CNA the white atoms are liquid/amorphous solid, blue atoms are bcc and yellow atoms are ico. Bond order coloring is shown in the color bar.

To estimate the different phases in the isothermally solidified Al, Fe and Mg, the bond orientational order parameters have been studied. To characterize the different structural order we took the density and Q_6 (see *Materials and Methods below*) parameter plot to specify the local symmetry. Both Q_4 and Q_6 can indicate the order in a system, but without thermal noises the Q_4 parameter for ico is 0, so we utilized the Q_6 parameter for our analysis as it has a positive values for all the crystalline materials. The Q_6 and density (ρ) have been studied during all the solidifications. For the analysis purpose ~5000 atoms are chosen around the first critical nuclei and have been analyzed for the different time steps during the solidification as shown in Figure 7.

Now we analyze the probability density function of the density of pure Al at 500 K isothermal solidification over the range of Q_6. The probability density of density will be referred to as $P(\rho)$. As shown in Figure 4(b) the initial area under the red dotted square for $Q_6 < 0.3$, is the atoms remains in liquid or short range order (SRO) for Al. Then the region $0.3 < Q_6 < 0.45$ in case of Al (Figure 7a) it's a mix of medium range order (MRO) and SRO. Anything above the $Q_6 > 0.45$ is considered to be crystalline fcc or hcp. The peak of the $P(\rho)$ remains within the same range but the range over Q_6 increases from short to medium range (Figure 7b). Finally when the SRO and MRO becomes crystalline fcc and hcp the range over Q_6 is narrow but the peak in probability density is much higher than its for SRO and MRO. This signifies that most atoms have been converted to fcc and hcp. For Fe (Figure 7d) and Mg (Figure 7f) the values for Q_6 changes but three different regions can be identified.

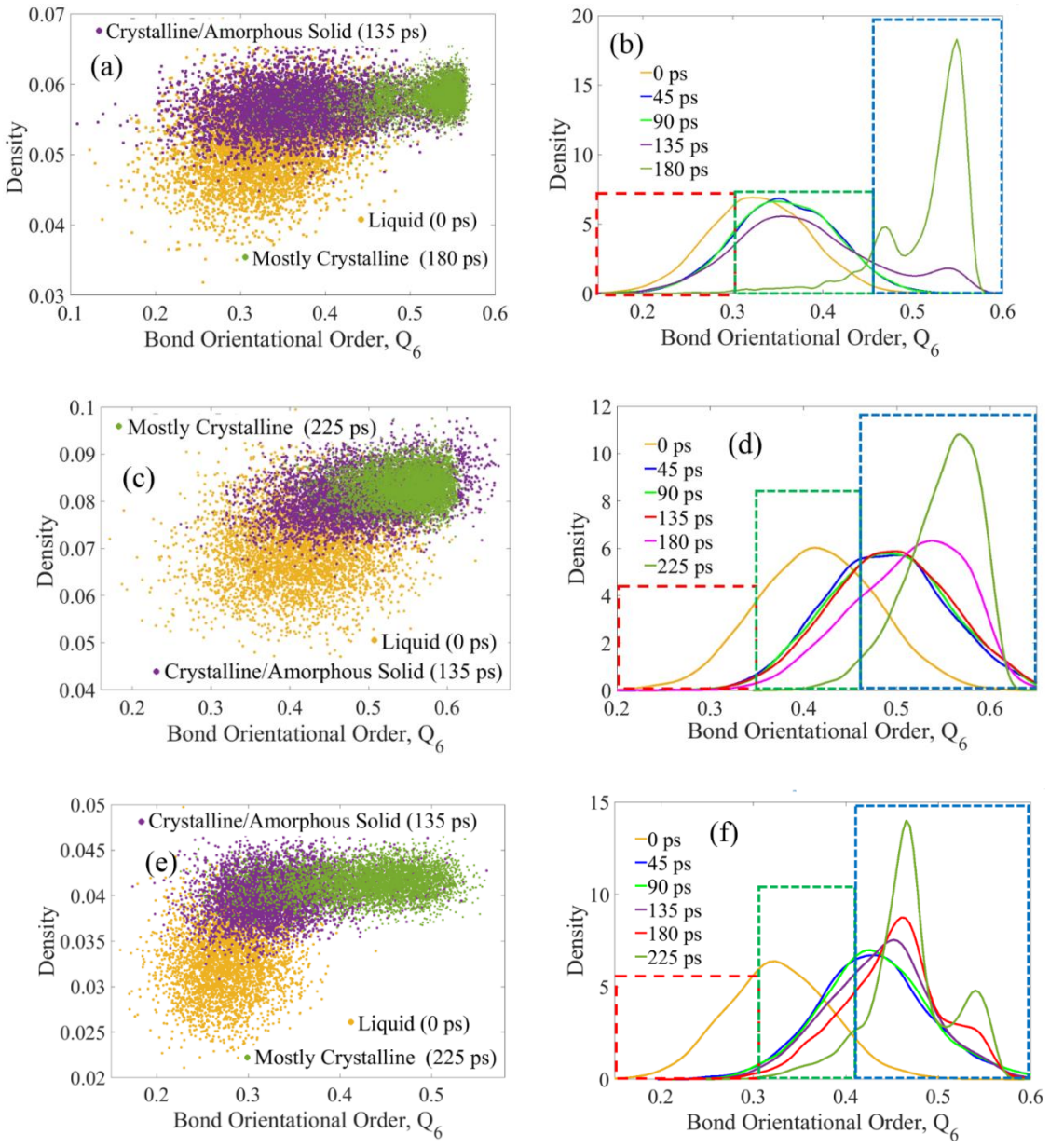

Figure 7**.** The respective density (ρ) vs the bond order parameters are plotted for (a) Al at 500 K, (c) Fe 1100 K and (e) Mg 550 K for the same probability distribution function. The probability density function of density $P(\rho)$ with respect to bond orientation order parameter Q_6 for (b) Al at 500 K, (d) Fe at 1100 K and (f) Mg at 550 K. The dotted red area shows the SRO atoms, the green area indicates the MRO and the blue area indicates crystalline atoms.

So overall the process of solidification by nucleation process is referred as two-step crystallization: the first step involves the formation of dense liquid/solid regions, and the second step is the nucleation of the crystal phase inside these dense regions. This is hard to differentiate between exactly the solid of liquid region by any method. But the atoms referred to as SRO in the beginning of the solidification can be considered as liquid and later stages of solidification those SRO are glassy solid.

As shown in (Figure 7a, c, e) we can clearly observe a two-step process of crystallization as the super saturated liquid first forms a dense metastable phase which contain several short range and medium range ordered atoms, then the crystallization starts. The two-step mechanism is thus not strictly due to critical fluctuations of thermodynamics quantities, rather due to the formation of a dense liquid/solid phase that is thermodynamically stabilized below the critical point. Away from the metastable critical point, the system was found to crystallize classically in one step, where densification and structural ordering happen simultaneously. However, overall the bond order parameters can indicate that the crystallization in single crystal metallic system is accompanied by several other SRO and MRO phases which initiate the nucleation phenomena. This is how we get a clear evidence of existence of heterogeneity in homogenous nucleation from the bond order parameter analysis.

In the perspective of the solidification, we can also look into the details of whether the nuclei appear in dense-precursors or in bond orientational-ordered precursors. A very recent analysis of the simulation trajectories of ("density first" case) showed a simultaneous increase of density and bond-orientational order leading up to nucleation [45]. In the case of homogenous nucleation of the metallic system, we define the Landau

free energy by taking joint probability of Q_6 and density(ρ) such as, $F(Q_6) = -k_B T \log P(Q_6, \rho)$ [46, 47]. Figure 8 represents the joint probability plot of Q_6 and ρ. It displays a good decoupling between $P(Q_6)$ and $P(\rho)$, expressing the fact that Q_6 and ρ capture independently the fluctuations in bond orientational order and density. We assume a cubic fit to the free energy that shows that the dominant cubic term is of the form $Q_6\rho^2$ for possible free energy functional. The similar function had been used for studying the comparison of bond order and density[47, 48]. Because the interaction is quadratic in ρ and linear in Q_6, the system can increase its orientational order without increasing the translational order, but the contrary is not true. This constrains the fluctuations towards a stronger increase in its orientational order. The analysis also shows a weak linear coupling between ρ^2 and Q_6, from the lower values of correlation coefficient (~0.20). This linear term also indicates that regions of high orientational order will, on average, have also higher density than the melt. As we observed in Figure 8, there is a (weak) linear coupling between bond-orientational order and density which ensures that fluctuations toward high bond-orientational order will on average lead to a higher density than the melt. This also means, as found in Berryman et al. [49], that following crystal nucleation in time will lead to a simultaneous increase of density and bond orientational order.

Overall in the context of the heterogeneity in homogenous nucleation this can be claimed that the order appears at a very early stages of the solidification as both density and order parameter increases. Initially it can be called an amorphous SRO or MRO. SRO and MRO can be also compared with glassy structures. The long range crystalline order

appears from the random fluctuations of the glassy structure in a highly dense environment. As shown in Figure 8a in the initial liquid structure the atoms are having both low $P(Q_6)$ and $P(\rho)$.

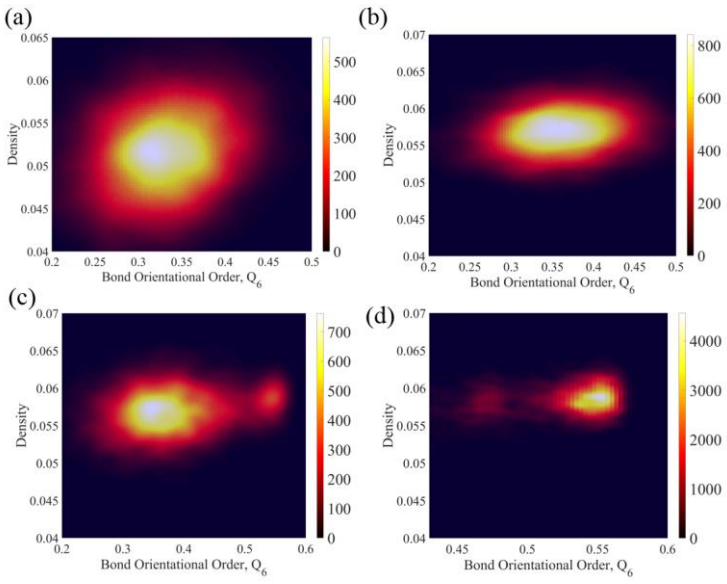

Figure 8. Landau free energy is shown from the joint probability $P(Q_6, \rho)$. The density vs bond orientational order parameter joint probability plot for Al at 500 K at (a) 0 ps, (b) 90 ps, (c) 135 ps and (d) 180 ps.

As the simulation box of Al at 500 K is solidified at a constant temperature the atoms move towards a higher density region but as shown in Figure 8b, Q_6 doesn't change significantly but $P(\rho)$ increases monotonically. The number of atoms having higher $P(Q_6)$ also increases as shown in the color bar. At this intermediate stage the SRO and MRO appears (Figure 8b). The SRO and MRO can be designated as part of the heterogeneity in homogenous nucleation. This heterogeneity exists while the crystalline

atoms form. As the solidification continues the atoms eventually branch out towards the crystalline region and the joint probability moves towards the higher Q_6 at a constant ρ (Figure 8(c-d)). The steps of solidifications are also similar for Fe and Mg (see Figure S1, S2) at different temperatures.

3. DISCUSSION

In summary, the homogenous nucleation during solidification from undercooled Al, Fe and Mg is studied by utilizing 2NN MEAM interatomic potential in MD simulation. In the process of studying nucleation it was also shown that million atoms MD simulation is optimum to study homogenous nucleation when the interatomic potential predicts the experimental high temperature and solid-liquid interface properties. MD simulation of homogenous nucleation predicts the bcc in Fe, fcc in Al and hcp in Mg melt nucleation. Al and Mg always nucleate with stacking faults and twin boundaries.

The TB and GB acts as a catalyst to the nucleation process, as different orientation of the neighboring nuclei creates a wetting angle and as a result in reducing the free energy of the nucleation. There are also clear evidence of purely heterogeneous nucleation during the homogenous nucleation process, when an embryo forms on top of a previously existing solid nuclei. The heterogeneities were further explored by using bond order parameters for the short range ordering. Bond order parameter shows the intermediate non-crystalline solid phases, which remains as a heterogeneity in homogenous nucleation for Al, Fe, Mg. The ico atoms are not the precursor of the bcc-Fe, rather than the SRO are responsible for forming the initial bcc-nuclei. The similar pathways can be also considered for fcc-Al and

hcp-Mg. Al and Mg doesn't have a precursor like ico. But all the fcc or hcp atoms form from the random movement of the SRO atoms at a undercooled temperature. Overall the sequence of crystallization from melt can be described as: (i) initial homogeneous equilibrium liquid, (ii) A mix of intermediate supercooled liquid with bond orientation order and intermediate semi-ordered phase (crystalline and non-crystalline solids), (iii) final crystalline phase.

The probability density function of bond order parameter $P(Q_6)$ indicates short and medium range order when plotted against the density. The joint probability distribution of order parameter and density shows a weak linear coupling as the correlation coefficient remains in a low range (~0.2). The joint probability also represents the Landau free energy functional and the joint probability $P(Q_6, \rho)$ is assumed to be $Q_6\rho^2$. The interaction is quadratic in ρ and linear in Q_6 so the system can increase its orientational order without increasing the translational order. This constrains the fluctuations towards a stronger increase in its orientational order. And this results into large number of SRO and MRO atoms.

Our findings confirm the heterogeneity in homogenous nucleation during solidification, which has been suspected before. A supercooled liquid at an isothermal temperature is intrinsically heterogeneous as the instant change in temperature creates solids with or without crystalline structures. The heterogeneous phases doesn't always accelerate or decelerate the homogenous nucleation, but the coexistence of different metastable phases are very obvious.

4. METHODS

The predicted melting point of Al using a 2NN MEAM MD simulation is 925 K [24], which is in a very good agreement with the experimental value of 934 K. We found that at a temperature close to the melt temperature, the liquid has a fluctuating number of fcc atoms. the interatomic potentials also predict the melting point for Fe 1811 K [50] and Mg 924 K[51]. We found that at a temperature close to the melt temperature, the liquid has a fluctuating number of fcc atoms. We wanted to start the nucleation simulations with a pure liquid having no solid regions. In order to find the temperature at which a completely melted simulation box with no fcc crystal can be achieved in a relatively short simulation time (~150 ps), several simulations were performed by increasing the temperature of the simulation box higher than 925 K using 25 K intervals. After 16 intervals, when the temperature reached 1,325 K, we could obtain a completely melted simulation box in ~150 ps. The simulation is continued to 300 ps to make sure the initial melt is properly equilibrated. The CNA of the simulation box for very large time scale is provided in Figure S1(a). The percentage of amorphous liquid atoms keeps increasing with increasing the annealing temperature. Finally, the box had no crystalline atoms at 1,325 K. The radial distribution function (RDF, g(r)) of the simulation box was calculated for all the temperatures, which is plotted in Figure 1(b). There are no long-range peaks at 1,325 K. The CNA analysis and RDF plots confirmed that Al was completely melted at 1,325 K. We repeat the same procedure for Fe and Mg. To create a completely liquid simulation box Fe and Mg have been equilibrated for 300 ps at 3500 K and 1250 K respectively.

MD simulations of homogenous nucleation from pure Al, Fe and Mg melt were performed in a simulation box with size of 25, 23 and 29 nm^3 respectively. The details of the simulations has been provided in Table S1. We apply isothermal-isobaric (NPT) ensemble and time step of 3 for all simulations. Temperature and pressure were controlled by Nose-Hoover thermostat and Parrinello-Rahman barostat [52] respectively. Periodic boundary conditions were employed in all three directions. All the MD simulations were performed in LAMMPS [53]. Generally the nucleation occurs as low as 300 K for both Al and Mg. In case of Fe the nucleation doesn't occur below 800 K. However at the lower temperature due to the lower kinetic energies of the atoms the nucleation rate decrease and the nuclei get smaller. Similarly, at higher temperature such as above $0.7T_m$ (melting temperature) the kinetic energy of the atoms are too high to form stable crystalline structure. So we chose the optimum temperature range of 200-300 K when the nuclei size and nucleation rates are stable. The simulation box has been solidified isothermally with 50 K steps. The number of simulation runs performed were 5, 7 and 4 for Al, Fe and Mg respectively. Then each temperature runs were replicated 5 times, so overall 80 simulations performed isothermally. Each isothermal simulation was repeated five times to evaluate the possible errors. Each isothermal simulation was run for a total of 3000 ps (1 million time steps) to simulate the crystal nucleation and solidification. The details of all the simulations have been provided in Supplementary information in Table S1.

The second nearest neighbor modified embedded-atom method (2NN-MEAM) [54, 55] was introduced to include the directionality of bonding in covalent materials in the EAM formalism, as a result the 2NN MEAM potential predict more accurate results and almost overlap the experimentally determined high temperature properties. The second

nearest neighbor modified embedded atom method (2NN MEAM) interatomic potential of Al developed by Lee and Baskes [54] was used is this work to study solidification of Al, Fe and Mg by MD simulation. We recently tested this 2NN MEAM interatomic potential for Al and Mg [23, 24] and modified the potential for Fe [25] for both low and high temperature properties. The results provided in Table S2. (Supplementary information) show accurate prediction of solid-liquid coexistence properties (i.e. melting point, solid-liquid energy, melting point, specific heat etc.) of Al, Fe and Mg. As the results shown in Table S2, suggests the 2NN-MEAM potential predict good high temperature properties, it can be used for solidification studies.

CNA was used to distinguish part of the crystal from those that belong to the liquid. But CNA only detects the purely fcc/bcc or hcp crystalline phases, but not very effective for detecting the intermediate crystal structures. So, we apply average local bond order parameter to analyze the structure of the nuclei. CNA needs a reference frame such as 12 neighbors for fcc/hcp and 8 neighbor for bcc.

Averaged local bond order parameters however independent of the specific crystal structure and does not require the definition of a reference frame, is provided by the following algorithm based on spherical harmonics [27, 56]. The complex vector $q_{lm}(i)$ of particle i can be defined as below Eqn. (7),

$$Q_{lm}(i) = \frac{1}{N_b(i)} \sum_{j=1}^{N_b(i)} Y_{lm}(r_{ij}) \tag{3}$$

Here, $N_b(i)$ is the number of nearest neighbors around an atom i, l is a free integer parameter, m is also an integer that runs through $m = -l$ to $m = +l$. The function $Y_{lm}(r_{ij})$ are

the spherical harmonics and r_{ij} is the vector from particle i to j. Using the complex vector q_{6m} we can define the scalar product like below Eqn. (8),

$$S_{ij} = \sum_{m=-6}^{6} Q_{6m} Q_{6m}^{*}(j) \tag{4}$$

Eqn. (8) measures the correlation between the surrounding atoms i and j, the * represents the complex conjugate. An atom in the simulation box is solidlike if the number of connections it has with its neighbors is above a certain threshold, typically close to 8 or 12 for our case. If an atom is connected to number of atoms close to 8 or 12, it is considered to be solidlike. If the particle is connected to less number of particle then it will be considered as liquidlike. Using this criterion to distinguish solidlike from liquidlike particles one can then search for clusters of connected solidlike particles.

This procedure is very efficient distinguishing soli-liquidlike atoms but unlike CNA it doesn't actually determine the crystal structures. A set of parameters holds the information of local structures is called the bond order parameters defined below in Eqn. (5),

$$Q_l(i) = \sqrt{\frac{4\pi}{2l+1} \sum_{m=-l}^{l} \left| Q_{lm}(i) \right|^2} \tag{5}$$

Depending on the choice of l, bond order parameters give different values as the sensitivity of the parameters differs for different crystal symmetries. Different approaches based on these local bond order parameters were developed to analyze the structure of the crystalline nucleus during the freezing event. Especially Q_4 and Q_6 are often used as they are a good choice to distinguish between cubic and hexagonal structures [18, 57]. It is to be noted that at the zero temperature (without thermal noises) the simple cubic lattice has

$(Q_4, Q_6)_{sc} = (0.764, 0.354)$, the body-centered cubic lattice has $(Q_4, Q_6)_{bcc} = (0.036, 0.511)$, the fcc has $(Q_4, Q_6)_{fcc} = (0.191, 0.574)$, the hcp has $(Q_4, Q_6)_{hcp} = (0.097, 0.485)$, and the icosahedral symmetry gives $(Q_4, Q_6)_{ico} = (0, 0.663)$ [57].

REFERENCES

[1] J. A. Dantzig and M. Rappaz, *Solidification*: EPFL press, 2009.

[2] R. Asthana, A. Kumar, and N. B. Dahotre, *Materials processing and manufacturing science*: Elsevier, 2006.

[3] H. Wang, H. Gould, and W. Klein, "Homogeneous and heterogeneous nucleation of Lennard-Jones liquids," *Physical Review E,* vol. 76, p. 031604, 2007.

[4] R. Schubert, A. Meyer, D. Baitan, K. Dierks, M. Perbandt, and C. Betzel, "Real-time observation of protein dense liquid cluster evolution during nucleation in protein crystallization," *Crystal Growth & Design,* vol. 17, pp. 954-958, 2017.

[5] J. D. Roehling, D. R. Coughlin, J. W. Gibbs, J. K. Baldwin, J. C. Mertens, G. H. Campbell, *et al.*, "Rapid solidification growth mode transitions in Al-Si alloys by dynamic transmission electron microscopy," *Acta Materialia,* vol. 131, pp. 22-30, 2017.

[6] G. Neilson and M. Weinberg, "A test of classical nucleation theory: crystal nucleation of lithium disilicate glass," *Journal of Non-Crystalline Solids,* vol. 34, pp. 137-147, 1979.

[7] D. Erdemir, A. Y. Lee, and A. S. Myerson, "Nucleation of crystals from solution: classical and two-step models," *Accounts of chemical research,* vol. 42, pp. 621-629, 2009.

[8] G. Kahl and H. Löwen, "Classical density functional theory: an ideal tool to study heterogeneous crystal nucleation," *Journal of Physics: Condensed Matter,* vol. 21, p. 464101, 2009.

[9] S. Toxvaerd, "Molecular-dynamics simulation of homogeneous nucleation in the vapor phase," *The Journal of Chemical Physics,* vol. 115, pp. 8913-8920, 2001.

[10] X. Sui, Y. Cheng, N. Zhou, B. Tang, and L. Zhou, "Molecular dynamics simulation of solidification process of multicrystalline silicon from homogeneous nucleation to grain coarsening," *CrystEngComm*, 2018.

[11] K. Oh and X. C. Zeng, "Formation free energy of clusters in vapor-liquid nucleation: A Monte Carlo simulation study," *The Journal of chemical physics*, vol. 110, pp. 4471-4476, 1999.

[12] D. Srolovitz, G. Grest, and M. Anderson, "Computer simulation of recrystallization—I. Homogeneous nucleation and growth," *Acta metallurgica*, vol. 34, pp. 1833-1845, 1986.

[13] B. Böttger, J. Eiken, and I. Steinbach, "Phase field simulation of equiaxed solidification in technical alloys," *Acta materialia*, vol. 54, pp. 2697-2704, 2006.

[14] L. Gránásy, T. Börzsönyi, and T. Pusztai, "Nucleation and bulk crystallization in binary phase field theory," *Physical review letters*, vol. 88, p. 206105, 2002.

[15] L. Gránásy, T. Pusztai, D. Saylor, and J. A. Warren, "Phase field theory of heterogeneous crystal nucleation," *Physical review letters*, vol. 98, p. 035703, 2007.

[16] L. Liu, S. Pian, Z. Zhang, Y. Bao, R. Li, and H. Chen, "A cellular automaton-lattice Boltzmann method for modeling growth and settlement of the dendrites for Al-4.7% Cu solidification," *Computational Materials Science*, vol. 146, pp. 9-17, 2018.

[17] L. Gránásy, F. Podmaniczky, G. I. Tóth, G. Tegze, and T. Pusztai, "Heterogeneous nucleation of/on nanoparticles: a density functional study using the phase-field crystal model," *Chemical Society Reviews*, vol. 43, pp. 2159-2173, 2014.

[18] T. Kawasaki and H. Tanaka, "Formation of a crystal nucleus from liquid," *Proceedings of the National Academy of Sciences*, vol. 107, pp. 14036-14041, 2010.

[19] Y. Shibuta, S. Sakane, T. Takaki, and M. Ohno, "Submicrometer-scale molecular dynamics simulation of nucleation and solidification from undercooled melt: Linkage between empirical interpretation and atomistic nature," *Acta Materialia*, vol. 105, pp. 328-337, 2016.

[20] M. Finnis and J. Sinclair, "A simple empirical N-body potential for transition metals," *Philosophical Magazine A*, vol. 50, pp. 45-55, 1984.

[21] W. C. Swope and H. C. Andersen, "10 6-particle molecular-dynamics study of homogeneous nucleation of crystals in a supercooled atomic liquid," *Physical Review B*, vol. 41, p. 7042, 1990.

[22] M. A. Z. Avik Mahata, "Size Effect on Nucleation Process during Solidification of Pure Metals by Atomistic Simulations," *Submitted to Journal of Crystal Growth,* 2019.

[23] E. Asadi and M. A. Zaeem, "The anisotropy of hexagonal close-packed and liquid interface free energy using molecular dynamics simulations based on modified embedded-atom method," *Acta Materialia,* vol. 107, pp. 337-344, 2016.

[24] E. Asadi, M. A. Zaeem, S. Nouranian, and M. I. Baskes, "Two-phase solid–liquid coexistence of Ni, Cu, and Al by molecular dynamics simulations using the modified embedded-atom method," *Acta Materialia,* vol. 86, pp. 169-181, 2015.

[25] E. Asadi, M. A. Zaeem, S. Nouranian, and M. I. Baskes, "Quantitative modeling of the equilibration of two-phase solid-liquid Fe by atomistic simulations on diffusive time scales," *Physical Review B,* vol. 91, p. 024105, 2015.

[26] D. Faken and H. Jónsson, "Systematic analysis of local atomic structure combined with 3D computer graphics," *Computational Materials Science,* vol. 2, pp. 279-286, 1994.

[27] P. J. Steinhardt, D. R. Nelson, and M. Ronchetti, "Bond-orientational order in liquids and glasses," *Physical Review B,* vol. 28, p. 784, 1983.

[28] Y. Shibuta, S. Sakane, E. Miyoshi, S. Okita, T. Takaki, and M. Ohno, "Heterogeneity in homogeneous nucleation from billion-atom molecular dynamics simulation of solidification of pure metal," *Nature communications,* vol. 8, p. 10, 2017.

[29] P. M. Larsen, S. Schmidt, and J. Schiøtz, "Robust structural identification via polyhedral template matching," *Modelling and Simulation in Materials Science and Engineering,* vol. 24, p. 055007, 2016.

[30] V. Dubrovskii, "Fundamentals of Nucleation Theory," in *Nucleation Theory and Growth of Nanostructures,* ed: Springer, 2014, pp. 1-73.

[31] B. Chalmers, "Principles of solidification," in *Applied solid state physics*, ed: Springer, 1970, pp. 161-170.

[32] M. Rajagopalan, M. Bhatia, M. Tschopp, D. Srolovitz, and K. Solanki, "Atomic-scale analysis of liquid-gallium embrittlement of aluminum grain boundaries," *Acta Materialia,* vol. 73, pp. 312-325, 2014.

[33] D. Wolf, "Correlation between the energy and structure of grain boundaries in bcc metals I. Symmetrical boundaries on the (110) and (100) planes," *Philosophical Magazine B,* vol. 59, pp. 667-680, 1989.

[34] C. D. Barrett, A. Imandoust, and H. El Kadiri, "The effect of rare earth element segregation on grain boundary energy and mobility in magnesium and ensuing texture weakening," *Scripta Materialia,* vol. 146, pp. 46-50, 2018.

[35] M. Yoo, J. Morris, K. Ho, and S. Agnew, "Nonbasal deformation modes of HCP metals and alloys: role of dislocation source and mobility," *Metallurgical and Materials Transactions A,* vol. 33, pp. 813-822, 2002.

[36] D. L. Olmsted, S. M. Foiles, and E. A. Holm, "Survey of computed grain boundary properties in face-centered cubic metals: I. Grain boundary energy," *Acta Materialia,* vol. 57, pp. 3694-3703, 2009.

[37] M. Gündüz and J. D. Hunt, "Solid-liquid surface energy in the Al□Mg system," *Acta Metallurgica,* vol. 37, pp. 1839-1845, 1989/07/01/ 1989.

[38] H. Zhang, M. Upmanyu, and D. Srolovitz, "Curvature driven grain boundary migration in aluminum: molecular dynamics simulations," *Acta materialia,* vol. 53, pp. 79-86, 2005.

[39] G. Lu, N. Kioussis, V. V. Bulatov, and E. Kaxiras, "Generalized-stacking-fault energy surface and dislocation properties of aluminum," *Physical Review B,* vol. 62, pp. 3099-3108, 08/01/ 2000.

[40] B. Hammer, K. W. Jacobsen, V. Milman, and M. C. Payne, "Stacking fault energies in aluminium," *Journal of Physics: Condensed Matter,* vol. 4, pp. 10453-10460, 1992/12/14 1992.

[41] D. Wolf, "Correlation between the energy and structure of grain boundaries in bcc metals. II. Symmetrical tilt boundaries," *Philosophical Magazine A,* vol. 62, pp. 447-464, 1990.

[42] J. L. Nilles and D. L. Olson, "Energy of a bcc Iron Deformation Twin Boundary," *Journal of Applied Physics,* vol. 41, pp. 531-532, 1970/02/01 1970.

[43] P. Bristowe and A. Crocker, "A computer simulation study of the structures of twin boundaries in body-centred cubic crystals," *Philosophical Magazine,* vol. 31, pp. 503-517, 1975.

[44] R. L. Fleischer, "Stacking fault energies of HCP metals," *Scripta metallurgica,* vol. 20, pp. 223-224, 1986.

[45] T. Schilling, H. J. Schöpe, M. Oettel, G. Opletal, and I. Snook, "Precursor-mediated crystallization process in suspensions of hard spheres," *Physical review letters,* vol. 105, p. 025701, 2010.

[46] H. Tanaka, "Bond orientational order in liquids: Towards a unified description of water-like anomalies, liquid-liquid transition, glass transition, and crystallization," *The European Physical Journal E,* vol. 35, p. 113, 2012.

[47] J. Russo and H. Tanaka, "Crystal nucleation as the ordering of multiple order parameters," *The Journal of Chemical Physics,* vol. 145, p. 211801, 2016.

[48] J. Russo and H. Tanaka, "Role of bond orientational order in the crystallization of hard spheres," in *AIP Conference Proceedings*, 2013, pp. 232-237.

[49] J. T. Berryman, M. Anwar, S. Dorosz, and T. Schilling, "The early crystal nucleation process in hard spheres shows synchronised ordering and densification," *The Journal of Chemical Physics,* vol. 145, p. 211901, 2016.

[50] M. Asadian Nozari, R. Taghiabadi, M. Karimzadeh, and M. Ghoncheh, "Investigation on beneficial effects of beryllium on entrained oxide films, mechanical properties and casting reliability of Fe-rich Al–Si cast alloy," *Materials Science and Technology,* vol. 31, pp. 506-512, 2015.

[51] E. Lee, K.-R. Lee, M. Baskes, and B.-J. Lee, "A modified embedded-atom method interatomic potential for ionic systems: 2 NNMEAM+ Qeq," *Physical Review B,* vol. 93, p. 144110, 2016.

[52] M. Parrinello and A. Rahman, "Polymorphic transitions in single crystals: A new molecular dynamics method," *Journal of Applied physics,* vol. 52, pp. 7182-7190, 1981.

[53] S. Plimpton, "Fast parallel algorithms for short-range molecular dynamics," *Journal of computational physics,* vol. 117, pp. 1-19, 1995.

[54] B.-J. Lee and M. Baskes, "Second nearest-neighbor modified embedded-atom-method potential," *Physical Review B,* vol. 62, p. 8564, 2000.

[55] B.-J. Lee, M. Baskes, H. Kim, and Y. K. Cho, "Second nearest-neighbor modified embedded atom method potentials for bcc transition metals," *Physical Review B,* vol. 64, p. 184102, 2001.

[56] W. Lechner and C. Dellago, "Accurate determination of crystal structures based on averaged local bond order parameters," *The Journal of chemical physics,* vol. 129, p. 114707, 2008.

V. SOLID-LIQUID COEXISTANCE OF BINARY AL ALLOYS BY MOLECULAR DYNAMICS SIMULATION USING MODIFIED EMBEDDED METHOD

Avik Mahata[1] and Mohsen Asle Zaeem[1,2*]

[1] Department of Materials Science and Engineering, Missouri University of Science and Technology, Rolla, MO 65409, USA

[2] Department of Mechanical Engineering, Colorado School of Mines, Golden, CO 40801, USA

ABSTRACT

Interatomic potentials for binary Al alloys were developed based on modified embedded-atom method (MEAM) potentials for predicting low temperature and melting properties. The binary alloys chosen for this study are, Al-Cu, Al-Fe, Al-Ni, Al-Si and Al-Ge. Using these interatomic potentials, we compare calculated low-temperature properties of the binary Al alloys such as formation energy of stable and unstable intermetallic, elastic constants, lattice parameters, enthalpy of solid and liquid mixing with experimental data. In addition, we also compare the liquidus temperature of the Al-alloys from the phase diagram to the molecular dynamics (MD) simulation. Available MEAM potential for Al-Mg is also considered for solid-liquid coexistence.

1. INTRODUCTION

The goal of any computer simulation is to predict the material properties as accurate to the experimental data. Due to the rapid progress in computer technology, there are several physics based methods developed and made progress. The computational methods

can be classified in different classes depending on the time and length scale studied by those methods [4, 5]. In particular to the study of computational metallic solidifications, there are several methods have been applied such as, density functional theory (DFT) [7], MD [13, 14], Monte Carlo (MC) [16], phase field [17, 18], front tracking (FT) model [19], extended finite element method (FEM) [21, 22] etc. The issues with most of the methods are with the length scale, accuracy or practicality. Solidification in metallic systems begins at the atomistic realm at the interior part of the liquid. Phase field is a popular method to study solidification but the studies are in micrometer scale and mostly analytical then direct observation of solidification from atomistic nucleation stages. DFT can be used to study melting properties can be derived accurately but its limited to very small scale, which prevents it from directly observing solidification from atomistic scale. MC simulations are also performed in a much smaller scale, whereas FT or FEM methods for solidification are analytical.

MD has gained popularity in nucleation-solidification research due to its flexibility in the length scale. MD has been used to study solidification from a few thousand atoms to multibillion atom systems [24, 25]. Along with flexible length scale solidification study in MD is also very accurate. In our previous work [27] and various other recent MD works [28-30] shows a good agreement of critical nucleus size, nucleation temperature, incubation time etc. with experimental and classical nucleation theory (CNT) results. However, the accuracy of MD simulation depends on the interatomic potential. The initial MD studies of solidification based on pair potential such as, Lennard-Jones potential [31-33], hard sphere model [42, 43] could produce quantitative details (free energy, critical temperature, nuclei size etc.) of nucleation and solidification the scale of simulations were

limited. Later the development of many body interatomic potential such as, embedded atom method (EAM) [44, 45] and Finnis–Sinclair (FS) [46] enhanced the capability and accuracy. However, both EAM and FS do not predict the high thermal properties temperature properties very accurately.

The MEAM was introduced to include the directionality of bonding in covalent materials in the EAM formalism [47, 48]. Today, the MEAM potential is widely used in the computational materials science and engineering community to simulate unary, binary, ternary and multi-component metallic systems with microstructural features, such as grain boundaries, defects, free surfaces, etc. The MEAM formalism reproduces successfully the physical properties of face-centered cubic (fcc) [49, 50], body-centered cubic (bcc) [39], hexagonal close-packed (hcp) [51] and diamond cubic [52] crystal structures. Recently MEAM potential has also been extended to binary [53, 54] and ternary alloys [55, 56]. In our recent studies of solid-liquid coexistence for Al, Cu, Ni, Fe and Mg we showed the comparisons of accuracy predicting the high temperature melting properties of MEAM potential compare to EAM and other interatomic potentials [57-59]. In a different study by Ryu et. al. [60] also shows the accuracy of predicting thermal properties by MEAM formalism over other many body interatomic potential such as, FS, EAM and Stillinger-Weber (SW) potential [9]. By including the electrostatic parameters MEAM has been also applied to oxides and corrosion studies [61, 62].

In the present study, we developed and modified the interatomic potential for melting-solidification studies of Al-Cu, Al-Fe, Al-Ni, Al-Si and Al-Ge. In previous studies the thermal properties and melting temperature has been verified for Al, Cu, Ni, Fe and Mg by Asadi et. al. [57-59] and Kim et. al. [63]. The MEAM potential developed by Jelinek

et. al. [54], is also studied for high temperature properties and melting point in this work. The melting point of Ge predicted by the MEAM is 2200 K, In the first step, the interatomic potential has been parameterized for formation energy for the B1 crystal structure or the available stable compounds. Then, the next stage of parameterization is done while verifying the solid and liquid mixing enthalpy of the alloys, thermal expansion, higher temperature lattice parameters. After the interatomic potential perform reasonably, with the low and high temperature properties we calculate the solid-liquid coexistence properties at different composition of Al and its alloying elements. Then we also, determine the formation energies of intermetallic and imaginary structures, which can be crucial doing the precipitating studies of the Al alloys. The MEAM potential for Al-Mg [63] was also studied for liquidus temperature by changing the Mg atomic composition in Al-Mg.

2. COMPUTATIONAL METHODOLOGY

The interatomic potential parameters for single elements presented in Table 1. The single element potential parameters for Al, Cu, Ni, Fe and Mg predicts the melting points 925, 1552, 1998, 1807 and 926 K [57-59, 63] respectively. This reasonably close to the experimental data. Further analysis on solid-liquid coexistence on these single elements also shows good agreement with experimental solid-liquid interface free energy [57-59]. The interatomic potential for Si was developed by Jelinek et. al. was fitted for all the low temperature properties (i.e. elastic modulus, vacancy formation energy, formation energy etc.) [54]. We verify the high temperature properties in this work and shows promising results compare to experiments. The MEAM interatomic potential for Ge predicts the

melting point 2200 K [52] because the interatomic potential was primarily developed for Si-Ge alloys, where the melting point was less important than constancy between Si and Ge. However, as the Al-Ge phases at higher Ge concentration generally happen at higher temperature and large pressure, we only focus on the Al-rich Al-Ge alloys. So, the melting point of Ge is not important for studying solidification nucleation in Al-rich Al-Ge alloys.

Table 1. 2NN MEAM parameters for binary Al alloys are shown. $E_c(eV)$ is the cohesive energy; $R_0(\AA)$ is the nearest neighbor distance in the equilibrium reference structure. α^0 is the exponential decay factor for the UEOS of Rose et al. [64]; A is the electron density scaling factor for the embedding function; $\beta^{(0-3)}$ are the exponential decay factors for the atomic electron densities; $t^{(1-3)}$ are the weighting parameters for the atomic electron densities; and $C_{\min}$ and $C_{\max}$ are the screening parameters. $C_{\max}$ is taken 2.8 for all the cases.

Element	$E_c(eV)$	$R_0(\AA)$	A	α^0	$\beta^{(0)}$	$\beta^{(1)}$	$\beta^{(2)}$	$\beta^{(3)}$	$t^{(1)}$	$t^{(2)}$	$t^{(3)}$
Al	3.36	2.86	1.16	4.61	3.20	2.60	6.0	2.60	3.05	0.51	7.75
Cu	3.54	2.56	0.99	5.20	3.83	2.20	6.0	2.20	2.72	3.04	0.85
Fe	4.90	2.47	0.57	5.03	3.67	1.00	1.00	1.00	2.90	1.00	-8.7
Mg	1.55	3.20	0.52	4.61	2.30	1.00	3.00	1.00	9.00	-2.00	-9.50
Ni	4.45	2.49	0.99	5.08	2.56	1.50	6.0	1.50	3.10	1.80	2.20
Si	4.63	2.58	1.00	4.87	4.40	5.50	5.50	5.50	2.05	4.47	-1.80
Ge	3.85	2.45	0.66	5.04	3.95	2.00	0.00	7.50	2.90	5.77	-2.20

In MEAM for single element can be extended to alloys system if the potential parameters are verified for physical mechanical properties of the alloy systems. In MEAM, E_c, R_0, α and the attraction-repulsion term describe the material properties. So, the

experimental data available from the literature can fitted by altering the E_c, R_0, α and the attraction-repulsion parameters for the alloys. Instead of E_c, we fit the heat of formation ΔH for alloy, which is the difference of the cohesive energy of the alloy to the average of each of the element of in the alloy. In all the binary alloys, we utilized the experimental data for B1 (Al-Si and Al-Ge), B2 (Al-Fe, Al-Ni) or other stable phases (Al_2Cu for Al-Cu) for the initial parameterization. Then we study the formation enthalpy by changing the alloying component from 0 to 100 atomic (at.) %. If the results are doesn't replicate the experimental results then we modify the ΔH, R_0, α, $C_{\min}$, $C_{\max}$ and the attraction-repulsion parameters and recalculate the elastic properties and formation energies. Depending on the accuracy of predicting heat of formation, solidus liquidus temperature, we compromise on the elastic properties of formation energies at 0K. The MEAM parameters for Mg-Al is directly utilized from Kim et. al. as it was fitted heat of formation of solid and liquid, thermal expansion, lattice parameters etc. and reproduce the experimental or computational results [63].

For the initial fitting to B1 and B2 structures we utilized MEAM Parameter Calibration (MPC) tool [65] and the MD simulations were performed in LAMMPS [66]. The two-phase solid–liquid coexistence is to determine the exact liquidus line for the binary components. The exact liquidus line in the phase diagram is calculated by simultaneously equilibrating the solid and liquid phases in a simulation box. The methods have been discussed in details in our previous works [57-59]. The methods used for single elements, has one single phase, however for alloy the solid and both the liquid has been chosen at the same at. % of the alloying elements.

Table 2. The MEAM potential parameters for element pairs. $\Delta H_{B1/B2}^{XY}(eV)$ B1(NaCl) or B2(AlFe) reference structure. B2 is compared with the type-X and type-Y elements relative to the energies of elemental X and Y in their equilibrium reference state, $r_e^{XY}(\AA)$ is their equilibrium nearest neighbor distance, α^{XY} is the exponential decay factor for the universal energy, $C_{\min}$ and $C_{\max}$ are screening parameters (C^{XYX} denotes type-Y element between two elements). All the $C_{\max}$ are 2.8.

X	Y	$\Delta H_{B1/B2}^{XY}(eV)$	$R_0^{XY}(\AA)$	α^{XY}	$C_{\min}^{XYX}$	$C_{\min}^{YXY}$	$C_{\min}^{XXY}$	$C_{\min}^{XYY}$
Al	Cu	0.20	2.53	4.65	0.50	1.00	0.00	0.90
Al	Fe	0.27	2.49	5.50	2.00	2.00	0.00	2.00
Al	Mg	0.46	2.95	7.63	0.36	0.36	0.49	0.36
Al	Ni	0.25	2.75	5.58	2.00	2.00	2.00	1.60
Al	Si	0.28	2.58	3.57	2.00	2.00	0.50	2.00
Al	Ge	0.24	2.56	3.94	2.00	2.00	0.49	1.41

3. RESULTS AND DISCUSSIONS

3.1 INTERATOMIC POTENTIAL FOR AL-CU

Al_2Cu-θ and θ' phases are very stable and well researched Al-Cu compound. The interatomic potential studied for the prediction of the experimental properties for Al_2Cu-θ phase. Table 3 shows the formation energies, elastic properties, interfacial energies, surface energies for both Al_2Cu precipitates. For some properties, the experimental data for all the different properties are not available for the propitiates, so we supply the first principle data for some of the cases.

Table 3. The formation energy, elastic properties, surface and interfacial energies for Al_2Cu-θ and θ' phases predicted from 2NN-MEAM MD. The results are compared with experimental/first principle data. Superscript a, b and c denotes experimental, first principle/DFT of previous MD simulations respectively.

	Al_2Cu-θ (C16)		**Al_2Cu-θ' (C1)**	
Properties	Experiments/First Principle/MD	MEAM MD	Experiments/First Principle	MEAM MD
Formation Energy (eV/atom)	-0.135[a] [67], -0.139[a] [68], -0.184[b][69], -0.169[b] [70], -0.190[c][72], 0.180[c] [74]	-0.187	-0.199b [75], -0.203-0.74[c] [72]	-0.161
Bulk Modulus (GPa)	113.4[a] [76] 99.4[b] [70], 147.6[c] [72]	113.11	117[b] [69], 135.9-199.2[c] [72]	121.845
C_{11} (GPa)	186.20[a] [76], 150.3[b] [70], 199.3[c] [72]	166.23	190[b] [75], 192.8-310.5[c] [72]	188.724
C_{12} (GPa)	71.5[a] [76], 86.1[b] [70], 98.2[c] [72]	86.33	80[b] [77]	88.352
C_{44} (GPa)	29.2[a] [71], 29.4[b] [70], 59.7-78.6[c] [72]	40.0	90[b] [77]	77.312

In order to verify the applicability of the interatomic potential, the thermal linear expansion coefficient of Al_2Cu, Al_4Cu_9, AlCu and $AlCu_3$ is verified. As shown in Figure 1(a), it reproduces the experimental results. In Figure 1(b) and (c) the enthalpy of formation of solid and liquid alloys is shown. To determine the liquid enthalpy the liquid of Al-Cu alloys has been equilibrated at a very high temperature to produce a homogenous liquid. Then the liquid has been brought down to the desired temperatures such as 1373-1773 K (Figure 1(c)). Then again it was equilibrated for 1000 ps and then the formation energies are taken accordingly. A similar system of pure Al and Cu also equilibrated at the same temperature after producing the liquid at a higher temperature, then energy of liquid Al and Cu is used as the reference. The time steps in MD simulations are limited to picosecond or nanosecond level. If the system can be equilibrated for a longer amount of time the formation energies can be even more close to the experimentally available data.

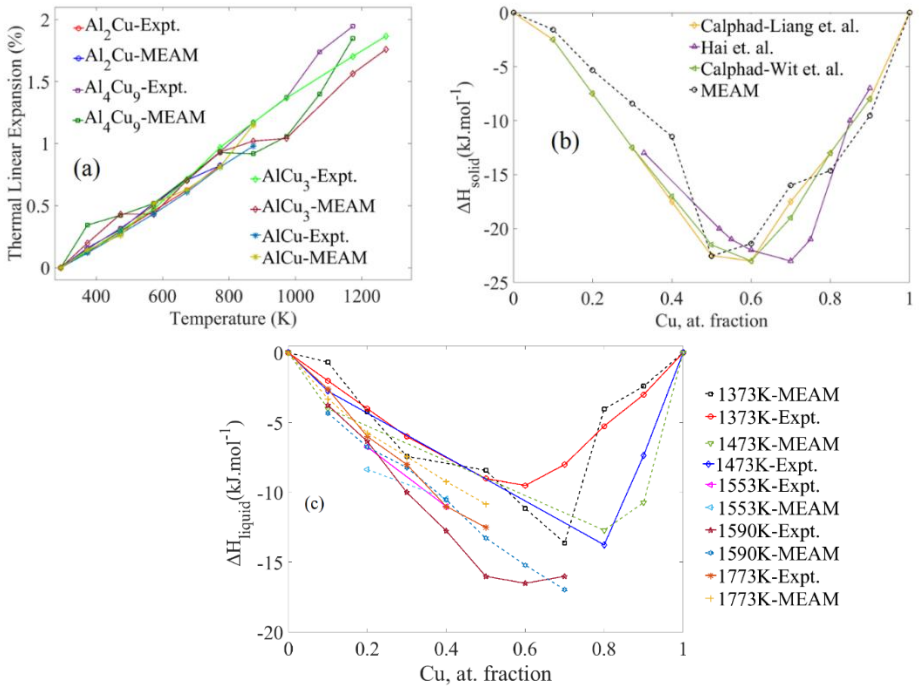

Figure 1. Therml expansion coefficiet, solid and liquid mixing enthalpy prediction by MEAM potential for Al-Cu. (a) Calculated thermal linear expansion for different Al-Cu compounds and intermetallic such as Al_2Cu, Al_4Cu_9, AlCu and $AlCu_3$. The experimental data of thermal expansion is obtained from Touloukian et. al. [78]. (b) The enthalpy of formation of solid phases is compared with experimental data at 773K from Liang et. al. [79], Witusiewicz et. al. [80], Hair et. al. [81]. (c) Liquid mixing enthalpy for Al-Cu with increasing Cu content. The experimental values for different temperature between 1373-1773 K have been taken from the literature [82-87].

By changing the Cu content and also the temperature of the Al-Cu solid solution formation energy can be changed. To verify the solid solution formation energies, we evaluate the Al-Cu formation energies for different phases. The reference structure used for pure Al and Cu are fcc solid single crystal at 298 K and 773 K as the temperature shown in Table 4. The experimental data has been taken from Murray et. al. [73]. As shown in Table 4, the computed formation energies for the different alloying phase for Al-Cu remain reasonable close to the data available from the experimental works.

Table 4. Enthalpy of formation ($kJ.mol^{-1}$) of solid alloys at 298 K and 773 K referred to pure fcc Al and fcc Cu from 2NN-MEAM MD is compared with experimental data.

Temperature	Phase [73]	Composition at.-% Cu	Experimental [73]	MEAM
773 K	Al (fcc)	0.4	-0.170	-0.057
	θ	33	-13.050	-12.288
	η_2	51	-19.920	-11.04
	Cu	93	-6.190	-3.840
298 K	θ	33	-13.390	-12.960
	η_2	50	-20.040	-15.370
	Cu (fcc)	85	-9.560	-9.600
		90	-7.637	-7.680

In the Al-Cu phase diagram, the experimental or theoretical solidus and liquidous line for changing amount of Cu in Al in Al-Cu alloy [88]. For studying solidification, the prediction of solid-liquid coexistence is necessary. In Table 5 the solid-liquid coexistence has been calculated with the current 2NN-MEAM potential and the prediction are almost similar to the temperatures predicted by the phase diagram. At 100% Al and the eutectic point the solidus and liquidous lines are expressed by a single point. As shown in Table 5, the prediction from MD simulations are close to the experimentally available liquidus line. Finally, the interatomic potential is tested for various other Al-Cu compounds (Table 6). The prediction from the MEAM poitential also works well for most of the theoretical and experimental phases of Al-Cu. It also matches the previous values of first principle calclulation or experimental data from previous work. So, along with the single metals the MEAM potential works well for the binary alloys such as Al-Cu.

Table 5. The liquidous temperature from the experimental phase diagram is compared with the prediction of 2NN-MEAM results. The * is the eutectic point.

Al-Cu Composition (Al-at. % of Cu)	**Liquidous Temperature (K) (Expt.) [89]**	**Meam (K)**
Al-10% Cu	873.0	868±5
Al-15% Cu*	821.2	821±5

The MEAM potential predicts the energies for B1 and the other Cu rich composition such as, $L1_2$, A15 and $D0_{22}$. MEAM overestimates the formation energy for the low Al rich compounds. This is consistent with other interatomic potential in MD [72].

Table 6. Formation energies of different possible Al-Cu compounds compared with first-principle data and previous MD simulation.

		ΔE_f (eV/atom)		
Formula	Structure	This Work	DFT	MD
Al_3Cu	$L1_2$	-0.18	-0.284 [54]	-0.040 [54]
Al_3Cu_2	$D5_{19}$	-0.299	-0.164 [77]	-0.345 [72], 0.0047 [72]
AlCu	B2	-0.435	-0.198 [54], -0.195 [90]	-0.635 [72], -0.198 [54]
AlCu	B1	-0.205	-0.190 [54]	0.195 [72], -0.079 [72]
AlCu	“40”(NbP)	-0.0159	-0.191 [91]	-0.257 [72]

3.2 INTERATOMIC POTENTIAL FOR AL-NI

Similar to Al-Cu, Al-Ni has the $L1_2$ and B2 crystal structure available naturally. The lattice parameters, formation energy and bulk modulus for Al-Ni B2 structures are initially utilized. Then MEAM parameters are modified to also reproduce the formation

energies and of the $L1_2$ $AlNi_3$ phases. As shown in Table 7 MEAM reproduce the experimental and first principle results very accurate. The interface energy for γ -Ni and γ'-$AlNi_3$ is also available from Silva et. al. [92], which we calculated utilizing a larger supercell (50 x 25 x 25 unit cells). Then, the internal energy of the supercell is calculated by relaxing the simulation box. We also create a similar box of γ -Ni and Ni_3Al and calculate the per atom energy. After the three different per-atom energies are available, the surface energy can be calculated from the difference of the average energy Al and Ni to the supercells.

Table 7. The formation energy, elastic properties, surface and interfacial energies for $AlNi_3$-$L1_2$ and AlNi-B2 phases predicted from 2NN-MEAM MD. Results are compared with experimental/first principle, MD simulation data. Superscript a, b and c denotes experimental, first principle/DFT of previous MD simulations respectively.

	$AlNi_3$ ($L1_2$)		**AlNi (B2)**	
Properties	Experiments/First Principle	This Work	Experiments/First Principle/MD	This Work
Lattice Parameters (Å)	3.567[a] [93]	3.566	2.886[a] [93], 2.866[c] [92]	2.867
Formation Energy (eV/atom)	-0.436[a] [94], -0.436[c] [92],	-0.437	-0.604-0.69[a] [94-98], -0.50-0.83[b] [99-102], -0.71.5[c] [92, 103],	-0.600
Bulk Modulus (GPa)	177[a] [104]	179	158[a] [105]	160.26
C_{11} (GPa)	230[a] [104]	254	199[a] [105]	192.92
C_{12} (GPa)	150[a] [104]	142.70	137[a] [105]	143.94
C_{44} (GPa)	131[a] [104]	115	116[a] [105]	127.58

The thermal properties of Al-Ni alloys have been shown in Figure 2. The thermal linear expansion has very good agreement with the experimental data (Figure 2(a)). The mixing enthalpy of solid alloys at 980 and 1100 K also replicate the experimental results presented in Figure 2(b). The small difference in the energy in the solid solution can be attributed to the strain energy that can resulted in comparatively higher formation energy as the Ni content increase in Al-Ni alloys. In liquid, the strain energy doesn't play any role, as it remains close to the experimental results (Figure 3(c)).

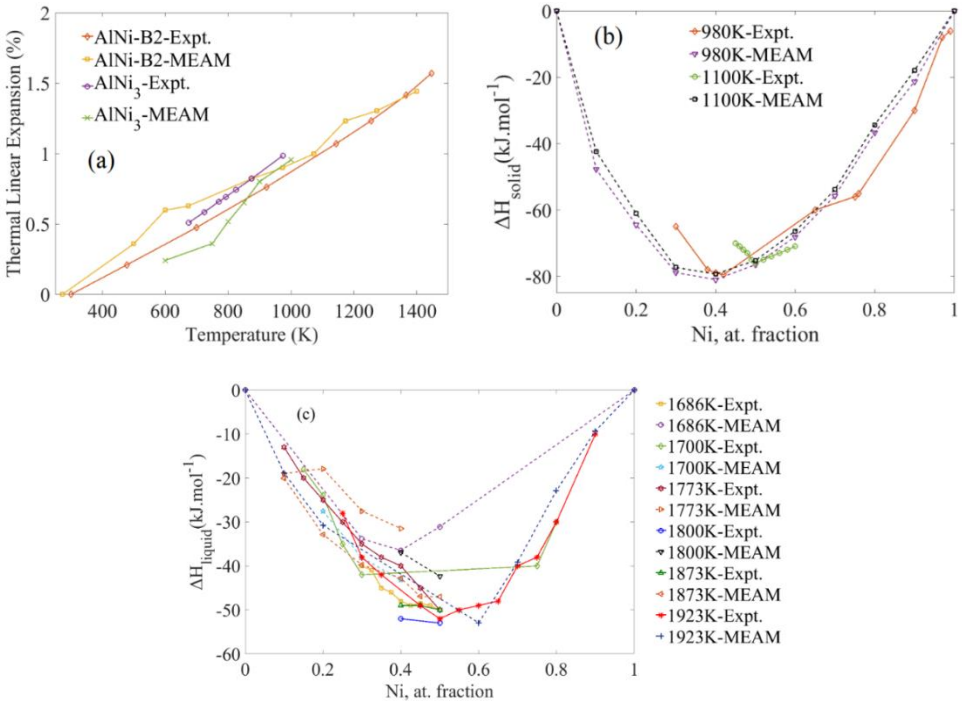

Figure 2. Therml expansion coefficiet, solid and liquid mixing enthalpy prediction by MEAM potential for Al-Ni. (a) Calculated thermal linear expansion for different Al-Ni compounds and intermetallic such as AlNi and $AlNi_3$. The experimental data of thermal expansion is obtained from Touloukian et. al. [78]. (b) The enthalpy of formation of solid phases is compared with experimental data at 980 and 1100 K from Rzyman et. al. [106], Ansara et. al. [107] and Hcnig et. al. [108] (c) Liquid mixing enthalpy for Al-Ni with increasing Ni content. The experimental values for different temperature between 1686-1923 K have been taken from various Calphad or experimental data [99, 107, 109-112].

Finally, the liquidus temperature has been verified for different Ni content (Table 8). At lower Ni content the liquidus temperature remains close to phase diagram data, however as the Ni content increase the liquidus temperature is overestimated. This may happen as the MEAM interatomic potential predicts the melting temperature for Cu 14 K higher than experimental values where as it predicts 8.5 K lower melting point for Al. However, the margin of error remains within 5% of the experimental results.

Table 8. The liquidous temperature from the experimental phase diagram is compared with the prediction of 2NN-MEAM results. The * is the eutectic point.

Al-Ni Composition (Al-at. % of Ni)	**Liquidous Temperature (K) (Expt.) [89]**	**Meam (K)**
Al-0%Ni	933.5	925
Al-2% Ni*	917	922±2
Al-10% Ni	1050	1074±2
Al-20% Ni	1150	1180±10
Al-50% Ni	1949	2039±50
Al-75% Ni	1624	1689±20
Al-90% Ni	1700	1720±8
Al-100% Ni	1728	1742

The Al-Ni intermetallic and imaginary compounds have also been studied for their formation energies. The formation energies for most intermetallic remains with small margin of errors for most of the compositions (Table 9). There are also different formation energies were reported in different publications [82, 102, 113] because the computed values of formation energies depend on the crystallographic structures used in the work.

We relaxed our structures before calculating the formation energies and as it works well with naturally existing Al-Ni compounds as shown in Table 7, we expect the predictions from MEAM potentials are consistent with the other structures.

Table 9. Formation energies of different possible Al-Ni compounds compared with first-principle data and previous MD simulation. Superscript a, b and c denotes experimental, first principle/DFT of previous MD simulations respectively.

		ΔE_f (eV/atom)	
Formula	Structure	This Work	Expt.*/DFT
Al_3Ni	DO_3	-0.375	-0.393[a] [82], -0.439[b] [113], -0.236[b] [102]
	DO_{20}	-0.603	-0.019[b] [102]
	$L1_2$	-0.232	-0.250[b] [102], -0.401[b][114]
Al_4Ni_3	I112	-0.478	-0.683[b] [113]
Al_3Ni_2	$D5_{13}$	-0.209	-0.499[b] [102]
AlNi	B32	-0.215	-0.485[b] [102]
	$L1_0$	-0.486	-0.572[b] [102]
Al_2Ni_3	P4	-0.534	-0.509[b] [114]
Al_3Ni_5	C16	-0.170	-0.63[b] [113], -0.583[b] [115]
$AlNi_3$	DO_3	-0.223	-0.262[b] [102]
	DO_{22}	-0.589	0.949[b] [102]

3.3 INTERATOMIC POTENTIAL FOR AL-FE

For Al-Fe, we first fit the parameters for Al-Fe-B2 structures, which naturally happens and expensively studied experimentally for its physical properties [116-118]. Once it fitted for the B2 Al-Fe formation energies and elastic properties, then the properties

are fitted for $D0_3$ and $L1_2$. As we have to fit all the formation energies and get reasonable values, so the potential parameters are compromised accordingly. As shown in Table 10, the formation energies and lattice parameters are reproduced with less than 1% of the error. The results of the elastic properties underestimate the C44, which comes with the expense of fitting all the formation energies and elastic properties and also the high temperature melting properties.

Table 10. The formation energy, elastic properties, surface and interfacial energies for FeAl-B2, Fe_3Al-DO_3 and Fe_3Al-$L1_2$ phases predicted from 2NN-MEAM MD. Results are compared with experimental/first principle, MD simulation data. Superscript a, b and c denotes experimental, first principle/DFT of previous MD simulations respectively.

	AlFe (B2)		**Al Fe_3 (DO_3)**		**Al Fe_3 ($L1_2$)**	
Properties	Experiments/First Principle/MD	MEAM MD	Experiments/First Principle/MD	MEAM MD	Experiments/First Principle/MD	MEAM MD
Formation Energy (eV/atom)	-0.250-0.280[a] [82, 97, 123, 127], -0.311-0.420[b] [71, 115, 128, 129], -0.342[c] [54], 0.298[c] [120]	-0.267	-0.202[a] [82], -0.321[a] [130], -0.200-0.230[b] [54, 71, 115, 123, 131], -0.206[c] [120]	-0.223	-0.187-0.222[b] [71, 115, 123, 128]	-0.177
Bulk Modulus (GPa)	136[a] [104], 155-172[b] [122-124], 124.6[c] [120]	135.676	144.1[a] [104], 151-174[b] [122-124], 148.9[c] [120], 137.5[c] [54]	146.00	143-185[b] [122, 123, 126], 166.3[c] [54], 149.6[c] [120], 139.5[c] [54]	145.293
C_{11} (GPa)	181.1[a] [104], 143-185[b] [122-124, 126], 124.6[c] [120]	172.641	171.0[a] [104], 164[b] [122], 159.2[b] [124], 222.5[c] [120]	212.08	184[b] [122], 174.3[c] [120]	181.289
C_{44} (GPa)	127.1[a] [104], 138.8[b] [54], 78.0[c] [120], 111.7[c] [54]	88.00	131.7[a] [104], 140[b] [54], 109.1[c] [120], 129[c] [54]	97.50	160[b] [122], 125.1[b] [54], 96.9[c] [54], 76.0[c] [120]	72.00

Once the low temperature properties are fitted thermal expansion, solid-solution enthalpy and liquid mixing enthalpy of Al-Fe alloys have been studied (Figure 3). The thermodynamic properties (enthalpy of formation and enthalpy of mixing) are reproduced well within the scattering range of experimental or first principles data. We also compare the result of the MEAM results to previous MEAM for Al-Fe alloys by Lee et. al. [120].

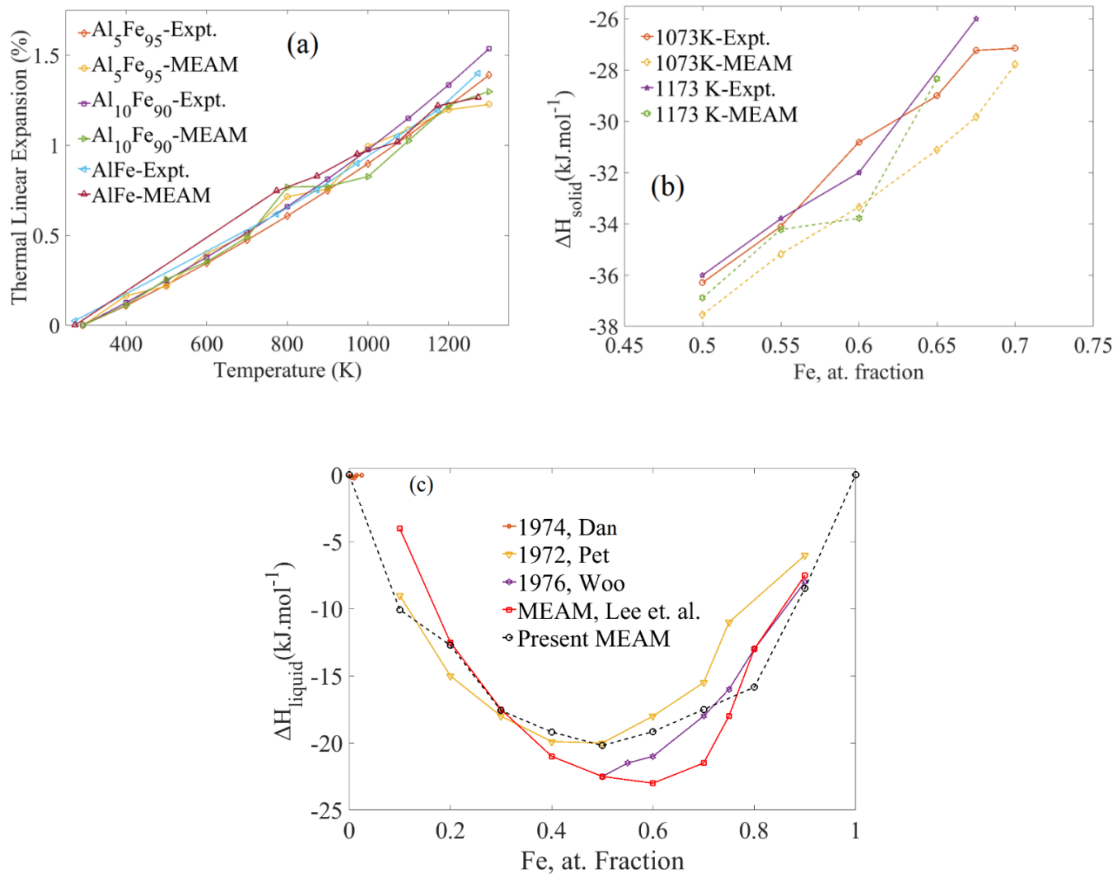

Figure 3. Therml expansion coefficiet, solid and liquid mixing enthalpy prediction by MEAM potential for Al-Fe. (a) Calculated thermal linear expansion for different Fe content in Al-Fe alloy. The experimental data of thermal expansion is obtained from Touloukian et. al. [78]. (b) The enthalpy of formation of solid phases is compared with experimental data at 1073 and 1173 K from Breuer et. al. [133] and Eldridge et. al. (c) Liquid mixing enthalpy for Al-Fe with increasing Fe content. The experimental values for liquid has been taken from various MD data from Lee et. al. [120] or experimental data from Elliott and Woolley [134], Petrushevsky et. al. [135] and Dannöhl et. al. [136].

As the potential parameters fitted for the thermal properties, now high temperature solid-liquid coexistence temperatures have been calculated for different at. % of Fe. The prediction from MD simulation is very close to the experimental data. Fe–Al binary system is characterized by a large solubility of Al (up to 50 at. % Al) in the body-centered cubic (bcc) solid solution. Due to mostly single phase bcc or fcc dominates at a particular at. % of Fe in Al-Fe and as a result the two phase solid-liquid temperature coexistence remains very close to the experimental data.

Table 11. The liquidous temperature from the experimental phase diagram is compared with the prediction of 2NN-MEAM results.

Al-Fe Composition (Al-at. % of Fe)	**Liquidous Temperature (K) (Expt.) [89]**	**Meam (K)**
Al-0%Fe	933.5	925
Al-10% Fe	1273	1302±10
Al-25% Fe	1435	1432±10
Al-50% Fe	1650	1663±15
Al-80% Fe	1790	1780±15
Al-90% Fe	1805	1805±5
Al-100% Fe	1809	1807

The formation energies bulk modulus for various intermetallic and imaginary structures have been calculated by utilizing the MEAM potentials and similar to the other alloys Al-Fe alloys also have large difference in literature data. However, as most of the cases the energy remains close to first principle data, it is possible that these alloys can form during the MD simulation of the solidification of Al-Fe alloys. The difference in the formation in all the alloying structures

Table 12. Formation energies and Bulk modulus of different possible Al-Fe compounds compared with first-principle data and previous MD simulation. Superscript a, b and c denotes experimental, first principle/DFT of previous MD simulations respectively.

		ΔE_f (eV/atom)		Bulk Modulus (GPa)	
Formula	Structure	This Work	DFT/MD	This Work	DFT/MD
Al_6Fe	C8	-0.172	-0.196[b] [114]	122.491	106 [114]
Al_9Fe_2	P32	0.114	-0.236[b] [114]	83.36	95.38 [114]
Al_3Fe	A15	0.481	-0.161[b] [54], 0.321[c] [54]	73.349	67.7 [54], 1.8[c] [54]
	$L1_2$	0.428	-0.122[b] [54] -0.105 [115], -0.049[c][54]	150.0	126.5 [54], 98.8 [123], 108.5[c] [54]
	DO_3	0.223	-0.025[b] [54] , 0.266[c] [54]	117.378	126 [54], 119 [123], 93.8[c][54]
Al_2Fe	$C11_b$	0.280	-0.371[b], -0.42[b] [115], 0.106[c][54]	125.869	149 [54]
	C1	-0.051	-72[b] [54], -76[c] [54]	103.128	98.6 [54], 90.4[c] [54]
$Al_{12}Fe_7$	P4	0.099	-0.313 [114]	129.32	129.12[b] [114]
Al_8Fe_5	I52	-0.272	-0.283 [114]	123.456	133.72[b] [114]
AlFe	hp6	0.973	0.807 [114]	135.799	85 [114]
$AlFe_2$	C15	0.042	-0.099[114] -0.115[54], -0.060[115], 0.925[c][54]	139.563	130.2[54], 127.8[c][54], 117 [114]
$AlFe_4$	B24	-0.025	-0.060 [114]	180.363	185.17 [114]

3.4 LIQUIDUS TEMPERATURES OF AL-MG

The MEAM potential developed by Kim et. al. [63] was studied for formation energy, elastic properties, solid and liquid mixing enthalpies, melting temperature of Mg and Al-Mg alloy. As it was tested for all different thermal properties of Al-Mg, it is expected the MEAM can replicated the experimental solid-liquid coexistence properties. As shown, in Table 13, the temperature for liquidus line for Al-Mg alloys, remains very close to the experimental/theoretical values. So, along with the other binary Al alloys, Al-Mg can also be studied for melting and solidification phenomena.

Table 13. The liquidous temperature from the experimental phase diagram is compared with the prediction of 2NN-MEAM results. The * is the eutectic point.

Al-Mg Composition (Al-at. % of Mg)	**Liquidous Temperature (K) (Expt.) [137]**	**Meam (K)**
Al	933.5	925
Al-10% Mg	895	900±10
Al-20% Mg	845	862±10
Al-50% Mg	731	740±15
Al-75% Mg	750	760±10
Al-90% Mg	860	865±10
Mg	923.2	937.9

3.5 HIGH TEMPERATURE AND MELTING POINT OF SI

The MEAM potential for Si developed by Jelinek et. al. [54], was not studied for all the high temperature and melting properties of Si. To utilize the Si interatomic potential for AL-Si alloy melting and solidification, the Si interatomic potential should be verified for its application in Si high temperature properties such as latent heat, thermal expansion, change in volume in melting, coordination number and also amorphous structure. As shown in Table 14.1 and 14.2 the melting properties are close to the experimental predictions. The enthalpy of melting is predicted higher than the expected values. However, it could be modified by changing the heat of formation. But with a change the heat of formation (ΔH), it can alter all other properties. As the prediction need to kept in a reasonable error margin for all the different alloy system, we kept the parameters unchanged.

The liquid structure factor shown in Figure 4is compared with first principle calculation by Štich et. al. [138]. The MEAM-MD calculations of the liquid structure factor match the alternative experimental curves, even for the height of the first peaks (15%) except for the height of the first peak for Cu. The reason for this error might be the difference in the liquid structures used for first principle calculations. The study of ab-initio MD [138] of Si-melt was also performed only on 64 atoms, whereas the MD simulation has been performed on ~10,000 atoms. So, these differences may have resulted in a difference between the peaks.

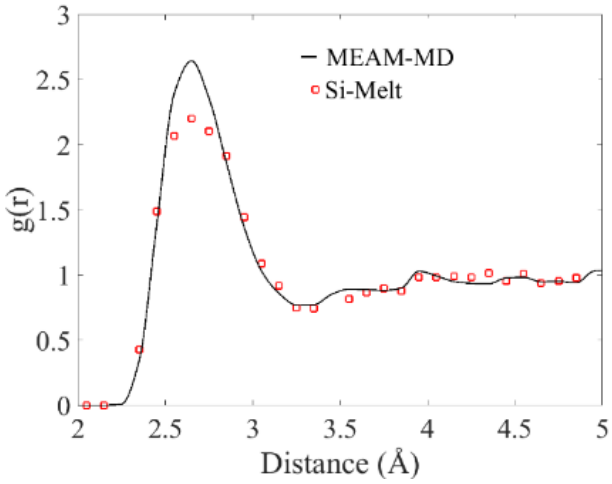

Figure 4. The radial distribution function of Si melt compared with first principle calculation data. High temperature properties of Si compared with data from experiments, first principle or MD simulation.

3.6. INTERATOMIC POTENTIAL FOR AL-SI

After verifying the melting properties of Si, the formation energies and elastic properties of AlSi alloys have been verified with previous first principle and MD data. Unlike the other metallic alloys, Al-Si has positive formation energies (Table 15). The MEAM potential is primarily fitted for the AlSi B1 structure. Then, we verify the results with other AlSi compounds, and modify the MEAM parameters ΔH, R_0, α, $C_{\min}$, $C_{\max}$ accordingly.

Once the MEAM parameters are fitted for the low temperature properties, the enthalpy of of Al-Si liquid with increasing Si content is calculated. As, shown in Figure 5 the enthalpy of liquid predicted by the MEAM potential is reasonably close to experimental data.

Table 14. The formation energy, elastic properties for AlSi phases predicted from 2NN-MEAM MD is compared with experimental/first principle. Superscript a, b and c denotes experimental, first principle/DFT of previous MD simulations respectively.

		ΔE_f (eV/atom)		Bulk Modulus (GPa)		C_{44}	
Formula	Structure	This Work	DFT/MD	This Work	DFT/MD	This Work	DFT/MD[54]
Al_4Si	R4	0.160	0.085[b] [114]	77.37	77.12[b] [114]	4.269	-
Al_3Si	$L1_2$	0.124	0.121[a] [54], 0.113[c] [54]	75.220	74.3, 96.7[c] [54]	21.923	24.1[b], 31.2[c]
Al_2Si	C1	0.231	0.178[b] [54], 0.157[c] [54]	62.689	62.9, 73.6[c] [54]	11.160	25.4[b], 15.3[c]
AlSi	B1	0.28	0.28[b] [54], 0.28[c] [54]	74.490	76.7, 76.4[c] [54], 85[c] [139]	19.255	10[b], -13[c]
	B2	0.206	0.291[b][54], 0.150[c][54]	71.0	78.8[a] [54], 102.1[c] [54]	25.756	22.4[b], 29.1[c]

The enthalpy of mixing could be modified to fit the experimental data, however the elastic properties at low temperature may alter slightly. As Al-Si has positive formation energies, the compounds will rarely occur naturally. The solubility of Si in Al will depend on the pressure applied on the solid solution. However, as the goal of the interatomic potential is to study nucleation and solidification, which can be done anyways as the melting properties are verified for both Si and Al. Along with that as the low temperature mechanical properties are also studied , the MEAM interatomic potentials can be directly use for mechanical failure of Al, Si and Al-Si alloys as well.

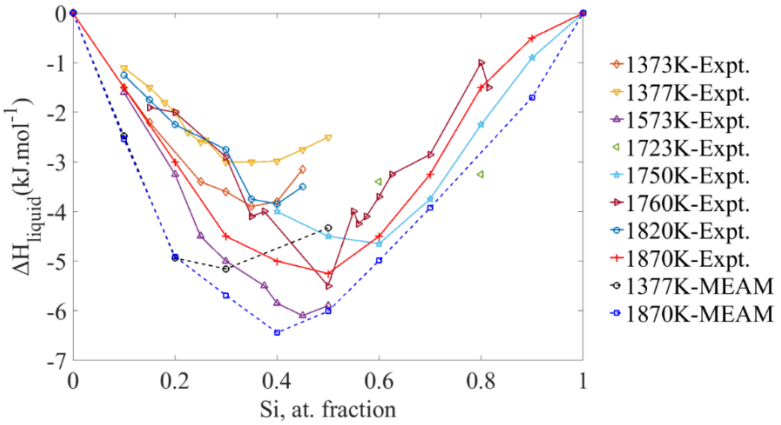

Figure 5. Liquid mixing enthalpy for Al-Si with increasing Si content. The experimental values for liquid Al-Si alloys has been taken from various experimental data [84, 140-142].

The liquidus temperature has been studied for Al-Si alloys up to 50 at. % Si. The solid-liquid coexistence temperatures are close to experimental data when the Si content is less. However, increasing Si content need high pressure to stabilize the Al-Si solid phases. Most applications on Si based alloy systems are done in low content of Si [143-145].

Table 15. The liquidous temperature from the experimental phase diagram is compared with the prediction of 2NN-MEAM results. The * is the eutectic point.

Al-Si Composition (Al-at. % of Si)	**Liquidous Temperature (K) (Expt.) [146]**	**Meam (K)**
Al	933.5	925
Al-5% Si	857	886±20
Al-12.2% Si*	850	1037±50
Al-20% Si	985	1107±50
Si	1690	1713

3.7 INTERATOMIC POTENTIAL FOR AL-GE

The MEAM interatomic potential for Ge has been developed by combining the Ge potential developed by Kim et. al. [52]. The melting point of Ge is estimated to be 2200 K by this MEAM, however similar to Al-Si, the solubility of Ge in Al-Ge alloys depends on the pressure. So, the focus here will be lower Ge content. As shown in Table 17, the formation energy and per atom volume data available for Al-Ge. The formation energies are good for B1, DO_3 and $L1_2$. The formation energies are also positive, which is similar to Al-Si alloys. After the formation energies and atomic volumes are fitted to the first principle data, we fit the potential for potential for Al-Ge radial distribution function (RDF), lattice parameters and liquid enthalpies. The results shown in Figure 6 (a), shows in long range the RDF is lower than the experimental results, which can be attributed to the difference in the structures of our study and previously performed first principle results.

Table 16. The formation energy and per atom volume for Al-Ge is compared with first principle data.

		ΔE_f (eV/atom)		V_0 (Å^3/atom)	
Formula	Structure	This Work	DFT [147]	This Work	DFT [147]
Al_3Ge	DO_3	0.198	0.170	17.499	17.699
	$L1_2$	0.128	0.102	17.494	17.146
AlGe	B1*	0.163	0.164	19.627	19.137
	B2	-0.084	0.195	17.061	17.831
	$L1_0$	0.214	0.175	17.857	17.823
	B19	-0.084	0.181	17.064	17.651
	B3	0.537	0.230	20.608	23.101

This is also to be noted that the first principle study on the structure factors were done on only 50 atoms. The first peak however, very close to the first principle results, which indicates that the first nearest neighbor is at the same position as it was found in the first principle studies. The lattice parameters also show upward trend with increasing Ge content (Figure 2(b)). The enthalpy of liquid also remains close to experimental data, but as the Ge content increases the solubility reduces, which in fact deviates the liquid formation energies for Al-Ge alloy.

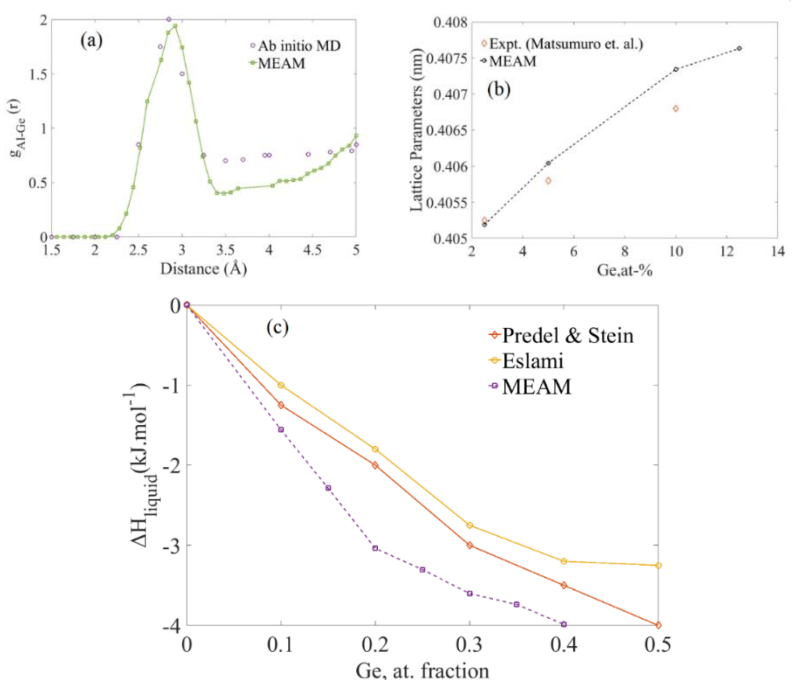

Figure 6. Therml expansion coefficiet, solid and liquid mixing enthalpy prediction by MEAM potential for Al-Ge. (a) Calculated radial distribution function of liquid Al-Ge. The Ab-inito MD data is taken from Wang et. al. [148]. (b) The increasing lattice parameter of Al-Ge alloy with increasing Ge content. The experimental data has been taken from Matsumuro et. al. [149]. Similar low temperature data can be also found in Degtyareva et. al. [150] (c) Liquid mixing enthalpy for Al-Ge with increasing Ge content is shown for 1273 K. The experimental values for liquid Al-Ge alloys has been taken from various experimental work [151, 152].

After fitting the low and high temperature properties, we verify the liquidus temperature for Al-Ge alloys. The results are close to the experimental data up to 40 at. % Ge. However, above 40% of the Ge content the temperature predicted by MD is considerably higher than the Al-Ge phase diagram. This can be attributed to the solubility as well as the prediction of Ge melting point by the MEAM potential. However, for lower Ge content the MEAM potential can predict reasonably good results for melting and solidification.

Table 17. The liquidous temperature from the experimental phase diagram is compared with the prediction of 2NN-MEAM results. The * is the eutectic point.

Al-Ge Composition (Al-at. % of Ge)	**Liquidous Temperature (K) (Expt.) [146]**	**MEAM (K)**
Al	933.5	925
Al-5% Ge	900	887.9±9
Al-10% Ge	875	854.2±6
Al-20% Ge	790	780±10
Al-28.4% Ge*	693	699.5±10
Al-40% Ge	840	860±10
Ge	1211.4	2200

4. CONCLUSION

In this study, we developed MEAM potentials for binary Al alloys for both lower and higher temperature applications. These binary potentials reproduce melting properties and

solid-liquid coexistence temperatures as predicted in the phase diagram of the Al-binary alloys. The fully metallic alloys such as Al-Cu, Al-Fe, Al-Ni and Al-Mg reproduces the enthalpies and coexistence temperatures more accurate than Al-Si and Al-Ge. Al-Si and Al-Ge has been studied up to 50 and 40 at. % of the alloying elements. The potentials are however, subject to further testing and improvements for Al-Si and Al-Ge. However, these potentials are one step toward designing multicomponent metallic alloys by simulations.

REFERENCES

[1] F. Buda, R. Car, and M. Parrinello, "Thermal expansion of c-Si via ab initio molecular dynamics," *Physical Review B,* vol. 41, p. 1680, 1990.

[2] H. Watanabe, N. Yamada, and M. Okaji, "Linear thermal expansion coefficient of silicon from 293 to 1000 K," *International journal of thermophysics,* vol. 25, pp. 221-236, 2004.

[3] M. Baskes, J. Nelson, and A. Wright, "Semiempirical modified embedded-atom potentials for silicon and germanium," *Physical Review B,* vol. 40, p. 6085, 1989.

[4] J. Allison, D. Backman, and L. Christodoulou, "Integrated computational materials engineering: a new paradigm for the global materials profession," *Jom,* vol. 58, pp. 25-27, 2006.

[5] M. F. Horstemeyer, *Integrated Computational Materials Engineering (ICME) for metals: using multiscale modeling to invigorate engineering design with science*: John Wiley & Sons, 2012.

[6] B.-J. Lee, "A modified embedded atom method interatomic potential for silicon," *Calphad,* vol. 31, pp. 95-104, 2007/03/01/ 2007.

[7] Y. A. Chang, S. Chen, F. Zhang, X. Yan, F. Xie, R. Schmid-Fetzer, *et al.*, "Phase diagram calculation: past, present and future," *Progress in Materials Science,* vol. 49, pp. 313-345, 2004.

[8] S. J. Cook and P. Clancy, "Comparison of semi-empirical potential functions for silicon and germanium," *Physical Review B,* vol. 47, p. 7686, 1993.

[9] F. H. Stillinger and T. A. Weber, "Computer simulation of local order in condensed phases of silicon," *Physical review B,* vol. 31, p. 5262, 1985.

[10] K. Laaziri, S. Kycia, S. Roorda, M. Chicoine, J. Robertson, J. Wang, *et al.*, "High-energy x-ray diffraction study of pure amorphous silicon," *Physical Review B,* vol. 60, p. 13520, 1999.

[11] R. A. Street, "Doping and the Fermi energy in amorphous silicon," *Physical Review Letters,* vol. 49, p. 1187, 1982.

[12] J. Fortner and J. Lannin, "Radial distribution functions of amorphous silicon," *Physical Review B,* vol. 39, p. 5527, 1989.

[13] M. H. Grabow, G. H. Gilmer, and A. F. Bakker, "Molecular dynamics studies of silicon solidification and melting," *MRS Online Proceedings Library Archive,* vol. 141, 1988.

[14] A. Mahata, M. A. Zaeem, and M. I. Baskes, "Understanding homogeneous nucleation in solidification of aluminum by molecular dynamics simulations," *Modelling and Simulation in Materials Science and Engineering,* vol. 26, p. 025007, 2018.

[15] M. M. J. Treacy and K. B. Borisenko, "The Local Structure of Amorphous Silicon," *Science,* vol. 335, pp. 950-953, 2012.

[16] A. Das, S. Ji, and Z. Fan, "Morphological development of solidification structures under forced fluid flow: a Monte-Carlo simulation," *Acta Materialia,* vol. 50, pp. 4571-4585, 2002.

[17] W. J. Boettinger, J. A. Warren, C. Beckermann, and A. Karma, "Phase-field simulation of solidification," *Annual review of materials research,* vol. 32, pp. 163-194, 2002.

[18] A. Karma, "Phase-field formulation for quantitative modeling of alloy solidification," *Physical Review Letters,* vol. 87, p. 115701, 2001.

[19] M. Zhu, C. Hong, D. Stefanescu, and Y. Chang, "Computational modeling of microstructure evolution in solidification of aluminum alloys," *Metallurgical and Materials Transactions B,* vol. 38, pp. 517-524, 2007.

[20] W. Luedtke and U. Landman, "Preparation, structure, dynamics, and energetics of amorphous silicon: A molecular-dynamics study," *Physical Review B,* vol. 40, p. 1164, 1989.

[21] J. Chessa, P. Smolinski, and T. Belytschko, "The extended finite element method (XFEM) for solidification problems," *International Journal for Numerical Methods in Engineering,* vol. 53, pp. 1959-1977, 2002.

[22] A. Dalhuijsen and A. Segal, "Comparison of finite element techniques for solidification problems," *International journal for numerical methods in engineering,* vol. 23, pp. 1807-1829, 1986.

[23] S. Roorda, W. Sinke, J. Poate, D. Jacobson, S. Dierker, B. Dennis, *et al.*, "Structural relaxation and defect annihilation in pure amorphous silicon," *Physical review B,* vol. 44, p. 3702, 1991.

[24] K. Kadau, T. C. Germann, and P. S. Lomdahl, "Molecular dynamics comes of age: 320 billion atom simulation on BlueGene/L," *International Journal of Modern Physics C,* vol. 17, pp. 1755-1761, 2006.

[25] Y. Shibuta, S. Sakane, E. Miyoshi, S. Okita, T. Takaki, and M. Ohno, "Heterogeneity in homogeneous nucleation from billion-atom molecular dynamics simulation of solidification of pure metal," *Nature communications,* vol. 8, p. 10, 2017.

[26] L. Pastewka, A. Klemenz, P. Gumbsch, and M. Moseler, "Screened empirical bond-order potentials for Si-C," *Physical Review B,* vol. 87, p. 205410, 2013.

[27] A. Mahata, M. Asle Zaeem, and M. I. Baskes, "Understanding homogeneous nucleation in solidification of aluminum by molecular dynamics simulations," *Modelling and Simulation in Materials Science and Engineering,* vol. 26, p. 025007, 2018.

[28] M. Horsch, J. Vrabec, and H. Hasse, "Modification of the classical nucleation theory based on molecular simulation data for surface tension, critical nucleus size, and nucleation rate," *Physical Review E,* vol. 78, p. 011603, 2008.

[29] X.-M. Bai and M. Li, "Test of classical nucleation theory via molecular-dynamics simulation," *The Journal of chemical physics,* vol. 122, p. 224510, 2005.

[30] G. C. Sosso, J. Chen, S. J. Cox, M. Fitzner, P. Pedevilla, A. Zen, *et al.*, "Crystal nucleation in liquids: Open questions and future challenges in molecular dynamics simulations," *Chemical reviews,* vol. 116, pp. 7078-7116, 2016.

[31] M. J. Mandell, J. P. McTague, and A. Rahman, "Crystal nucleation in a three-dimensional Lennard-Jones system: A molecular dynamics study," *The Journal of Chemical Physics,* vol. 64, pp. 3699-3702, 1976/05/01 1976.

[32] S.-N. Luo, A. Strachan, and D. C. Swift, "Nonequilibrium melting and crystallization of a model Lennard-Jones system," *The Journal of Chemical Physics,* vol. 120, pp. 11640-11649, 2004/06/22 2004.

[33] M. Maddox and K. Gubbins, "A molecular simulation study of freezing/melting phenomena for Lennard-Jones methane in cylindrical nanoscale pores," *The Journal of chemical physics,* vol. 107, pp. 9659-9667, 1997.

[34] P. L. Silvestrelli, A. Alavi, M. Parrinello, and D. Frenkel, "Ab initio molecular dynamics simulation of laser melting of silicon," *Physical review letters,* vol. 77, p. 3149, 1996.

[35] K. Yamaguchi and K. Itagaki, "Measurement of high temperature heat content of silicon by drop calorimetry," *Journal of Thermal Analysis and Calorimetry,* vol. 69, pp. 1059-1066, 2002/07/01 2002.

[36] M. Olette, "Measurements of the Heat Content of Silicon Between 1200° and 1550°," *Compt. rend.,* vol. 244, pp. 1033-36, 1957.

[37] P. Kantor, A. Kisel, and E. Fomichev, "Measurement of enthalpy and heat capacity of silicon at 1200-1900 K," *Ukr. Fiz. Zh,* vol. 5, pp. 358-62, 1960.

[38] A. T. Dinsdale, "SGTE data for pure elements," *Calphad,* vol. 15, pp. 317-425, 1991/10/01/ 1991.

[39] L. Lucas and G. Urbain, "Chimie physique-densite du silicium, du germanium, de lantimoine et du bismuth a letat liquide," *comptes rendus hebdomadaires des seances de l academie des sciences,* vol. 255, pp. 2414-&, 1962.

[40] M. Gayler, "Melting point of high-purity silicon," *Nature,* vol. 142, p. 478, 1938.

[41] T. B. Massalski, "Binary alloy phase diagrams," *ASM international,* vol. 3, p. 2874, 1992.

[42] I. Maxwell and A. Hellawell, "A simple model for grain refinement during solidification," *Acta Metallurgica,* vol. 23, pp. 229-237, 1975.

[43] L. Gránásy and T. Pusztai, "Diffuse interface analysis of crystal nucleation in hard-sphere liquid," *The Journal of Chemical Physics,* vol. 117, pp. 10121-10124, 2002/12/08 2002.

[44] M. S. Daw and M. I. Baskes, "Embedded-atom method: Derivation and application to impurities, surfaces, and other defects in metals," *Physical Review B,* vol. 29, p. 6443, 1984.

[45] S. Foiles, M. Baskes, and M. S. Daw, "Embedded-atom-method functions for the fcc metals Cu, Ag, Au, Ni, Pd, Pt, and their alloys," *Physical review B,* vol. 33, p. 7983, 1986.

[46] A. Sutton and J. Chen, "Long-range finnis–sinclair potentials," *Philosophical Magazine Letters,* vol. 61, pp. 139-146, 1990.

[47] M. I. Baskes, "Modified embedded-atom potentials for cubic materials and impurities," *Physical Review B,* vol. 46, pp. 2727-2742, 08/01/ 1992.

[48] M. I. Baskes and R. A. Johnson, "Modified embedded atom potentials for HCP metals," *Modelling and Simulation in Materials Science and Engineering,* vol. 2, pp. 147-163, 1994/01/01 1994.

[49] B.-J. Lee, J.-H. Shim, and M. Baskes, "Semiempirical atomic potentials for the fcc metals Cu, Ag, Au, Ni, Pd, Pt, Al, and Pb based on first and second nearest-neighbor modified embedded atom method," *Physical Review B,* vol. 68, p. 144112, 2003.

[50] S. M. Valone, M. I. Baskes, M. Stan, T. E. Mitchell, A. C. Lawson, and K. E. Sickafus, "Simulations of low energy cascades in fcc Pu metal at 300 K and constant volume," *Journal of nuclear materials,* vol. 324, pp. 41-51, 2004.

[51] M. Baskes and R. Johnson, "Modified embedded atom potentials for HCP metals," *Modelling and Simulation in Materials Science and Engineering,* vol. 2, p. 147, 1994.

[52] E. H. Kim, Y.-H. Shin, and B.-J. Lee, "A modified embedded-atom method interatomic potential for Germanium," *Calphad,* vol. 32, pp. 34-42, 2008.

[53] Y.-M. Kim and B.-J. Lee, "Modified embedded-atom method interatomic potentials for the Ti–C and Ti–N binary systems," *Acta materialia,* vol. 56, pp. 3481-3489, 2008.

[54] B. Jelinek, S. Groh, M. F. Horstemeyer, J. Houze, S.-G. Kim, G. J. Wagner, *et al.*, "Modified embedded atom method potential for Al, Si, Mg, Cu, and Fe alloys," *Physical Review B,* vol. 85, p. 245102, 2012.

[55] B.-J. Lee, W.-S. Ko, H.-K. Kim, and E.-H. Kim, "The modified embedded-atom method interatomic potentials and recent progress in atomistic simulations," *Calphad,* vol. 34, pp. 510-522, 2010.

[56] D. E. Dickel, M. I. Baskes, I. Aslam, and C. D. Barrett, "New interatomic potential for Mg–Al–Zn alloys with specific application to dilute Mg-based alloys," *Modelling and Simulation in Materials Science and Engineering,* vol. 26, p. 045010, 2018.

[57] E. Asadi, M. A. Zaeem, S. Nouranian, and M. I. Baskes, "Two-phase solid–liquid coexistence of Ni, Cu, and Al by molecular dynamics simulations using the modified embedded-atom method," *Acta Materialia,* vol. 86, pp. 169-181, 2015.

[58] E. Asadi, M. A. Zaeem, S. Nouranian, and M. I. Baskes, "Quantitative modeling of the equilibration of two-phase solid-liquid Fe by atomistic simulations on diffusive time scales," *Physical Review B,* vol. 91, p. 024105, 2015.

[59] E. Asadi and M. Asle Zaeem, "The anisotropy of hexagonal close-packed and liquid interface free energy using molecular dynamics simulations based on modified embedded-atom method," *Acta Materialia,* vol. 107, pp. 337-344, 2016/04/01/ 2016.

[60] S. Ryu and W. Cai, "Comparison of thermal properties predicted by interatomic potential models," *Modelling and Simulation in Materials Science and Engineering,* vol. 16, p. 085005, 2008/10/01 2008.

[61] W. J. Joost, S. Ankem, and M. M. Kuklja, "A modified embedded atom method potential for the titanium–oxygen system," *Modelling and Simulation in Materials Science and Engineering,* vol. 23, p. 015006, 2014.

[62] E. Lee, K.-R. Lee, M. Baskes, and B.-J. Lee, "A modified embedded-atom method interatomic potential for ionic systems: 2 NNMEAM+ Qeq," *Physical Review B,* vol. 93, p. 144110, 2016.

[63] Y.-M. Kim, N. J. Kim, and B.-J. Lee, "Atomistic modeling of pure Mg and Mg–Al systems," *Calphad,* vol. 33, pp. 650-657, 2009.

[64] J. H. Rose, J. R. Smith, F. Guinea, and J. Ferrante, "Universal features of the equation of state of metals," *Physical Review B,* vol. 29, pp. 2963-2969, 03/15/ 1984.

[65] J. M. Hughes, M. F. Horstemeyer, R. Carino, N. Sukhija, W. B. Lawrimore, S. Kim, *et al.*, "Hierarchical Bridging Between Ab Initio and Atomistic Level Computations: Sensitivity and Uncertainty Analysis for the Modified Embedded-Atom Method (MEAM) Potential (Part B)," *JOM,* vol. 67, pp. 148-153, 2015/01/01 2015.

[66] S. Plimpton, "Fast parallel algorithms for short-range molecular dynamics," *Journal of computational physics,* vol. 117, pp. 1-19, 1995.

[67] Y. Grin, F. R. Wagner, M. Armbrüster, M. Kohout, A. Leithe-Jasper, U. Schwarz, *et al.*, "CuAl2 revisited: Composition, crystal structure, chemical bonding, compressibility and Raman spectroscopy," *Journal of Solid State Chemistry,* vol. 179, pp. 1707-1719, 2006/06/01/ 2006.

[68] A. Meetsma, J. L. De Boer, and S. Van Smaalen, "Refinement of the crystal structure of tetragonal Al2Cu," *Journal of Solid State Chemistry,* vol. 83, pp. 370-372, 1989/12/01/ 1989.

[69] C. Wolverton and V. Ozoliņš, "Entropically Favored Ordering: The Metallurgy of ${\mathrm{Al}}_{2}\mathrm{Cu}$ Revisited," *Physical Review Letters,* vol. 86, pp. 5518-5521, 06/11/ 2001.

[70] W. Zhou, L. Liu, B. Li, Q. Song, and P. Wu, "Structural, Elastic, and Electronic Properties of Al-Cu Intermetallics from First-Principles Calculations," *Journal of Electronic Materials,* vol. 38, pp. 356-364, 2009/02/01 2009.

[71] M. M. a. M. Widom, "Alloy database [http://euler.phys.cmu.edu/alloy/]," 2009.

[72] F. Apostol and Y. Mishin, "Interatomic potential for the Al-Cu system," *Physical Review B,* vol. 83, p. 054116, 2011.

[73] J. L. Murray, "The aluminium-copper system," *International metals reviews,* vol. 30, pp. 211-234, 1985.

[74] S. Hu, M. Baskes, M. Stan, and L. Chen, "Atomistic calculations of interfacial energies, nucleus shape and size of θ′ precipitates in Al–Cu alloys," *Acta materialia,* vol. 54, pp. 4699-4707, 2006.

[75] V. Vaithyanathan, C. Wolverton, and L. Q. Chen, "Multiscale Modeling of Precipitate Microstructure Evolution," *Physical Review Letters,* vol. 88, p. 125503, 03/06/ 2002.

[76] F. R. Eshelman and J. F. Smith, "Single-crystal elastic constants of Al2Cu," *Journal of Applied Physics,* vol. 49, pp. 3284-3288, 1978/06/01 1978.

[77] C. Ravi, C. Wolverton, and V. Ozoliņš, "Predicting metastable phase boundaries in Al–Cu alloys from first-principles calculations of free energies: The role of atomic vibrations," *EPL (Europhysics Letters),* vol. 73, p. 719, 2006.

[78] Y. S. Touloukian, "Thermal expansion: metallic elements and alloys," *Thermophysical properties of matter,* vol. 12, 1975.

[79] S.-M. Liang and R. Schmid-Fetzer, "Thermodynamic assessment of the Al–Cu–Zn system, part II: Al–Cu binary system," *Calphad,* vol. 51, pp. 252-260, 2015.

[80] V. Witusiewicz, U. Hecht, S. Fries, and S. Rex, "The Ag–Al–Cu system: Part I: Reassessment of the constituent binaries on the basis of new experimental data," *Journal of alloys and compounds,* vol. 385, pp. 133-143, 2004.

[81] J. Hair and D. Downie, "Thermodynamic properties of the Cu-Al system: correlation with bonding mechanisms," in *Faraday Symposia of the Chemical Society*, 1973, pp. 56-63.

[82] R. Hultgren, P. D. Desai, D. T. Hawkins, M. Gleiser, and K. K. Kelley, "Selected values of the thermodynamic properties of binary alloys," National Standard Reference Data System1973.

[83] K. Itagaki and A. Yazawa, "Heats of Mixing in Liquid Copper or Gold Binary Alloys," *Transactions of the Japan Institute of Metals*, vol. 16, pp. 679-686, 1975.

[84] D. S. Kanibolotsky, O. A. Bieloborodova, N. V. Kotova, and V. V. Lisnyak, "Thermodynamic properties of liquid Al-Si and Al-Cu alloys," *Journal of Thermal Analysis and Calorimetry*, vol. 70, pp. 975-983, 2002/10/01 2002.

[85] V. Sandakov, S. VD, Y. ESIN, and P. GELD, "HEATS OF FORMATION OF LIQUID COPPER-ALUMINUM ALLOYS," *RUSSIAN JOURNAL OF PHYSICAL CHEMISTRY, USSR*, vol. 45, pp. 1150-&, 1971.

[86] V. Witusiewicz, U. K. Stolz, I. Arpshofen, and F. Sommer, "Thermodynamics of Liquid Al-Cu-Zr Alloys," *Zeitschrift fur Metallkunde*, vol. 89, pp. 704-713, 1998.

[87] H. Flandorfer, M. Rechchach, A. Elmahfoudi, L. Bencze, A. Popovič, and H. Ipser, "Enthalpies of mixing of liquid systems for lead free soldering: Al–Cu–Sn system," *The Journal of Chemical Thermodynamics*, vol. 43, pp. 1612-1622, 2011/11/01/ 2011.

[88] B. Predel, "Al-Cu (Aluminum-Copper)," in *Ac-Au – Au-Zr*, O. Madelung, Ed., ed Berlin, Heidelberg: Springer Berlin Heidelberg, 1991, pp. 1-9.

[89] B. Predel, H. Landolt, and R. Börnstein, *Phase equilibria, crystallographic and thermodynamic data of binary alloys* vol. 5: Springer, 1991.

[90] D. Nguyen-Manh and D. Pettifor, "Electronic structure, phase stability and elastic moduli of AB transition metal aluminides," *Intermetallics*, vol. 7, pp. 1095-1106, 1999.

[91] D. Nguyen-Manh and D. G. Pettifor, "Electronic structure, phase stability and elastic moduli of AB transition metal aluminides," *Intermetallics*, vol. 7, pp. 1095-1106, 1999/10/01/ 1999.

[92] A. C. e Silva, J. Ågren, M. T. Clavaguera-Mora, D. Djurovic, T. Gomez-Acebo, B.-J. Lee, *et al.*, "Applications of computational thermodynamics—the extension from phase equilibrium to phase transformations and other properties," *Calphad*, vol. 31, pp. 53-74, 2007.

[93] W. Pearson, "Lattice spacings and structures of metals and alloys," *Vols. I and II (Pergamon Press, Oxford, 1964, 1967),* 1958.

[94] K. Rzyman and Z. Moser, "Calorimetric studies of the enthalpies of formation of Al3Ni2, AlNi and AlNi3," *Progress in Materials Science,* vol. 49, pp. 581-606, 2004.

[95] H. L. L. H.D. Dannohl, *Z. Metall.,* vol. 65, p. 642, 1974.

[96] H. L. L. E.Th. Henig, *Z. Metall.,* vol. 66 p. 98, 1975.

[97] O. Kubaschewski and W. A. Dench, "The heats of formation in the systems titanium-aluminium and titanium-iron," *Acta Metallurgica,* vol. 3, pp. 339-346, 1955/07/01/ 1955.

[98] S. Meschel, O. Kleppa, J. Faulkner, and R. Jordan, "Metallic alloys: experimental and theoretical perspectives," *NATO ASI Series E: Applied Sciences,* vol. 256, p. 103, 1994.

[99] K. Rzyman and Z. Moser, "Calorimetric studies of the enthalpies of formation of Al3Ni2, AlNi and AlNi3," *Progress in Materials Science,* vol. 49, pp. 581-606, 2004/01/01/ 2004.

[100] P. A. Korzhavyi, A. V. Ruban, A. Y. Lozovoi, Y. K. Vekilov, I. Abrikosov, and B. Johansson, "Constitutional and thermal point defects in B 2 NiAl," *Physical Review B,* vol. 61, p. 6003, 2000.

[101] O. Kubaschewski, "The heats of formation in the system aluminium + nickel + titanium," *Transactions of the Faraday Society,* vol. 54, pp. 814-820, 1958.

[102] A. Pasturel, C. Colinet, A. T. Paxton, and M. v. Schilfgaarde, "First-principles determination of the Ni-Al phase diagram," *Journal of Physics: Condensed Matter,* vol. 4, pp. 945-959, 1992/01/27 1992.

[103] A. Kumar, A. Chernatynskiy, T. Liang, K. Choudhary, M. J. Noordhoek, Y.-T. Cheng, *et al.*, "Charge optimized many-body (COMB) potential for dynamical simulation of Ni–Al phases," *Journal of Physics: Condensed Matter,* vol. 27, p. 336302, 2015.

[104] G. Simmons and H. Wang, "Single crystal elastic constants and calculated aggregate properties," 1971.

[105] G. Simmons, "Single crystal elastic constants and calculated aggregate properties," SOUTHERN METHODIST UNIV DALLAS TEX1965.

[106] K. Rzyman, Z. Moser, R. Watson, and M. Weinert, "Enthalpies of formation of Ni 3 Al: Experiment versus theory," *Journal of phase equilibria,* vol. 17, pp. 173-178, 1996.

[107] I. Ansara, N. Dupin, H. L. Lukas, and B. Sundman, "Thermodynamic assessment of the Al□Ni system," *Journal of Alloys and Compounds,* vol. 247, pp. 20-30, 1997/01/30/ 1997.

[108] E.-T. H. a. H. L. Luke, *Z. Mrtulltie,* vol. 66, p. 98, 1975.

[109] F. R. De Boer, W. Mattens, R. Boom, A. Miedema, and A. Niessen, "Cohesion in metals," 1988.

[110] S. Kek, C. Rzyman, and F. Sommer, "Determination of the Enthalpy of Formation of Ternary Ni3Al-Based Alloys," *An. Fis. Ser. B,* vol. 86, pp. 31-38, 1990.

[111] K. Rzyman, Z. Moser, R. E. Watson, and M. Weinert, "Enthalpies of formation of AlNi: Experiment versus theory," *Journal of Phase Equilibria,* vol. 19, p. 106, 1998/04/01 1998.

[112] P. Nash and O. Kleppa, "Composition dependence of the enthalpies of formation of NiAl," *Journal of Alloys and Compounds,* vol. 321, pp. 228-231, 2001/06/14/ 2001.

[113] D. Shi, B. Wen, R. Melnik, S. Yao, and T. Li, "First-principles studies of Al–Ni intermetallic compounds," *Journal of Solid State Chemistry,* vol. 182, pp. 2664-2669, 2009/10/01/ 2009.

[114] A. Jain, S. P. Ong, G. Hautier, W. Chen, W. D. Richards, S. Dacek, *et al.*, "Commentary: The Materials Project: A materials genome approach to accelerating materials innovation," *APL Materials,* vol. 1, p. 011002, 2013/07/01 2013.

[115] R. E. Watson and M. Weinert, "Transition-metal aluminide formation: Ti, V, Fe, and Ni aluminides," *Physical Review B,* vol. 58, pp. 5981-5988, 09/01/ 1998.

[116] A. Fourdeux and P. Lesbats, "Annealing out of quenched-in vacancies in an ordered B2 type Fe-Al single crystal," *Philosophical Magazine A,* vol. 45, pp. 81-93, 1982.

[117] N. Junqua, J. Desoyer, and P. Moine, "Electron microscopy observation of quenching defects in an ordered alloy of B2 type: Fe–40 at% Al," *Physica status solidi (a),* vol. 18, pp. 387-395, 1973.

[118] M. Mendiratta and C. Law, "Dislocation energies and mobilities in B2-ordered Fe-Al alloys," *Journal of materials science,* vol. 22, pp. 607-611, 1987.

[119] C. Vailhé and D. Farkas, "Shear faults and dislocation core structure simulations in B2 FeAl," *Acta Materialia,* vol. 45, pp. 4463-4473, 1997/11/01/ 1997.

[120] E. Lee and B.-J. Lee, "Modified embedded-atom method interatomic potential for the Fe–Al system," *Journal of Physics: Condensed Matter,* vol. 22, p. 175702, 2010/04/12 2010.

[121] G. P. Das, B. K. Rao, P. Jena, and S. C. Deevi, "Electronic structure of substoichiometric Fe-Al intermetallics," *Physical Review B,* vol. 66, p. 184203, 11/12/ 2002.

[122] D. Connétable and P. Maugis, "First principle calculations of the κ-Fe3AlC perovskite and iron–aluminium intermetallics," *Intermetallics,* vol. 16, pp. 345-352, 2008/03/01/ 2008.

[123] F. Lechermann, M. Fähnle, and J. M. Sanchez, "First-principles investigation of the Ni–Fe–Al system," *Intermetallics,* vol. 13, pp. 1096-1109, 2005/01/01/ 2005.

[124] L. Shaojun, D. Suqing, and M. Benkun, "First-principles calculation of vibrational entropy for Fe-Al compounds," *Physical Review B,* vol. 58, pp. 9705-9709, 10/15/ 1998.

[125] N. Sodré, P. Guillermo Gonzales-Ormeño, H. M. Petrilli, and C. G. Schön, "Ab initio calculation of the BCC Fe–Al–Mo (Iron–Aluminum–Molybdenum) phase diagram: Implications for the nature of the τ2 phase," *Calphad,* vol. 33, pp. 576-583, 2009/09/01/ 2009.

[126] A. Kellou, T. Grosdidier, J. M. Raulot, and H. Aourag, "Atomistic study of magnetism effect on structural stability in Fe3Al and Fe3AlX (X = H, B, C, N, O) alloys," *physica status solidi (b),* vol. 245, pp. 750-755, 2008/04/01 2008.

[127] C. J. Smithells and E. A. Brandes, *Smithells metals reference book,* 1992.

[128] P. Maugis, J. Lacaze, R. Besson, and J. Morillo, "Ab Initio calculations of phase stabilities in the Fe−Al−C system and CALPHAD-Type assessment of the iron-rich corner," *Metallurgical and Materials Transactions A,* vol. 37, pp. 3397-3401, 2006/12/01 2006.

[129] P. G. Gonzales-Ormeño, H. M. Petrilli, and C. G. Schön, "Ab-initio calculations of the formation energies of BCC-based superlattices in the Fe□Al system," *Calphad,* vol. 26, pp. 573-582, 2002/12/01/ 2002.

[130] P. D. Desai, "Thermodynamic Properties of Selected Binary Aluminum Alloy Systems," *Journal of Physical and Chemical Reference Data,* vol. 16, pp. 109-124, 1987/01/01 1987.

[131] M. Friák and J. Neugebauer, "Ab initio study of the anomalous volume-composition dependence in Fe–Al alloys," *Intermetallics,* vol. 18, pp. 1316-1321, 2010/07/01/ 2010.

[132] C. L. Fu and M. H. Yoo, "Deformation behavior of B2 type aluminides: FeAl and NiAl," *Acta Metallurgica et Materialia,* vol. 40, pp. 703-711, 1992/04/01/ 1992.

[133] J. Breuer, A. Grün, F. Sommer, and E. Mittemeijer, "Enthalpy of formation of B2-Fe 1− x Al x and B2-(Ni, Fe) 1− x Al x," *Metallurgical and Materials Transactions B,* vol. 32, pp. 913-918, 2001.

[134] J. Elliott and F. Woolley, "Heats of solution of aluminum, copper, and silicon in liquid iron," *Trans Metall Soc AIME,* vol. 239, pp. 1872-1883, 1967.

[135] M. Petrushevsky, Y. Esin, P. Geld, and V. Sandakov, "Concentration Dependence of the Enthalpy of Formation of Molten Fe-Al Alloys," *Izvest. Akad. Nauk SSSR Metally,* pp. 193-197, 1972.

[136] H.-D. Dannöhl, "Kalorimetrische Bestimmung der Bildungsenthalpien einiger intermetallischer Phasen," Verlag nicht ermittelbar, 1971.

[137] H. Okamoto, "Al-Mg (aluminum-magnesium)," *Journal of Phase Equilibria,* vol. 19, p. 598, 1998/12/01 1998.

[138] I. Štich, R. Car, and M. Parrinello, "Structural, bonding, dynamical, and electronic properties of liquid silicon: An ab initio molecular-dynamics study," *Physical Review B,* vol. 44, pp. 4262-4274, 09/01/ 1991.

[139] K. Gall, M. Horstemeyer, M. Van Schilfgaarde, and M. Baskes, "Atomistic simulations on the tensile debonding of an aluminum–silicon interface," *Journal of the Mechanics and Physics of Solids,* vol. 48, pp. 2183-2212, 2000.

[140] J. Bros, H. Eslami, and P. Gaune, "Thermodynamics of Al—Si and Al—Ge—Si liquid alloys: Enthalpies of formation by high temperature calorimetry," *Berichte der Bunsengesellschaft für physikalische Chemie,* vol. 85, pp. 333-336, 1981.

[141] D. Kanibolotsky, O. Bieloborodova, N. Kotova, and V. Lisnyak, "Thermodynamic properties of liquid Al-Si and Al-Cu alloys," *Journal of thermal analysis and calorimetry,* vol. 70, pp. 975-983, 2002.

[142] V. Sudavtsova, G. Batalin, and V. Tutyevich, "Heat of Mixing Liquid Alloys of the Si--Al--Ti System," *Sov. Prog. Chem.,* vol. 52, pp. 23-25, 1986.

[143] H. Torabian, J. Pathak, and S. Tiwari, "Wear characteristics of Al-Si alloys," *Wear,* vol. 172, pp. 49-58, 1994.

[144] E. Ogris, A. Wahlen, H. Lüchinger, and P. Uggowitzer, "On the silicon spheroidization in Al–Si alloys," *Journal of Light Metals,* vol. 2, pp. 263-269, 2002.

[145] V. S. Zolotorevsky, N. A. Belov, and M. V. Glazoff, *Casting aluminum alloys* vol. 12: Elsevier Amsterdam, 2007.

[146] J. L. Murray and A. J. McAlister, "The Al-Si (Aluminum-Silicon) system," *Bulletin of Alloy Phase Diagrams,* vol. 5, p. 74, 1984/02/01 1984.

[147] J. E. Saal, S. Kirklin, M. Aykol, B. Meredig, and C. Wolverton, "Materials design and discovery with high-throughput density functional theory: the open quantum materials database (OQMD)," *Jom,* vol. 65, pp. 1501-1509, 2013.

[148] S. Wang, C. Wang, F.-C. Chuang, J. R. Morris, and K. Ho, "Ab initio molecular dynamics simulation of liquid Al x Ge 1− x alloys," *Physical Review B,* vol. 70, p. 224205, 2004.

[149] A. Matsumuro, K. Murata, K. Sakai, and M. Senoo, "Elastic and superconducting properties of supersaturated Al-Si and Al-Ge solid-solution alloys treated under a 5.4 GPa pressure," *Journal of Materials Science,* vol. 28, pp. 5836-5842, 1993/01/01 1993.

[150] V. F. Degtyareva, G. V. Chipenko, I. T. Belash, O. I. Barkalov, and E. G. Ponyatovskii, "F.C.C. Solid Solutions in Al□Ge and Al□Si Alloys under high Pressure," *physica status solidi (a),* vol. 89, pp. K127-K131, 1985/06/16 1985.

[151] S. Srikanth, D. Sanyal, and P. Ramachandrarao, "A re-evaluation of the Al□Ge system," *Calphad,* vol. 20, pp. 321-332, 1996/09/01/ 1996.

[152] H. Eslami, J. De Franceschi, M. Gambino, and J. Bros, "An Electromotive-Force Study of the Activity of Aluminium in Al-Ga, Al-Ge and Al-Ga-Ge Systems," *Zeitschrift fuer Naturforschung A,* vol. 34, pp. 810-817, 1979.

VI. EFFECTS OF SOLIDIFICATION DEFECTS ON NANOSCALE MECHANICAL PROPERTIES OF RAPID DIRECTIONALLY SOLIDIFIED AL-CU ALLOY

Avik Mahata[1] and Mohsen Asle Zaeem[1,2*]

[1] Department of Materials Science and Engineering, Missouri University of Science and Technology, Rolla, MO 65409, USA

[2] Department of Mechanical Engineering, Colorado School of Mines, Golden, CO 40801, USA

ABSTRACT

Directional solidification of Al-11 at % Cu is investigated by molecular dynamics (MD) simulations utilizing second nearest neighbor modified embedded atom method (2NN-MEAM) interatomic potential. The condition for directional solidification is produced by imposing dissimilar temperatures at the model boundaries along the [100] solidification direction to create a temperature gradient. During solidification, the solid-liquid front travels through the Al-Cu liquid along the [100] direction towards the high temperature end. At the initial stages of solidification, several solidification defects such as twins, stacking faults, and grain boundaries form. As directional solidification progresses, grains elongate along the solidification direction, and at the final stages of solidification no new defects or grain boundaries form. The elongated grain boundaries form a few layers with lamellar like structures along [100]. When the solidified polycrystalline is deformed in the [001] direction, glide of partial dislocations happen around the grain boundaries, whereas during elongation along [100] some defects from in the Al-Cu matrix. Since formation of defects requires more energy, the solidified samples

show a higher tensile strength and strain when deformed along the [100] solidification direction.

1. INTRODUCTION

Rapid directional solidification happens in several manufacturing processes, especially in additive manufacturing (AM) of metals and alloys. AM has become an exciting technique for manufacturing complex components and/or functionally graded materials from the instructions provided digitally [1]. In AM, instead of conventional joining and machining, manufacturing is done layer by layer addition of materials. The most common way to add metals and alloys is by layer by layer through rapid unidirectional melting and solidification. State of the art AM have successfully printed components made of several metallic systems such as, Al, Co, Ni, Ti, Fe and their alloys [1-4]. For metallic systems, the AM processes are generally based on fusion, and the ease of fusion can be determined by the weldability of the metals/alloys. If a metallic system is easy to weld, it will be also practical for AM processing. Compared to the conventional machining process, AM needs much less material and most of the material converts to the final product. Most of the AM materials researches are focused on harder materials such as Ti and Ni and their alloys [5]. Al and its alloys are known for lower weight to density ratio and lower melting point, but there has not been sufficient research on these alloys for AM processing.

AM processes, such as selective laser melting (SLM) [6] and powder-feeding-based laser metal deposition (LMD) [7], involve rapid melting followed by rapid solidification.

The influence of nano/microstructures developed after the rapid liquid- solid transformation on mechanical properties is not fully understood. Although Al cast alloys seem to be well suited for AM processing, they suffer from lower mechanical performance relative to precipitation hardened wrought aluminum alloys [8-10]. Thus, studying deformation and mechanical behavior after rapid unidirectional solidification of Al can provide useful insights for further development of Al alloys for AM processing.

Computational modeling can play a critical role in understanding the nano/microstructure-property-processing relationships in AM processes. Integrating models at several length and time scales are required to replicate the experimental melting-solidification in AM processes. Different theoretical or computational tools such as the classical nucleation theory (CNT) [11, 12], density function theory (DFT) calculations [13], molecular dynamics (MD) [14-16], Monte Carlo (MC) [17, 18], phase-field [19-23], cellular automata [24, 25] have been used to study solidification and nucleation phenomena. However, solidification by nucleation is an atomistic phenomenon, which starts in the interior part of the liquid. Phase-field, cellular automata, and finite-element models generally represent length and time scales much larger than those of the crystal nucleation and can't inherently account for solidification defects, whereas DFT or Monte Carlo simulations can only represent a few hundred atoms, which is barely enough to represent a single critical crystal nucleus. MD simulations with proper and efficient interatomic potentials are capable of nanoscale study of solidification [16, 26, 27]. MD simulation has been also extended to billions of atoms, which is in submicron length scales [28].

There are a few studies in which atomistic simulations are utilized to study rapid melting and solidification process in AM processes [29, 30]. For example, Monte Carlo simulations were recently used to preform uncertainty quantification in mechanical properties of laser sintered nanoparticles [30], and in a separate work MD simulations were utilized to simulate the melting of nanoscale powders in SLM [29]. There is no study on directional solidification at nanoscale and the subsequent mechanical properties.

In this work, we perform rapid directional solidification of Al-Cu alloy (Al-11 at% Cu) by applying three different temperature gradients. The directional solidification produces inhomogeneous polycrystalline structures. We study solidification defects, such as twins, GBs, Cu segregation, and Al_2Cu precipitation. We also investigate the deformation behavior and mechanical properties of the rapid directionally solidified polycrystalline Al-Cu alloy by uniaxial tensile simulations.

2. COMPUTATIONAL METHODOLOGY

In Al-11 at% Cu mixture there are three fundamental interactions between atoms: Al-Al, Cu-Cu and Al-Cu. The second nearest neighbor modified embedded atom method (2NN MEAM) interatomic potential of Al developed by Lee and Baskes [31] was used is this work for the interaction between Al-Al and Cu-Cu. We recently tested this interatomic potential which showed reliable predictions of low and high temperature properties of Al and Cu [16, 32]. Table 1 shows the detailed properties of Al and Cu predicted by 2NN-MEAM MD simulations. The interatomic potential was recently extended for Al-Cu

interactions, which also shows good agreement with experimental phase diagram of Al-Cu (up to 33 at% Cu) and various properties of Al2Cu θ/θ' [33].

Table 1. The low temperature elastic properties and high temperature melting properties of Al predicted by 2NN-MEAM MD simulations.

	Al		**Cu**	
Properties	Experiments	MEAM MD [32]	Experiments	MEAM MD [34]
Bulk Modulus (GPa)	76.4[a]	79.4	143.5[a]	166
C_{11} (GPa)	111.5[a]	114.3	176.8[a]	176.8
C_{12} (GPa)	58.8[a]	61.9	126.9[a]	125.0
C_{44} (GPa)	29.5[a]	31.6	81.8[a]	81.8
Specific Heat (J mol^{-1} K^{-1})	26.15[b]	24.70	25.30[b]	24.50
Thermal Expansion Coeff. (10^6 K^{-1})	17.31[b]	23.50	14.76[b]	17.0
Melting Point (T_m) (K)	934[c]	925	1357[c]	1320
solid–liquid interface free energy (mJ/m^2)	168.9±21 to 158±30[d]	172.6	237±26 to 270[d]	255.0

[a] Reference [35] , [b] Reference [36], [c] Reference [36-38], [d] Reference [39-41].

The Al-Cu simulation box with size of 50×50×50 nm^3 (125×125×125 unit cells, with ~8 M atoms) was created by randomly distributing 11 at% Cu in Al. Figure 1(a) shows the initial dimensions for the simulation box. To prepare the homogenous Al-Cu melt, the simulation box was equilibrated at 1,500 K for 150 ps with a time step of 3 fs. Temperature and pressure were controlled by Nose-Hoover thermostat and Parrinello-Rahman barostat

[42], respectively. Periodic boundary conditions were employed in all three directions during the melt preparation. All the MD simulations were performed in parallel LAMMPS [43] code. The OVITO visualization package was used to monitor the melting, solidification and deformation processes [44]. Within OVITO, common neighbor analysis (CNA) was used [45] to identify the local crystalline structure of atoms. We also utilized orientation coloring to study the grain orientations. CNA was used to identify the primary fcc crystal structures. These fcc atoms are always align along the coordination axes (i.e., x', y', z'), but these coordination axes are not always aligned with the principle axes (i.e., x, y, z) of simulation box. The orientation coloring shows, orientation of the grains from the principle axes, and for the coloring purposes we only considered the orientation from the principle axis Z. The coloring scheme was applied in Ovito, and the details of the implementation can be found in Larsen et al. work [46].

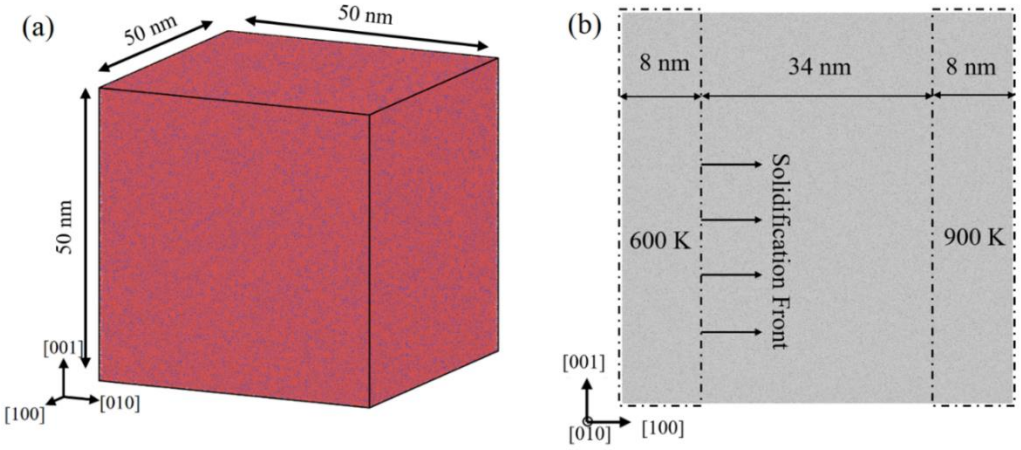

Figure 1. Simulation box at (a) initial melt with temperature of 1,500 K. The red atoms are Al and 11 at% Cu is distributed in the Al matrix is colored blue. (b) The initial simulation set up for the directional solidification. The solid front travel in the [100] direction towards the hotter region (900 K in this case).

To facilitate directional solidification, two regions are created at the two end of the simulation box in the [100] direction, Figure 1(b). The low temperature region is kept at a constant temperature of 600 K, and three different temperatures (800 K, 850 K and 900 K) is applied at the high temperature region for three distinct simulations. We refer to the 600-800 K box as Case-1, 600-850 K box as Case-2, and 600-900 K box as Case-3 throughout the paper. At the two temperature regions, each with 8 nm thickness (Figure 1(b)), the temperature is kept constant by applying Langevin thermostat. The temperature is not controlled for 34 nm region in the middle region creating a temperature gradient. Non-periodic boundary condition was applied in the direction of the solidification. The details of the different simulations performed is provided in Table 2.

Table 2. Simulation cases; three different temperature gradient for directional solidification, and two strain rates for uniaxial tensile deformation in two directions (total of 3 solidification simulations and 12 deformation simulations). A single crystal Al-Cu is also deformed at the same strain rates and temperatures (2 cases).

Temperature Regions	600-800 K (Case-1), 600-850 K (Case-2), and 600-900 K (Case-3)
Strain rate (s^{-1})	10^9 (SR1) and 10^{10} (SR2)
Deformation temperature	300 K

3. RESULTS AND DISCUSSIONS

3.1. DIRECTIONAL SOLIDIFICATION

In rapid directional solidification process, serval twins form (red atoms in Figure 2(a) and (b)) inside the fcc grains (green atoms in Figure 2(a) and (b)), especially in the

beginning of the process when smaller grains are forming. At each spontaneous time, the solidified part of the Al-Cu simulation box acts as solid seeds for rest of the liquid. The solidification font moves towards the liquid and gradually transform it into solid crystalline. The new solid formation happens in a much slower pace than the initial solidification, as a result there is not much defects or twins observed after initial solidification stages. Three dimensional (3D) views are shown in Figure 2(b) and (c). The grains generally elongate along the temperature gradient. Figure 2(c) shows the grain boundaries (GBs) and grain orientations. Initially several randomly orientated grains form, however as the solidification font travelled towards the liquid region, many of them dissolved in the surviving grains. It can be also visualized from Figure 2 that only few grains actually elongate.

The average temperature was measured along the solidification direction and shown in Figure 3(a). The temperature gradually increases from the lower to the higher temperature region. The amount of solidified Al-Cu can also be identified from the percentage of crystalline atoms, which is plotted in Figure 3(b).

3.2 FORMATION OF TWINS AND DETWINNING

Directional solidification creates different types of nanostructures in different planes. The nanostructures in the (001) plane plane (Figure 4(a) and (010)plane (Figure 4(b)) look very similar; at the left side of the domain, where initial stage of solidification occurs, smaller grain sizes and both coherent twin boundaries (CTBs) and five-fold twin are present. Figure 4(d) and (e) show 3D and 2D slices of planes from the simulation box along the (100) plane. Only CTBs are seen in the (100) plane.

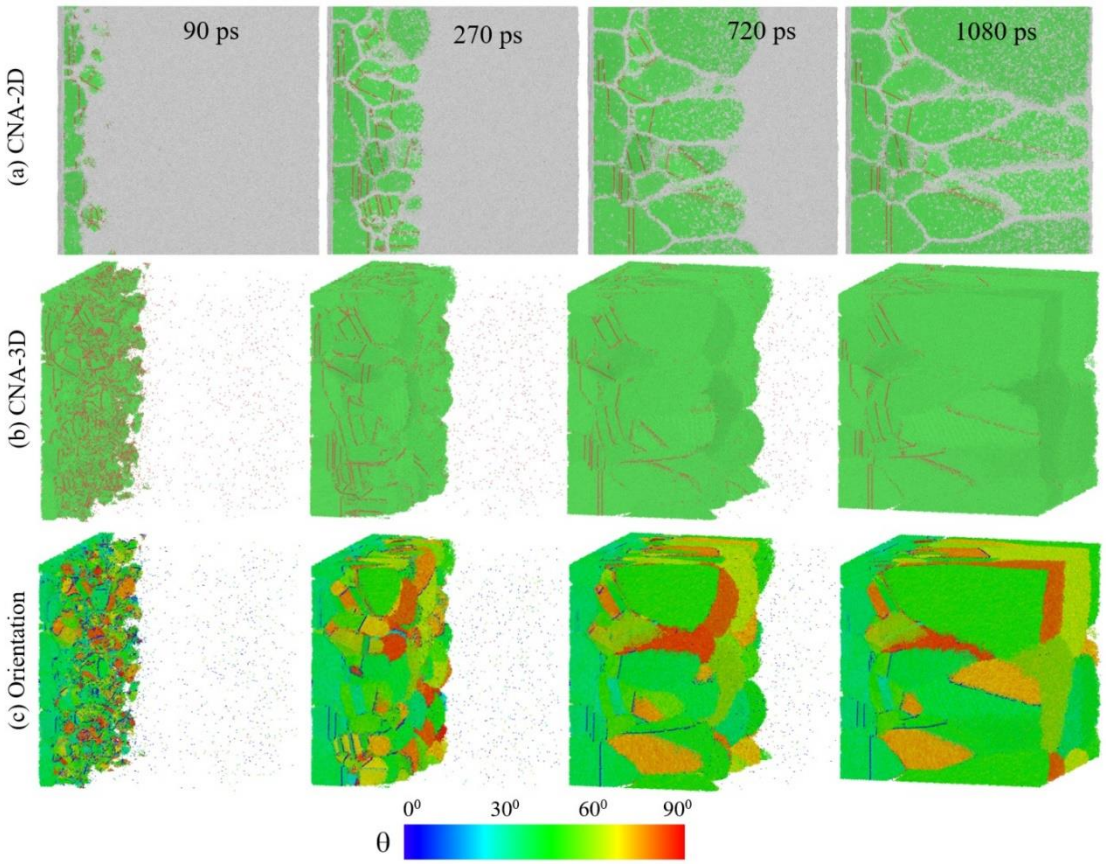

Figure 2. Snapshots of the directional solidification of Al-11 at% Cu for Case-3 solidification. The figures are (a) 2D and (b) 3D views of solidification font travelling through the simulation box; atoms are colored by CNA coloring: green atoms are fcc, red atoms are hcp and the white atoms represents the liquid and amorphous solids. (c) 3D views of grains forming during the solidification with different orientations.

As the solidification progresses and some grains become elongated and larger, no CTBs or five-fold twins are observed. The average grain size in (010) plane is shown in a trapezoidal form in Figure 5 for Case-2 solidification. Fivefold twins is observed during the initial stages of solidification, as shown in Figure 4(a) and (b). In general, fivefold twinning can happen in metals in a layer-by-layer growth during nucleation, successive growth twinning, or by deformation [47]. We previously observed formation of similar

fivefold twins in solidification of pure Al [48], and the process of forming successive twin boundaries is similar to what we observe here for Al-11 at% Cu.

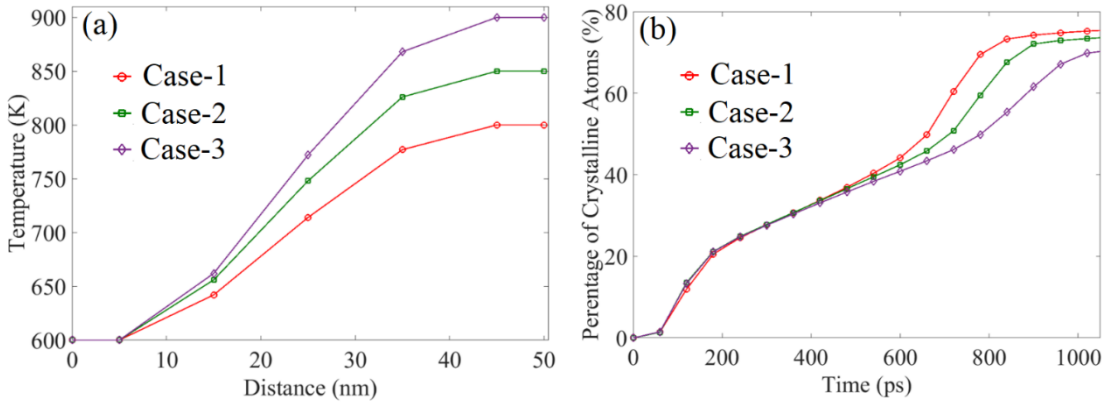

Figure 3. (a) Average temperature of atoms along the [100] solidification direction for three different initial simulation set ups, (b) Number of crystalline atoms in each of the simulations during the solidification.

During the initial stages of solidification and packing of atoms to form nanocrystalline fcc Al, small size ordered subunits of hcp atoms also form as twin boundaries to compensate the angular misfit between different fcc growth planes. Formation of CTB and fivefold twins is consistent with the literature data on other fcc metals [47, 49, 50]. Also, fivefold twin structure formations by successive twinning growth on alternate cozonal twin planes was also previously observed in the solid phase crystallization of metal [51]. However, in our cases of directional solidification, formation of fivefold twins is only possible at the (001) and (010) planes. In the (100) plane, which is the solidification font, no multifold twins are observed (Figure 4(e)). We can also

observe from Figure 4(e) that the grains from slice II to slice IV gradually become defect free.

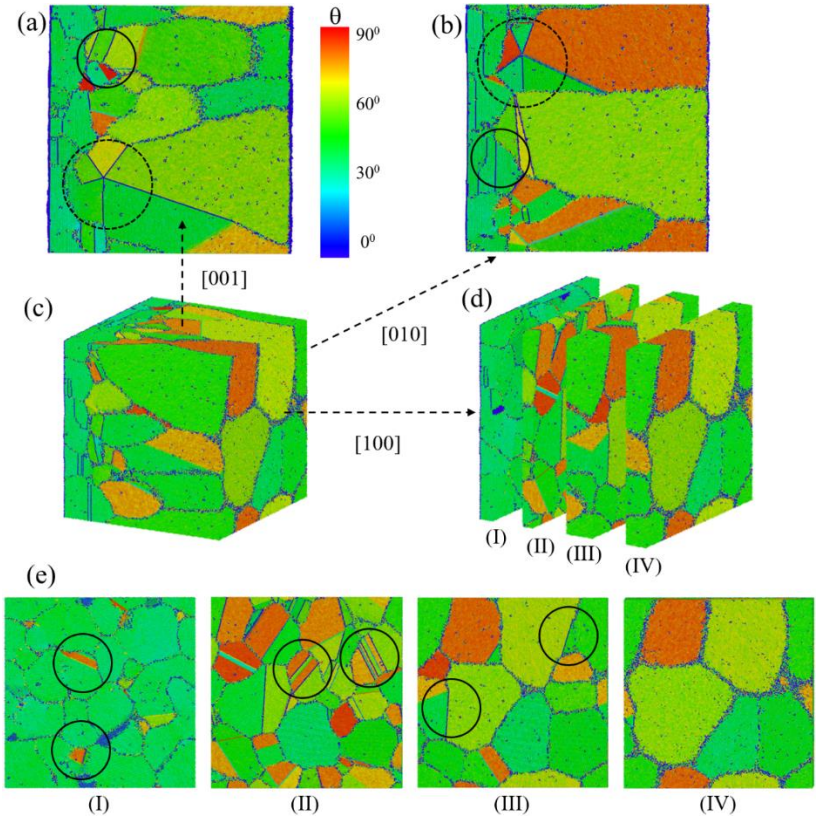

Figure 4. Orientation coloring of the twins and nanostructures of the directional solidification for sample Case-3. The figures are the following, (a) Twins and GBs are viewed from the top of the simulation box, (b) the grains and twins along the [100] solidification direction viewed from [010] direction, (c) the entire simulation box and the arrows shows the viewing directions (d) four layers has been sliced along the [100] solidification direction to observed the nanostructure facing the solidification font, (e) the nanostructures corresponding to the slices made in (d). The solid circles show coherent twin boundaries and dotted circles show fivefold twinning.

3.3. CU SEGREGATION AT GRAIN BOUNDARIES

Previously, Cu segregation in Al-Cu alloys was studied by atom probe tomography in Al-5 at% Cu [52], and Al-2 at% Cu [53], and MD simulation was only used to study the solid-state segregation of Cu to GBs by strain effects [54]. Al and Cu both are fcc, however there is a lattice mismatch between Al and Cu: the lattice constant for Al is 4.05 Å and Cu is 3.54 Å. As mentioned by Liu et al. [54], there is a strain effect that mediates diffusion of Cu atoms to GBs. To investigate and visualize Cu segregation during solidification and possible formation of precipitates, a slice with 5 nm thickness from the simulation box is taken (dotted plane in Figure 6(a)).

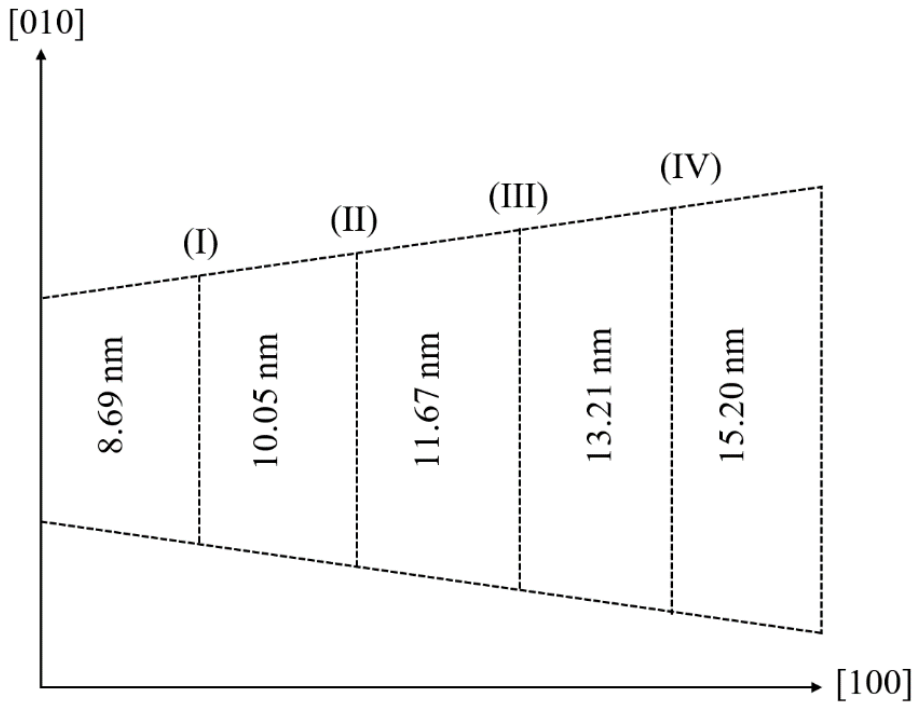

Figure 5. The average grain size on the (010) plane along the solidification direction for Case-3.

First, we visualize the copper atoms on the solidification font, and the 3D surface mesh in Figure 6(b) shows the topology of the solidification front; the blue Cu atoms are shown at the grain surfaces and GBs. This results suggests segregation of Cu atoms from the primary Al-Cu matrix onto GBs. Figure 6(c) shows the [100] plane at the slice shown in Figure 6(a); crystalline fcc and GBs contain both Al and Cu atoms. In Figure 6(d), Al atoms are removed and only Cu atoms are shown. It is clear that a large number of Cu atoms are deposited or segregated at the GBs.

To measure the Cu segregation on the GB, we used the same slice of the simulation in Figure 6(a). This surface is chosen from a distance of 10 nm from isothermal region at 600 K. In this way the chosen slice has a spontaneous temperature of between 650 and 700 K (Figure 3(a)) for different solidification cases. All the Al atoms are removed from this and only copper atoms are kept, then we calculated the ratio of Cu atoms on GBs to the all Cu atoms in the slice. The result is shown in Figure 6(e); the percentage of Cu atoms on GBs gradually increases as the annealing progresses in that area. This results suggest that a portion of Cu segregation onto GBs happens during solidification, but the majority of Cu segregation happens after the region in solidified but while it is being annealed.

3.4.AL_2CU PRECIPITATION

If concentration of Cu atoms is locally increased, formation of Al_2Cu precipitates especially at the GBs is probable. In Figure 7, two stages of solidification (450 ps and 900 ps) for the Case-1 solidification are presented. Both liquid and solid amorphous atoms are shown and then we performed coordination number (CN) analysis. The CN for Al_2Cu is

derived to be remained within 12 to 13 for the temperature range between 600 to 800 K [55]. All Al and Cu atoms with crystalline fcc and hcp atoms are removed in Figure 7.

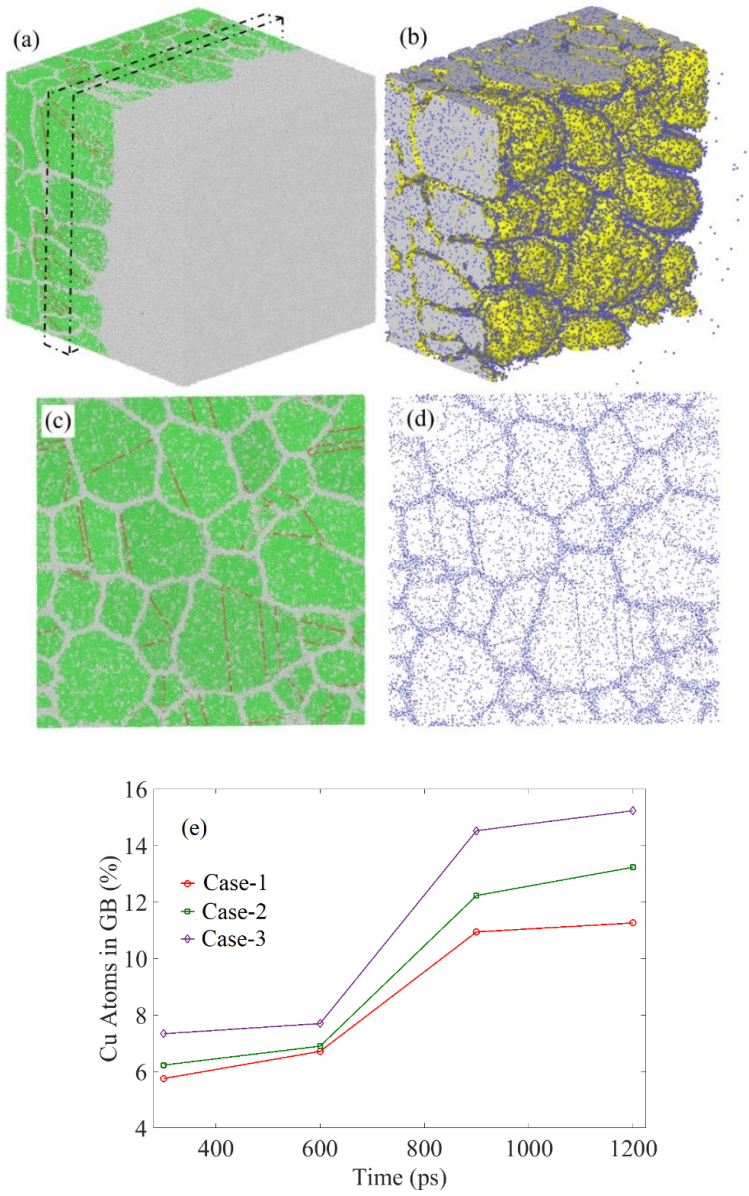

Figure 6. Detection of Al2Cu Precipitation during directional solidification of Al-Cu. (a) The 3-Dimesnional simulation box at 350 ps for Case-2. The dotted line shows the sliced planes for studying the interior of the solid font. (b) Surface mesh shows the copper atoms (blue) at the solid font and the GB regions. (c) The GB with both Al and Cu atoms from the sliced plane, (d) Only copper (blue) atoms shown on the GB and in the matrix.

As Figure 7 suggests, there are several precipitates that can be detected inside the grains and on the GBs. A low CN (blue or green colors) suggests that there is no particular structures for the liquid or solid atoms. The cluster of red atoms are having the exact CN for Al_2Cu, so those atom clusters can be identified as Al_2Cu precipitates. One of the areas with high CN is enlarged in Figure 7(c) where the bigger atoms represents the Cu and smaller atoms represents the Al, clearly shows a higher density of Cu atoms locally. Experimentally Al_2Cu-θ precipitates can reach have sizes in a range of 25-50 nm [56, 57], which is beyond the scope of this study. If the simulation size can be extended to billions of atoms (submicron length scale), one can expect to visualize Al_2Cu-θ precipitates similar to those observed by scanning electron microscopy.

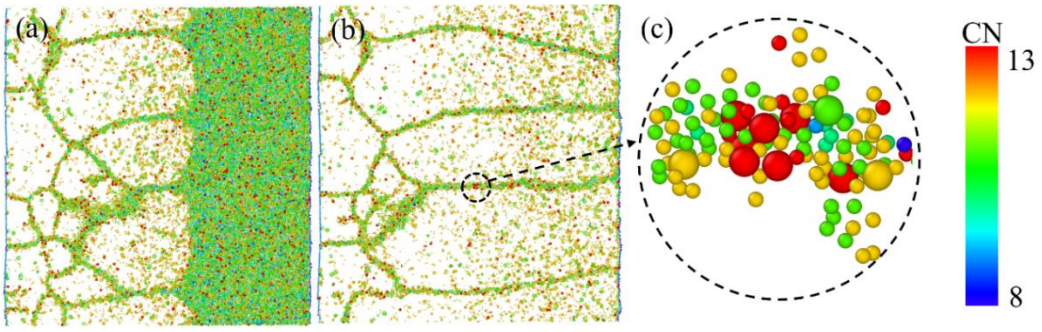

Figure 7. (a) GBs facing the solid font in [100] direction for Case-1 solidification at 450 ps and (b) 900 ps. Atoms are colored with coordination number. All the crystalline fcc and hcp atoms are removed. Amorphous solid and liquid are having same coordination. (c) An enlarged GB area that shows a much higher density of Cu and a high CN which is suitable for forming Al_2Cu precipitates. The bigger atoms represent Cu and smaller atoms represents Al.

3.5 MECHANICAL PROPERTIES

After obtaining the solidified polycrystalline structures of Al-11 at% Cu, the structures are deformed under uniaxial tension with two strain rates (10^9 s^{-1} -SR1 and 10^{10} s^{-1} -SR2) along ([100]) and perpendicular ([001]) to the solidification direction. The typical deformation process is shown in Figure 8. The snapshots on top of the stress-strain plot is the deformation along [100] direction and the bottom snapshots represents the deformation in the [001] direction. The trend for the stress strain curves are similar for all the other cases and strain rates in this work. The stress-strain curves in Figure 8 indicate the ductile nature of the polycrystalline Al-Cu alloy. After the simulation box reaches the elastic limit and plastic begins, partial dislocations glide in the opposite direction of deformation for tensile stress along [100] direction. Consequently, detwinning happens with a combination of reduction in twin thickness and the layer-by-layer twin boundary removal by the opposite glide of partial dislocations with a Burgers vector ($\frac{1}{2}[10\bar{1}]$) identical to that of the twinning partial dislocations. Typical detwinning of deformation twins is also observed while the sample is plastically deformed, which is similar to the observations in experimental work [58]. The stages of detwinning of deformation twins is similar to those of the solidification twins, and the details are discussed in our recent work [59]. The fivefold twins also detwin as the tensile deformation continues. The driving force behind the detwinning comes from the variation in the excess energy of the system during the tensile deformation.

As shown in the Figure 8, the bottom snapshots don't show any detwinning phenomena for deformation along the [001] direction. The difference in newly formed

deformation twins in two different deformation directions are significant. As shown in Figure 8, the twins formed during deformation along [100] direction are much smaller than those formed by deformation along [001] direction. In the fcc crystal structure, the dislocations glide by $\frac{1}{2}[10\bar{1}](full) \rightarrow \frac{1}{6}[11\bar{2}](partial) + \frac{1}{6}[2\bar{1}\bar{1}](partial)$. When stretching in the solidification direction, the dislocations get compressed and only remain partial for most cases causing formation of shorter twins, whereas deformation in [001] direction the dislocation can be stretched to a longer length and the defects becomes persistent. This is also another reason that UTS is lower when deforming perpendicular to the solidification direction.

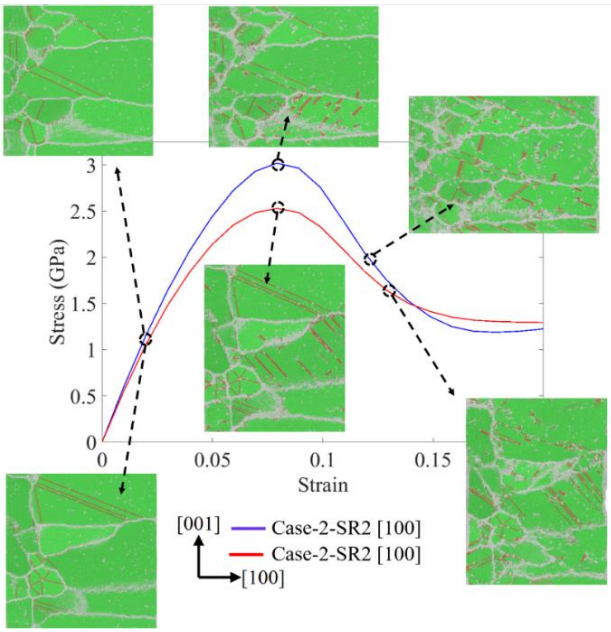

Figure 8. Stress-strain curves for uniaxial deformation along and perpendicular to the solidification direction [001] of solidified Al-Cu for Case-2 at 300 K. The corresponding snapshot of the Al-Cu simulation box is also shown on the stress-strain plot. The [100] and [001] directions are same for all the deformation snapshots.

Stress-strain curves for different polycrystalline cases produced by rapid solidification are presented in Figure 9 and compared with single crystal cases. Single crystal Al-Cu cases show a much higher yield stress, but fail immediately after the yield point us reached, suggesting a brittle behavior. The polycrystalline Al-Cu shows a long plastic region in the stress-strain plot. This indicates the ductile nature of polycrystalline Al-Cu and its ability to deform plastically. The stress–strain curve of polycrystalline Al-Cu under tensile loading has a trend identical to that of conventional polycrystalline metals, and it can be characterized into three stages: an initial elastic region, a yielding region, and a failure region. The ultimate tensile strength for single crystal Al-Cu is found to be 6.87 and 7.09 GPa for the strain rates of SR1 and SR2, respectively, which is much higher than the directionally solidified polycrystalline Al-Cu.

The failure strength for Al-11at% Cu remains in the range between 2 to 3 GPa for all the cases at different strain rates. The investigation of mechanical properties shows that the ultimate tensile strength (UTS) when deformed in the direction of solidification [100] is always higher than cases deformed perpendicular to the solidification direction, Figure 9(b). Figure 9(c) shows that the strain at UTS is also higher for cases deformed along [100] direction. This can be explained based on the grain orientations and the evolution of grains and twins during deformation. As shown in Figure 2 and Figure 4, during directional solidification grains forms in a lamellar pattern along [100] direction. Due to the formation of the elongated grains along [100] and lack of GBs oriented perpendicular to the solidification direction, the tensile deformation along [100] direction sees less influence from GBs. During the tensile deformation along the [001] direction, GBs act as weak links

and somewhat cause discontinuity in the Al-Cu matrix, therefore a lower yield point and plasticity at a lower stress are expected.

The orientation and alignment of the twins inside the grains also play a crucial role on determining the UTS. As shown in Figure 8 for the deformation along the solidification direction, partial dislocations glide in the opposite direction of twin boundary growth and also the [100] direction. Due to this reason the ultimate tensile strength as well as the ultimate tensile strain (Figure 9(a-b)) both remain higher for deformation along the solidification direction. When deformed in the [001] direction the twins only get stretched, and once it becomes plastic there are several partial dislocation glides at the GBs.

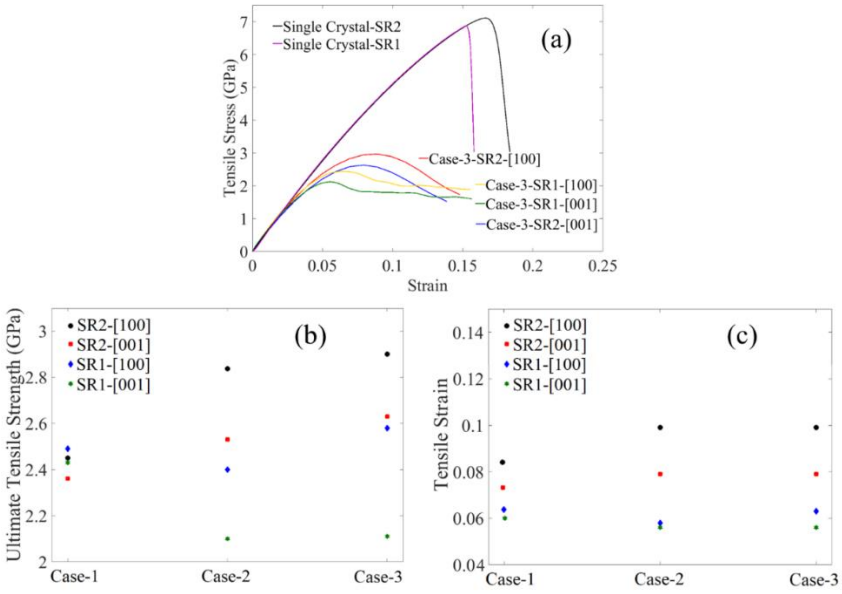

Figure 9. (a) The comparison of strength of Al-Cu single crystal and directionally solidified polycrystalline Al-11 at% Cu. (b) The ultimate tensile strength and (c) tensile strain is shows for strain rate of 10^9 (SR1) and 10^{10} s^{-1} (SR2) along the solidification direction, [100], and perpendicular to the solidification direction, [001]. The different solidification model is shown in the X axis. All deformation is performed at 300 K.

4. CONCLUSION

In this paper, we performed MD simulations utilizing 2NN MEAM interatomic potential to study rapid directional solidification of Al-11 at% Cu, and studied Cu segregation, Al_2Cu precipitation and deformation mechanisms of solidified polycrystalline under uniaxial tension. Initial solidification was performed with three different temperature gradients, and then mechanical properties were studied by uniaxial tensile deformation under two different strain rates.

At the initial stages of solidification, several small grains, twin boundaries and GBs formed, but as solidification progressed only a few of these grains grew and elongated towards the solidification direction. These elongated grains contained less defects, twins or GBs. The elongation of GBs also formed a layer by layer fcc matrix along the solidification direction. As the solidification font traveled along the [100] direction, some Cu atoms segregated to the liquid side of the solid-liquid interface, and the Cu segregation increased gradually during annealing after the region was solidified. The percentage of segregated Cu atoms increased as the solidification proceeds. Utilizing CN analysis, Al_2Cu precipitations were identified in the solid and liquid and at the GBs.

Deformation simulations suggested that the directionally solidified Al-Cu alloy has more strength when deformed in the direction of the solidification than other directions. When the simulation box was deformed perpendicular to the solidification direction, deformation occurred easier because GBs which are weak links were perpendicular to the loading direction. Also, the newly formed deformation twins by partial dislocation glide,

aligned along $\frac{1}{2}[10\bar{1}]$ direction, got stretched in the [001] direction and caused the Al-Cu matrix to fail at a lower strength than [100] direction.

Overall, we demonstrated some capabilities of MD simulations in study of rapid directional solidification of a binary system. With larger computational resources, solidification studies of metallic alloys in submicron scale are possible and comparable to experimental data. In the future, this computational approach can be applied to more realistically replicate several fundamental aspects of manufacturing processes involving solidification.

REFERENCES

[1] W. E. Frazier, "Metal additive manufacturing: a review," *Journal of Materials Engineering and Performance*, vol. 23, pp. 1917-1928, 2014.

[2] L. E. Murr, S. Gaytan, A. Ceylan, E. Martinez, J. Martinez, D. Hernandez, *et al.*, "Characterization of titanium aluminide alloy components fabricated by additive manufacturing using electron beam melting," *Acta materialia*, vol. 58, pp. 1887-1894, 2010.

[3] R. Dehoff and S. Babu, "Characterization of interfacial microstructures in 3003 aluminum alloy blocks fabricated by ultrasonic additive manufacturing," *Acta Materialia*, vol. 58, pp. 4305-4315, 2010.

[4] E. Uhlmann, A. Bergmann, and W. Gridin, "Investigation on additive manufacturing of tungsten carbide-cobalt by selective laser melting," *Procedia CIRP*, vol. 35, pp. 8-15, 2015.

[5] A. Bandyopadhyay and S. Bose, *Additive manufacturing*: CRC Press, 2015.

[6] J.-P. Kruth, L. Froyen, J. Van Vaerenbergh, P. Mercelis, M. Rombouts, and B. Lauwers, "Selective laser melting of iron-based powder," *Journal of materials processing technology*, vol. 149, pp. 616-622, 2004.

[7] J. Zhang, "Selective Separation Shaping: An Additive Manufacturing Method for Metals and Ceramics," University of Southern California, 2016.

[8] M. Morris and D. Morris, "Microstructures and mechanical properties of rapidly solidified Cu□ Cr alloys," *Acta metallurgica,* vol. 35, pp. 2511-2522, 1987.

[9] Y. Kawamura, K. Hayashi, A. Inoue, and T. Masumoto, "Rapidly solidified powder metallurgy Mg97Zn1Y2Alloys with excellent tensile yield strength above 600 MPa," *Materials Transactions,* vol. 42, pp. 1172-1176, 2001.

[10] M. De Sanctis, "Structure and properties of rapidly solidified ultrahigh strength Al□ Zn□ Mg□ Cu alloys produced by spray deposition," *Materials Science and Engineering: A,* vol. 141, pp. 103-121, 1991.

[11] G. Neilson and M. Weinberg, "A test of classical nucleation theory: crystal nucleation of lithium disilicate glass," *Journal of Non-Crystalline Solids,* vol. 34, pp. 137-147, 1979.

[12] D. Erdemir, A. Y. Lee, and A. S. Myerson, "Nucleation of crystals from solution: classical and two-step models," *Accounts of chemical research,* vol. 42, pp. 621-629, 2009.

[13] G. Kahl and H. Löwen, "Classical density functional theory: an ideal tool to study heterogeneous crystal nucleation," *Journal of Physics: Condensed Matter,* vol. 21, p. 464101, 2009.

[14] S. Toxvaerd, "Molecular-dynamics simulation of homogeneous nucleation in the vapor phase," *The Journal of Chemical Physics,* vol. 115, pp. 8913-8920, 2001.

[15] X. Sui, Y. Cheng, N. Zhou, B. Tang, and L. Zhou, "Molecular dynamics simulation of solidification process of multicrystalline silicon from homogeneous nucleation to grain coarsening," *CrystEngComm,* 2018.

[16] A. Mahata, M. Asle Zaeem, and M. I. Baskes, "Understanding homogeneous nucleation in solidification of aluminum by molecular dynamics simulations," *Modelling and Simulation in Materials Science and Engineering,* vol. 26, p. 025007, 2018.

[17] K. Oh and X. C. Zeng, "Formation free energy of clusters in vapor-liquid nucleation: A Monte Carlo simulation study," *The Journal of chemical physics,* vol. 110, pp. 4471-4476, 1999.

[18] D. Srolovitz, G. Grest, and M. Anderson, "Computer simulation of recrystallization—I. Homogeneous nucleation and growth," *Acta metallurgica,* vol. 34, pp. 1833-1845, 1986.

[19] B. Böttger, J. Eiken, and I. Steinbach, "Phase field simulation of equiaxed solidification in technical alloys," *Acta materialia,* vol. 54, pp. 2697-2704, 2006.

[20] L. Gránásy, T. Börzsönyi, and T. Pusztai, "Nucleation and bulk crystallization in binary phase field theory," *Physical review letters,* vol. 88, p. 206105, 2002.

[21] L. Gránásy, T. Pusztai, D. Saylor, and J. A. Warren, "Phase field theory of heterogeneous crystal nucleation," *Physical review letters,* vol. 98, p. 035703, 2007.

[22] S. Wang, M. Asle Zaeem, M. F. Horstemeyer, and P. T. Wang, "Investigating thermal effects on morphological evolution during crystallisation of hcp metals: three-dimensional phase field study AU - Wang, S," *Materials Technology,* vol. 27, pp. 355-363, 2012/11/01 2012.

[23] M. Asle Zaeem, H. Yin, and S. D. Felicelli, "Modeling dendritic solidification of Al–3%Cu using cellular automaton and phase-field methods," *Applied Mathematical Modelling,* vol. 37, pp. 3495-3503, 2013/03/01/ 2013.

[24] L. Liu, S. Pian, Z. Zhang, Y. Bao, R. Li, and H. Chen, "A cellular automaton-lattice Boltzmann method for modeling growth and settlement of the dendrites for Al-4.7% Cu solidification," *Computational Materials Science,* vol. 146, pp. 9-17, 2018.

[25] M. Asle Zaeem, H. Yin, and S. D. Felicelli, "Comparison of Cellular Automaton and Phase Field Models to Simulate Dendrite Growth in Hexagonal Crystals," *Journal of Materials Science & Technology,* vol. 28, pp. 137-146, 2012/02/01/ 2012.

[26] K. Li, D. Li, J. Liang, Y. Ye, Y. Liao, R. Liu, *et al.*, "Performance analysis of parallel algorithms in physics simulation for molecular dynamics simulation liquid metals solidification processes," *Computers & Fluids,* vol. 110, pp. 19-26, 2015.

[27] Y.-F. Mo, R.-S. Liu, Y.-C. Liang, H.-T. Zhang, Z.-A. Tian, Z.-Y. Hou, *et al.*, "Formation and evolution of nano-clusters in a large-scale system of Cu–Zr alloy during rapid solidification process," *Computational Materials Science,* vol. 98, pp. 1-9, 2015.

[28] J. N. Glosli, D. F. Richards, K. Caspersen, R. E. Rudd, J. A. Gunnels, and F. H. Streitz, "Extending stability beyond CPU millennium: a micron-scale atomistic simulation of Kelvin-Helmholtz instability," in *Supercomputing, 2007. SC'07. Proceedings of the 2007 ACM/IEEE Conference on*, 2007, pp. 1-11.

[29] A. Sorkin, J. Tan, and C. Wong, "Multi-material modelling for selective laser melting," *Procedia engineering,* vol. 216, pp. 51-57, 2017.

[30] Z. Hu and S. Mahadevan, "Uncertainty quantification in prediction of material properties during additive manufacturing," *Scripta Materialia,* vol. 135, pp. 135-140, 2017.

[31] B.-J. Lee and M. Baskes, "Second nearest-neighbor modified embedded-atom-method potential," *Physical Review B,* vol. 62, p. 8564, 2000.

[32] E. Asadi, M. Asle Zaeem, S. Nouranian, and M. I. Baskes, "Two-phase solid–liquid coexistence of Ni, Cu, and Al by molecular dynamics simulations using the modified embedded-atom method," *Acta Materialia,* vol. 86, pp. 169-181, 2015.

[33] A. Mahata and M. Asle Zaeem, "Modified embedded atom method potential for binary Al alloys for melting and solid-liquid coexistence properties," *Submitted to Acta Materillia* 2019.

[34] E. Asadi, M. Asle Zaeem, S. Nouranian, and M. I. Baskes, "Quantitative modeling of the equilibration of two-phase solid-liquid Fe by atomistic simulations on diffusive time scales," *Physical Review B,* vol. 91, p. 024105, 2015.

[35] G. Simmons and H. Wang, "Single crystal elastic constants and calculated aggregate properties," 1971.

[36] W. F. Gale and T. C. Totemeier, *Smithells metals reference book*: Butterworth-Heinemann, 2003.

[37] A. M. James and M. P. Lord, *Macmillan's chemical and physical data*: Macmillan, 1992.

[38] J. G. Speight, *Lange's handbook of chemistry* vol. 1: McGraw-Hill New York, 2005.

[39] Q. Jiang and H. Lu, "Size dependent interface energy and its applications," *Surface Science Reports,* vol. 63, pp. 427-464, 2008.

[40] L. Gránásy, M. Tegze, and A. Ludwig, "Solid–liquid interfacial free energy," in *Rapidly Quenched Materials*, ed: Elsevier, 1991, pp. 577-580.

[41] M. Gündüz and J. Hunt, "The measurement of solid-liquid surface energies in the Al-Cu, Al-Si and Pb-Sn systems," *Acta Metallurgica,* vol. 33, pp. 1651-1672, 1985.

[42] M. Parrinello and A. Rahman, "Polymorphic transitions in single crystals: A new molecular dynamics method," *Journal of Applied physics,* vol. 52, pp. 7182-7190, 1981.

[43] S. Plimpton, "Fast parallel algorithms for short-range molecular dynamics," *Journal of computational physics,* vol. 117, pp. 1-19, 1995.

[44] A. Stukowski, "Visualization and analysis of atomistic simulation data with OVITO–the Open Visualization Tool," *Modelling and Simulation in Materials Science and Engineering,* vol. 18, p. 015012, 2009.

[45] H. Tsuzuki, P. S. Branicio, and J. P. Rino, "Structural characterization of deformed crystals by analysis of common atomic neighborhood," *Computer physics communications,* vol. 177, pp. 518-523, 2007.

[46] P. M. Larsen, S. Schmidt, and J. Schiøtz, "Robust structural identification via polyhedral template matching," *Modelling and Simulation in Materials Science and Engineering,* vol. 24, p. 055007, 2016.

[47] H. Hofmeister, "Forty Years Study of Fivefold Twinned Structures in Small Particles and Thin Films," *Crystal Research and Technology,* vol. 33, pp. 3-25, 1998.

[48] T. Shen, Y. Wu, and X. Lu, "Structural evolution of five-fold twins during the solidification of Fe 5601 nanoparticle: a molecular dynamics simulation," *Journal of molecular modeling,* vol. 19, pp. 751-755, 2013.

[49] A. J. Cao and Y. G. Wei, "Formation of fivefold deformation twins in nanocrystalline face-centered-cubic copper based on molecular dynamics simulations," *Applied Physics Letters,* vol. 89, p. 041919, 2006/07/24 2006.

[50] Y. T. Zhu, X. Z. Liao, and R. Z. Valiev, "Formation mechanism of fivefold deformation twins in nanocrystalline face-centered-cubic metals," *Applied Physics Letters,* vol. 86, p. 103112, 2005/03/07 2005.

[51] J. Narayan, "Dislocations, twins, and grain boundaries in CVD diamond thin films: Atomic structure and properties," *Journal of Materials Research,* vol. 5, pp. 2414-2423, 1990.

[52] C. Srivastava, G. Thompson, D. Reinhard, J. Sebastian, T. Prosa, D. Larson, *et al.*, "Atom Probe Tomography of Al-Cu Precipitation in an Al-5 at.%Cu Thin Film," *Microscopy and Microanalysis,* vol. 12, pp. 1752-1753, 2006.

[53] P.-P. Choi, T. Al-Kassab, and R. Kirchheim, "Investigation of sputter-deposited Al–2at.%Cu layers by means of the tomographic atom probe (TAP)," *Scripta Materialia,* vol. 53, pp. 323-327, 2005/08/01/ 2005.

[54] X.-Y. Liu, W. Xu, S. a. Foiles, and J. Adams, "Atomistic studies of segregation and diffusion in Al-Cu grain boundaries," *Applied physics letters,* vol. 72, pp. 1578-1580, 1998.

[55] L. Xiong, F. Guo, X. Wang, Q. Cao, D. Zhang, Y. Ren, *et al.*, "Structural evolution and dynamical properties of Al2Ag and Al2Cu liquids studied by experiments and ab initio molecular dynamics simulations," *Journal of Non-Crystalline Solids,* vol. 459, pp. 160-168, 2017.

[56] G. Simmons, "Single crystal elastic constants and calculated aggregate properties," SOUTHERN METHODIST UNIV DALLAS TEX1965.

[57] Y. Huang, J. D. Robson, and P. B. Prangnell, "The formation of nanograin structures and accelerated room-temperature theta precipitation in a severely deformed Al–4wt.% Cu alloy," *Acta Materialia,* vol. 58, pp. 1643-1657, 2010/03/01/ 2010.

[58] B. Li, M. Sui, B. Li, E. Ma, and S. Mao, "Reversible twinning in pure aluminum," *Physical review letters,* vol. 102, p. 205504, 2009.

[59] A. Mahata and M. Asle Zaeem, "Evolution of Solidification Defects in Deformation of Nano-Polycrystalline Aluminum " *Under Review, Computational Materials Science, 2019*.

SECTION

3. CONCLUSION

This Ph.D. research aimed to study the solidification phenomena by utilizing molecular dynamics and also develop interatomic potential parameters to simulate the similar solidification by nucleation for binary Al-alloys. The results from the solidification can be replicated to any other materials systems and can be compared with experimentally available data of the nucleation and solidification process. This proves the accuracy and predictability of molecular dynamics methods as well as the applicability of the MEAM interatomic potentials. The study of size effect on solidification simulation by MD simulation predicts an optimum size to study the homogenous nucleation.

The study of homogenous nucleation then extended to study the more fundamental aspects of nucleation such as, heterogeneity in homogenous nucleation. By utilizing very accurate MEAM interatomic potential, twinning and initial short range order in liquid orders is observed in all different materials systems (fcc Al, bcc Fe and hcp Mg). This study also argued that ico is not the precursor for the crystalline Fe atoms, rather than the short-range order in the supercooled liquid transform to bcc-Fe.

The binary interatomic potentials developed during in my PhD will be able to replicate the same mechanical and solidification properties of those alloys. As both low and high temperature properties are fitted to parameterize the potentials it can be also used for studying mechanical properties of the different binary Al alloys. The interatomic potential for Al-Cu was utilized to analyze the directional solidification.

4. RECOMMENDATIONS FOR FUTURE WORK

- *Multiscale modelling by bridging atomic and mesoscale*

There are several quantities from MD simulation such as solid-liquid interface free energy, diffusion coefficient, anisotropy, surface energy etc. can be obtained and then those data can be used to simulate the phase field model. Those the atomistic scale calculation can be linked to mesoscale and a multiscale modellig framework can be developed. In this work, all the interatomic potential has been developed considering both soliid and liquid properties, low and high temperature melting properties. Interatomic potential of this kind is a step towards a true multiscale modelling framework.

- *Extending the alloying interatomic potential to ternary alloys*

The interatomic potential for binary alloys can be easily extended to ternary by mixing the potential parameters. The single crystal was fitted to melting properties, the mixed binary alloys predicted reasonable results to compare with experimental or first principle data. In the same way, the ternary alloy interatomic potential can also be developed. As the MEAM potential for single crystal Al, Fe and Ni was already available, and the binary combination such as Al-Fe, Al-Ni is deleoped, it is possible to extend the interatomic potential to Al-Fe-Ni or similar ternary interatomic potential.

- *Development interatomic potential for metallic oxides*

In order to study the realistic solidification in open atmosphere, it is necessary to have interatomic potential that can replicate the oxidation behavior at lower and higher temperature for metals and its alloys. To develop interatomic potentials for oxidation the electrostatic parameters should be taken into consideration. The approach of this kind is

state of art and the interatomic potential should be parameterized by considering have both the metallic and oxide properties.

- *Billion to multibillion atom simulation*

Although the solid nuclei in the interior part of the liquid can be analyzed by only a million atoms simulation, to compare the MD results for validation of experimental data for solidification and mechanical properties, the simulation size can be extended to billion atoms (or micrometer scale). In directional solidification if the box size can be kept up to micrometer scale, it is possible to replicate dendritic structures in solidification.

BIBLIOGRAPHY

[1] J. Campbell, *Complete casting handbook: metal casting processes, metallurgy, techniques and design*: Butterworth-Heinemann, 2015.

[2] J. W. Christian, *The theory of transformations in metals and alloys*: Newnes, 2002.

[3] D. Hu and R. Kovacevic, "Sensing, modeling and control for laser-based additive manufacturing," *International Journal of Machine Tools and Manufacture,* vol. 43, pp. 51-60, 2003.

[4] D. W. Oxtoby, "Homogeneous nucleation: theory and experiment," *Journal of Physics: Condensed Matter,* vol. 4, p. 7627, 1992.

[5] P.-P. E. de Moor, T. P. Beelen, and R. A. van Santen, "In situ observation of nucleation and crystal growth in zeolite synthesis. A small-angle X-ray scattering investigation on Si-TPA-MFI," *The Journal of Physical Chemistry B,* vol. 103, pp. 1639-1650, 1999.

[6] D. Zhang and B. Cantor, "Heterogeneous nucleation of In particles embedded in an AI matrix," *Philosophical Magazine A,* vol. 62, pp. 557-572, 1990.

[7] D. Uhlenhaut, J. Kradolfer, W. Püttgen, J. Löffler, and P. Uggowitzer, "Structure and properties of a hypoeutectic chromium steel processed in the semi-solid state," *Acta Materialia,* vol. 54, pp. 2727-2734, 2006.

[8] C. Ho and B. Cantor, "Heterogeneous nucleation of solidification of Si in Al-Si and Al-Si-P alloys," *Acta metallurgica et materialia,* vol. 43, pp. 3231-3246, 1995.

[9] D. Turnbull and R. Cech, "Microscopic observation of the solidification of small metal droplets," *Journal of Applied Physics,* vol. 21, pp. 804-810, 1950.

[10] S. Ringer, K. Hono, I. Polmear, and T. Sakurai, "Nucleation of precipitates in aged Al Cu Mg (Ag) alloys with high Cu: Mg ratios," *Acta Materialia,* vol. 44, pp. 1883-1898, 1996.

[11] F. Humphreys, "The nucleation of recrystallization at second phase particles in deformed aluminium," *Acta Metallurgica,* vol. 25, pp. 1323-1344, 1977.

[12] B. Cantor and K. O'Reilly, *Solidification and casting*: CRC Press, 2016.

[13] G. Neilson and M. Weinberg, "A test of classical nucleation theory: crystal nucleation of lithium disilicate glass," *Journal of Non-Crystalline Solids,* vol. 34, pp. 137-147, 1979.

[14] D. Erdemir, A. Y. Lee, and A. S. Myerson, "Nucleation of crystals from solution: classical and two-step models," *Accounts of chemical research,* vol. 42, pp. 621-629, 2009.

[15] S. J. Lindsay, "Very High Purity Aluminum: An Historical Perspective," *JOM,* vol. 66, pp. 217-222, 2014.

[16] M. Kondo, H. Maeda, and M. Mizuguchi, "The production of high-purity aluminum in Japan," *Jom,* vol. 42, pp. 36-37, 1990.

[17] S. Lee, H. S. Wi, W. Jo, Y. C. Cho, H. H. Lee, S.-Y. Jeong, *et al.*, "Multiple pathways of crystal nucleation in an extremely supersaturated aqueous potassium dihydrogen phosphate (KDP) solution droplet," *Proceedings of the National Academy of Sciences,* vol. 113, pp. 13618-13623, 2016.

[18] R. E. Schreiber, L. Houben, S. G. Wolf, G. Leitus, Z.-L. Lang, J. J. Carbó, *et al.*, "Real-time molecular scale observation of crystal formation," *Nature Chemistry,* 2016.

[19] P. Yi and G. C. Rutledge, "Molecular origins of homogeneous crystal nucleation," *Annual review of chemical and biomolecular engineering,* vol. 3, pp. 157-182, 2012.

[20] G. Kahl and H. Löwen, "Classical density functional theory: an ideal tool to study heterogeneous crystal nucleation," *Journal of Physics: Condensed Matter,* vol. 21, p. 464101, 2009.

[21] D. Juric and G. Tryggvason, "A Front-Tracking Method for Dendritic Solidification," *Journal of Computational Physics,* vol. 123, pp. 127-148, 1996.

[22] R. Kobayashi, "Modeling and numerical simulations of dendritic crystal growth," *Physica D: Nonlinear Phenomena,* vol. 63, pp. 410-423, 1993.

[23] Z. H. Li, D. Bhatt, N. E. Schultz, J. I. Siepmann, and D. G. Truhlar, "Free Energies of Formation of Metal Clusters and Nanoparticles from Molecular Simulations: Al n with n= 2-60," *The Journal of Physical Chemistry C,* vol. 111, pp. 16227-16242, 2007.

[24] S. L. Girshick, P. Agarwal, and D. G. Truhlar, "Homogeneous nucleation with magic numbers: Aluminum," *The Journal of chemical physics,* vol. 131, p. 134305, 2009.

[25] P. R. ten Wolde and D. Frenkel, "Homogeneous nucleation and the Ostwald step rule," *Physical Chemistry Chemical Physics,* vol. 1, pp. 2191-2196, 1999.

[26] A. Laaksonen, V. Talanquer, and D. W. Oxtoby, "Nucleation: Measurements, theory, and atmospheric applications," *Annual Review of Physical Chemistry,* vol. 46, pp. 489-524, 1995.

[27] H. Reiss, W. Kegel, and J. Katz, "Role of the model dependent translational volume scale in the classical theory of nucleation," *The Journal of Physical Chemistry A,* vol. 102, pp. 8548-8555, 1998.

[28] A. Cacciuto, S. Auer, and D. Frenkel, "Onset of heterogeneous crystal nucleation in colloidal suspensions," *Nature,* vol. 428, pp. 404-406, 2004.

[29] M. Mandell, J. McTague, and A. Rahman, "Crystal nucleation in a three-dimensional Lennard-Jones system: A molecular dynamics study," *The journal of chemical physics,* vol. 64, pp. 3699-3702, 1976.

[30] M. Horsch, J. Vrabec, and H. Hasse, "Modification of the classical nucleation theory based on molecular simulation data for surface tension, critical nucleus size, and nucleation rate," *Physical Review E,* vol. 78, p. 011603, 2008.

[31] S. Wonczak, R. Strey, and D. Stauffer, "Confirmation of classical nucleation theory by Monte Carlo simulations in the 3-dimensional Ising model at low temperature," *The Journal of Chemical Physics,* vol. 113, pp. 1976-1980, 2000.

[32] K. Kelton and A. Greer, "Test of classical nucleation theory in a condensed system," *Physical Review B,* vol. 38, p. 10089, 1988.

[33] R. Heady and J. Cahn, "Experimental test of classical nucleation theory in a liquid-liquid miscibility gap system," *The Journal of Chemical Physics,* vol. 58, pp. 896-910, 1973.

[34] H. Vehkamäki, *Classical nucleation theory in multicomponent systems*: Springer Science & Business Media, 2006.

[35] L. Filion, R. Ni, D. Frenkel, and M. Dijkstra, "Simulation of nucleation in almost hard-sphere colloids: The discrepancy between experiment and simulation persists," *The Journal of chemical physics,* vol. 134, p. 134901, 2011.

[36] P. Rein ten Wolde, M. J. Ruiz-Montero, and D. Frenkel, "Numerical calculation of the rate of crystal nucleation in a Lennard-Jones system at moderate undercooling," *The Journal of chemical physics,* vol. 104, pp. 9932-9947, 1996.

[37] S. Auer and D. Frenkel, "Prediction of absolute crystal-nucleation rate in hard-sphere colloids," *Nature,* vol. 409, pp. 1020-1023, 2001.

[38] E. Asadi, M. A. Zaeem, S. Nouranian, and M. I. Baskes, "Two-phase solid–liquid coexistence of Ni, Cu, and Al by molecular dynamics simulations using the modified embedded-atom method," *Acta Materialia,* vol. 86, pp. 169-181, 2015.

[39] S. Wang, M. Asle Zaeem, M. F. Hortsmeyer, and P. T. Wang, "Thermal effects on the morphological evolution during crystallization of HCP metals: A three dimensional phase-field study," *Materials Technology,* vol. 27(5), pp. 355-363, 2012.

[40] M. Asle Zaeem and S. Felicelli, "Simulation of dendrite growth in solidification of Al-3% Cu using cellular automaton and phase-field methods," *Applied Mathematical Modeling,* 2013.

[41] M. Asle Zaeem, H. Yin, and S. D. Felicelli, "Comparison of Cellular Automaton and Phase Field Models to Simulate Dendrite Growth in Hexagonal Crystals," *Materials Science & Technology,* vol. 28, pp. 137-146, 2012.

[42] Y. Shibuta, S. Sakane, T. Takaki, and M. Ohno, "Submicrometer-scale molecular dynamics simulation of nucleation and solidification from undercooled melt: Linkage between empirical interpretation and atomistic nature," *Acta Materialia,* vol. 105, pp. 328-337, 2016.

[43] Z. Hou, K. Dong, Z. Tian, R. Liu, Z. Wang, and J. Wang, "Cooling rate dependence of solidification for liquid aluminium: a large-scale molecular dynamics simulation study," *Physical Chemistry Chemical Physics,* vol. 18, pp. 17461-17469, 2016.

[44] K. Yasuoka and M. Matsumoto, "Molecular dynamics simulation of homogeneous nucleation in supersaturated water vapor," *Fluid Phase Equilibria,* vol. 144, pp. 369-376, 1998.

[45] M. Finnis and J. Sinclair, "A simple empirical N-body potential for transition metals," *Philosophical Magazine A,* vol. 50, pp. 45-55, 1984.

[46] T. Kawasaki and H. Tanaka, "Formation of a crystal nucleus from liquid," *Proceedings of the National Academy of Sciences,* vol. 107, pp. 14036-14041, 2010.

[47] W. C. Swope and H. C. Andersen, "10 6-particle molecular-dynamics study of homogeneous nucleation of crystals in a supercooled atomic liquid," *Physical Review B,* vol. 41, p. 7042, 1990.

[48] M. A. Z. Avik Mahata, "Size Effect on Nucleation Process during Solidification of Pure Metals by Atomistic Simulations," *Submitted to Journal of Crystal Growth,* 2019.

[49] E. Asadi and M. Asle Zaeem, "The anisotropy of hexagonal close-packed and liquid interface free energy using molecular dynamics simulations based on modified embedded-atom method," *Acta Materialia,* vol. 107, pp. 337-344, 2016/04/01/ 2016.

[50] E. Asadi, M. A. Zaeem, S. Nouranian, and M. I. Baskes, "Quantitative modeling of the equilibration of two-phase solid-liquid Fe by atomistic simulations on diffusive time scales," *Physical Review B,* vol. 91, p. 024105, 2015.

[51] Y.-M. Kim, N. J. Kim, and B.-J. Lee, "Atomistic modeling of pure Mg and Mg–Al systems," *Calphad,* vol. 33, pp. 650-657, 2009.

[52] B. Jelinek, S. Groh, M. F. Horstemeyer, J. Houze, S.-G. Kim, G. J. Wagner, *et al.*, "Modified embedded atom method potential for Al, Si, Mg, Cu, and Fe alloys," *Physical Review B,* vol. 85, p. 245102, 2012.

VITA

Avik Kumar Mahata was born in Midnapore, India. He received his PhD degree in Materials Science and Engineering from Missouri University of Science and Technology, Rolla, Missouri in May 2019. He pursued his PhD on computational materials science research. His research study was primarily focused in: 1) computational study of nucleation during solidification at atomic scale; 2) development the underlying interatomic potential responsible for predicting materials properties.

Before joining his PhD program, he completed his Bachelors of Engineering in Mechanical Engineering from Indian Institute of Engineering Science & Technology, Shibpur, India (2006-2010) and then he completed his Masters in Material Science & Engineering (2012-2014) from National Institute of Technology, Trichy, India. Avik also worked in the field of Software Engineering for 2 years (2010-2012). Avik's research career began in Indian Institute of Science in the department of Aerospace Engineering, where he worked as a project associate in 2014-2015.